

Raphael Renato Neuhaus

»New manufacturing and integration methods of CNT-based ionic EAP actuators and their application potential in adaptive building envelopes«



Raphael Neuhaus

» New manufacturing and integration methods
of CNT-based ionic EAP actuators
and their application potential
in adaptive building envelopes «

Herausgeber

Univ.-Prof. Dr.-Ing. Thomas Bauernhans^{1,2}

Univ.-Prof. Dr.-Ing. Dipl.-Kfm. Alexander Sauer^{1,3}

Univ.-Prof. Dr.-Ing. Kai Peter Birke⁴

Univ.-Prof. Dr.-Ing. Marco Huber^{1,2}

¹ Fraunhofer-Institut für Produktionstechnik und Automatisierung IPA, Stuttgart

² Institut für Industrielle Fertigung und Fabrikbetrieb (IFF) der Universität Stuttgart

³ Institut für Energieeffizienz in der Produktion (EEP) der Universität Stuttgart

⁴ Institut für Photovoltaik (*ipv*) der Universität Stuttgart

Kontaktadresse:

Fraunhofer-Institut für Produktionstechnik und Automatisierung IPA
Nobelstr. 12
70569 Stuttgart
Telefon 0711 970-1100
info@ipa.fraunhofer.de
www.ipa.fraunhofer.de

Bibliographische Information der Deutschen Nationalbibliothek

Die Deutsche Nationalbibliothek verzeichnet diese Publikation in der Deutschen Nationalbibliographie; detaillierte bibliografische Daten sind im Internet über <http://dnb.de> abrufbar.

Zugl.: Stuttgart, Univ., Diss., 2022

D 93

2023

Druck und Weiterverarbeitung:

Fraunhofer Verlag Mediendienstleistungen, Stuttgart, 2023
Für den Druck des Buches wurde chlor- und säurefreies Papier verwendet.

Dieses Werk ist einschließlich aller seiner Teile urheberrechtlich geschützt. Alle Rechte, insbesondere die der Übersetzung, des Nachdrucks, der Wiedergabe, sind vorbehalten.

New manufacturing and integration methods of CNT-based ionic EAP actuators and their application potential in adaptive building envelopes

Von der Fakultät für Konstruktions-, Produktions- und Fahrzeugtechnik
der Universität Stuttgart
zur Erlangung der Würde eines Doktor-Ingenieurs (Dr.-Ing.)
genehmigte Abhandlung

Vorgelegt von

Raphael Renato Neuhaus

aus Offenbach am Main

Hauptberichter: Univ.-Prof. Dr.-Ing. Thomas Bauernhansl

Mitberichter: Univ.-Prof. Dr.-Ing. Edwin Jäger

Tag der mündlichen Prüfung: 13.12.2022

Institut für Industrielle Fertigung und Fabrikbetrieb (IFF)
der Universität Stuttgart

2023

Vorwort des Autors

Diese Arbeit entstand während meiner Zeit am Institut für Industrielle Fertigung und Fabrikbetrieb (IFF) an der Universität Stuttgart. Als wissenschaftlicher Mitarbeiter war ich in vollem Umfang in die Abteilung für funktionale Materialien am Fraunhofer Institut für Produktionstechnik und Automatisierung (IPA) eingegliedert, wodurch mir eine breite Infrastruktur in Form von modernen Laboren und Forschungsanlagen für meine Arbeiten zur Verfügung stand. Mein größter Dank gilt somit den Wissenschaftlern und Wissenschaftlerinnen am IPA, die mich über Jahre kollegial begleitet und in meinem Vorhaben konsequent unterstützt haben.

Namentlich erwähnen möchte ich meinen Gruppenleiter Carsten Glanz und meinen Abteilungsleiter Ivica Kolaric, die mich an EAPs herangeführt und mir sowohl bei der Fokussierung des Themas als auch bei der Finanzierung über Forschungsprojekte geholfen haben. Durch sie wurde eine enge Kooperation mit Wissenschaftlern des Japanischen Forschungsinstitut AIST in Kansai ins Leben gerufen, auf deren Vorarbeiten und Methodik diese Arbeit fußt. Mein besonderer Dank gilt Dr. Takushi Sugino, einer der Väter der CNT-Aktoren, der mir stets mit seiner Fachkenntnis zur Seite stand und mich während meines Forschungsaufenthalts in Japan und in unzähligen Gastbesuchen am IPA lehrte, dass Geduld, Beharrlichkeit und Akribie zu den fundamentalen Tugenden eines Wissenschaftlers gehören.

Des Weiteren geht mein Dank an die Akteure im Sonderforschungsbereich 1244, der im Jahr 2017 an der Uni Stuttgart eingerichtet wurde, um an adaptiven Tragwerken und Hüllen für die Gebäude der Zukunft zu forschen. Als Teil eines interdisziplinären Konsortiums und unter Leitung von Prof. Werner Sobek durfte ich vier intensive Jahre aktiv am wissenschaftlichen Diskurs über die Zukunft des Bauens teilnehmen, was meinen weiteren Lebensweg nachhaltig prägen wird.

Zu guter Letzt danke ich meinem Institutsleiter und Doktorvater Herrn Prof. Bauernhansl für sein Vertrauen und die exzellente Betreuung dieser Arbeit.

Preface of the author

This thesis was prepared during my time working for the institute for industrial manufacturing and management (IFF) at the University of Stuttgart. As a research associate I was fully embedded in the Department of Functional Materials at the Fraunhofer Institute for Manufacturing Engineering and Automation (IPA), where I had access to a broad scientific infrastructure in terms of modern laboratories and technical equipment. My greatest thanks therefore goes to my fellow scientists at IPA, who have accompanied me in a collegial manner over the years and consistently supported me in my project.

I would like to mention by name my group leader Carsten Glanz and my department head Ivica Kolaric, who introduced me to EAPs and helped me both in focusing the topic and in obtaining funding through research projects. They have established a close cooperation with scientists from the Japanese Research Institute AIST in Kansai, who have developed the underlying IEAP technology on which this thesis is based. My special thanks go to Dr. Takushi Sugino, one of the fathers of CNT actuators, who supported me with his expertise and taught me during my research stay in Japan and in countless guest visits at IPA that patience, perseverance and meticulousness are fundamental virtues of a scientist.

Furthermore, my thanks go to my former colleagues from the Collaborative Research Center 1244, which was established at the University of Stuttgart in 2017 to conduct research on adaptive load-bearing structures and envelopes for the buildings of the future. As part of an interdisciplinary consortium and under the leadership of Prof. Werner Sobek, I was able to actively participate in the scientific discourse on the future of buildings and construction for four intensive years, which will have a lasting impact on my future life.

Last but not least, I would like to thank my institute director and doctoral supervisor Prof. Bauernhansl for his trust and excellent supervision of this thesis.

Content

List of illustrations	v
List of Tables.....	viii
List of abbreviations	ix
Abstract	xi
Kurzzusammenfassung.....	xiii
1 Introduction	1
1.1 Societal relevance and general context	2
1.1.1 Demographic changes and their effects on the building sector	2
1.1.2 Potentials in reducing construction materials and grey energy	3
1.1.3 Lightweight membrane structures as building skins	4
1.1.4 The need for adaptivity in building envelopes.....	6
1.1.5 Soft actuators for breathable building skins.....	7
1.2 Electroactive polymers for adaptive building envelopes	10
1.2.1 Dielectric EAP	10
1.2.2 Ionic EAP.....	11
1.3 Objectives	13
1.3.1 Problem statement	13
1.3.2 Derived research questions	14
1.3.3 Focus, work objectives and tasks.....	15
1.4 Conclusion of Chapter 1 and structure of this thesis	16
2 State of scientific and technical knowledge.....	19
2.1 Requirements for IEAPs used in adaptive building envelopes.....	20
2.1.1 Qualitative requirements.....	20
2.1.2 Quantitative requirements	20
2.2 Why CNT actuators?	23
2.2.1 Ionic EAP – an overview	23

2.2.2	Benchmarking performance characteristics of IEAP.....	25
2.2.3	Benchmarking of material and production related characteristics.....	28
2.2.4	Assessment of benchmarking results.....	31
2.3	CNT-based actuators – History and working principles.....	33
2.3.1	Individual CNT actuators.....	33
2.3.2	Buckypaper actuators.....	34
2.3.3	From Buckypaper to Bucky gel actuators.....	36
2.3.4	Properties of CNT actuators.....	38
2.3.5	Past and current efforts of performance optimization.....	40
2.4	State of the art regarding the manufacturing of CNT actuators.....	44
2.4.1	Mixing and dispersion techniques used for CNT actuator fabrication.....	44
2.4.2	General remarks about dispersing CNTs.....	46
2.4.3	State of the art casting, printing and drying techniques.....	48
2.4.4	Actuator assembly, encapsulation and testing techniques.....	51
2.5	State of the art regarding integration and application of CNT actuators.....	54
2.5.1	Mechanical and electrical integration techniques.....	54
2.5.2	Current applications and potential use cases.....	57
2.6	Conclusion and potentials for improvement.....	58
3	Materials and Methods.....	59
3.1	Carbon nanotubes.....	60
3.1.1	History and fabrication techniques.....	60
3.1.2	General properties of carbon nanotubes.....	64
3.1.3	Multi-walled CNTs.....	65
3.2	Other CNT actuator materials and components.....	67
3.2.1	Ionic liquids.....	67
3.2.2	PVDF(HFP) as backbone polymer.....	68
3.2.3	Additives and dispersing agents for CNT actuators.....	69
3.3	Design of Experiments (DoE) for tailored electrodes.....	70
3.3.1	Prerequisites and general targets of DoE.....	70
3.3.2	Procedure for DoE.....	71
3.3.3	Description of adopted dispersion techniques.....	74
3.3.4	Characterization techniques for assessing DoE target figures.....	77
3.4	Printing techniques for scalable actuator manufacturing.....	81

3.4.1	Screen printing	81
3.4.2	Blade coating.....	82
3.4.3	Stencil printing	83
3.4.4	Slot-die coating	83
3.5	New assembly and integration techniques for CNT actuators	86
3.5.1	Assembly methods for printed electrode and electrolyte layers	86
3.5.2	Proposed materials for embedded electric connections.....	87
3.5.3	A simple and cost-efficient method for encapsulation	88
4	Implementation of the proposed methods	89
4.1	DoE – Material compositions and dispersion methods	90
4.1.1	Pretest 1 – Initial investigations of MWCNT slurries and layers.....	90
4.1.2	Pretest 2 – Adaptation of the dispersing techniques and equipment.....	97
4.1.3	Main experiment.....	103
4.2	Printing CNT actuators and components	112
4.2.1	Screen printing of CNT actuator electrodes.....	112
4.2.2	Blade coating.....	114
4.2.3	Stencil printing	114
4.2.4	Semi-automated discontinuous slot-die coating.....	115
4.2.5	Evaluation of printing methods	118
4.2.6	Conclusion	120
4.3	Actuator assembly from printed layers.....	122
4.3.1	Fusing-cutting approach for large-scale printed actuator layers	122
4.3.2	Cutting-fusing approach.....	124
4.3.3	Embedded electric contacts.....	125
4.3.4	Encapsulation	128
4.4	Summary and conclusion of Chapter 4	130
5	Validation – Experimental Demonstrators	133
5.1	Simulation of aperture and actuator deformation	134
5.1.1	FEM simulation of CNT actuator deformation kinematics	134
5.1.2	Evaluation of aperture actuation kinematics.....	135
5.2	Demonstrator design and manufacturing.....	138
5.2.1	Demonstrator design	138
5.2.2	Preparation of textile membrane fabric	141

5.2.3	Actuator integration.....	143
5.3	Experimental test results and evaluation	146
5.3.1	Test setup and procedure	146
5.3.2	Actuation properties of integrated IEAPs	147
5.3.3	Sensing properties of integrated IEAPs	149
5.4	Power consumption and Life Cycle Assessment (LCA).....	152
6	Summary and Conclusion	155
6.1	Summary of the most important results.....	155
6.2	Conclusion	158
6.2.1	General reflection	158
6.2.2	Derived measures for future CNT actuator optimization	159
6.2.3	Outlook.....	160
7	Bibliography	163
	Appendix	A-1
A.1.1	Hygrothermal conflicts in building envelopes	A-1
A.1.2	Author's reasoning for quantitative requirements.....	A-4
A.1.3	Benchmarking parameters for IEAPs	A-5
A.1.4	Buckypaper fabrication and electrochemical analysis.....	A-9
A.1.5	Web of Science Search Terms.....	A-12

List of illustrations

All illustrations without references are the illustrations of the author.

Figure 1 – Structural membranes as part of the building envelope	5
Figure 2 – Inspirational concepts for breathing structures	8
Figure 3 – Wall element “FLOW”	9
Figure 4 – Pre-study regarding the integration of controllable apertures	9
Figure 5 – Textile building envelope	9
Figure 6 – DEA based 'artificial pore'	11
Figure 7 – Number of EAP publications	12
Figure 8 – Structure of this thesis	17
Figure 9 – Benchmarking of EAPs.....	26
Figure 10 – Reported IEAP actuation cycles from 2000 until 2020	27
Figure 11 – Assessment of material cost and manufacturing times.....	29
Figure 12 – CNT nanotweezers.	34
Figure 13 – Performance of Bucky gel actuators	37
Figure 14 – Illustration of CNT ‘Bucky gel’ actuator	38
Figure 15 – Illustration of the back-relaxation effect	40
Figure 16 – Illustration of IEAP manufacturing steps	44
Figure 17 – Manual slurry casting process.....	49
Figure 18 – 3D printed Bucky gel actuator.....	50
Figure 19 – Manual actuator assembly.....	51
Figure 20 – Characterization of IEAP actuators	53
Figure 21 – Integration of CNT actuators and electric connectors.....	56
Figure 22 – CNT actuator micropipette	57
Figure 23 – Schematic representations of CNT synthesis methods	64
Figure 24 – Pictures of baseline dispersion equipment.....	75

Figure 25 – Laboratory and pilot plant scale ultrasonication equipment	76
Figure 26 – Blade stirring equipment	77
Figure 27 – Depiction of the four-point measurement device	79
Figure 28 – Automated laboratory test setup	80
Figure 29 – Actuator assembly from printed films.	86
Figure 30 – Baseline material composition and dispersing procedure	90
Figure 31 – Scanning electron microscopy images	91
Figure 32 – Agglomeration and sedimentation of non-dispersed particles	92
Figure 33 – Disassociation of dried MWCNT electrode layers.....	93
Figure 34 – Optical microscopy of dried layer	95
Figure 35 – Dispersion viscosities over strain rates	100
Figure 36 – Edge separation of dried layers	101
Figure 37 – Experimental three roll milling	102
Figure 38 – Effect of CNT mass fractions	105
Figure 39 – Effect of CNT mass fractions	106
Figure 40 – Effect of CNT mass fractions	106
Figure 41 – Main Effects Plot for induced bending strain	107
Figure 42 – Microscope images of dried MWCNT electrode layer	108
Figure 43 – Size distribution and average dimensions	109
Figure 44 – Manual screen printing of CNT actuator electrodes.....	112
Figure 45 – Screen-printed CNT actuator electrode	113
Figure 46 – Blade coating of electrode layers.....	114
Figure 47 – Stencil-printing of CNT actuator electrodes	115
Figure 48 – Discontinuous coating machine Easycoater EC63	116
Figure 49 – Illustration of external feeding pump assembly	116
Figure 50 – Slot-die printed large-scale separator layers	117
Figure 51 – EC 63 electrode printing tests	118
Figure 52 – Laser microscopy analysis of dry film	119
Figure 53 – Induced bending strains of printed electrodes.....	120

Figure 54 – Manual preparation of actuator layers for fusing-cutting approach.....	123
Figure 55 – Calender used to fuse multilayer CNT actuator laminates	123
Figure 56 – Successful calendaring and manual cutting of actuator laminates	124
Figure 57 – Illustration of embedded contact materials	125
Figure 58 – Measurement results for initial contact resistance	126
Figure 59 – Embedded electric contacts.....	127
Figure 60 – Influence of embedded contact yarns	128
Figure 61 – Actuator encapsulation via dip-coating	129
Figure 62 – Impact of dip-coated PVDF encapsulation layers	129
Figure 63 – Simulation of the bimorph bending.....	135
Figure 64 – Motion principles for controllable apertures	136
Figure 65 – Kinematic simulations of apertures	137
Figure 66 – Simulation assisted demonstrator design.....	140
Figure 67 – Concepts for IEAP integration and distribution	141
Figure 68 – Automated membrane fabric preparation	142
Figure 69 – Illustration examples of IEAP actuator/sensor integration.....	144
Figure 70 – Final demonstrators	145
Figure 71 – Examples of successfully controlled membrane apertures	148
Figure 72 – Results of IEAP sensitivity tests.....	151
Figure 73 – Results of the Life Cycle Analysis	154

List of Tables

Table 1 – Main work objectives and tasks	15
Table 2 – Structured list of the main requirements for IEAPs	22
Table 3 – List of carbon nanotubes used for CNT actuator	66
Table 4 – Properties of ionic liquids.....	67
Table 5 – Starting point and targets of DoE.....	71
Table 6 – Description of pretest 1.....	72
Table 7 – Description of pretest 2.....	73
Table 8 – Description of main experiment parameters.....	74
Table 9 – Details on screen printing.....	82
Table 10 – Details on blade coating.....	82
Table 11 – Details on stencil printing.....	83
Table 12 – Details on slot-die coating.....	84
Table 13 – Overview of proposed printing & coating methods.....	85
Table 14 – Dimension and resistivity values	88
Table 15 – Influence of different types of solvent.....	94
Table 16 – Influence of decreasing the amount of 4M2P	94
Table 17 – Wet and dry layer quality results	96
Table 18 – DoE sonication parameters and results	97
Table 19 – DoE blade stirring parameters and results.....	99
Table 20 – Main experiment material compositions.....	103
Table 21 – Compilation of final actuator components	110
Table 22 – Compilation of dispersion techniques.....	111

List of abbreviations

AFM	Atomic Force Microscopy
BET	Brunauer Emmett Teller (specific surface area analysis)
BMIM-BF ₄	1-Butyl-3-methylimidazolium tetrafluoroborate
CDC	Carbide Derived Carbon
CDE	Carbon Dioxide Equivalent
CED	Cumulative Energy Demand
CNT	Carbon Nanotube
CP	Conductive/conjugated Polymer
CRC	Collaborative Research Center
CCVD	Catalytic Carbon Vapor Deposition
CVD	Chemical Vapor Deposition
DAP	Direct Assembly Process
DEA	Dielectric Elastomer Actuator
DMAc	Dimethylacetamide
DoE	Design Of Experiments
EAP	Electroactive Polymer
EC	Easy Coater
EMIM-BF ₄	1-Ethyl-3-methylimidazolium tetrafluoroborate
GWP	Global Warming Potential

HFP	Hexafluoropropylene
HVAC	Heating, Ventilation and Air-Conditioning
IEAP	Ionic Electroactive Polymer
IL	Ionic Liquid
IPMC	Ionic Polymer-Metal Composite
MWCNT	Multi-Walled Carbon Nanotube
NEMS	Nanoelectromechanical Systems
NiO	Nickel Oxide
NMP	N-Methyl-2-pyrrolidone
PANI	Polyaniline
PC	Propylene Carbonate
PDMS	Polydimethylsiloxane
PECVD	Plasma-Enhanced Chemical Vapor Deposition
PENRT	Primary Energy Non-Renewable Total
PTFE	Polytetrafluoroethylene
PU	Polyurethane
PVDF	Polyvinylidene difluoride
rGO	Reduced Graphene Oxide
SGCNT	Super-Growth Carbon Nanotube
SMA	Shape Memory Alloy
SCBI	Supersonic Cluster Beam Implantation
SWCNT	Single-Walled Carbon Nanotube

Abstract

The rise of lightweight building envelopes with built-in adaptive features is believed to play a key role in reducing global resource consumption and emissions in the construction industry. However, adaptive building skins need stimulus-responsive materials and intelligent control systems to adapt their building-physical properties in response to changing environmental conditions and user comfort requirements. Ionic electroactive polymers (IEAP) have been used as soft and flexible actuators and sensors with material-intrinsic deformation capabilities and thus represent a potential technology that could be advantageous for such tasks.

Often referred to as artificial muscles, IEAP exhibit large deformations at low operational power and have been proposed for soft robotics applications and microfluidic systems. But even today, these devices are mainly employed in the scientific realm and have never been used for construction-related operations. Their complex manufacturing process, sophisticated material compositions, rather poor performance characteristics and their strong sensitivity to changing environmental conditions have limited a wider application range until now.

Representing a relatively new species of IEAP, carbon nanotube (CNT-) based polymer actuators feature some useful properties such as good power characteristics, operability in air, integrated sensor functionality, freedom of noise and comparatively simple fabrication. This thesis examines novel material compositions, fast and scalable manufacturing techniques and unprecedented integration methods for these nanoparticle charged devices.

At first, the Design of Experiments method was employed to find optimized material compositions and dispersion parameters that are needed to manufacture CNT actuator electrodes. The focus was on stable nanomaterial dispersions that are suitable to be printed in industrial printing processes. This work comprised the adoption of various

substitute substances that are either less toxic or more cost-efficient compared to previously employed chemicals and materials. Thus, a 90% reduction of overall dispersion time and an 85% reduction of material costs was accomplished.

In a second step, automated printing methods were investigated to fabricate large and highly homogeneous electrode layers in much shorter time. The process of multi-layer slot-die coating proved to be particularly successful and led to a significantly higher performance reproducibility of printed CNT actuators and sensors.

Subsequently, new techniques for embedded electric connectors (heat pressing), actuator assembly (calendaring) and automatable actuator encapsulation (dip-coating) were studied, resulting in robust actuators with enhanced environmental stability yet moderate power characteristics.

For validation purposes, two experimental demonstrators were designed and built to investigate the actuation and sensing behavior of CNT-based IEAP integrated into a fabric membrane skin. Simulation-assisted design approaches comprised the evaluation and verification of the actuation kinematics of IEAP-driven apertures and the conceptual strategy for the positioning and distribution of actuators. Extensive demonstrator tests have shown that a practicable and reliable integration of such complex electrochemical devices remains a challenge, particularly because their performance is still highly sensitive to many non-application-related factors. For example, diffusion of ionic liquid electrolyte may occur from the actuator electrodes into the conductive pathways. This may result in varying electric contact resistances that are difficult to control and thus may cause differences in performance degradation and life cycle stability of individual actuators.

The principal motivation for this thesis was to advance the general practicability of IEAP actuators and sensors and to investigate and exemplify their potential to be used as a smart material for adaptive building skins. Hence, this thesis constitutes the very first experimental approach of using IEAP technology in a building-related application.

Kurzzusammenfassung

Im Bauwesen kommt leichten und adaptiven Gebäudehüllen eine Schlüsselrolle bei der Reduzierung des globalen Ressourcenverbrauchs und der damit einhergehenden Emissionen zu. Adaptive Gebäudehüllen benötigen smarte Materialien und intelligente Steuerungssysteme, um ihre bauphysikalischen Eigenschaften wie z.B. ihre Atmungsaktivität als Reaktion auf veränderte Umweltbedingungen anzupassen. Ionische elektroaktive Polymere (IEAP) besitzen die Fähigkeit zur kontrollierbaren materialintrinsic Verformung und stellen eine potenzielle Aktortechnologie für solche Anwendungen dar.

IEAPs werden oft auch als „künstliche Muskeln“ bezeichnet und sind seit über zwei Jahrzehnten Gegenstand der Erforschung flexibler und nachgiebiger Stellantriebe. Sie reagieren mit teils großen Auslenkungen auf kleine elektrische Spannungen und wurden bereits für Soft-Robotik-Anwendungen und mikrofluidische Systeme vorgeschlagen. Bis heute sind sie jedoch vorwiegend Gegenstand wissenschaftlicher Untersuchungen und wurden trotz ihrer interessanten Eigenschaften noch nie für den Einsatz in Gebäuden angepasst. Ihr komplexer Herstellungsprozess, ihre hochentwickelten Materialzusammensetzungen, ihre bislang unzureichenden Leistungsmerkmale und ihre Empfindlichkeit gegenüber Umweltfaktoren standen einer kommerziellen Verbreitung in neuen Anwendungsbereichen bisher entgegen.

Als jüngster Vertreter unter den IEAP weisen Kohlenstoff-Nanoröhren (CNT) basierte Polymeraktoren einige vorteilhafte Eigenschaften auf, wie z.B. eine gute Kraftübertragung, Funktionsfähigkeit in Luft, integrierte Sensorfunktionalität, absolute Geräuschlosigkeit und eine vergleichsweise einfache Herstellung. In dieser Arbeit werden kosteneffiziente Materialzusammensetzungen, schnelle und skalierbare Herstellungstechniken und neue Integrationsmethoden für CNT-Aktoren untersucht.

Zunächst wurde die Methode der statistischen Versuchsplanung angewendet, um opti-

mierte Materialzusammensetzungen und Dispersionsparameter zu finden, die zur Erzeugung stabiler Nanomaterialdispersionen benötigt werden. Dabei wurden verschiedene Ersatzwerkstoffe eingesetzt, die entweder weniger toxisch oder kostengünstiger als die bisher verwendeten Materialien sind. Insgesamt wurde eine Verkürzung der Dispersionszeiten um bis zu 90% sowie eine Reduzierung der Materialkosten um bis zu 85% ohne größere Einbußen bei der Funktionalität erreicht.

In einem zweiten Schritt wurden automatisierbare Druckverfahren wie das mehrlagige Schlitzdüsenbeschichten erfolgreich getestet, wodurch großflächige Elektrodenschichten in deutlich kürzerer Zeit und mit verbesserter Schichtdickenhomogenität hergestellt werden konnten.

Des Weiteren wurden neuartige Verfahren für eingebettete elektrische Anschlüsse (Heißpressen), für den Zusammenbau der Aktoren (Kalandrieren) und für eine automatisierbare Aktorverkapselung (Tauchbeschichten) untersucht und teilweise bis zum Technikumsmaßstab weiterentwickelt, so dass sich nun stabile Aktoren mit reproduzierbaren, wenn auch moderaten Leistungseigenschaften herstellen lassen.

Zwei experimentelle Demonstratoren wurden entworfen und gebaut, um das Aktor- und Sensorverhalten von CNT-basierten IEAP zu untersuchen, die in eine Stoffmembran integriert sind. Simulationsgestützte Entwurfsansätze umfassten die Evaluierung der Aktuierungskinetik von IEAP-getriebenen Membranöffnungen und Blenden sowie ein Konzept für die Positionierung und Verteilung von Aktoren auf der Membran. Umfangreiche Demonstrator tests haben gezeigt, dass eine praktikable und zuverlässige Integration solch komplexer elektrochemischer Aktoren eine Herausforderung bleibt, insbesondere, weil ihre Leistungseigenschaften noch stark von nicht anwendungsbezogenen Faktoren abhängen. Zum Beispiel kann die Diffusion ionischer Flüssigkeiten aus den Aktor-Elektroden in die Leiterbahnen zu unterschiedlichen elektrischen Übergangswiderständen führen, die nur schwer zu kontrollieren sind und somit Unterschiede im Zeitverhalten und in der Lebensdauer der einzelnen Aktoren verursachen können.

Die Hauptmotivation für diese Arbeit war es, die allgemeine Praxistauglichkeit von IEAP-Aktoren und -Sensoren voranzutreiben und ihr Potenzial als intelligentes Material für

adaptive Gebäudehüllen zu untersuchen und zu veranschaulichen. Somit stellt diese Arbeit den ersten experimentellen Ansatz dar, die IEAP-Technologie in einer gebäudebezogenen Anwendung einzusetzen.

1 Introduction

The first subchapter of the introduction elaborates on the societal need to reduce building materials and energy consumption in the construction sector. It covers the recent trend to employ lightweight membrane structures as building envelopes and the growing awareness that such structures would benefit from adaptive building-physical functionalities to increase energy efficiency, sustainability and human comfort. It is also presented in detail that embedded soft and flexible actuators could be particularly useful for such adaptive features and, inter alia, have been proposed to accomplish breathable building skins.

The second subchapter introduces electroactive polymers (EAP) as potential candidates for such actuators. It briefly touches on the two main groups of EAP and addresses their general potentials and drawbacks. The third subchapter preemptively describes the material and process limitations of ionic EAP (IEAP) actuators and derives research questions on how to overcome these limitations specifically in regards to carbon nanotube based IEAP. In reference to these research questions, technical objectives and tasks are defined which set the foundation of this thesis. The fourth subchapter concludes the introduction and illustrates the structure of this thesis.

1.1 Societal relevance and general context

The research activities conducted for this dissertation have been embedded in the Collaborative Research Center CRC1244 “Adaptive skins and structures for the built environment of tomorrow” which was installed at the University of Stuttgart in January 2017. The aim of the CRC 1244 is to find answers to the urgent ecological and social questions of our time for the construction industry. 14 institutes are working in a concerted interdisciplinary cooperation on the question of how – in view of a growing world population and shrinking resources – more housing with less material and energy consumption can be created in the future. The integration of adaptive elements into load-bearing structures, enveloping systems and interior design is considered as an important approach (Klein et al. 2015; Sobek 2015; Košir 2016). The CRC 1244 explores the basics, potentials, and implications of this approach.

1.1.1 Demographic changes and their effects on the building sector

Many scientists, governments and international institutions predict a constantly growing world population throughout the 21st century with a strong diversity in population growth rates across different world regions. Between 2017 and 2050 a net growth in global population of up to 2.2 billion people is anticipated. More than half of this growth is expected to occur in Africa, with Asia being the second largest contributor and Europe having the least population gain (United Nations 2017).

Regarding this demographic increase, it is self-evident that additional buildings, roads, bridges, tunnels and other infrastructure facilities have to be built to provide future generations with the same housing standards and societal living conditions prevalent today. Global trends such as urbanization (migration to urban centers) and demographic changes (e.g. shrinking households and aging population in industrialized nations) are believed to strongly increase future construction volumes in almost all parts of the world (Tauber et al. 2019).

Both the construction of new buildings and additional infrastructure as well as the modernization of the already existing built environment entails a growing demand for construction materials and energy resources. Even today the construction industry is responsible for approximately 60% of global resource consumption, 50% of mass waste occurrence and 35% of both energy consumption and global immission (effects of noise, pollution and radiation on living organisms and objects) (Abergel et al. 2017). The mining and transport of raw materials such as steel, wood, cement, gravel, sand or natural stone and their refinement and further processing to mineral and non-mineral building materials are very energy intensive. The production of cement alone – a mineral binder material necessary for making concrete – accounts for approximately 7-8% of global CO₂-emissions (Andrew 2018). This leads to new and necessary considerations regarding the future organization and design of our built environment. The building materials and construction industries must adopt new practices to meet the increased demand for materials to build the housing and transportation infrastructure needed to support the anticipated increase in city dwellers while reducing CO₂ emissions in a resource-constrained environment. This in term requires a broad awareness and a well-concerted action plan in all branches of research and development relevant to the construction industry.

1.1.2 Potentials in reducing construction materials and grey energy

Load-bearing structures in housing and infrastructure buildings are designed to withstand peak loads that occur under very rare external circumstances, e.g. earthquakes, strong wind loads or heavy cases of snow loads. This means that they are substantially oversized for the predominant part of their operating lifetime (see semi-probabilistic design approaches defined in Eurocode 0, DIN EN 1999). A significant reduction of building material for load-bearing structures could be achieved by manipulating internal stress conditions through the employment of integrated actuators. Such adaptive devices have been shown to mitigate peak loads by superimposing the external loads with specific structure-internal tension fields in order to yield a forced homogenization of the stress distribution. Individual projects reported mass savings of more than 50% (Neuhaeuser et al. 2013).

Building envelopes – besides being exposed to climatic impacts like rain, wind, and wide temperature ranges – are regulating light transmission, humidity transport and ventilation. Thus they are significantly involved in controlling the thermal and energy balance of the building (Košir 2016). Nevertheless, their distinct features and operation principles are usually based on either high materials usage (thermal energy storage, noise protection) or high energy usage (heating, cooling, ventilation, illumination). They are mostly built with stationary building-physical properties because they are designed and installed for specific use cases to operate within certain climatic conditions which are strongly related to the building's geographic location. Often no adaptive functionality is required because energy-intensive artificial climate control still dominates the current practices in regulating comfort settings.

As a direct consequence, building envelopes not only contribute to the total energy and material resource consumption of the building, but their physical qualities strongly determine the physical and mental well-being of the users and residents. New ideas in designing lightweight and energy-efficient building envelopes go way beyond today's passive membrane structures, with some approaches currently exploring active concepts that include adaptive building-physical functionalities that can promote comfortable indoor settings (Aelenei et al. 2016; Attia et al. 2018).

1.1.3 Lightweight membrane structures as building skins

In the second half of the 20th century, lightweight building skins such as multi-layer textile or foil-based membrane structures have been brought to the attention of architects and engineers and increasingly found their way into civil engineering projects around the globe (Habermann et al. 2004). Referred to as the fifth building material after wood, stone, glass, and metal, membranes use significantly less material and energy resources and often yield a wide architectural design freedom. Figure 1 shows three examples of membrane structures being used as building envelopes in well-known infrastructure and commercial buildings.

New advances in polymer technology have brought new membrane materials to the market, accounting for improved life spans, optimized mechanical properties, dirt-repellent and UV-resistant characteristics and other important features such as translucency (fabrics) and transparency (foils). Modern building envelopes usually make use of multifunctional single-layer membranes and profit from their low material thicknesses of usually below one millimeter. The resulting low weight of the membrane cover leads to a relief of the load-bearing structures and thus to a reduction of necessary construction materials (Paech 2016). The downsides of low material thicknesses and mass are poor thermal insulation properties and a lack of thermal storage, respectively, which eliminates the application of single-layer membranes as heat-insulating building envelopes (Adamczewski 2008).

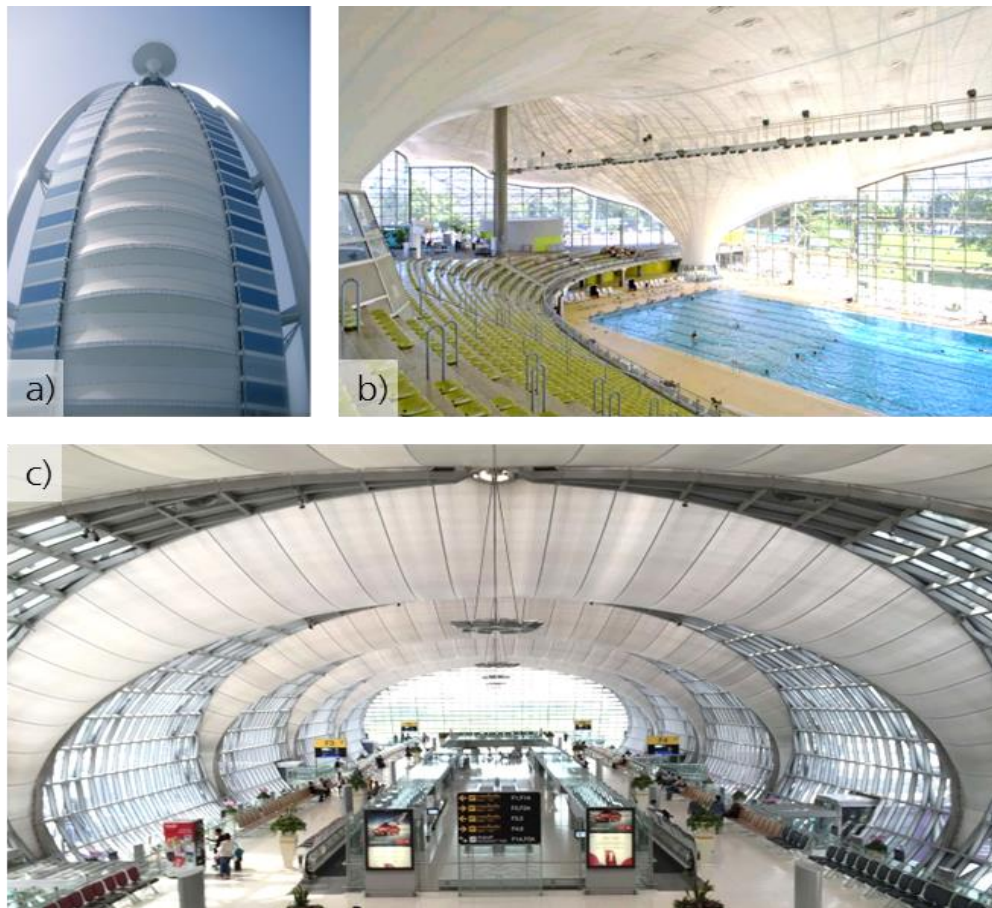


Figure 1 – Structural membranes as part of the building envelope. a) Burj al Arab Hotel, Dubai, United Arab Emirates (© Girvin.com, 2009). b) Suspended ceiling of the Olympic Swimming Facility in Munich, Germany (© Schlaich Bergermann und Partner, 2008). c) Bangkok Suvarnabhumi International Airport (BKK), Bangkok, Thailand (© Thaiest.com, 2020)

Multi-layer membrane systems provide better thermal performance with reduced U-values and often have optimized UV-blocking and noise-canceling characteristics. Such systems are either inflated membrane cushions with two, three or even more layers or a system of two pre-stretched membrane layers with intermediate insulation. In both cases, the designer has to consider hygro-thermal conflicts and carefully verify that no condensation will occur for the chosen system (Paech 2016).

The latter is one of the main reasons why membrane structures are rarely used for building envelopes. Especially during wintertime, the temperature drop between the inside and the outside of a building's skin can be significant. If humidity is trapped inside a confined multi-layer membrane structure and if the vapor pressure sets below the saturation pressure, condensation may occur. Condensation is an unwanted phenomenon as it may cause dampness, mold health issues, corrosion, material fatigue, and energy penalties due to increased heat transfer (Haase et al. 2011). Contemporary multi-layer membrane structures cannot breathe like conventional masonry walls, where humidity is simply dried out over time due to capillary diffusion processes. For this reason, mechanical air heaters are often used to blow hot air into the membrane cushions or through the interstitial space to remove residual moisture or excessive humidity. A more detailed explanation of such hygro-thermal conflicts in multi-layer membrane structures is provided in the Appendix 1.1.

1.1.4 The need for adaptivity in building envelopes

To yield long-lived energy efficiency and maximum building performance, lightweight building envelopes need to respond dynamically to changing environmental conditions and user comfort requirements. Following (Loonen et al. 2015), the term *adaptive building envelope* is defined as

“The physical separator between the interior and exterior environment, that – through incorporation of multifunctional materials, components and systems – is able to repeatedly and reversibly change its functions, features and behavior over time in response to transient

performance requirements and environmental boundary conditions, with the aim of improving the overall building performance”.

Adaptive building envelopes offer a high potential to reduce the energy demand for lighting and space conditioning. According to Aelenei et al. 2016), the most influential environmental factors that building envelopes need to manage are solar radiation, outdoor temperature, wind, humidity, precipitation and noise. For example, switchable breathability may be desired to manage hygro-thermal conflicts in multi-layer membrane structures to prevent interstitial condensation (Janssens 1998; Cremers et al. 2016), and inflexible light transmission rates of membrane structures may be overcome with novel adaptive sun shading strategies involving kinetic devices or actuators directly integrated into the building skin (Loonen et al. 2013). Most adaptive façades currently in use have been installed for solar radiation control. They perform active shading regulation with mechanical sun blinds or by changing the shape or structure of a second façade layer.

To initiate any mechanical or physical reactions, adaptive building envelopes generally require the incorporation of sensors that continually measure the current state of the structure as well as ambient conditions. For example, it is often desired to have locally resolved sensor data about induced mechanical stresses inside membrane structures for health monitoring purposes and to ensure the serviceability and safety of the structure (Tang et al. 2019).

1.1.5 Soft actuators for breathable building skins

A variety of control elements have been developed and tested for adaptive ventilation, humidity control and sun shading purposes in building envelopes. Traditional actuators that were proposed for such tasks include pneumatic and electronic actuators, electro-magnetic motors and hydraulic cylinders (Janocha 2004; Haase et al. 2011). However, the weight and size penalties, complex transmissions, high induced noise levels, restrictive shapes and the

need for resource-intensive maintenance of such actuators have led researchers to investigate alternative technologies for more effective substitutes with larger mechanical flexibility and compliance, smaller dimensions, high power-to-weight and power-to-volume ratios and higher efficiencies. Finding such substituting systems is specifically necessary for the application in building skins made of flexible and lightweight membrane structures where traditional rigid actuators are difficult to integrate (Albag et al. 2020).

Smart materials such as thermally triggered bi-metal actuators and shape memory alloys (SMA) which both react to ambient temperature changes have been proposed for adaptive ventilation and shading systems in architectural skins (Sung 2011; Dewidar 2013). In many cases, biological occurrences like so-called stomata, where self-regulated apertures in plant leaves control the gas exchange vital for photosynthesis, serve as a source for inspiration when designing such systems (Figure 2a). Hygroscopic wooden bilayer composites have been explored to enable adaptive ventilation apertures (Figure 2b) that react to changing humidity and temperature conditions (Menges et al. 2013; Reichert et al. 2015). Such self-controlled materials, however, cannot be directly stimulated or controlled by humans. Direct control over ventilation and humidity transport is only possible if the apertures in the building skin can be operated on demand and independent of environmental influences. For this reason, soft and flexible actuators with material-intrinsic yet externally triggered deformation capabilities are needed.

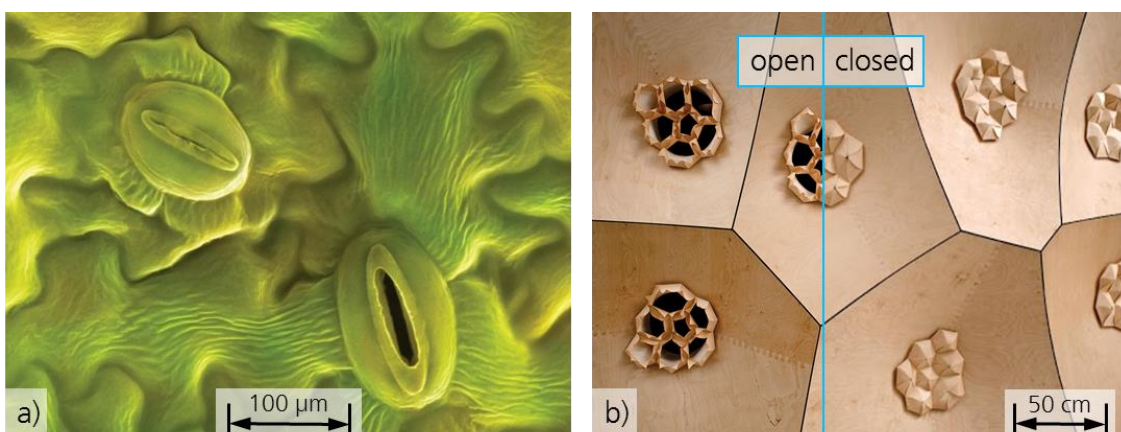


Figure 2 – Inspirational concepts for breathing structures. a) Biological inspiration from stomata pores in plant leaves. Gas exchange for photosynthesis is regulated by controlling the size and shape of so-called guard cells via internal ionic transportation processes (© Power and Syred – Science Photo Library, 2019). b) HygroSkin - Meteorosensitive Pavilion (© ICD, University of Stuttgart)

Figures 3, Figure 4 and Figure 5 depict breathing wall demonstrators that generate controllable apertures in building envelopes for means of lighting and ventilation.



Figure 3 – Wall element “FLOW” – Flexible Lightweight Operable Wall (© ILEK Uni Stuttgart, 2011)

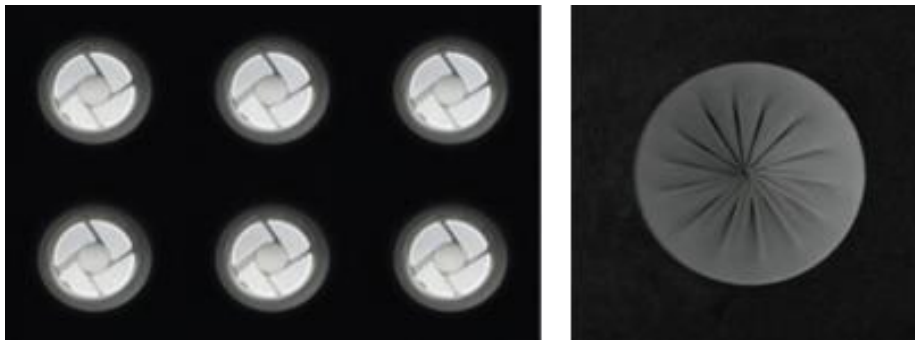


Figure 4 – Pre-study regarding the integration of controllable apertures into fabric membrane structures, via integrated wire-draw mechanism (© ILEK Uni Stuttgart, 2011)



Figure 5 – Textile building envelope with integrated pneumatic apertures for controlled ventilation of interstitial membrane spaces (© ILEK Uni Stuttgart, 2011)

1.2 Electroactive polymers for adaptive building envelopes

In recent years, several smart and multifunctional materials and compounds have been evaluated for their use as soft and flexible motion transducers in various engineering fields. Among such actuators, electroactive polymers (EAP) have attracted large interest and have been proposed for various applications in civil engineering and architecture (Kretzer et al. 2012; Juaristi et al. 2018). EAP are smart material systems that exhibit a change in size or shape when stimulated by an electric field. EAP actuators show useful properties, such as sizeable active strains and stresses, high mechanical flexibility, light-weight, structural simplicity and versatility, ease of material processing, scalability, no acoustic noise, and comparably low cost (Carpi et al. 2010).

There are two main groups of EAP prevailing in R&D today: Dielectric elastomer actuators (DEA) whose operation mode is based on purely physical effects, and various sub-types of ionic EAP (IEAP), where actuation is based on electrochemical working principles.

1.2.1 Dielectric EAP

Most attention is currently drawn to dielectric elastomer actuators (DEA), which have been investigated since the late 1990s. They have a passive elastomer film with a high dielectric constant sandwiched between two compliant electrodes. Upon applying high electric voltages, the elastomer film is squeezed together by the electrostatic pressure between the electrodes and therefore expands in size in planar direction.

DEA have been proposed for ventilation control purposes in buildings, either as “artificial pores” (Kolodziej et al. 2013) depicted in Figure 6, as “autonomous material agents system” (Kolodziej et al.) or as an “airflow actuator” in HVAC systems (Berardi 2010). Another application related to architecture has been proposed in the project “Reef” (Mossé et al. 2012) who experimentally investigated how DEAs can be “appropriated so as to re-establish a relationship of interconnectivity between nature, the home and its inhabitants”. They used

DEA for a dynamic and responsive indoor art installation which has been mounted to a room ceiling and reacted to individual users moving inside the room.

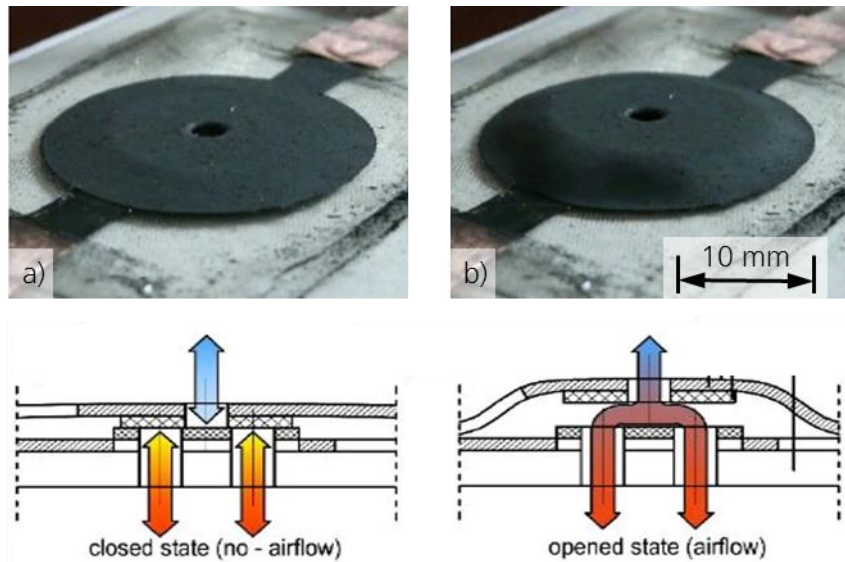


Figure 6 – DEA based 'artificial pore' developed by Kolodziej et al. 2013 (Kolodziej et al. 2013): a) in a deactivated state; b) in an activated state – excited with 4.5 kV voltage.

Deformations of DEA are well controlled, reversible, and capable of high-frequency operation, but very high driving electric fields of up to $100 \text{ V } \mu\text{m}^{-1}$ are required. Taking into consideration the thinnest possible elastomer layers producible today, actuation still requires driving voltages of several kilovolts. For this reason, DEA are not considered as potential actuators for future building envelopes in this thesis.

1.2.2 Ionic EAP

Ionic electroactive polymers (IEAP) – compared to dielectric EAP – operate on the principle of electrically stimulated ion transport within a bi- or trilayer setup and usually perform a bimorph bending motion. Some exhibit large deformation and medium force transmission at low operational power making them highly attractive for many applications where soft, non-hazardous and noise-free actuation is desired. Looking at the EAP-related academic research in terms of publications, it is clear that activities have steadily increased over the

past twenty years (Figure 7). Dielectric EAPs clearly dominate the scientific output and have been subject to more publications each year than all species of IEAP actuators combined, which is not surprising given their higher power characteristics and their technological advantage. A closer look at IEAP-related research reveals that the majority of publications investigate new materials and compositions, novel modelling techniques or different manufacturing methods. Only more recent papers report on potential applications, none of which is attributed to architectural or building-physical use cases. These findings convey the existence of an underexplored frontier in the domain of soft and flexible IEAP actuators.

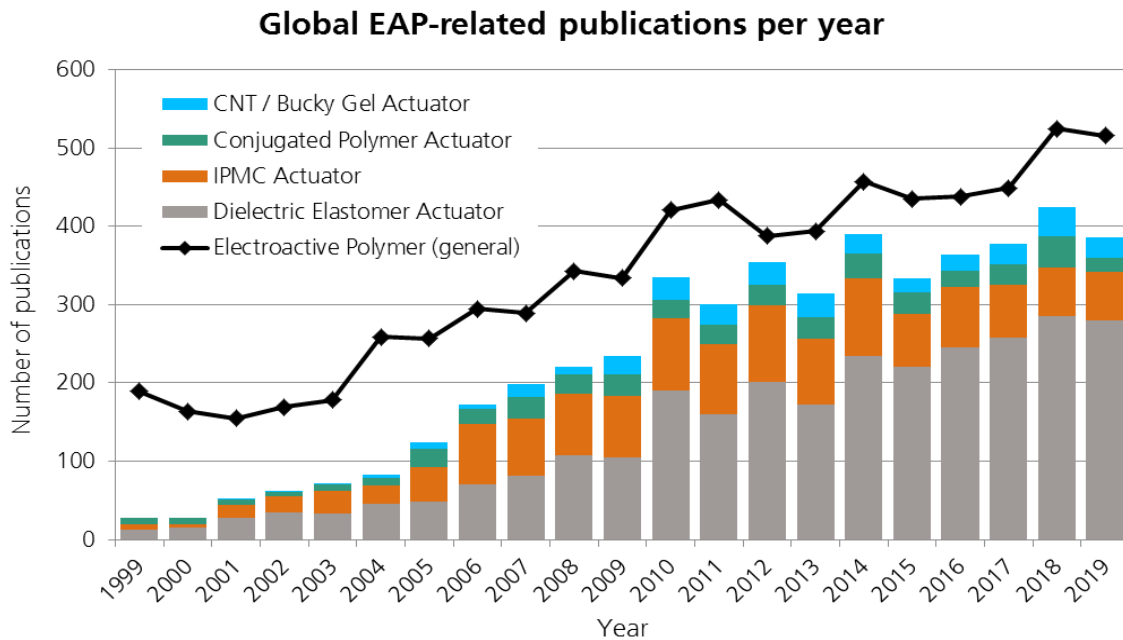


Figure 7 – Number of EAP publications per type of EAP per year (Web of Science, April 2020). The exact search terms can be found in the Appendix A.1.5. (Source: own diagram)

1.3 Objectives

The overarching objective of this thesis is to present experimental methods and results regarding the fabrication and integration of soft and flexible polymer actuators that can be used as motoric actuators and sensors in adaptive building envelopes. Since the current state of science and technology does not provide any data about the applicability of IEAPs in fabric membrane structures, it is unknown whether and how exactly their reported performance characteristics can be utilized to generate adaptive features in such building skins.

The objectives and methods reported in this thesis clearly target the design and realization of efficient artificial objects and thus follow the utilitarian principles of technological sciences, as described by (Ulrich et al. 1976).

1.3.1 Problem statement

Even though their materials and properties have been known for many decades, IEAPs have not replaced traditional actuators (electromagnetic, pneumatic, hydraulic, and piezoelectric) because of poor actuation performance, costly materials and complex manufacturing techniques (Chang et al. 2018). They are complex electrochemical devices with mostly low actuation forces, tedious handling characteristics and – for the most part – laboratory manufacturing techniques. During the last decade, the primary goals of research and development in the field of IEAPs were to increase the generated force and displacement as well as to achieve long durability of the actuators, meaning that they should perform their rated power reproducibly for as many cycles as possible. Other criteria for the adoption of IEAPs in building envelopes are constant and reproducible performance characteristics in varying temperature and humidity conditions, simple manufacturing techniques and low cost of both materials and fabrication processes.

1.3.2 Derived research questions

The superordinate research question of this dissertation has been formulated as follows:

“Can IEAP actuators and sensors be used for adaptive building envelopes?”

This core question connects the three scientific disciplines of (nano-) material science, production technology and civil engineering. It is useful to define subordinate research questions to further specify the targeted knowledge gain within these disciplines.

Materials:

“Which materials and compositions combine the highest potential to be used in IEAP sensors and actuators for building envelopes, particularly in terms of availability, cost, toxicity, durability, performance, ease of fabrication and recyclability?”

Production technology:

“How can robust IEAPs be fabricated and processed reproducibly, reliably, in large quantities and with necessary auxiliary features to be integrated and controlled in the target application?”

Civil engineering:

“How can IEAPs be integrated into building envelopes to perform building-specific adaptive functionalities and how can they be controlled?”

1.3.3 Focus, work objectives and tasks

The use of IEAP technology entails a large variety of materials and processes. This thesis focuses on the material composition and manufacturing techniques of one species of IEAP, namely CNT-based tri-layer polymer actuators. It is clear that the existing material compositions and fabrication methods of CNT actuators constitute a considerable hindrance towards future market adoption (see Chapter 2). The high material cost, the energy-intensive and time-consuming laboratory manufacturing methods and the poor performance reproducibility need to be improved considerably.

On the application side, this thesis focuses on IEAPs employed for two different functionalities in building skins: a switchable breathability through controllable active apertures, and distributed sensors that are sensitive to mechanical loads and deformations.

Table 1 defines the four main work objectives of this thesis and preemptively formulates the explicit tasks to reach these objectives:

Table 1 – Main work objectives and tasks

Work objectives	Deduced tasks
Reduction of CNT actuator material costs and toxicity for enhancing chances of future market adoption.	<i>Develop reproducible and scalable dispersion methods utilizing cost-efficient and less toxic materials</i>
Advancing the manufacturing processes of CNT actuators from laboratory methods to industrially scalable procedures.	<i>Investigate conventional and up-scalable printing techniques for fast and reliable mass-production of CNT actuator components (electrodes and separators).</i>
Finding new and/or suitable methods for CNT actuator assembly in consideration of the desired target application.	<i>Perform experimental investigations on the incorporation of embedded electric contacts, deduce suitable encapsulation methods and find reliable techniques for system integration</i>
Investigation of general feasibility, elaborating potential limitations and showcasing of the technology by building functional demonstrators.	<i>Integrate CNT actuators into pre-stretched textile membrane structures and perform tests on their sensor and actuator capabilities.</i>

1.4 Conclusion of Chapter 1 and structure of this thesis

This chapter has set the social and scientific framework of this thesis. Dwindling resources, climate change and population growth call for a paradigm shift in the construction industry to use less material and build lighter structures. This goes hand in hand with a growing interest in adaptive building technologies where soft and active materials are regarded as a key enabler for embedded sensors and actuators, particularly in future building skins. In this respect, EAP deliver some useful properties and promise to develop rapidly, but their limited performance, high complexity and costly components still pose a significant threat to an imminent commercial deployment. The author's decision to rule out high-voltage DEA and the fact that no species of IEAP actuators has ever been tailored, integrated or tested for applications in the built environment propel the topic of this thesis into a completely new and unexplored territory.

Figure 8 depicts the structure of this thesis and may serve as an additional overview besides the table of contents.

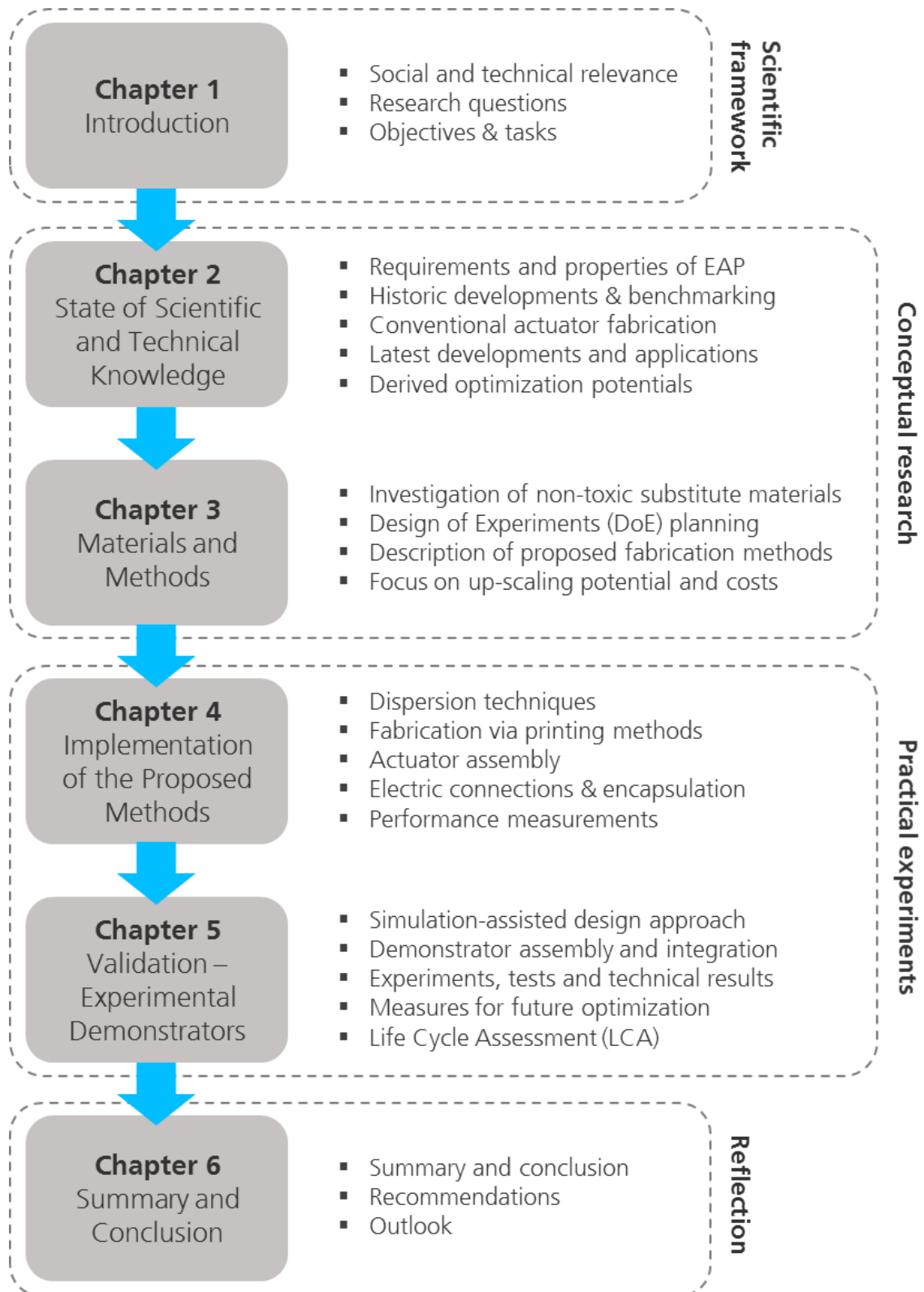


Figure 8 – Structure of this thesis

2 State of scientific and technical knowledge

The previous chapter has built the scientific framework in which this thesis is allocated and has provided background information about the social relevance and the technical objectives of this thesis. This chapter provides information about the past and current state of the art in regards to IEAP actuators that work with carbon nanotubes.

The first subchapter derives general and application-specific requirements for IEAP to identify the technical targets and to serve as a reference for subsequent benchmarking.

The second subchapter elucidates the three prevailing types of IEAP and their basic working principles and explains why CNT-based actuators have been chosen for this project.

The third subchapter elaborates on the history of CNT actuator development and covers their general properties and global efforts of optimization in more detail.

The fourth and fifth subchapters identify state-of-the-art manufacturing techniques and integration methods, respectively.

The last subchapter summarizes the current weak points of the CNT actuator technology and concludes by highlighting the potentials for improvement.

2.1 Requirements for IEAPs used in adaptive building envelopes

Given the premise that some species of IEAP may be suitable or even beneficial to be used as active features in adaptive building envelopes, it is necessary to specify the qualitative and quantitative requirements that they need to meet. In light of the focus application of this thesis, this section derives requirements for materials, production methods and performance characteristics of IEAP actuators that are explicitly used to generate controllable apertures in pre-stretched membrane fabrics.

2.1.1 Qualitative requirements

Most qualitative requirements can be derived from the objectives and research questions stated in the previous chapter. Generally, IEAPs should be made of accessible, cost-efficient and as little toxic materials as possible, be fast and safe to produce in large quantities and exhibit auxiliary features for system integration, for example robust electrical interfaces. When used in building envelopes, they should have the ability to operate in air and under harsh environmental conditions such as excessive moisture and wide temperature ranges. When used as actuators, IEAPs must produce enough power to generate apertures in textile membranes. In the case of a sensor application, IEAPs must produce load-triggered electric signals that are measurable, repeatable and strong enough to be processed and interpreted by state-of-the-art control units. In both cases, IEAPs should ideally have an operating life expectancy equal to the life expectancy of the building envelope to avoid premature system breakdowns and complex repair activities.

2.1.2 Quantitative requirements

The previously defined qualitative requirements provide a rough framework. Some of them can be specified further and turned into quantitative requirements by setting up upper and/or lower boundary or target values. However, such values often depend on other pa-

rameters specific to the desired application. For example, the minimum and maximum temperature range in which an IEAP must operate strongly depends on the building's geographic location. Similarly, the force required by an IEAP actuator to cause a deformation of a pre-stressed membrane depends on multiple parameters such as the level of the prestress, the thickness of the membrane, the type of actuator attachment and the size of the aperture. In this respect, some of the quantitative requirements in this section are based on assumptions made by the author, while others constitute fixed parameters obtained from external sources.

For example, all IEAP species are reported to have lifetime expectancies (sometimes referred to as "cycle life") of 10^4 – 10^7 working cycles, depending on the test environment, the applied power settings, and choice of materials (see section 2.2.2). Taking the lowest value of 10^4 working cycles and assuming an estimated average actuation frequency of five cycles per day, the proposed application in building membranes would yield a minimum life expectancy of little over five years. Considering that textile building envelopes are designed to last 30 years or longer (Habermann 2004; Paech 2016), a minimum of 10^5 performed working cycles with no more than 50% strain degradation may serve as a reasonable requirement parameter for any IEAP-driven actuation.

Table 2 provides an overview over the most important qualitative and quantitative requirements for IEAPs, categorized in material-, production- and application-related criteria.

Table 2 – Structured list of the main requirements for IEAPs

	Qualitative IEAP requirements	Quantitative IEAP requirements		Sources
	Description	Parameter (type)	Value (range)	
Material	Avoid substances classified as CMR category 1A/1B or assigned with hazard statement codes H340, H350 or H360			Restricted by REACH annex XVII (RAC 2014)
	Avoid excessive use of environmentally harmful auxiliary substances and waste materials e.g. solvents			12 Principles of Green Chemistry (Warner 2000)
	Commercial accessibility, availability, and durability of raw materials	Overall material cost per IEAP unit*	< 1 EUR	Author's assumption (see Appendix 1.2)
	Reasonable costs (e.g. no gold contacts)			
Production	<ul style="list-style-type: none"> Avoid manual labor and batch-to-batch processes Use industrially up-scalable & automatable processes with existing equipment 	Production capacity IEAPs - (units* per week per line)	appr. 10.000	Author's assumption (see Appendix 1.2)
	Equipment and tools must guarantee work safety at all times			ISO 11014 ISO 45001
	Ensure process reproducibility, e.g. use in-line-monitoring of process variables for quality checks	Tolerances of component dimensions	± 2%	Author's assumption (see Appendix 1.2)
	Allow integration of auxiliary components e.g. IEAP control interfaces and protection			(Kaasik et al. 2017)
Application performance	Operability in (humid) air	Rel. air humidity	20% to 100%	(Košir 2016)
	Functional within appropriate temperature window (with max. 25% performance degradation)	Ambient temperature range	-10°C to +40°C	(Košir 2016))
	Low long-term operational energy demand	Cumulative energy per unit per year	< 25 MJ	Assumptions of the author based on reasonable criteria (see section 2.2.2)
	Real time response of IEAP-based adaptive features	Max. reaction time (→ 80% deflection)	10 sec.	
	Generate sufficient bending force and strain to deform pre-stressed fabric membranes	Bending stress Bending strain	>10 MPa, 1%	
	Exhibit long cycle life with little performance degradation for reliable and continuous operation (both sensor and actuator mode)	Full actuation cycles until 50% degradation	> 10 ⁵	

2.2 Why CNT actuators?

Various types of IEAPs that can be operated under low voltage conditions (less than 3 V) have been developed and a large number of potential applications have been attempted over the years, but even today these devices are still mainly employed in the scientific realm. This section shortly explains conducting or conjugated polymers (CPs), ionic polymer–metal composites (IPMCs) and carbon nanotube (CNT-) or Bucky gel polymers and deduces the grounds on which CNT actuators were selected by using an unsophisticated benchmarking study.

2.2.1 Ionic EAP – an overview

The most commonly known IEAP is the **ionic polymer-metal composite (IPMC)** which is predominantly used as an actuator. IPMCs are composed of an ionic polymer membrane, typically Nafion, sandwiched between a pair of noble metal electrodes (Nakshatharan et al. 2018b; Tamagawa et al. 2019). When a voltage is applied to the metal electrodes of an IPMC, it causes directional motion of mobile cations together with water molecules from the ionic membrane to the electrode surfaces, where they form an electrochemical double layer. The excess of cations and water near the negatively charged electrode causes swelling which results in bending toward the positive electrode. IPMCs are, like CNT- or Bucky gel actuators, capable of self-sensing (Kruusamäe et al. 2015b).

Even though this type of actuator is well studied, wider deployment of these materials for applications is limited, mainly because of their complex manufacturing, limitation in obtaining large electrode surface area, and unstable operation caused by evaporation and electrolysis of the water, which is typically used as a solvent (Nakshatharan et al. 2018a).

Conjugated polymers (CPs) represent a class of intrinsically conducting polymers such as polypyrrole, polyaniline, PEDOT:PSS and polythiophene that have unique actuation prop-

erties (Melling et al. 2019). Their working principle is based on volume change in the electrodes due to the insertion and extraction of counter-ions into the polymer matrix. In contrast to other IEAP, chemical oxidation and reduction processes occur at the ion-polymer interfaces. CPs usually operate in liquid electrolyte environments and are thus often proposed for biomedical applications, where the surrounding fluids (e.g. blood) can serve as an electrolyte. There are concepts of in-air operating CP actuators using an Interpenetrating Polymer Network (IPN) that contains the liquid electrolyte (Plesse et al. 2005). Such IPNs use one polymer network as ion-conducting material and a second polymer network to provide the required mechanical properties. Early works have predominantly covered microfabrication of CP actuators for medical applications (Jager et al. 2000) while newer research has proposed ink-jet printing of PEDOT:PSS on IPN networks for mass production of air-operating artificial muscles and supercapacitors (Põldsalu et al. 2018). Other findings provided fast and durable CP actuators using graphene and a percolation network of silver nanowires to enhance the conductivity of the PEDOT:PSS electrodes (Park et al. 2018b). An advantageous feature of CPs is that they hold their produced strain under DC voltage and at open circuit states.

Unlike IPMCs, **CNT-based IEAPs** employ a pair of polymer-supported Bucky gel electrodes containing CNTs instead of noble metal electrodes. Bucky gel is a highly viscous and electrically conductive gel obtained by physical cross-linking of highly entangled CNT bundles in the presence of imidazolium-based ionic liquids (IL). Such gels are stable at wide temperature ranges and do not shrink or dry out under reduced pressure due to the non-volatility of the ionic liquid. They can also be incorporated into a polymeric composite matrix to form free-standing conductive electrodes, which were used to build the first Bucky gel actuator that could operate in air without external electrolytes at comparably low applied voltages (± 3.0 V) (Fukushima et al. 2005). Other carbon-based IEAP possess electrodes fabricated with activated carbon, carbide-derived carbon, carbon aerogels or graphene. Many studies have investigated hybrid carbonaceous actuators containing two or more of the aforementioned materials as active material.

2.2.2 Benchmarking performance characteristics of IEAP

For a decision about which type of IEAP is most suitable for the desired target applications, it is useful and important to compare their individual performance characteristics. To generate apertures in fabric membranes for building envelopes, long operation lifetimes and reproducibly strong forces and displacements are necessary. Slow actuation responses on the other hand should not have a negative impact, because changes in ambient temperature and humidity are also slow. Maximum internal material strains are key performance indicators for IEAP bending actuators. They indicate the unidirectional change of length within the electrode layers and, therefore, relate directly to the induced stress due to ionic transport forces. Induced bending strain and stress values are independent of the size or geometry of IEAP actuators, thus they can be used for direct comparison of their performance.

For benchmarking purposes, induced strain and stress values of different reported IEAP species have been collected from a variety of publications and are assembled in Figure 9. The illustrated performance boundaries take into consideration actuators operable in air only and depict values obtained under very low actuation frequencies (< 0.1 Hz). Other actuator technologies such as SMA, DEA, skeletal muscles and others are also included for comparison.

Most IEAP species exhibit similar stress-strain combinations around 1 MPa and 1%, respectively, however, CNT Bucky gel actuators appear to be especially promising regarding the results of (Sugino et al. 2011) demonstrating a bending strain of 1.9% and an induced stress value of 10 MPa at 0.05 Hz actuation frequency.

Regarding IPMC actuators, most reported examples exhibit substantial back-relaxation effects, which is the unwanted behavior of a DC-excited actuator to slowly relax back towards its initial shape instead of holding its bent state (Vunder et al. 2012).

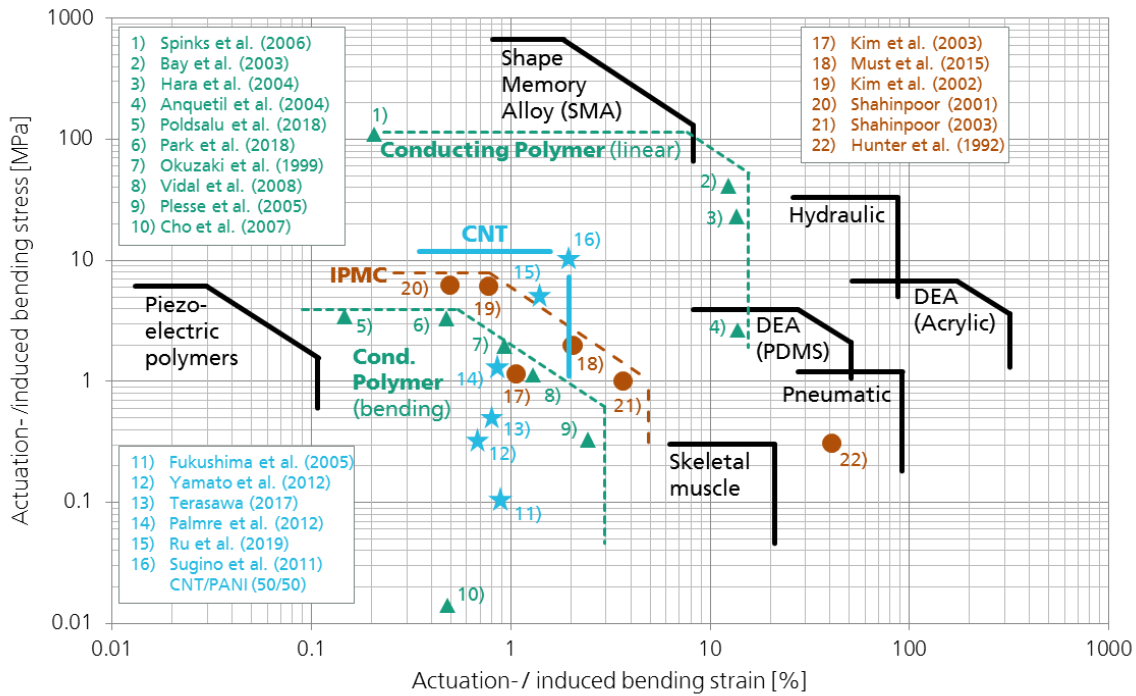


Figure 9 – Benchmarking of EAPs. Stress vs strain of typical actuator technologies (solid black lines) and some state-of-the-art ionic EAP actuators operable in air – inspired by (Simaitte 2015) and based on sources referenced in the diagram.

Other important performance characteristics of IEAP are cycle life and degradation behavior over time. Generally, cycle life is strongly dependent on the material composition of the actuator, on its stress and strain outputs and on the frequency under which it is tested. The reported cycle life of different IEAPs varies between thousands and millions of cycles. Some authors praise the large strain of their samples, while cycle life tests are implemented at high frequency and almost imperceptible strain, which puts the usefulness of such results into question. Obviously, the reason behind data discrepancy is the absence of a generally recognized methodology (Punning et al. 2014).

The degradation in any type of IEAP is commonly evaluated from the decrease of either the peak-to-peak displacement or the tip angle (Punning et al. 2014). Gradual degradation is observed and reported most often and occurs due to fatigue of the polymer, i.e. change in

the mechanical properties, chemical degradation of the material (Madden et al. 2007), receding electrolyte or irreversible redox reactions (Simaite 2015) and reduction in the charge transfer.

Fig. 10 provides a collection of cycle life data for each of the three main types of IEAP actuators. The data points are chronologically arranged over their time of publication between the year 2000 and 2020.

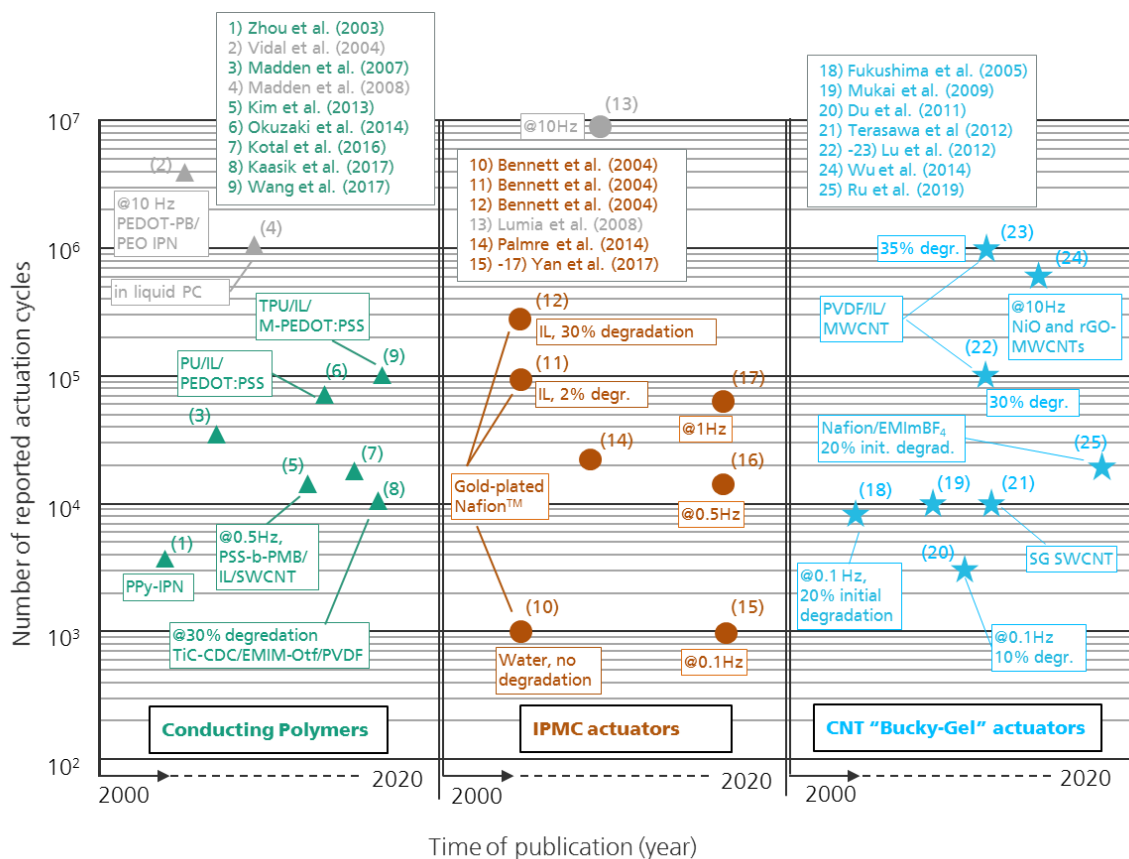


Figure 10 – Reported IEAP actuation cycles from 2000 until 2020

In terms of lifetime investigations, CP actuators constitute a well-studied species of IEAP. Starting with 3600 actuation cycles reported for early polypyrrole-based IPNs (Zhou et al. 2003) their performance continuously improved up to 70,000 cycles for CPs having a polyurethane (PU) electrolyte layer with PEDOT:PSS electrodes (Okuzaki et al. 2014). A few years later, 100,000 stable cycles were achieved with MWCNTs incorporated into similar

electrode layers (Wang et al. 2017). Only those actuation cycles measured at an actuation frequency of 1.0 Hz or below were taken into account. Higher frequencies admittedly lead to much higher cycle numbers, but they produce much lower forces and almost undetectable displacements which is not a useful scenario for the intended application.

Early long-term studies on IPMC actuators based on ionic liquids have shown promising stability properties, demonstrating as much as 100.000 actuation cycles with no serious degradation and up to 300.000 cycles with only 30% decrease in tip deflection (Bennett et al. 2004). These results have triggered intense global research, but even though great improvements were reported in the field of power characteristics and applications (Zhao et al. 2013; Tamagawa et al. 2019) it was not possible to increase the in-air operating lifetime of IPMCs significantly. Only nanostructured compliant electrodes that were produced by supersonic cluster beam implantation (SCBI) achieved some 76.000 cycles (Yan et al. 2017b). Nevertheless, they were claimed to be cost-effective and suitable for industrial production scale-up.

The absence of sufficient data for CNT actuators makes it difficult to assess the true development of their cycle stability. Existing reports suggest a persistent improvement in cycle life, going from 8.000 cycles in 2005 (Fukushima et al. 2005) to 100.000 in 2012 and finally reaching 500.000 in 2014 (Terasawa et al. 2012; Wu et al. 2014). Even though CNT actuators are usually subject to performance degradation – either initially or continuously over time (Lu et al. 2012) – their overall long-term behavior seems to be in no way inferior to their competition.

2.2.3 Benchmarking of material and production related characteristics

Across all species of IEAP, there is not much data available regarding total material cost and manufacturing times. Most material costs are subject to economy of scales and strongly depend on the industrial level of the manufacturing process and the quantity of the produced samples. The prices of most raw material for IEAP have dramatically decreased within the last two decades, except for gold which is sometimes used for IPMC electrodes.

Total IEAP manufacturing times – if not directly reported – were derived from detailed descriptions of individual manufacturing methods in selected publications. Organizational and auxiliary activities such as purchasing, laboratory preparation, and safety precautions are not considered here. Long manufacturing times do not necessarily mean long working hours for scientific staff, because individual fabrication stages comprise automatic processes without human interaction, e.g. chemical or physical vapor deposition processes. Figure 11 presents literature values for manufacturing times and material costs per square centimeter of actuator laminate for each of the three species of IEAP. The underlying data for most data points can be found in the Appendix A1.3. For some data points, the duration of individual fabrication steps is based on sound assumptions and the expertise of the author. Furthermore, most cost values in Figure 11 are based on reasonable estimations and range between substantiated cost boundaries that were extracted from well-founded but sparse literature sources.

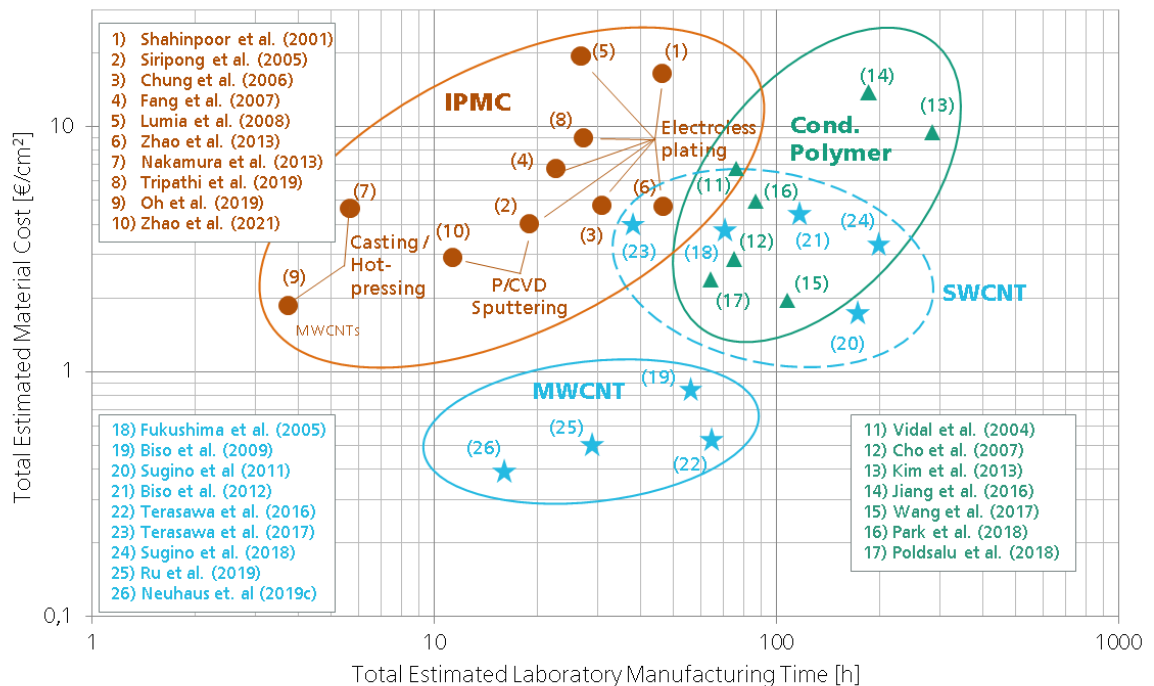


Figure 11 – Assessment of material cost and manufacturing times for IEAP actuators

For IPMCs, the most contributing cost factors are the polymer membrane, the electrode material, and the fabrication method. The polymer is commonly made of expensive per-fluorinated ionomers, such as commercially available Nafion™, Flemion™, or Aciplex™ membranes, which are relatively expensive at a price of ~ 1.00 €/cm² for films with a thickness of 50 μm (Nafion N-117 or N-1110). Just the polymer membrane of a 250 μm thick actuator thus costs more than 5.00 € per cm², which is tremendously expensive and always makes up the largest part of the total actuator cost. The electrodes are made of noble metals such as platinum, gold, silver or palladium, and sometimes carbon nanoparticles are used. IPMCs require complex chemical reaction-based manufacturing methods to create the noble metal electrodes including electroless plating, physical deposition (PVD) methods such as sputtering, electroplating and tapping with conductive films. Among them, electroless plating is the most common fabrication method employed so far. It is not only a costly process due to utilization of special precious metal complex salts, but also time consuming. The total manufacturing times are calculated from three individual phases which are frequently reported in IPMC related studies: ionic membrane preparation (e.g. Nafion™ casting) and pretreatment (surface roughening), initial impregnation-reduction with subsequent electroding process (typically physical deposition and electroplating), and ion exchange. Fabrication times could be considerably reduced by faster electroless plating processes (Fang et al. 2007), the adoption of sputtering (Tripathi et al. 2019) and finally by trying simple casting and heat-pressing methods with only a few hours needed for the entire process (Oh et al. 2019). Further information about manufacturing and cost influences of IPMC can be found in literature (Bhandari et al. 2012; Hao et al. 2019; Zhao et al. 2021).

Research on CP actuators has made tremendous progress in counteracting delamination and improving the electromechanical coupling efficiency and their cycle stability. The laboratory production of typically very thin actuators has resulted in relatively low blocking forces that have so far hindered a greater commercial adoption of this IEAP technology. Linear actuators made from polymerized pyrrole on Platinum rods have shown strong actuation merits but require long polymerization, doping and drying processes, similar to CP bending actuators. The total estimated material costs of this type of IEAP are roughly in the

same range as IPMCs. However, their manufacturing times are much higher due to their complex manufacturing techniques required for synthesizing and doping conductive polymers such as polypyrrole or PEDOT:PSS.

Regarding CNT actuators, one gram of certain types of single-walled carbon nanotubes (SWCNT) still costs up to USD 1.000,- and more, which is roughly half the price compared to ten years ago. The cost of one gram of multi-walled carbon nanotubes (MWCNTs) is almost negligible for certain commercially available products (see last row in Table 3). Importantly, inexpensive polyvinylidene fluoride (PVDF) films can be used as actuator membranes instead of ionic polymers like Nafion[®]. Then, if MWCNTs are also used instead of SWCNTs, the overall material cost ranges well below IPMCs and CPs, in some cases even by an order of magnitude. Additionally, the reported casting and printing techniques for CNT actuators suggest potentially fast and simple printing methods, offering direct control over the fabrication process.

2.2.4 Assessment of benchmarking results

Although only a few researchers admit that manufacturing of IEAP leads to non-reproducible performance characteristics (Liu et al. 2007), it is obvious that even no two samples from the same laboratory have identical properties. As a result, the situation with IEAPs is very different from mass production industries, for example, where millions of identical samples are always available for testing. Nevertheless, the benchmarking data presented in the previous sections allows for a preliminary assessment of the power characteristics, the material costs and the fabrication times for all three types of IEAP actuators.

It has been established that CNT actuators have reproducibly delivered strong actuation merits which have been confirmed by the author in previous projects (Addinall et al. 2014). Similarly, it has been demonstrated that the lifetime characteristics of CNT actuators are considerably better than their IPMC or CP counterparts. Most of the recent investigations have confirmed that CNT actuators have a cycle life beyond the required 10^5 cycles. It has also been made clear that CNT actuators outclass the other IEAPs in terms of low material

cost with a price of less than 1 €/cm² of IEAP laminate. Individual publications have shown that the fabrication of CNT-based actuators can be accomplished in much shorter time compared to CP actuators and is on average less complex than both IPMC and CP actuators.

When comparing the power characteristics of IEAP, it seems clear that both IPMC and CP actuators fall short of the requirement specifications that were elaborated in chapter 2.1. Only CNT actuators meet the requirements of 10 MPa of strain, a cycle life beyond the required 10⁵ cycles and a cost of below 1 €/cm². However, the complexity and the current state-of-the-art in all relevant steps of the mostly lab-scale manufacturing process for CNT actuators will be subject of the following sub-chapters. Generally, the author believes that their potential to be produced by simple and up-scalable manufacturing techniques such as automated layer printing, their flexibility to customize electrode properties, their proven in-air operability and their distinct sensory capabilities are important features when assessing their application potential for adaptive building skins. Without eliminating the possibility of other IEAP species also being compatible for the described application scenario, CNT actuators were regarded as a premium choice.

2.3 CNT-based actuators – History and working principles

This subchapter provides the scientific background and the current state of the art of CNT actuators. In the first three sections, the three basic physical and electrochemical working principles are derived in chronological order of their discovery, accompanied by a simultaneous description of the historic scientific achievements. The last two sections cover general properties and past and current efforts of performance optimization regarding CNT-based IEAP actuators and sensors.

2.3.1 Individual CNT actuators

After their discovery by Iijima in 1991 (Iijima 1991), CNTs have been subject to many studies due to their unique mechanical, electrical and electrochemical actuation properties. In 1999, the first investigation of visible light-induced actuation of SWCNT bundles was reported (Zhang et al. 1999). In the following years, a variety of actuation methods have been investigated to operate micro- or nanoscopic actuators based on different configurations of individual CNTs or CNT bundles. These investigations included electromechanical, thermal and optomechanical actuation mechanisms of free-standing CNTs (Roth et al. 2002), bimorph cantilever CNTs (Ke et al. 2004), sandwiched individual CNTs (Ikuno et al. 2005) and two arms of nanotubes in the form of nanotweezers that bend towards each other due to electrostatic attraction when stimulated with a low DC voltage (Akita et al. 2002). Due to the reduced scale of such devices, they perform very small motoric bending or switching displacements of several nanometers to a few micrometers (Figure 12) and the generated forces usually do not exceed the sub-micronewton range (Sul et al. 2009).

Intended applications were in the area of nanomaterial or atom manipulation via atomic force microscopes (AFM), current transfer and logical switches in nanoelectromechanical systems (NEMS) and resonant micro-oscillators and gap-sensing devices (Shabani et al. 2012). Such CNT-based nanoactuators do not comprise any polymeric structures and their

working principles are based on purely physical stimuli such as thermal expansion and electrostatic forces. For this reason, they are technically not considered as EAP or IEAP actuators. However, their actuation principle constitutes the first of three fundamental effects relevant for the actuation of CNT-based IEAP actuators: electrostatic attraction (or repulsion) between differently (or equally) charged neighboring CNTs.

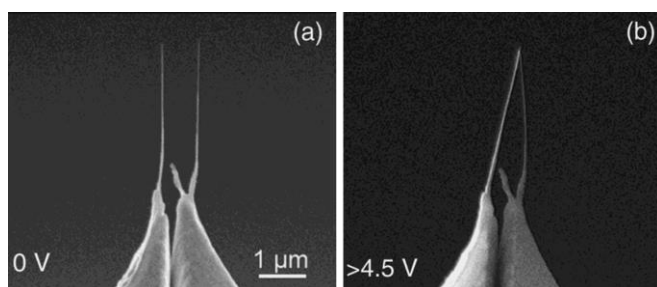


Figure 12 – CNT nanotweezers. SEM images of the motion of nanotube arms in a pair of nanotweezers as a function of the applied voltage. Reprinted with permission from Akita et al. 2002

2.3.2 Buckypaper actuators

Parallel to the development of nanoscopic non-IEAP CNT actuators, the unique mechanical and electrochemical properties of CNTs were also exploited for macroscopic actuators often referred to as artificial muscles. Also in 1999, two-dimensional sheets of macroscopic aggregates of randomly oriented SWCNT – an architecture which is also called Buckypaper – were reported to show an electromechanical response when laminated together with double-sided Scotch tape and submerged in an aqueous electrolyte solution (Baugman et al. 1999). The Buckypaper sheets acted like electrodes in an electrochemical cell, where the applied voltage between them induced electronic charge injection into the CNTs. The induced charge is compensated by the electrolyte ions at the nanotube/electrolyte interface, forming a so-called electrochemical double layer. This double layer allowed for much more charge injection into the CNTs compared to the purely electrostatic actuators of individual CNTs mentioned above. A maximum in-plane strain of 0.2% was reported for the observed bimorph actuation of a nanotube sheet and a stress of 0.75 MPa was generated during the isomeric contraction, which is significantly higher than the maximum stresses that can be

achieved by human muscles (0.3 MPa) (McGinnis 2013). Even though immersing such actuator systems into an electrolyte solution was not a viable option for real actuator applications, this experimental approach proved helpful in obtaining a fundamental understanding of the underlying actuation mechanisms themselves. Initially, the exact contribution of each individual CNT to the overall motion of the Buckypaper could not be fully explained due to the fact that billions of CNTs were randomly oriented within the sheets as individual actuator units. Furthermore, the effect of van der Waals forces led to a natural agglomeration of CNTs in ropes and bundles inside the electrodes which prevented the complete penetration of electrolyte ions inside the material. As a result, only the peripheral CNTs were subject to the observed actuation phenomenon and the entire actuation of the macroscopic Buckypaper sheet was far from optimal. Therefore it was considered very important to directly demonstrate and characterize the actuation principles of a single CNT and “gain a better understanding on how these properties are altered in small bundles and larger structures” (Frayse et al. 2001).

This investigation was carried out one year later by Roth et al. 2002 (Roth et al. 2002). They inserted electric charges into a single “free-standing” CNT that was contacted with gold electrodes on a silicon substrate using photolithographic methods. The actuation effect was measured by placing the tip of an AFM over the nanotube and monitoring the expansion upon charge injection into the nanotube. For a square wave potential of $\pm 1V$ a tube stretching of just under 1% was observed, which correlated well with the expectations deduced from observations with intercalated graphite (Dresselhaus et al. 2002) and with the results obtained on macroscopic Buckypaper (Baughman et al. 1999). Considering the large elastic Young’s modulus of CNTs (~ 1 TPa), this large actuation strain corresponded with a stress generation 30 times greater than the best known ferroelectric, electrostrictive and magnetostrictive actuator materials at that time (Zhang et al. 1998; Bar-Cohen 2003). The stretching of the CNT was explained with a change in bond length between two carbon atoms due to bond weakening upon charge injection. Both electrons and hole injection lead to bond weakening resulting in an increase in nanotube diameter and length. However, electron injection was found to be more efficient, so the bimorph actuation of the Buckypaper actuator was a direct consequence of the slight inequality of the bond weakening for

electron and hole injection, respectively. The second basic underlying effect of CNT actuation has thus been verified: C-C bond elongation within individual CNTs upon charge injection. More about the properties and research activities on Buckypaper can be found in Appendix 1.4.

2.3.3 From Buckypaper to Bucky gel actuators

Already in 2003, a Japanese research group around Takanori Fukushima observed that heavily entangled SWCNT bundles undergo an automatic untangling process when ground in the presence of imidazolium-based ionic liquids (Fukushima et al. 2003). The two materials formed a highly viscous gel by physical cross-linking of the nanotube bundles, mediated by local molecular ordering of the ionic liquids rather than by entanglement of the nanotubes. The gels were stable at wide temperature ranges and did not shrink or dry out under reduced pressure due to the non-volatility of the ionic liquid. This gel was later coined “Bucky gel” and was predicted to form a highly conductive composite material when mixed with an absorbent polymer matrix material. This was achieved two years later when the same group used this gel to build the first Bucky gel actuator, which could operate in air without external electrolytes (Fukushima et al. 2005). The actuator had a bimorph configuration and consisted of a polymer-supported IL electrolyte layer sandwiched between two polymer-supported Bucky gel electrodes. The polymer used was poly(vinylidene fluoride-co-hexafluoropropylene) or PVdF(HFP) and the IL was 1-butyl-3-methylimidazolium tetrafluoroborate (BMIBF₄). It has earlier been reported that these two materials can form stable rubbery gel electrolytes with high ionic conductivities when properly mixed (Fuller 1997). Because both the ionic liquid and the PVdF(HFP) are nonvolatile and chemically and thermally stable, such gels could be operated in ambient environmental conditions and even at elevated temperatures without performance degradation.

The Bucky gel/polymer electrodes were reported to allow rapid and long-lived operation in air (80% of initial displacement after 8000 cycles) with similar strain and stress values (0.9% at 0.01 Hz, 0.1 MPa) compared to Buckypaper actuators at comparably low applied voltages of ± 3.0 V (Figure 13).

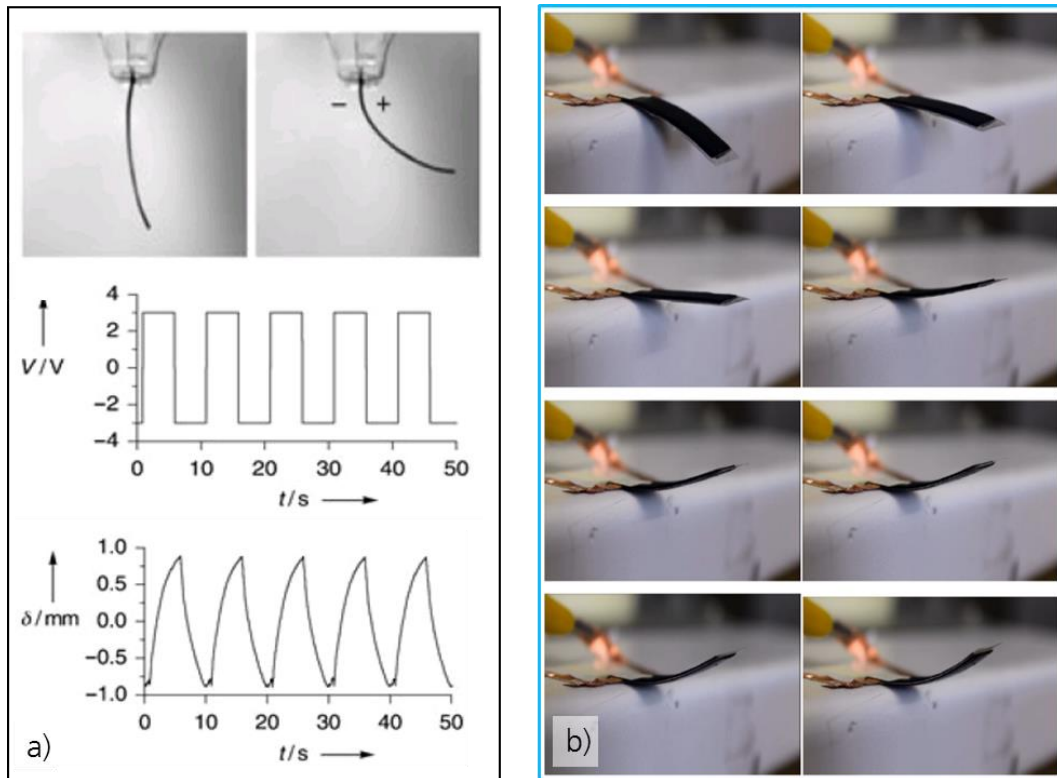


Figure 13 – Performance of Bucky gel actuators a) First CNT bending actuator operating in air (15 mm in length, 1 mm in width, 0.28 mm in thickness) in the non-actuated (left) and actuated state (right) in response to alternating square-wave electric potentials (3V) with a frequency of 0.1 Hz (middle) and typical displacements (bottom). Reprinted with permission from Fukushima et al. 2005. b) Self-fabricated CNT actuator (25 mm in length, 10 mm in width, 0.54 mm in thickness) excited with similar actuation parameters (Neuhaus et al. 2020).

The bending motion of the presented actuator was attributed to dimensional changes of the soft Bucky gel/polymer electrodes in response to the alternating applied voltages. The dimensional changes were assumed to be a result of the imidazolium (BMI^+) and tetrafluoroborate (BF_4^-) ions of the IL being drawn from the electrolyte layer to opposite electrodes where they form electrochemical double layers with the negatively and positively charged SWCNTs within the porous Bucky gel/polymer structure. Since the dimensions of a BMI^+ cation ($9.7 \times 7.0 \times 3.3 \text{ \AA}$) are much larger than the dimensions of a BF_4^- anion ($3.1 \times 3.1 \times 3.1 \text{ \AA}$), the opposite ion transport leads to swelling of the anode and shrinking of the cathode side, respectively (Liu et al. 2010a). Consequently, the actuator was observed to bend towards the anode side. This internal transfer mechanism of differently sized electrolyte ions thus constitutes the third and last underlying basic effect of CNT-based IEAP actuation.

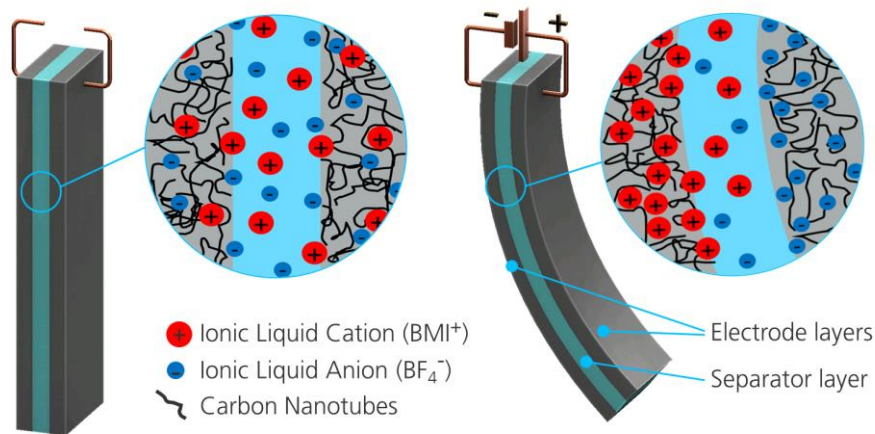


Figure 14 – Illustration of CNT ‘Bucky gel’ actuator in the non-actuated (left) and in the actuated state (right). The curvature is mainly caused by charge induced transport and accumulation of differently sized ions in the electrode structures (source: author’s illustration)

The development of such polymer-based CNT actuators has sparked global interest in this technology and these devices have since been treated as a new species of IEAP actuators next to IPMCs and conjugated polymer actuators (Kamamichi et al. 2007b; Higuchi et al. 2010).

2.3.4 Properties of CNT actuators

Electrolyte layers (separator) have reported thicknesses between 5 μm and 200 μm and Bucky gel electrodes have thicknesses between 30 μm to 350 μm . Typical values are 50 μm to 100 μm for the electrolyte and 100 μm to 150 μm for the electrodes. Thicker actuator electrodes lead to higher bending forces while an overall thinner actuator results in a faster speed and larger displacement (Fukuda et al. 2011; Bubak et al. 2014). CNT actuators exhibit bending strains of around 1% and bending stresses of rarely more than 1 MPa at frequencies between 0.1 Hz and 1 Hz and 3 V bipolar actuation voltage. Regarding the time-dependent behavior of Bucky gel actuators, a higher conductivity of the actuator electrodes naturally leads to a faster bending movement because of a faster build-up of the double layer. A remarkable thermal dissipation during the actuation cycles has been reported by Kruusamäe et al. 2014. In a different publication (Kruusamäe et al. 2014) the same research

team reported that the electrode areas near the electric contacts (fixing clamp, i.e. the voltage source) experience a faster build-up of the double layer compared to those areas further away from the contacts. The electrode thus behaves like a transmission line causing the actuator to have a higher capacitance build-up (and thus bending curvature) close to the clamping, which results in a non-uniform and time-varying distribution of bending curvature over the length of the actuator strip. This *transmission line effect* was found to go along with the so-called *back-relaxation effect* whose mechanical interpretation has been proposed by Liu et al. 2010 (Liu et al. 2010) and Vunder et al. 2012 (Vunder et al. 2012). The back-relaxation effect describes the unwanted behavior of a DC-excited actuator which, instead of holding its bent state, relaxes slowly back towards its initial shape. This effect occurs predominantly for IPMC actuators, but for some CNT-actuator configurations, it has been observed that, along the length of the actuator, sections closer to the electrical input clamp exhibit back-relaxation already when the far end of the bending strip is still in forward motion (Figure 15). Back-relaxation is dependent on many macroscopic parameters such as the input voltage, the actuator length and thickness, and Joule heating reducing the elastic properties of the polymer electrodes. On a microscopic level, the so-called two-carrier model was developed (Liu et al. 2010) and later optimized (Kruusamäe et al. 2015). It suggests that differences in anion and cation size and mobility in any given IL species are the main cause for the unsolicited decrease of actuation force and displacement over time. It states that, at the beginning of actuation, the smaller ion species has little effect on the deformation while the larger ions accumulate at the cathode electrode, leading to its expansion and to bending in the anode direction. But eventually smaller ions are increasingly able to penetrate smaller pores of the opposite electrode (anode), balancing the volumetric expansion of the two electrodes and causing the back-relaxation. Finally, the strain contribution of the smaller ions in the anode becomes larger than that of the bigger ions in the cathode, so the bending direction of the actuator is reversed.

The time-depending behavior of any ionic EAP actuator thus is a combination of ion dimensions and their mobility, which must be taken into account for any application design where such types of actuators play a key role.

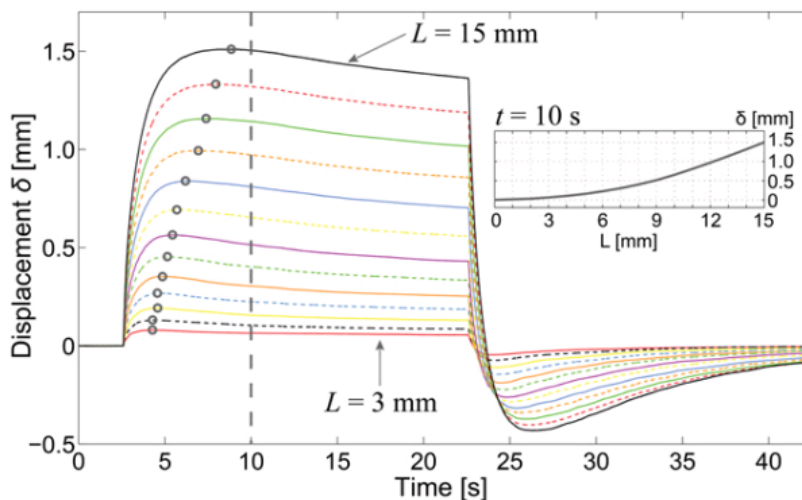


Figure 15 – Illustration of the back-relaxation effect, taken from (Kruusamäe et al. 2014b). The time of maximum displacement (marked as the dark circle on each curve) is different along the distance L of the actuator.

Japanese researchers used molecular dynamics and Monte Carlo simulations to claim that the internal electrode pressure induced by voltage can dramatically change depending on the internal conditions of the actuator electrodes such as the pore size and the dielectric constant of the polymer matrix (Kiyohara et al. 2011). An optimized pore size for each IL species is desirable; however, there is very little influence during the manufacturing process.

Multi-layer Bucky gel devices were reported to have sensory properties (Kamamichi et al. 2007b). Upon manual deflection of a conventional SWCNT Bucky gel actuator clamped between two pickup electrodes, measurable output signals of up to 0.1 mV were emitted that correlated synchronously with the deflection even at high frequencies. This phenomenon was used to build integrated actuator-sensor devices by utilizing two Bucky gel laminates that were stacked on top of each other (Kamamichi et al. 2007a) or connected in parallel (Tanaka et al. 2010).

2.3.5 Past and current efforts of performance optimization

Bucky gel actuators have received considerable attention in the context of their performance optimization. Most activities have targeted a better understanding of the internal actuation mechanisms while varying the active materials and their compositions, changing

individual manufacturing techniques or adopting new modeling and characterization methods. The latter has proven very useful for accurately benchmarking the individual findings of various groups that have formed since Fukushima's paper in 2005. The most important objectives that are targeted by all participating research groups up to this day are:

- an increase in reproducible actuation force, displacement and speed,
- longer cycle-life,
- ease and low cost of manufacturing,
- availability and low cost of materials and
- tailoring the above criteria for the creation of new and practicable applications for society.

Due to the sheer amount of publications and reported activities during the last decade, only those findings are mentioned here that were deemed relevant for the objectives of this thesis.

A different group of Japanese researchers has tested a variety of ILs for their applicability by measuring the double layer capacitance and the electrolyte layer conductivity for seven IL species (Takeuchi et al. 2009). They also introduced a first electrochemical kinetic model by describing the actuator layers with equivalent circuits and thus were able to explain the observed frequency dependence of the displacement response.

In another paper, they used Bucky gel actuators with a mixture of SWCNTs and activated carbon nanofibers for the same seven species of IL, showing higher displacements compared to SWCNT-only electrodes (Takeuchi et al. 2009a).

Other additives and active materials such as activated carbon (AC), carbide-derived carbons (CDC) and polyaniline (PANI) have been studied for improving the actuator's performance characteristics (Sugino et al. 2011; Palmre et al. 2012). PANI has been one of the most promising materials not only for early conductive polymer IEAP actuators (Kaneto et al. 1995) but also for supercapacitors (Prasad et al. 2002) because of its high specific capacitance, low cost, and due to its simple synthesis. When mixed with CNTs, the resulting composite had capacitive properties that outperform those of pure CNTs or PANI (Gupta et al.

2006; Zhang et al. 2009). The addition of conductive PANI nanoparticles to Bucky gel electrodes has been shown to have a particularly positive impact on the actuator's bending strain and stress values. The measured bending strains improved from 0.65% for pure SWCNT actuators to 1.9% for actuators that contained as much PANI as SWCNTs (50 mg of each substance). The bending stresses were increased from 1.8 MPa (no PANI) to 10 MPa (Sugino et al. 2011). Furthermore, cyclic voltammetry analysis of PANI-doped actuators has revealed elevated electrochemical properties such as an almost fourfold increase in electrode conductivity (15 S/cm) and specific capacitance (0.196 F/cm²). For all reported actuation frequencies, the strain efficiency of PANI enhanced actuators was much higher than for SWCNT actuators. Strain efficiency is a parameter that relates the stored electrical energy to the converted mechanical work.

Multi-walled CNTs (MWCNT) are considerably cheaper than SWCNTs and have been studied for Bucky gel electrodes (Biso et al. 2009). Due to their much larger diameter, the specific surface area of the electrode structure is considerably smaller. It therefore follows that the ion wettability is decreased compared to SWCNT electrodes, resulting in a lower overall double-layer capacitance of MWCNT electrodes. With achieved bending strains of 1% at very low frequencies, their performance did not surpass that of SWCNT actuators. However, oxygen-functionalized activated MWCNT actuators have been shown to outperform SWCNT actuators for certain ILs and in certain regions of actuation frequency (Terasawa et al. 2016).

A range of hybrid nanocomposite IEAP actuators has been developed that make use of the synergistic effects when combining CNTs and intrinsically conducting polymers (CPs) (Kosidlo et al. 2013). Especially electro- or oxidative polymerization of polypyrrole (PPy) in Bucky gel electrode slurries have yielded attractive bending performances with strains of up to 400% bigger compared to pure CNT actuators (Biso et al. 2012). The complex polymerization reactions of this technique required 20 hours of stirring in a nitrogen atmosphere and subsequent washing and vacuum assisted drying. Furthermore, the achieved strains strongly degraded over time as irreversible oxidation processes within the polypyrrole lead to a decrease of its pseudocapacitive charge storing capabilities.

A variety of names and abbreviations have been coined over the years to describe CNT-based IEAP actuators. Among those are Bucky gel actuators (BGA) ionic polymer carbon composites (IPCC), nano-carbon polymer (NCP) actuators and others. The author would like to emphasize that in this thesis the expression “CNT actuator” is adopted which refers to CNT-based tri-layer IEAP laminates with both actuator and sensor capabilities.

2.4 State of the art regarding the manufacturing of CNT actuators

For many years after the first CNT/Bucky gel actuators operating in air have been developed, the manufacturing process remained a lab-scale fabrication method using small batches of raw materials and involving laboratory dispersion, casting, drying and handling techniques (Kaasik et al. 2017). This process has been reported to be a linear step-by-step procedure and is schematically illustrated in Figure 16. This subchapter describes the individual manufacturing steps which have been adopted by the author to produce reference actuators that were compared to those manufactured with novel dispersing, printing and contacting techniques explained in chapter 3.

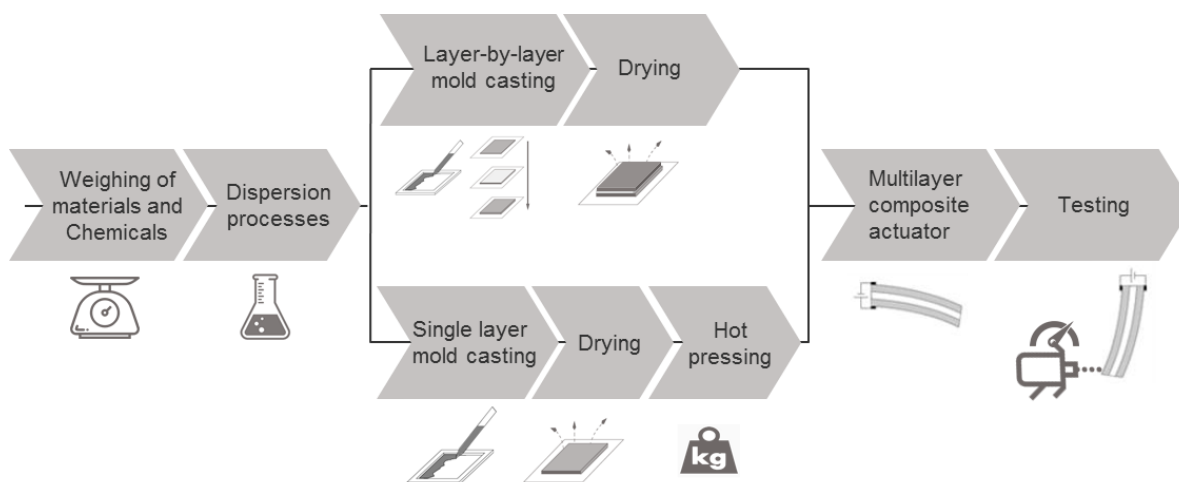


Figure 16 – Illustration of IEAP manufacturing steps. (source: Raphael Neuhaus, IFF 2019)

2.4.1 Mixing and dispersion techniques for CNT actuator fabrication

The first two steps in CNT actuator fabrication are weighing of the desired amounts of active material particles and additives, followed by mixing them into dispersions to facilitate further processing. For both the electrode dispersion and the electrolyte mixture the base polymer granulates are dissolved in a suitable solvent by heat-assisted magnetic stirring. The polymer – usually polyvinylidene fluoride-cohexafluoropropylene (PVDF(HFP)) – later serves as a matrix for the ionic liquid in all three actuator layers and is responsible for the

actuator's stiffness. Regarding the solvents, the latest publications report the use of a mixture of 4-methyl-2-pentanone (4M2P) and propylene carbonate (PC) for the electrolyte mixture and dimethylacetamide (DMAc) for the electrode dispersion (Terasawa et al. 2016). All solvents are organic solvents of which DMAc has the highest potency in reproduction- and hepatotoxicity and has been listed as a CMR Category 1B substance by the European Chemicals Agency (RAC 2014).

For the electrode dispersion, the IL and CNTs are either added directly to the PVDF solution for subsequent electromagnetic stirring (Fukushima et al. 2005; Palmre et al. 2012), or they are first ground manually with a mortar to obtain a gelatinous Bucky gel mixture which is subsequently mixed into the PVDF solution (Fukushima et al. 2005; Biso et al. 2009). After magnetic stirring, the solution is mostly exposed to ultrasonic treatment in an ultrasonic bath. This is done to disentangle the CNT agglomerates and obtain well-dispersed particles in the solution. Details are described in the next section. For the electrolyte mixture, the respective ionic liquid (IL) is directly added to the PVDF solution and mixed thoroughly via magnetic stirring until the finished slurry is obtained. The IL – usually EMI-BF₄ or BMI-BF₄ – serves as a non-volatile electrolytic ion reservoir within all three actuator layers. The PVDF-IL mass ratio is 1:1 in the majority of reported cases.

Japanese researchers (Mukai et al. 2008) have used a ball-milling process to obtain a well-dispersed SWCNT-IL Bucky gel slurry for an optimized electrode with an increased SWCNT content of 22 wt% (compared to only 13 wt% in 2005). They reported an increase in maximum induced bending stress and strain of 4.7 MPa and 1.9%, respectively. It was found that the actuation amplitude (maximum bending displacement at a fixed point of the actuator) is strongly correlated to the charge stored between the electrodes of the actuator. This means, that a high specific surface area inside the electrodes is desired to assist the formation of large double layers. This translates to the core statement that a higher content of well-dispersed CNTs within the Bucky gel polymer electrode leads to higher internal strains and stresses and thus to higher actuator deflections and forces.

Besides CNTs, the electrode dispersion may also receive additives such as Polyaniline (PANI), carbide-derived carbon (CDC) or other carbonaceous particles for enhanced electrochemical or electrical properties. To yield large electrochemical effects and thus high

internal material strains for actuator deflection, a thorough separation of CNT agglomerates and an even distribution of all material components in the final dispersion are essential. Electromagnetic stirring at room temperature and subsequent high-frequency treatment in an ultrasonic bath has been the preferred dispersion method for the electrode materials. Stirring has been reported to last from 3h (Biso et al. 2009) up to 72h (Sugino et al. 2011). Ultrasonication has been reported to last from 5h (Terasawa et al. 2016) up to 24h (Sugino et al. 2018) respectively, to yield sufficient homogenization (see next subsection 2.4.2 for further details about sonication). The types and amounts of CNTs, IL and additives have been varied and the effects investigated (see subsection 2.3.5). However, the basic laboratory dispersion methods have not changed considerably.

2.4.2 General remarks about dispersing CNTs

To date, controlled dispersion of CNTs in a solution or a composite matrix remains a challenge, due to the strong van der Waals binding energies associated with the CNT agglomerates. In conformity with the definitions proposed by (Nichols et al. 2002), in this thesis the term “agglomerate” is used instead of “aggregate” to describe particles that are loosely bonded together by contact to form macroscopic particle assemblages in powders and dispersions.

CNTs or other nano- and microscopic particles, when mixed in a solution by either rotating mixer blades or by cavitation in ultrasonication processes, are subjected to shear stresses in the medium that are ultimately responsible for dispersion. The mechanical energy density delivered by the mixing technique into the solution is opposed by and should be greater than the binding energy density of the CNT agglomerates. On the other hand, the supplied energy should be lower than the fracture resistance of individual nanotubes. To operate within this safe energy window, the correct choice of dispersing technique and energy settings is essential to obtain optimized CNT dispersions. The energy density required to separate a pair of parallel SWCNTs (length $L = 1 \mu\text{m}$, thickness $d = 1 \text{ nm}$, separation gap $H = 3.4 \text{ \AA}$) has been calculated to be 100 MPa (Huang et al. 2012). SWCNTs indeed tend to form

tightly packed parallel bundles, whereas MWCNTs predominantly exist in clusters with a crossed mesh configuration. Due to the fewer contact junctions of this configuration, where MWCNTs cross each other, and due to the stored bending deformation energy to form such crossings, the energy needed to separate MWCNT networks is much lower, only 16 kPa (calculated with a typical spacing value of 100 nm between crossings and average tube diameters of 80 nm).

The magnitude of energy density that can be delivered to the solution by shear mixing techniques depends on the solution viscosity η and the achievable strain rate $\dot{\gamma}$. Assuming a high viscosity medium of 5 Pa · s and maximum achievable strain rates of 4000 s⁻¹, the shear stress (and thus the energy density) induced by the mixer does not exceed $\sigma_s = \eta\dot{\gamma} = 20$ kPa, which is barely suitable for dispersion of MWCNT clusters and will utterly fail in dispersing SWCNT agglomerates. Ultrasonication uses a different mechanism to induce shear stress for agglomerate dispersion: Cavitation bubbles are created in the solution medium above a certain excitation amplitude threshold, due to the ultrasonic alternating pressure of high intensity. Once created, the cavitation bubbles collapse and induce extremely high strain rates of up to 100 MPa into the fluid surrounding the bubble, making this method at first sight suitable for separating even SWCNT agglomerates. However, with CNTs having high aspect ratios of 1000 or higher, the fracture resistance is often lower than the local stress input from sonication, which causes at least some CNTs to be broken before complete separation. Furthermore, the induced cavitation bubbles are distributed inhomogeneously in the medium, which is the reason why static sonication often leads to unsatisfactory dispersion results.

The long reported ultrasonication times of up to 24 hours mentioned in the last subsection were – to the best of the author's knowledge – intended to circumvent this dilemma. By subjecting the CNT-IL-polymer-blend to low power densities over an extended period of time, excessive CNT fracturing can be avoided. The CNT slurries – often pre-dispersed by heat assisted magnetic stirring – are treated in ultrasonic baths that are originally optimized for ultrasonic cleaning purposes. In ultrasonic baths the power of the ultrasound generator is scattered over a large volume of water (50 W to 150 W per liter) and finally propagates through the walls of an immersed beaker that contains the solution. Since the solution inside the beaker is not circulating, the CNT agglomerates do not deviate much from their

initial position and may thus serve as cavitation seeds when treated for long enough time periods, eventually loosening the tight bonds within the agglomerates. Soft sonication thus can ultimately minimize scission of SWCNTs and preserve their structural and electric properties, at the cost of very long sonication treatment times.

Ultrasonic homogenizers, on the other hand, induce large shearing forces directly into a small volume of solution under the flat tip of the vibrating sonotrode horn, the zone of maximum cavitation being only a few millimeters deep. The large induced energy densities quickly lead to CNT fracture, if the solution is not circulated within the beaker. For homogeneous sonication, liquid-cooled rosette cells or flow-through vessels may be used that permit an internally or externally triggered circulation of the dispersion through the main cavitation area.

Another challenge in regards to dispersing CNTs is the unwanted phenomena of re-agglomeration. When the external shear stress is removed, the dispersed CNTs reconfigure themselves to a new equilibrium state of low energy with van der Waals attraction being the driving force (Huang et al. 2012). This process will take place unless surfactants are added to provide steric hindrance or static charge repulsion to stabilize the particles. Soft pulsed ultrasonic homogenization of SDBS-stabilized SWCNT solutions and subsequent centrifugation has shown to yield highly disentangled individual tubes even after prolonged standing times of two months (Paredes et al. 2004). However, scientific investigations regarding the stabilization of well-dispersed high-CNT-loading solutions for actuator electrodes (including a species of IL and PVDF) have not yet been reported anywhere. In this regard, the experimental application of dispersing agents and additives in MWCNT actuator electrodes is considered an underexplored field that needs to be addressed for promoting efficient manufacturing techniques.

2.4.3 State of the art casting, printing and drying techniques

Electrode and electrolyte layers have been produced by manually casting the highly viscous dispersions into one or several molds made of aluminum or PTFE (Palmre et al. 2012;

Kruusamäe et al. 2015a; Sugino et al. 2018). Figure 17a) and b) show how the viscous electrode slurry is being cast from a glass vessel into a prepared PTFE mold and spread out with a laboratory spatula to generate an even surface.

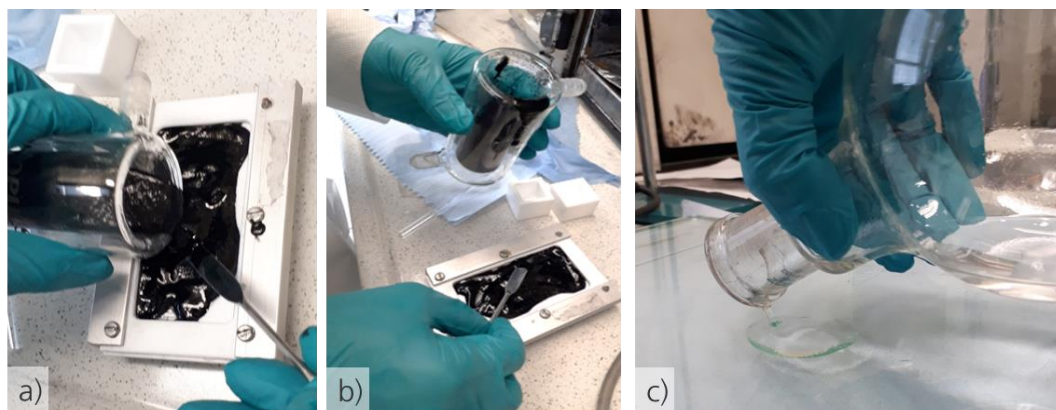


Figure 17 – Manual slurry casting process. a) casting of electrode slurry into a PTFE mold, b) spatula-aided spreading, c) casting of PVDF/IL electrolyte solution onto a glass substrate. (pictures: Raphael Neuhaus, IFF)

In some cases, the mixtures are not poured directly from the mixing flask, but transferred with a pipette to allow accurate distribution and metering of the material to multiple casting molds. Highly viscous mixtures are sometimes heated to increase the flowability into and inside the molds and to avoid dispersion residues inside the mixing flask or the pipette (Ru et al. 2019). If the layer-by-layer casting technique (Fukushima et al. 2005) is used, the heated electrolyte mixture is applied onto the first layer of electrode dispersion. After a short cooling phase, the second layer of electrode dispersion is applied. The wet layer thickness of every layer can be adjusted by removing the excess layer material with a doctor blade.

The cast wet layers are dried under reduced pressure at temperatures of up to 80°C for at least 24 hours. Particularly those electrode layers containing DMAc as a solvent need vacuum-assisted drying for up to 72 h (Sugino et al. 2018) because DMAc is a high-boiling polar organic solvent with a very high evaporation number of 172 compared to 4M2P with a rate of 5.6 (DIN 53170, reference: ether).

A fabrication of Bucky gel actuators based on a printing method has been proposed (Kamamichi et al. 2010). An automated pneumatic discharge dispenser with a three-axis

positioning system was used to apply electrode and electrolyte layers of various shapes onto a fixed substrate (Figure 18). A temperature control unit mounted to the syringe filled with the mixtures prevented the nozzle from clogging due to cooled polymer coagulates. Upon voltage application, a rectangular actuator showed similar bending behavior compared to actuators made by solution casting (approximately 1% bending strain). No further activities were reported in this regard.

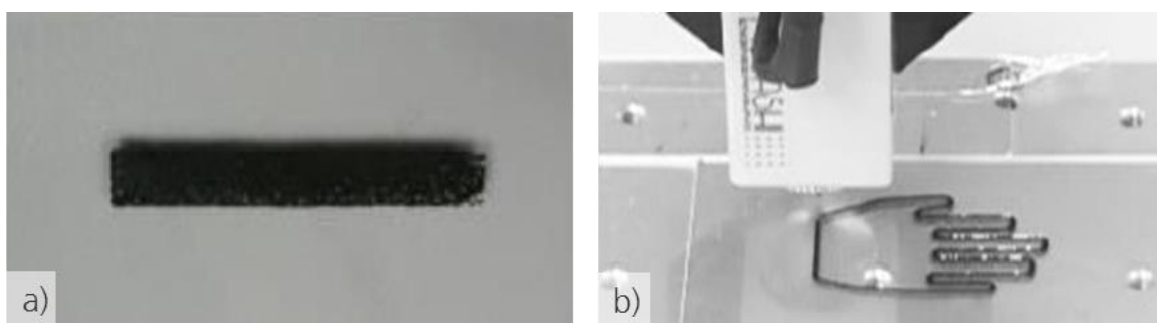


Figure 18 – a) 3D printed Bucky gel actuator. b) automated dispenser for printing Bucky gel electrodes of various shapes. Reprinted with permission from (Kamamichi et al. 2010). No scale bars given in original pictures.

IEAP actuators with carbide-derived carbon (CDC) based electrodes were fabricated by casting the electrolyte membrane only and then spray-painting the electrode dispersions onto the cast membrane (Must et al. 2015). Twenty electrode layers were applied on each side and warm air drying was performed in between every successive layer. This spraying process, which is also called Direct Assembly Process (DAP), has been demonstrated earlier for making hybrid CNT-IPMC actuators with Nafion-117 membranes (Akle et al. 2007). A disadvantage of this method is the anisotropic swelling of the free-standing electrolyte membrane during the spraying process, which can cause buckling of the laminate and can result in uneven electrode coverage. More importantly, the loss in mechanical strength of the membrane during the fabrication process limits the possibilities for scaling up the fabrication (Kaasik et al. 2017).

2.4.4 Actuator assembly, encapsulation and testing techniques

For a better understanding of the conventional assembly process for CNT actuators, all steps were reproduced by the author and are depicted in Figure 19. Actuator electrodes and electrolyte layers are habitually cut from the cast dry layers by hand (usually with a scalpel) to obtain small sheets. The two electrode layers and the electrolyte sheet are stacked carefully and fused by heat-pressing. The electrolyte sheet often has a slightly larger area than the electrode sheets to prohibit electric short circuits at the edges.

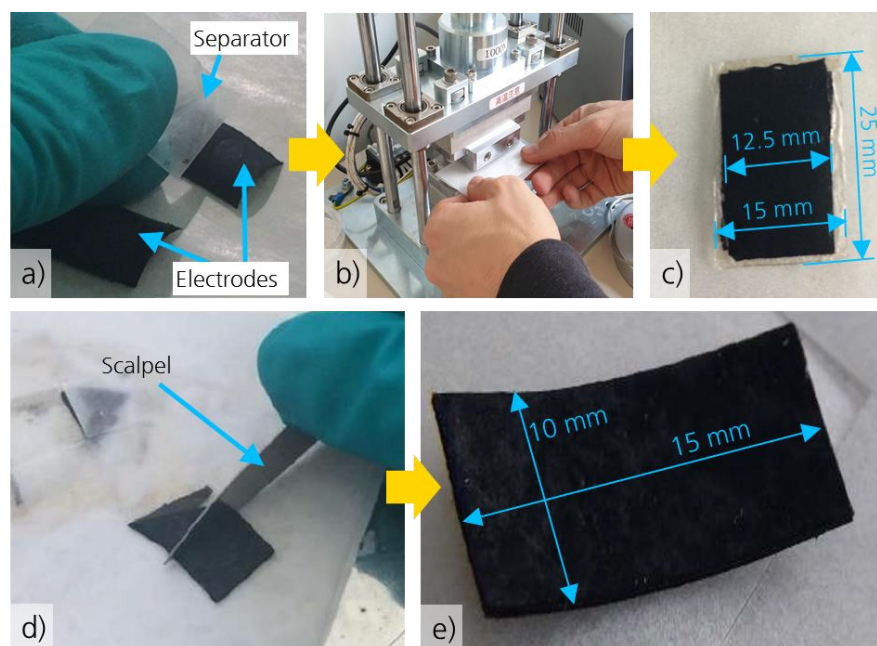


Figure 19 – Manual actuator assembly a) layer stacking, b) heat-pressing, c) pressed three-layer laminate with protruding PVDF-IL electrolyte layer, d) cutting, e) final CNT actuator. (pictures: Raphael Neuhaus, IFF)

There is only little information about temperatures, pressures and pressing times since these parameters are rarely reported. Available values range from 4.3 bar (270 N applied to a 2.5 cm x 2.5 cm sample) for 90 seconds at 70°C (Sugino et al. 2011) to 16 bar (= 16 kg cm⁻²) for 30 minutes at 180°C (Ru et al. 2019). Heat-pressing yields a fused tri-layer polymer laminate with a protruding separator layer in the middle (Figure 19c) which is cut to the final actuator shape (Figure 19d). Rectangular shapes with lengths between 10 mm and 20 mm and widths between 1 mm and 10 mm are dominating for simplicity and comparability purposes (benchmarking). Some IEAP actuators have been coated with a thin

layer of gold (Must et al. 2015) for optimized contact resistances during testing procedures.

After assembly, IEAP actuators are still in their natural form and their conductive electrode surfaces are directly exposed to air and humidity and thus capable of interacting with the surrounding environment. **Encapsulation** is necessary

- a) to provide a strong and anti-abrasive but flexible guard layer against mechanical disruption forces
- b) to protect the complex electrochemical processes inside the IEAP actuators and sensors from the influence of ambient humidity and
- c) for electrical insulation and safety purposes.

Various encapsulation materials like PDMS, PU, nitrocellulose and paraffin-composites have been tested for IEAP actuator laminates in a comprehensive study (Rinne et al. 2019). The encapsulating materials have been applied via dip-coating, spray coating, manual brushing or using tailored CVD processes. Another study has investigated long-time effects (20 hours) of encapsulated IEAP actuators on humidity gain and performance loss (Jaakson et al. 2016). Individual coatings such as sprayed Paraffin or PVDC films have been reported to tremendously prolong the cycle life of the actuator. Specifically for Bucky gel actuators, CVD coated Parylene C was tested, allowing actuators to operate in water for several hours (Bubak et al. 2015).

Testing of CNT actuators is usually done by applying a potential difference to the electrodes and measure the resulting displacement of either the tip or some fixed point on the actuator's bending surface. As stated in 2.2.2, the material strain inside the electrode layers is regarded as a key performance indicator for CNT actuators (Bubak et al. 2014). For thin actuator strips, the electrode strain ε can be directly calculated from the measured horizontal tip displacement δ using equation (1):

$$\varepsilon = \frac{2d\delta}{L^2 + \delta^2} \cdot 100\% \quad (1)$$

L is a fixed distance from the clamping of the actuator, marking the free length where the horizontal tip displacement δ is measured, whereas d is the thickness of the actuator strip. The strain indicates the unidirectional change of length within the electrode layers and therefore relates directly to the induced volumetric swelling or shrinking. Figure 20 helps to understand the relationship between bending curvature and induced strain difference. R is the curvature radius and ΔL_1 , ΔL_2 are the induced length changes in each electrode. Equation (1) holds for small deflections so that it can be assumed that the neutral fiber does not change its length and deforms into an arc. Thus a uniform bending curvature has been assumed for the actuator displacement, which is fairly accurate for fully actuated bending states. By measuring the Young's modulus of the stretched or squeezed electrode layers it is possible to obtain the induced stress values of each actuator. Strains of up to 2% and stresses of about 10 MPa have been reported.

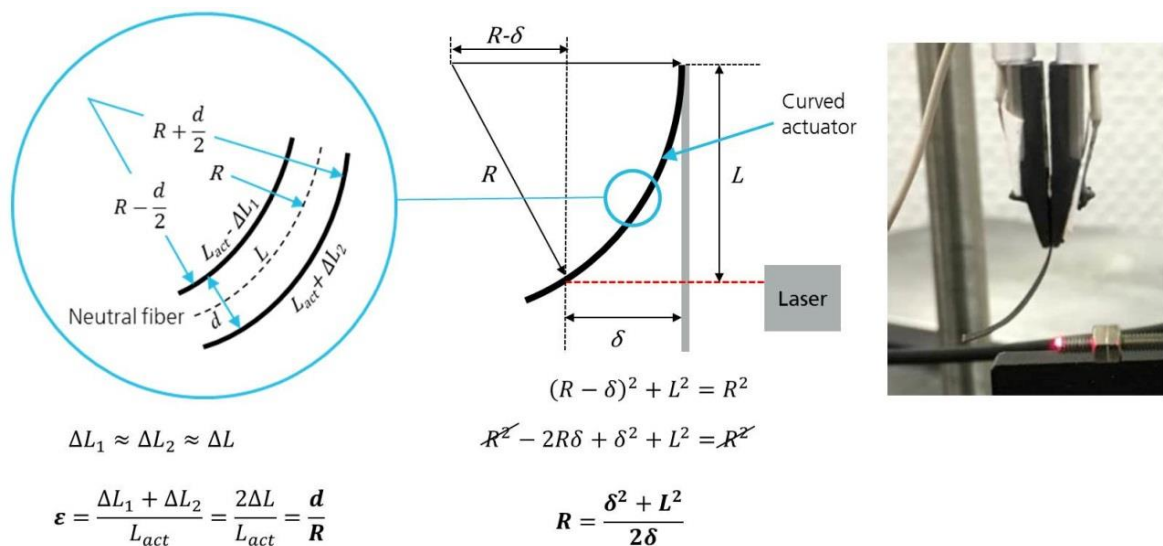


Figure 20 – Characterization of IEAP actuators. Schematic drawing for explaining the evaluation of the strain from displacement measurements using equation (1). (Illustration and picture: Raphael Neuhaus, IFF)

However, equation (1) does not take into consideration the width of the tested actuator sample and is only valid for thin strips. The free tip displacement decreases for wider actuator geometries because the volumetric changes also result in a curvature across the width that interferes with the longitudinal bending motion due to increased compression stress at both edges of the cross-section.

2.5 State of the art regarding integration and application of CNT actuators

The first section of this subchapter focuses on the topic of IEAP actuator integration which includes conventional techniques for embedding electrical connections into their soft polymeric structure and methods for mechanically attaching the actuators to target bodies. It exposes CNT actuators as a particularly neglected species in this respect. The second section briefly summarizes proposed applications and potential use cases of CNT-based actuators and sensors.

2.5.1 Mechanical and electrical integration techniques

For any intended application scenario, IEAP actuators need to interact with other objects to transform their deformation energy into physical work.

Some studies reported about actuators crawling over an object's surface (Must et al. 2015) or perform other operations without being attached to the object. Such self-propelled micro-robots must only overcome frictional forces and carry their own structural weight (including any auxiliary equipment such as on-board batteries and control units). In most reported use cases, however, actuators were firmly attached to an object or body to exert mechanical forces that are larger than their own gravitational weight. This applies, for example, for micro-gripper applications designed to lift heavy loads (Khan et al. 2017) and for swimming robots, where the actuator must oppose viscous shearing forces induced by the medium (Palmre et al. 2013). In all cases, the generated power is counteracted by the actuator's internal stiffness and by the stiffness and inertia of the object (or medium) it is interacting with.

The individual methods for mechanical actuator attachment can be allocated to three main categories: single, multiple and full-surface connections. Single connections often involve clamping or gluing cantilever-type actuators to a fixed object, allowing the other end to bend freely (Fukuda et al. 2011). Multiple connections are used when both actuator ends

are fixed to the same or two different objects. Full-surface connections are realized when one of the actuator's surfaces is fully bonded to an object (Addinall et al. 2014) or when the entire actuator strip is embedded into a flexible structure (Palmre et al. 2013).

Full-surface bonded soft polymeric actuators are relevant for this thesis because they will transfer their bending and twisting actuation into the structure and therefore enforce a controlled deformation of its surface, provided that they are properly connected and generate enough power. Due to their flexibility, they are also mechanically compliant and can be used in curved or even double-curved structures.

Apart from mechanical attachments, all species of IEAP also require stable electrical connections with preferably low line and contact resistances. In almost all reported studies the mechanical and electrical connections were joined in one entity by means of an electrically conductive clamping fixture (Sugino et al. 2011; Kruusamäe et al. 2015a), which was mostly used for performance measurements described in section 2.3.4. To date, only little research has been performed in respect to IPMC actuators, and only one study relates to electrical connection and integration methods for CNT actuators, to which the author of this thesis has contributed himself (Addinall et al. 2014). The study in question was conducted in collaboration with Japanese researchers at the Fraunhofer Institute for Manufacturing Engineering and Automation (IPA). It was examined how the deformation characteristics of CNT actuators can be employed for sucking and dispensing small amounts of liquid with a micropipette. The core task of the investigation was to find a reliable integration technique for small actuators that were attached to a thin elastic membrane, deforming it upon actuation and thus causing a vacuum in the cavity underneath. The main challenge was to ensure a tight and reliable connection between the actuators and the membrane and simultaneously incorporate force-locking or form-fit electric connectors to the top and bottom electrodes of each actuator. A variety of materials and shapes were tested (Figure 21). But the final prototype could only be implemented by a complex arrangement of mostly 3D-printed support elements that provided the necessary force-locking pressure between the connectors and the actuator electrodes. It was found that external electric connectors will always unavoidably limit the deformation of integrated actuators. Hence, an important finding of this study was that CNT actuators in particular and IEAP devices in

general could be integrated and operated much easier and safer if the mechanical and electrical connections were separated features.

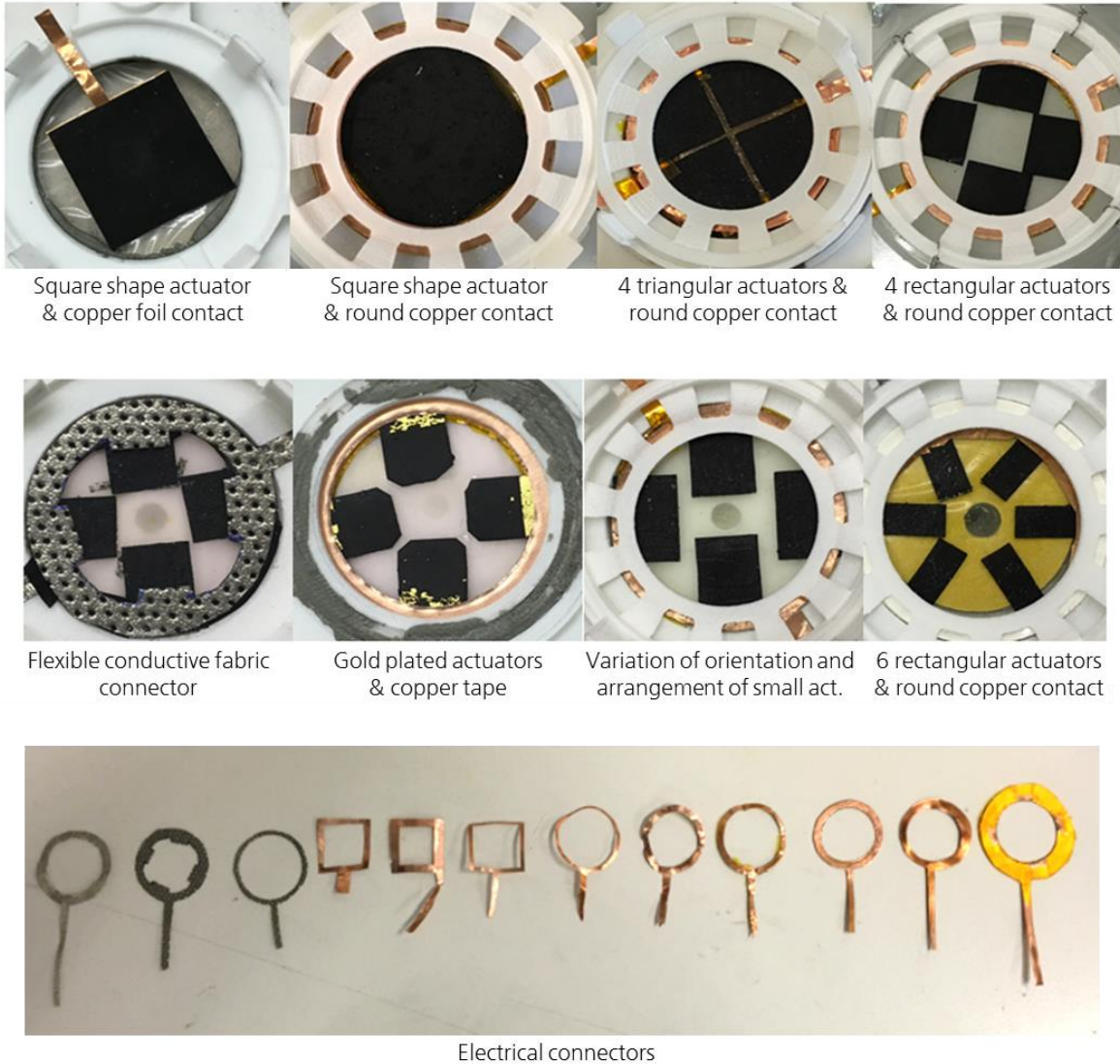


Figure 21 – Integration of CNT actuators and electric connectors into a micropipette application (source: Julian Stübing, Fraunhofer IPA 2016)

Embedded connectors were realized for MWCNT/PDMS deformation sensors by incorporation of copper and carbon fibers into the multi-layer laminates (Leemets et al. 2018).

2.5.2 Current applications and potential use cases

Even though all species of IEAP have been proposed for various potential use cases, none of them was put into commercial or industrial use. Prominent application scenarios were fish-like robots (Laurent et al. 2001; Chen et al. 2010; Palmre et al. 2013) and robotic jellyfish (Yeom et al. 2009), micro-grippers (Lumia et al. 2008; Khan et al. 2017) and biomedical devices (Fang et al. 2007; McDaid et al. 2014) and involved mostly IPMC and CP actuators. Worm-like self-propelling micro-robots (Arena et al. 2006; Must et al. 2015) and flapping beetle-inspired air vehicles (Zhao et al. 2018) have been proposed as biomimetic applications for showcasing the potential of ionic actuators. CNT actuators, however, have had a very small share in such developments, partly because other IEAP species were already quite advanced when Bucky gel actuators operating in air emerged.

One noticeable application example for CNT actuators was the micropipette system described in the previous section, which was further developed into a continuous suction device by arranging a set of additional valves (Goya et al. 2017). A switchable haptic braille display has been developed by Japanese and Italian researchers which utilized an array of small-sized (1 mm x 4 mm) bimorph cantilever actuators for driving small pins through the display surface, providing haptic information to visually impaired people (Fukuda et al. 2011; Bubak et al. 2014).

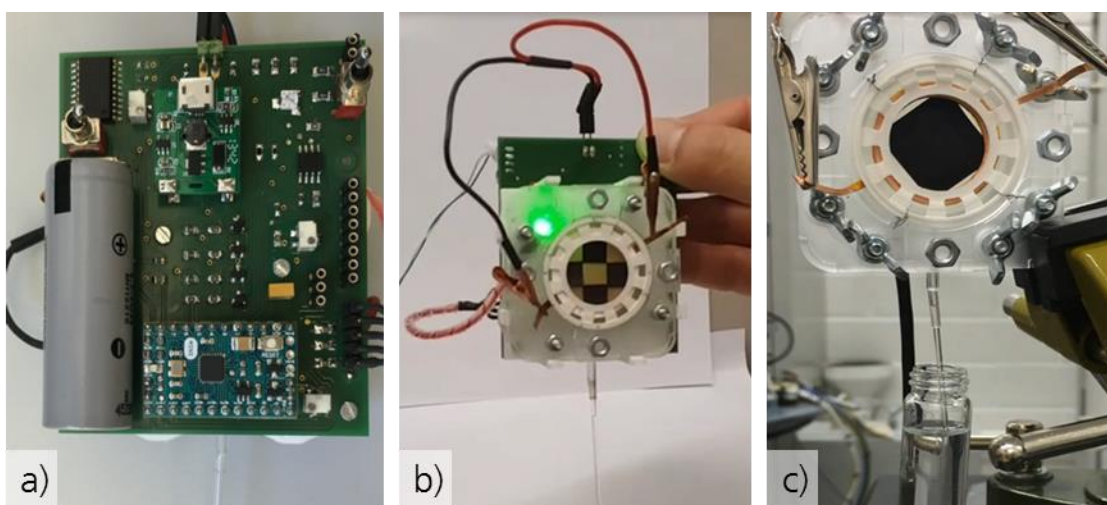


Figure 22 – CNT actuator micropipette developed at the Department of Functional Materials (Pictures: Raphael Neuhaus, ©Fraunhofer IPA, Stuttgart, 2017).

2.6 Conclusion and potentials for improvement

The application of CNT-based IEAP actuators in the domain of building physics and architecture represents a completely new frontier. CNT actuators have been shown to be the technology of choice in regards to actuation merits, low material cost, simple and fast fabrication, cycle life and fulfillment of the requirement specifications for adaptive building envelopes (see chapter 2.2). However, there is a distinct need for action that defines the roadmap to establish and further develop this technology for the proposed use case. In order to target potential commercialization of this technology it is essential to search for shorter and more efficient fabrication methods without any major performance loss of the actuators and sensors.

One of the most important tasks is to generate well-dispersed electrode suspensions that can subsequently be printed to obtain large-scale actuator components. To date, most reported manufacturing methods for CNT actuators involve long-lasting dispersion and drying processes, which account for the largest share in total manufacturing times. 72 hours of magnetic stirring followed by 24 hours of ultrasonication and another 72 hours of vacuum-assisted drying or curing yields an entire week needed to make one actuator electrode (Palmre et al. 2012; Sugino et al. 2018). Furthermore, all steps of actuator manufacturing involve mainly manual labor and laboratory-scale fabrication methods, ranging from small batches of material dispersion and inaccurate casting techniques to utterly tedious actuator assembly and complex encapsulation practices. Due to the lack of process consistency, the performance characteristics of individual actuators remain mostly unpredictable (Kaasik et al. 2017). On the far end of the production cycle, the integration of reliable electric contacts into IEAP actuator electrodes so far remains unsolved. Similarly, research on the application of thin protection layers for encapsulation of specifically CNT actuators is still in its infancy and is thus part of the roadmap for this thesis.

3 Materials and Methods

This chapter describes the scientific methods used to investigate the potential of CNT-based IEAP actuators to be manufactured faster, cheaper and with more reproducible performance characteristics compared to the current state of the art described in the previous chapter.

The first subchapter briefly covers the history, properties and economic aspects of CNTs. The second subchapter shortly elaborates on the other materials used for CNT actuator manufacturing and explains how their properties are relevant for manufacturing techniques and application scenarios. The third subchapter describes the Design of Experiments method employed to obtain optimized material compositions and dispersion parameters for printable actuator electrodes and the characterization techniques used to measure influencing factors and target figures. The fourth subchapter refers to four different manual and semi-automatic coating and printing techniques that were investigated to obtain large-scale actuator components with homogeneous material and performance properties. The fifth subchapter elucidates novel actuator assembly and integration concepts and provides details about the simulation-assisted design methods employed for the development of functional demonstrators.

3.1 Carbon nanotubes

Carbon is the chemical element participating in (by far) the largest number of compounds and it is one of the lightest elements that forms covalently bonded solids at room temperature. Therefore, it is not surprising that carbon also plays a special role in nanotechnology and that a variety of nano-technological applications are based on this material.

Carbon nanotubes (CNTs) are rolled-up monolayers of graphene that exhibit exceptional electrical and mechanical properties. Graphene is a special carbon allotrope (Novoselov et al. 2004) and consists exclusively of sp^2 bonded carbon atoms structured in a two-dimensional hexagonal lattice. It is the basic building block of all graphitic materials including 0D fullerenes, 1D carbon nanotubes and 3D graphite. If only one layer of graphene is rolled up to form a single-layer graphene tube, such tubes are referred to as single-walled carbon nanotubes (SWCNT). If they consist of multiple layers of graphene rolled up to form concentric tubes around each other, they are called multi-walled carbon nanotubes (MWCNT). Rolling up layers of graphene is of course not the usual way of making carbon nanotubes, but this theoretical illustration may help to better understand their structure.

This subchapter provides a brief overview of the history and manufacturing techniques of CNTs and describes their metric classification and physical properties, particularly focusing on the electrical properties. Individual manufacturing processes yield CNTs with different properties and thus have a strong influence on their commercial availability, price and applicability for CNT actuators which is an important aspect of this thesis. Furthermore, their dispersion behavior and their current state of application are being examined. Comprehensive further information about CNTs is provided by Saito et al. 1998, Dresselhaus et al. 2001, Krueger 2007, Li et al. 2013 and Roth et al. 2015.

3.1.1 History and fabrication techniques

The history of CNTs started with the discovery of so-called fullerenes. These football-like structures of pure sp^2 -hybridized carbon have been theoretically predicted and calculated

by the Japanese researcher Eiji Osawa in 1970, but since the publication was in Japanese (Osawa 1970) the results had a negligible impact in the global research community at that time. Only in 1985, when Robert F. Curl jr. (USA), Sir Harold W. Kroto (England) and Richard E. Smalley (USA) published an article in *Nature* (Kroto et al. 1985) about creating stable spheroidal carbon clusters with one predominant species consisting of exactly 60 carbon atoms, Osawa's prediction was verified and the researchers were awarded the Nobel Prize in Chemistry in 1996. With their spheroidal surface made up of pentagonal and hexagonal carbon lattices, these structures were named "fullerenes" after the American architect Richard Buckminster Fuller, who designed round geodesic domes for buildings fabricated with similarly structured surface elements. Referring to his nickname "Bucky", the terms Bucky Ball (also describing fullerenes) and Buckypaper (paper-like structures of agglomerated CNTs) have also been coined in his honor (Krueger 2007).

In search for other fabrication methods of fullerenes, in 1991 the Japanese scientist Sumio Iijima accidentally created nano-scale tubular carbon structures when he tried to synthesize fullerenes through arc-discharge evaporation between two charged graphitic electrodes. His publication in *Nature* (Iijima 1991) mentions carbon nanotubes for the first time in history and is generally regarded as the discovery of MWCNTs, although that Russian researchers have described similar findings decades before (Radushkevich et al. 1952). Also earlier than Iijima, M. Endo found „concentrically arranged graphitized carbon fibres“ already in 1976 and proposed a catalytic growth mechanism for their controlled fabrication (Oberlin et al. 1976). One year after their discovery, two scientists working on metallic nanostructures at NEC (Japan) managed to synthesize bulk quantities of MWCNTs with a conductivity of about 100 S cm^{-1} using the same method as in 1991 (Ebbesen et al. 1992). SWCNTs, however, were first discovered and reported by Iijima et al. 1993 (Iijima et al. 1993).

Mainly three different methods for CNT synthesis have been developed since their discovery and are still used in commercial production today. The **Arc-Discharge Evaporation method** mentioned above was originally intended for fullerene production and employs two graphitic carbon electrodes facing each other in a partially evacuated chamber with inert gas atmosphere. By applying a DC voltage of approximately 20 V, a current between

50 A and 100 A is triggered, generating arc plasma between the electrodes. As the anode is consumed through carbon evaporation, a soft fibrous deposit containing carbon nanotubes and other carbon particles is formed on the cathode (Journet et al. 1998). To achieve SWCNTs, the electrodes are doped with a suitable catalyst, such as Ni-Co, Co-Y or Ni-Y (Journet et al. 1997). The tubes produced by this method are usually tangled and of varied length and diameter. However, due to the high process temperatures (1700 °C) the CNTs are of high quality, with a low incidence of defects (Eatemadi et al. 2014).

In the **Laser Ablation method**, a graphite target is vaporized by focused laser irradiation under inert atmosphere at temperatures near 1200 °C. The generated carbon molecules settle on cooler regions within the reactor chamber and form MWCNTs with closed caps and little defects (40%) and other carbon species such as amorphous carbon and fullerenes. For SWCNT synthesis the graphite target is doped with a small amount of transition metals such Ni and Co, serving as catalysts in the deposition areas. Thess et al. 1996 (Thess et al. 1996) claimed that it is possible to create up to 1.5 g/h of SWCNT material using the laser technique. However, the actual reported yields and the amounts of energy needed for this process suggest that a profitable production process is not feasible (Meyyappan 2005).

The **Chemical Vapor Deposition (CVD) methods** are the most common manufacturing methods for CNTs (Nessim 2010). The main advantages of CVD are an easy control of the reaction course and high purity of the obtained material (Prasek et al. 2011). In contrary to the other methods that use solid graphitic material as a carbon source, CVD methods utilize carbonaceous gases such as methane, ethane, ethylene or acetylene. These precursor gases flow into the tempered reaction chamber and over a zeolite or silica substrate, where they are decomposed in the presence of small catalyst metal particles deposited on the substrate surface where the carbon atoms rearrange to form carbon nanotubes that grow either bottom-up or top-down. The lower temperatures (500 °C – 900 °C) used in this method reduce production costs (Xie et al. 2000). However, CNTs made by this method generally have a large number of defects (Nessim 2010) that could potentially be recovered by post-annealing processes at temperatures close to 2000 °C (Pinault et al. 2004). Modifications of the traditional CVD method are Plasma Enhanced CVD (PECVD), Hot Filament

CVD and radiofrequency- or microwave-assisted PECVD, all described by Prasek et al. 2011 (Prasek et al. 2011) and partially by Dresselhaus et al. 1996 (Dresselhaus et al. 1996). Newer methods employ magnetic enhanced CVD synthesis (Yokomichi et al. 2008).

A fourth synthesis technique developed at Rice University in Houston, Texas, is the **High-Pressure CO Conversion (HiPco) method** which is employed to produce SWCNTs by continuously flowing both the carbon monoxide gas phase (i.e. the carbon feedstock) and the catalyst precursor iron carbon monoxide Fe(CO) through a heated reactor (Nikolaev et al. 1999; Bronikowski et al. 2001). The average diameter of HiPco SWCNTs is approximately 1.1 nm and the yield has been growing from 70% (Nikolaev et al. 1999) to 90% (Isaacs et al. 2010), meaning that in 1999 30wt% of the fabricated material consisted of amorphous carbon, carbon oxides and Fe residues, and not SWCNTs. This method was presumed to be suitable for large-scale synthesis because the nanotubes are free from catalytic supports and the reaction can be operated continuously. However, the production rates are still low, ranging from 450 mg/hour/reactor (Bronikowski et al. 2001) to 500 mg/hour/reactor (Gangoli et al. 2019). Thus, up-scaling of production can only be achieved by setting up multiple reactors.

In 2004 Sumio Iijima introduced the **super-growth CVD method** or water-assisted CVD, where the activity and lifetime of the catalyst are enhanced by the addition of water into the CVD reactor (Hata et al. 2004). With this method dense, well-aligned SWCNT-forests free from amorphous carbon and metal particles are grown perpendicular to the substrate with heights up to 2.5 mm. Bucky-Gel actuators with super-growth CNTs (SGCNTs) have been assembled and benchmarked by Mukai et al. 2009 (Mukai et al. 2009), Biso et al. 2010 (2010) and Biso et al. 2011 (Biso et al. 2011). In 2012, SGCNTs were used to build IPMC actuators in combination with polypyrrole-doped electrodes (Yamato et al. 2012), resulting in induced actuation strains of up to 0.7%.

The schematic representations and the most important process parameters for the above-mentioned production methods for carbon nanotubes are shown in Figure 23.

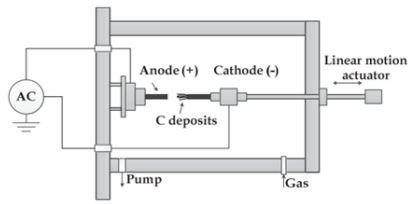
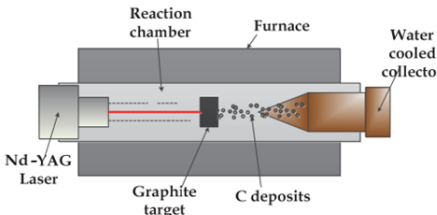
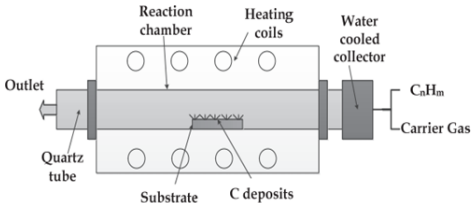
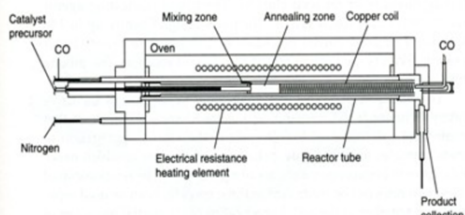
Method	Schematic representation	Process parameters
Arc discharge		Arc plasma generation between graphite electrodes Yield: ~ 1 g/h MWCNT for pure graphite rods, SWCNT for graphite anode containing metal catalyst (Fe or Co) Process temperature: approx. 1700 °C
Laser ablation		Vaporization of graphite target by laser irradiation Yield: ~1.5 g/h MWCNTs for pure graphite target, SWCNT for doped metal catalysts in the deposition area (Ni or Co) Process temperature: approx. 1200 °C
Chemical vapor deposition (CVD)		Controlled deposition of carbonaceous gases inside a tempered reaction chamber Yield: > 10 g/h (SWCNT), > 1000 g/h (MWCNT) Process temperature: 500 °C – 1200 °C Annealing (optional): 2000 °C
High-Pressure CO Conversion (HiPCo)		Simultaneous infusion of carbonaceous gas and catalyst precursor into a tempered reactor tube. Yield: ~ 0.5 g/h per reactor (high purity SWCNT) Process temperature: 700 °C – 950 °C

Figure 23 – Schematic representations of CNT synthesis methods with process parameters

3.1.2 General properties of carbon nanotubes

While carbon fibers typically have diameters between five and eight micrometers, the smallest SWCNTs have a diameter between 0.8 and 1.2 nanometers (Guan et al. 2008; Gangoli et al. 2019) and MWCNTs thicknesses vary between 10 and 50 nm (Thomsen et al. 2004).

For this thesis, no CNTs have been synthesized by the author. All CNTs used for fabricating CNT-based IEAP actuators have been purchased from industrial manufacturers. Commercial CNT materials are usually not available as pure, separate and uniform CNTs. In fact,

they are shipped as an inhomogeneous powder of macroscopic agglomerates. Such agglomerates have individual sizes, shapes and structures and include residues of amorphous carbon and contamination particles such as metallic catalyst residues. For this reason, all CNT materials must undergo purification processes done either by the manufacturer or by the end-user.

3.1.3 Multi-walled CNTs

One of the main targets of this thesis was the substitution of SWCNTs with MWCNTs. As stated in section 2.2.5, MWCNT actuators have been built which achieved maximum bending strains of approximately 1% for non-functionalized MWCNTs. It was further mentioned that the binding energy of MWCNT agglomerates is considerably lower compared to SWCNT agglomerates, which should have a positive effect on their dispersibility. NC7000™ from Nanocyl were chosen for this thesis, because they are available in large quantities and for reasonable prices. Their purchasing costs are more than 4000 times less expensive compared to HiPco synthesized SWCNTs which can be attributed to the lower production costs (Table 3).

Furthermore, they constitute a well-established product with good market adoption, which is an important factor in regards to material availability and consistency of relevant properties. Their primary applications are in electronic packaging, polymer amplification and as power enhancement additives for Li-ion batteries.

Table 3 – List of carbon nanotubes used for CNT actuator production and their properties (data collected and assembled by the author)

Data \ Brand (type)	Unidym HiPco (purified SWCNT)	HiPco SD (super purified SWNT)	Signis® CG300™ (SWCNT)	Nanocyl NC7000™ (MWCNT)
Relevance	Used in baseline dispersion (<i>Sugino et al. 2011</i>)	Used for SWCNT actuators today	Used in this thesis as <u>reference</u> material	Used in this thesis as <u>target</u> material
Manufacturer (country)	Unidym Inc. (until 2013) (California, USA)	NanoIntegris Technologies Inc. (Canada)	Chasm Advanced Materials (USA)	Nanocyl SA (Belgium)
Supplier / distributor	Unidym Inc.	NanoIntegris	Sigma Aldrich	Nanocyl SA
Manufacturing method	HiPco™ (CVD)		CoMoCAT™ (CVD)	Catalytic Carbon Vapor Deposition (CCVD)
Use	R&D		R&D	Industrial
Purity	> 95 wt% (CNT)		> 94 wt% (COOH-functionalized CNT)	> 90 wt% (carbon)
Length	100 – 1000 nm		1.0 µm (median)	1.5 µm (median)
Average Diameter	0.8 – 1.2 nm		0.84 nm	9.5 nm
Specific surface area (BET)	~400 – 1000 m ² /g	< 1315 m ² /g	> 700 m ² /g	250 – 300 m ² /g
Resistivity	n.a.	n.a.	< 10 ⁻⁴ Ω·cm (CNT yarns)	10 ⁻⁴ Ω·cm (on powder)
Production capacity (reference)	0.45 g/hour/reactor (<i>Isaacs et al. 2010</i>)	0.5 g/hour/reactor (<i>Gangoli et al. 2019</i>)	~10 g/hour/reactor (<i>UO 2004</i>)	>1000 g/hour/reactor (<i>Nanocyl 2017</i>)
Price per gram (reference)	\$2000 (<i>Isaacs et al. 2010</i>)	\$1900 (<i>NanoIntegris 2020</i>)	€1017 / ~ \$1160 (<i>Sigma Aldrich 2018</i>)	€0.25 / ~\$0.28 (<i>Nanocyl 2017</i>)

3.2 Other CNT actuator materials and components

This subchapter provides information about the material components that were used for the Design of Experiments (DoE) method described in the next subchapter and subsequently for the printing experiments explained in subchapter 3.4.

3.2.1 Ionic liquids

Ionic liquids (IL) are salts in the liquid state, some of which are liquid at ambient temperatures (Room Temperature Ionic Liquids – RTIL). They usually consist of heterocyclic cations and fluorinated anions and can thus be used as solvents and electrolytes for various applications, most of which are in the realm of pharmaceutical compounds extraction, dissolution of organic complexes, energy storage devices and dispersion of nanomaterials (Singh et al. 2020). They have been proposed for CNT actuators (Barisci 2004) due to their unique characteristics such as non-volatility, non-flammability, and high electric conductivity.

Table 4 lists some ILs that have been used for CNT actuators in the past and highlights their technical properties that are most relevant for this application.

Table 4 – Properties of ionic liquids that have been used for CNT polymer actuators

Designation	Abbreviation	Melting point	Electrochemical potential window (cathodic – anodic limit)	Electric conductivity (20°C)
1-Ethyl-3-methylimidazolium tetrafluoroborate	EMI-BF ₄	15°C	3.6 V (-1.8 V – 1.8 V)	14.1 mS/cm
1-Butyl-3-methylimidazolium tetrafluoroborate	BMI-BF ₄	-71°C	4.9 V (-2.7 V – 2.2 V)	3.15 mS/cm
1-Hexyl-3-methylimidazolium tetrafluoroborate	HMI-BF ₄	-82°C	5.1 V (-2.4 – 2.7 V)	1.18 mS/cm
1-Methyl-3-octylimidazolium tetrafluoroborate	OMI-BF ₄	-81°C	6 V (-3 V – +3 V)	0.43 mS/cm
1-Ethyl-3-methylimidazolium bis(trifluoromethylsulfonyl)imide	EMI-TFSI	-3°C	4.7 V (-2.1 V – 2.6 V)	6.63 mS/cm

For the desired application in adaptive membranes for buildings, the final system must be operational in preferably wide temperature ranges. EMI-BF₄, despite being the most used

IL for CNT actuators in academic research, will be frozen below 15°C and thus causes the actuator to fail in cold environments. EMI-TFSI is also not applicable for the proposed application in this regard.

Among the remaining ILs clearly BMI-BF₄ has the highest electric conductivity and a sufficiently large electrochemical potential window for the actuator to perform its deformation within an acceptable time period even at low applied voltages. It has shown significant results in CNT actuators (Takeuchi et al. 2009b; Terasawa 2017) and is chosen as the preferred IL for all actuators manufactured for this thesis.

3.2.2 PVDF(HFP) as backbone polymer

PVDF(HFP) is a semi-crystalline fluoropolymer that has weak ferroelectric and strong piezoelectric properties and a high dielectric constant. It is stable between -30°C and 140°C and has been used as a backbone polymer for IEAPs because of its exceptional chemical resistance, good mechanical strength and high hydrophobicity. These properties are mainly attributed to the incorporated HFP groups, which enhance the fluorine content of the copolymer and also lead to better solubility compared to pristine PVDF (Wang et al. 2018). A higher HFP content in the PVDF matrix, on the other hand, has been shown to cause a negligible decrease in bending strain yet considerably smaller bending stresses of SWCNT/PVDF(HFP)/EMI-BF₄ actuators compared to actuators made with pristine PVDF (Terasawa et al. 2011).

In regard to one of the main targets of this thesis, a good solubility of the matrix polymer is essential for a rapid dispersion process and thus for economic manufacturing. Only due to the HFP groups, PVDF(HFP) can be dissolved in 4M2P used in this thesis to replace the more toxic DMAc, which was proposed for Bucky gel actuator manufacturing particularly by Japanese researchers. Furthermore, the higher hydrophobicity of PVDF(HFP) is beneficial for actuators operating in areas of increased humidity. For this reason, PVDF(HFP) will be used as the polymer matrix and encapsulation material for all actuators manufactured in this thesis.

3.2.3 Additives and dispersing agents for CNT actuators

Polyaniline (PANI) has been mentioned as a performance-enhancing additive for CNT polymer actuators in section 2.3.5. It consists of nanoparticles with an average size of 40 nm and is available as a mix of 20% PANI deposited on 80% carbon black particles. In its protonated form as an emeraldine salt, it has a conductivity of 40 S/cm and a specific BET surface area of 690 m²/g. It has already been indicated that PANI was one of the most promising materials for early conductive polymer IEAP actuators (Kaneto et al. 1995). In this thesis, it was used as a conductive additive for CNT actuators to exploit the synergistic effects of redox charge transfer mechanisms associated with PANI and faradaic double-layer formation principles linked to CNTs. Consequently, the CNT actuators investigated herein are to a certain degree a hybrid combination of pure Bucky gel actuators and PANI-based CP actuators.

As stated in 2.4.2, dispersed CNTs will re-agglomerate themselves to a new equilibrium state of low energy. This process will take place unless surfactants are added to provide steric hindrance or static charge repulsion to stabilize the particles. Three surfactants are proposed for stabilizing MWCNT dispersions during and after treatment with individual dispersing techniques. SynperonicTM PE/L61 from Croda GmbH, Germany, is an ethylene oxide/propylene oxide block copolymer and is frequently used as a de-foaming agent. It has been successfully employed for dispersing nanoparticles such as carbon black in aqueous or polar solvents for energy storage applications. HypermerTM K1 is a cationic polymeric dispersant designed for creating stable solvent-based dispersions of nano-scaled particles. HypermerTM K24 is an anionic oligomeric dispersant created for dispersions of carbon particulates in both solvent-based and aqueous systems.

3.3 Design of Experiments (DoE) for tailored electrodes

Concluding from the current state of the art, industrial dispersion and manufacturing techniques are needed to enhance the performance reproducibility of CNT-based actuators while simultaneously increasing the manufacturing speed and decreasing material costs. The Design of Experiment (DoE) method is used to find dispersion parameters and material compositions that produce printable slurries for homogeneous, coherent and functional electrode layers. The statistics package Minitab 2018 (Minitab GmbH 2018) helped in planning individual experiments and test series for finding significant correlations between materials, process parameters and measured target figures.

3.3.1 Prerequisites and general targets of DoE

The material composition CNT/PANI(50/50) reported in (Sugino et al. 2011) has demonstrated outstanding performance characteristics in term of generated bending strains and stresses, which was the main reason why this composition was chosen to serve as a baseline for producing printable electrode slurries in this thesis. However, it contained expensive SWCNTs (Purified HiPco[®] from Unidym Inc.), and the toxic solvent DMAc has been used for slurry fabrication. For SWCNT replacement, MWCNTs from Nanocyl[®] (NC7000) were chosen because they are produced via the CCVD process and are commercially available in large quantities and for much lower prices. DMAc is not considered necessary for dissolving PVDF(HFP) and will be substituted by 4M2P, which is less toxic and has a higher volatility. This in turn is expected to be advantageous for much simpler and faster drying phases. Propylenecarbonate (PC), another solvent proposed for the electrolyte slurry, was also replaced by 4M2P.

Regarding the lengthy reported dispersion procedures and the time-consuming drying periods in lab-scale electrode fabrication, the need for a transition to pilot-plant scale techniques is self-evident. High-power dispersion devices such as ultrasonic sonotrodes and

dissolvers are expected to help reduce total production time and could be used for automated inline manufacturing processes.

Looking at the proposed material modifications and dispersion techniques, the main targets of the DoE method are to find new and applicable material compositions and to investigate the applicability of the proposed dispersion techniques in terms of appropriate power settings and other process parameters. These targets are demonstrated in Table 5.

Table 5 – Starting point and targets of DoE regarding materials and dispersion techniques




	State of the Art	Target of DoE
Materials & additives	Material composition "CNT/PANI(50/50)" for CNT actuator electrodes reported by SUGINO et al. (2011) <ul style="list-style-type: none"> • SWCNTs (16.7 wt%) • PANI (16.7 wt%) • PVDF(HFP) (26.7 wt%) • EMI-BF₄ (39.9 wt%) • Solvent: DMAC (9ml/electrode: 2.5 x 2.5 cm) 	Target material composition. Substitution of SWCNTs, IL and solvent <ul style="list-style-type: none"> • MWCNTs (? wt%) • PANI (? wt%) • PVDF(HFP) (? wt%) • BMI-BF₄ (? wt%) • Solvent: 4M2P (? ml/unit layer) • Dispersing agents (Type? Concentration?)
Dispersion & drying techniques	Pre-dispersion (IL and CNTs): <ul style="list-style-type: none"> • Manual grinding with mortar (n.a.) • Ball milling (1h – 3h) Main dispersion: <ul style="list-style-type: none"> • Magnetic stirring (3h – 72h) • Ultrasonication bath (5h – 24h) Drying: <ul style="list-style-type: none"> • Drying in air (24h) • Vacuum assisted drying (24h – 72h) 	Pre-dispersion (solvent and CNTs): <ul style="list-style-type: none"> • Ultrasonic sonotrode (< 15min) Main dispersion: <ul style="list-style-type: none"> • Magnetic stirring (< 60 min) • Blade stirring (dissolver) (< 10 min) Drying: <ul style="list-style-type: none"> • Drying in air (< 24h) • Heat assisted drying in air (< 2h)

3.3.2 Procedure for DoE

The DoE consists of two pretests and the main experiment. The first pretest evaluates the target material composition and shall yield tentative results regarding the type and amount of materials needed to obtain printable MWCNT slurries and non-cracking electrode layers (Table 6). This pretest is a sequence of pre-determined consecutive steps of material variations and does not apply any changes to the well-established dispersion techniques. The assessment of the target figure "dry film quality" shall be purely visual, which is deemed

sufficient for a qualitative statement about the influence of the individual material variation steps.

Table 6 – Description of pretest 1









Pretest 1 – adjustment & optimization of MWCNT slurry formulation				
Starting point	Material prerequisites	Consecutive optimization steps / parameter variation	Target figures / quality criterion	Assessment / method of evaluation
Baseline slurry formulation Baseline dispersing techniques 	Substitution of <ul style="list-style-type: none"> Carbon nanotubes: SWCNT → MWCNT Ionic liquid: EMI-BF₄ → BMI-BF₄ Solvent: DMAc → 4M2P 	<ol style="list-style-type: none"> 0. Pre-screening of solvent (variation of type of solvent) 1. Solvent reduction (4 steps) (variation of amount of solvent) 2. Variation of PVDF content (2 steps) 3. First (basic) adjustment of MWCNT content (3 steps) 	Dry film quality <ul style="list-style-type: none"> Continuous dry layers (no cracking) Visibility of agglomerates Film thickness homogeneity 	<ul style="list-style-type: none"> Visual  Optical microscopy 

The second pretest shall investigate the influence on dispersion and dry film quality when high power dispersion techniques are adopted. For generating homogeneous MWCNT/4M2P pre-dispersions with ultrasonic homogenization, the power and time settings of the device have a large influence on the dispersion quality. When large energy inputs are applied to the MWCNT dispersion for longer periods of time, it will cause damage to the CNTs and lead to faster solvent evaporation due to thermal energy dissipation. Low power and short treatment times will lead to insufficient separation of agglomerates and wetting of CNTs. Since viscosity and agglomerate formation in MWCNT dispersions are highly sensitive to MWCNT concentration, it is deemed necessary to modify the MWCNT loading, as well. This procedure will further refine the tentative results obtained in pretest 1, which should be readily available at this stage. By using a fractional factorial design for the ultrasonic sonotrode experiments, a full factorial design with 27 necessary experiment runs (three factors, three levels) can be avoided.

Examinations of disk stirring (dissolver) and three-roll-milling shall exploit the high shearing forces that can be induced into highly viscous slurries by two different types of rotational motion. As stated in section 2.4.2, constant exposure to high shearing forces could help to

disentangle MWCNT agglomerates and separate individual particles to obtain well-dispersed slurries for an optimized conductive percolation network within the nanocharged polymer matrix of the final actuator electrodes.

Table 7 – Description of pretest 2


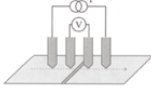

Pretest 2 – investigation of dispersion techniques & parameter optimization				
Starting point	Type and purpose of dispersion technique	Influencing factors / parameter variation	Target figure / quality criterion	Assessment / Method of eval.
MWCNT/4M2P pre-dispersion	Ultrasonic sonotrode High frequency/ high power sonication treatment for separating and wetting of MWCNT-agglomerates 	Influence of <ul style="list-style-type: none"> power settings (3 steps) time settings (3 steps) MWCNT loading (3 steps) 	Dispersion quality <ul style="list-style-type: none"> Size of residual agglomerates Viscosity Dry film quality	<ul style="list-style-type: none"> Grindometer  Rheometer 
Optimized dispersion from pretest 1 and/or Pre-dispersion from above + PANI, IL, PVDF 	Dissolver (disk stirring) De-agglomeration/ homogenization of full dispersion by high shearing forces 	Influence of <ul style="list-style-type: none"> rotation speed (2 steps) time settings (2 steps) 	<ul style="list-style-type: none"> No cracking, crumbling No curling 	<ul style="list-style-type: none"> Visual, optical microscopy 
	Three roll milling De-agglomeration/ homogenization of full dispersion by high shearing forces 	Variation of <ul style="list-style-type: none"> gap width (continuous) rotation speed (continuous) 	General feasibility Behavior of <ul style="list-style-type: none"> slurry viscosity solvent volatility 	<ul style="list-style-type: none"> Visual 

The main experiment shall principally investigate the influence of the material compositions and slurries on the performance of assembled CNT actuators. Two major objectives are the final specification of the MWCNT concentration and a quantitative examination of how strongly the presence of PANI affects the electrode conductivity and thus the actuator performance. Furthermore, the impact of three different stabilizing agents (auxiliary additives) on the dispersion quality and thus the electrode and actuator characteristics is explored.

The validation of the dispersions is performed by quantitative measurements of the slurry viscosity, the dry film thicknesses and conductivities, and the induced strains and stresses of assembled actuators at predetermined voltage levels and frequencies. Measurements of induced strains and stresses are obtained with a comprehensive test setup specifically designed for this task (see section 3.3.4).

The prospective dispersing agents chosen to stabilize the MWCNT dispersions are Synperonic™ PE/L, Hypermer™ K1 and Hypermer™ K24 described in section 3.2.3.

Table 8 – Description of main experiment parameters

Main experiment – influence of dispersing agents and additives on actuator performance			
Starting point	Influencing factors / parameter variation	Target figure / quality criterion	Assessment / Method of evaluation
Pre-optimized slurry formulation Types and sequence of dispersion steps incl. power and timing settings	Evaluation of final slurry formulation (material composition) Variation of <ul style="list-style-type: none"> • concentration of MWCNTs (3 steps) • content of PANI (2 steps – with and without) • type of dispersing agents (3 types) • concentration of dispersing agents (3 steps) 	Slurry printability <ul style="list-style-type: none"> • Viscosity 	Rheometer 
		Electrode characteristics <ul style="list-style-type: none"> • Dry film thickness • Dry film conductivity & surface resistivity 	4-point measurement 
		Actuator performance <ul style="list-style-type: none"> • Induced actuator strain 	Bending displacement measurement (test setup) 

3.3.3 Description of adopted dispersion techniques

Heat-assisted magnetic stirring was used to dissolve PVDF in a variety of solvents and to evenly distribute and wet the carbonaceous nanoparticles. In their initial state, the particles are present in the form of agglomerated particle clusters. A sealable conical laboratory flask (500 ml maximum capacity) was immersed in a shallow basin of heated water (80°C) located on a magnetic heating plate (Figure 24a). Magnetic stirrers can only be used for small

quantities of four liters or less. Moreover, the energy input from the magnetic agitator diminishes in viscous liquids or thick suspensions. Treating of more viscous liquids or larger volumes for industrial upscaling may be achieved with other mechanical stirring methods. The ultrasonic bath treatment of electrode dispersion has been adopted from the state-of-the-art techniques described in chapter 2. A BANDELIN SONOREX DIGIPLUS DL 102 H was utilized (Figure 24b).

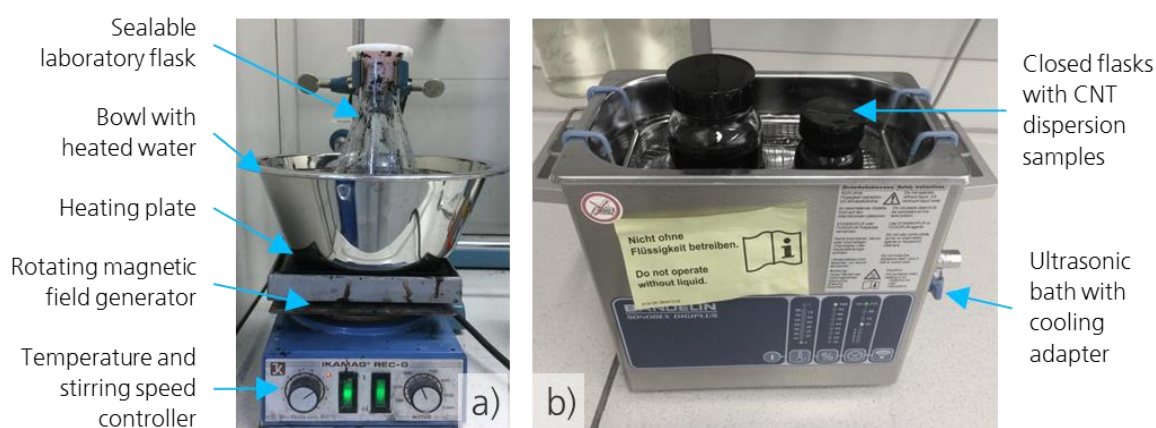


Figure 24 – Pictures of baseline dispersion equipment. a) the heat-assisted magnetic stirring setup and b) the ultrasonic bath utilized for electrode dispersion treatment (pictures: Veronika Bitzer, IFF)

An ultrasonic homogenizer system BANDELIN SONOPULS HD 2200.2 was used in pretest 2 and the main experiment of the DoE to obtain a preferably homogeneous solution of pre-dispersed MWCNTs in 4M2P solvent. In conjunction with a BANDELIN VS-70-T sonotrode horn (tip diameter 13 mm), peak mechanical amplitudes of 170 μm may be achieved at 35 kHz and 200 Watt generator power. The system is capable of automatic amplitude control by calculating the inertial load resistance encountered by the sonotrode tip at certain amplitude levels. This is beneficial for the user who wants to control the actual intensity (or energy) induced into the solution.

Solutions with less than 200 ml were probed in a double-walled SONOPULS DG5 flow-through vessel with water-assisted cooling provided by a HAAKE DC10 cooling pump controller and a HAAKE K10 cooling unit. To mitigate noise levels, all sonication activities were performed inside a BANDELIN SONOPULS LS4 sound-proof box. Larger solution quantities

needed for pilot plant scale printing trials were probed with a HIELSCHER UIP500hd ultrasonic processor with a capacity of two liters, operating at 20 kHz excitation frequency.

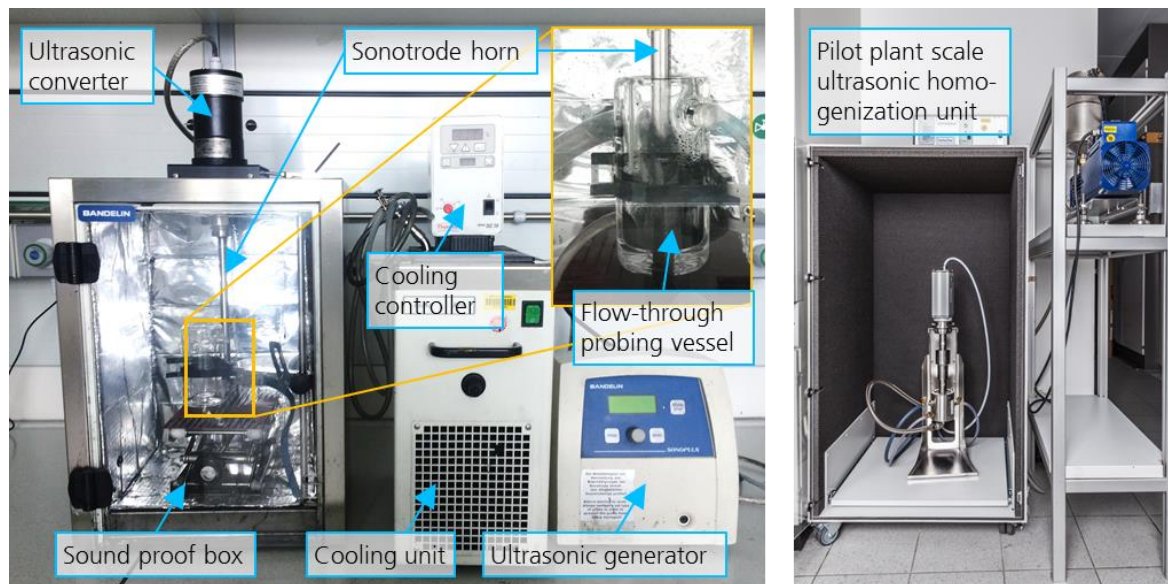


Figure 25 – Laboratory and pilot plant scale ultrasonication equipment for dispersing MWCNTs (pictures: Veronika Bitzer, IFF / Rainer Bez, IPA)

Blade stirring by means of a dissolver – often simply referred to as a disperser – is generally applied to rapidly break apart lumps of powdery material and to uniformly distribute and wet them in a liquid. A toothed disc-type mixer blade was mounted at the bottom end of the mixing shaft, equipped with sharp teeth alternatingly positioned at the top and bottom of the blade's perimeter. When rotated, the dissolver blade creates a suction that leads to the formation of a visible vortex current from the top of the mixture down to the top of the disc. A similar current is created below the disc extending from the bottom of the vessel to the underside of the disc. Rotation at high peripheral velocities imparts high shear forces into the particle-charged mixture. The dissolver DISPERMAT® LC30 from VMA-Getzmann (Germany) was utilized for the final treatment of the actuator electrode slurries produced during the DoE study in this thesis. (Figure 26). It provided a maximum power of 300 W, a top blade speed of 20000 rev/min and was suitable for dispersing suspensions of approximately one liter. The dimensions of the vessel, the distance between blade and bottom of the vessel and the amount of solution are important parameters that must be chosen in

accordance to the chosen mixer blade diameter D prior to dispersion runs. The features of the three-roll-mill employed for dispersion tests in pretest 2 are described in section 4.1.2.

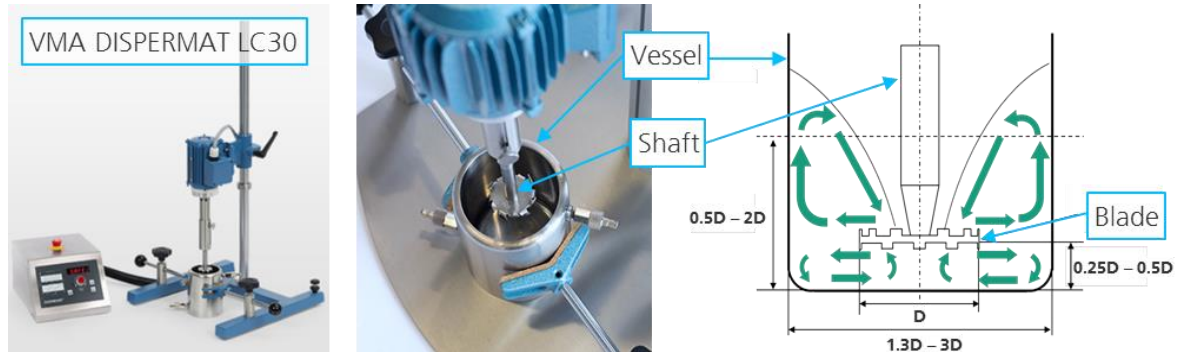


Figure 26 – Blade stirring equipment utilized in pretest 2 and main experiments for final treatment of CNT actuator electrode slurries (sources: VMA / Rainer Bez, Fraunhofer IPA)

3.3.4 Characterization techniques for assessing DoE target figures

Optical and laser microscopy investigations were performed to characterize the general surface quality of cast and printed CNT polymer blends. The Keyence LSR VK 9710 laser scanning microscope scans the 2D surface of an object with a laser and measures the local height information. A 3D picture is generated which accurately details the morphology of the object's surface structure. The digital optical microscope VHX-700F from Keyence (Japan) was used for a more general evaluation of agglomerates, cavities and other artifacts in electrode surfaces that might have a negative impact on the actuator's performance.

Scanning electron microscopy (SEM) analysis was performed to investigate the degree of agglomeration and the general structure of the as-received NC7000 MWCNTs from Nanocyl and the Signis CG300 SWCNTs from Chasm Technology.

Grindometers permit a fast but rough estimation of the particle size distribution within a suspension. They consist of a steel block with a channel of varying depth machined into it, starting at a convenient depth for the type of suspension to be measured, and becoming shallower until it ends flush with the block's surface. The suspension to be tested is filled into the deep part of the channel and scraped off towards the shallow part with a very

precise doctor blade. During the scraping process, those particles in the suspension that are larger than the current channel depth will get stuck and produce visible irregularities in the following part of the suspension film. The local depth of the channel – and thus the size of the settled particles – is marked on the side of the channel in regular intervals.

Viscosity measurements of slurries and dispersions produced during the DoE process were conducted with the cone-plate rotational rheometer RHEOPLUS/32 V3.40 from Anton Paar GmbH (Austria). Viscosity is a degree of flowability of a fluid and is defined as the constant of proportionality η in the equation

$$F = \eta A \frac{\partial v}{\partial x} \quad (2)$$

where F is the force, A the area, v the velocity and x the gap between two plates. The underlying concept includes two plates with a liquid in between them. If one plate is moved with the speed v the necessary force to achieve this speed is proportional to the area of the plates and inversely proportional to the gap width between them. If η is independent of the velocity gradient $\partial v / \partial x$ (i.e. the shear rate), the fluid is called a Newtonian fluid. If η increases or decreases at higher shear rates the fluid is called dilatant or shear-thinning, respectively.

In contrast to the linear concept described, the utilized rotational rheometer has a flat cone rotating above a fixed disk, with the test liquid filling the gap between the two bodies. During operation the torque of the rotating cone is measured for a series of increasing strain rates, usually starting at 0.1 s^{-1} and incrementally accelerating to 1000 s^{-1} or higher. It was found that all investigated solutions and slurries prepared for DoE exhibit extremely strong shear-thinning effects and have shear rate-dependent viscosities that are three orders of magnitude higher than the solvent 4M2P (0.6 mPas) used for the dispersions.

The **four-point probing** device Loresta-GP MCP-T610 from N&H Technology GmbH (Germany) was used in this thesis to quantify the differences in electrical conductivities of Bucky gel electrodes prepared by mold casting in the lab and by printing experiments. The four-point probe method is employed for measuring the electric resistivity of solid bodies and

delivers more accurate results than the simpler and more usual two-point method. Through separating the current supply from voltage metering it is possible to achieve a currentless measurement almost independent from contact and cable resistances. Since only surfaces of bodies are probed, the electric field inside the body has to be calculated. Assuming radially symmetrical fields, integration over the entire electric field along the path between two measuring probes yields for the specific electrical resistance (Smits 1958):

$$\rho = \frac{U}{I} \cdot \frac{\pi d}{\ln 2} \quad (3)$$

or – considering the relationship $\rho = d \cdot \rho_{\blacksquare}$ with d being the thickness of the measured layer – the sheet resistivity

$$\rho_{\blacksquare} = \frac{U}{I} \cdot \frac{\pi}{\ln 2} \quad (4)$$

The reciprocal value of the specific resistance is the specific electrical conductivity σ (sometimes κ or γ). The unit is S/m .



Figure 27 – Depiction of the four-point measurement device Loresta-GP MCP-T610 from N&H Technology GmbH (source: N&H)

For **measuring CNT actuator performance**, a fully automated test setup has been implemented (Figure 28). Actuators are clamped into a clamping fixture which provides electric contacts to both electrodes, allowing the actuator to bend freely in both directions. The displacement is measured via optical laser triangulation (MicroEpsilon OptoNCDT 1302) with a range of 20 mm and a displacement resolution of $\pm 4 \mu m$. A force sensor (KYOWA

LTS20GA, 500mN, 0.01 mN resolution) is mounted on the moving part of a linear positioner powered by a servomotor (Nanotec Munich KOWI), providing position-resolved blocking force measurements on one side of the actuator specimen. Actuation is triggered by a potentiostat that accurately keeps the voltage level defined by the user, varying the electric current according to the actuator's present impedance. Other parameters obtained are electric current values, motor positions, temperature variations and heat radiation images. All devices are connected to a National Instruments NI PCIE-6363 DAQ card and linked with a connector block NI SCB-68A for signal-PC-interface to the motherboard. All parameters and devices are controlled by a central LabVIEW user interface for real-time display and storage of measurement data.

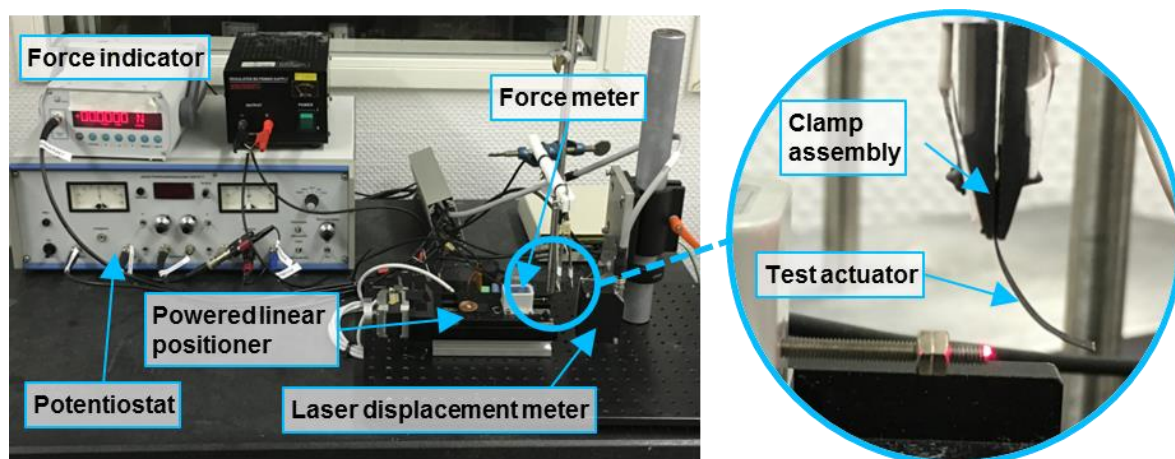


Figure 28 – Automated laboratory test setup for measuring force and displacement characteristics of CNT actuators (pictures: Raphael Neuhaus, IFF)

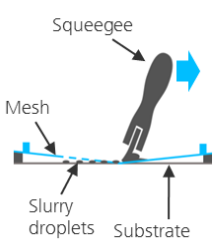
3.4 Printing techniques for scalable actuator manufacturing

The state-of-the-art fabrication method of lab-scale mold casting described in section 2.3.2 produces small-sized electrode and separator layers for only one or two actuators at a time. This is impeding their potential to be used in industrial applications where high volumes and low rejection rates are needed. Printing of electrode and separator layers could yield much larger production volumes with higher process repeatability and performance reproducibility. This section describes four printing techniques that were investigated to produce continuous large-scale layers, structured shape-variable layers and layer-on-layer systems of electrodes and separators using the modified MWCNT slurries developed through DoE.

3.4.1 Screen printing

In screen printing, a mesh (screen) is used to transfer viscous slurries or inks onto a substrate, except in those areas of the mesh that are made impermeable. A blade or squeegee is moved across the screen with vertical pressure applied, forcing the slurry to penetrate the open mesh apertures and to wet the substrate underneath. This process can be repeated by positioning the mesh on a different substrate area or by exchanging the substrate under the mesh. Industrial screen printing machines employ rotary screens to achieve a quasi-continuous printing or coating process. Some technical details, expected benefits and potential drawbacks of this printing method are listed in Table 9.

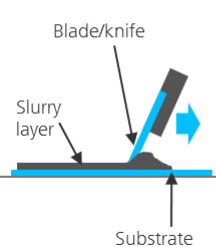
Table 9 – Details on screen printing and its intended use in CNT actuator production

Process Illustration	Print layout	Use cases	Technical parameters	Expected benefits for CNT actuators	Potential drawbacks
 <p>Squeegee</p> <p>Mesh</p> <p>Slurry droplets</p> <p>Substrate</p>	Structured Resolution 30 μm to 100 μm	Consumer: • Textiles (clothing) • Toys Industrial: • Printed electronics	Thickness range: 20 μm – 1 mm Viscosity range: 50 mPas – 100 Pas Printing speed: • Industrial: < 180 m^2/min • Consumer: < 1 m^2/min	• Fast and automatable process • Printing of large coherent layers OR structured slurry films for actuators of variable shapes and sizes • Potential for layer- on-layer printing	• Inhomogeneous wet layer thicknesses • Permanent mesh imprints on dried layers • Gradual drying of slurry residues in mesh apertures over time → mesh clogging → local layer defects and imperfections
	Non-structured	Industrial: • Thick film technology			

3.4.2 Blade coating

Blade coating – also known as knife coating or doctor blading – produces continuous thin-films by applying an excess of coating material to the substrate and then removing it with a metering blade to achieve the desired coating thickness. Either the blade moves over the stationary substrate or the substrate moves under the stationary blade. The predefined clearance gap between the blade tip and the substrate is not necessarily equal to the resulting thin-film thickness. For low-viscosity slurries, it is desirable to have a lateral boundary along the substrate to prevent the slurry from draining off to the sides of the coating area.

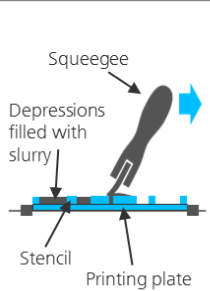
Table 10 – Details on blade coating and its intended use in CNT actuator production

Process Illustration	Print layout	Use cases	Technical parameters	Expected benefits for CNT actuators	Potential drawbacks
 <p>Blade/knife</p> <p>Slurry layer</p> <p>Substrate</p>	Non-structured No in-situ patterning possible Achievable resolution at layer edges: > 200 μm	Industrial: • Food industry • Polymer coatings • Paper industry • Surface treatment	Thickness range: 20 μm – 10 mm Viscosity range: 50 mPas – 10 Pas Printing speed: 0.1 m/min – 10 m/min	• Fast manual or semi- automatic process • Quick generation of large coherent layers on various substrates • Potential for layer- on-layer printing • Upscalable process	• Inhomogeneous wet layer thicknesses • Contamination of blade (e.g. MWCNT agglomerates) leads to streaks in the wet film → local layer defects and imperfections • Handling and transfer of printed coatings for drying

3.4.3 Stencil printing

The stencil printing method proposed here is a type of planar gravure printing (also called intaglio printing) with a thicker gravure stencil. A PTFE sheet of a predefined thickness (0.5 mm or 1.0 mm) and with multiple cutouts of desired shape was laminated onto a second non-perforated PTFE sheet. The resulting laminate serves as a stencil with depressions in the surface and is used as a printing plate. The depressions are filled with the printing slurry and any excess material is scraped off when a squeegee or doctor blade is moved over the surface of the printing plate. This process is similar to the well-established mold casting technique used for electrode fabrication (described in section 2.4.3). But this technique can fill multiple molds simultaneously and in an automated fashion. Some technical details, expected benefits and potential drawbacks of this printing method are listed in Table 8.

Table 11 – Details on stencil printing and its intended use in CNT actuator production

Process Illustration	Print layout	Use cases	Technical parameters	Expected benefits for CNT actuators	Potential drawbacks
 <p>The diagram illustrates the stencil printing process. It shows a printing plate with a stencil on top. The stencil has several rectangular depressions, some of which are filled with a blue slurry. A black squeegee is shown moving from left to right across the top of the stencil, pushing the slurry into the depressions and scraping the excess off the surface of the printing plate. Labels include 'Squeegee', 'Depressions filled with slurry', 'Stencil', and 'Printing plate'.</p>	<p>Structured</p> <p>Achievable resolution: 50 μm - 200 μm (gravure printing)</p>	<p>Consumer:</p> <ul style="list-style-type: none"> • Gravure printing <p>Industrial:</p> <ul style="list-style-type: none"> • Electric connections on PCBs (solder paste) • Packaging 	<p>Thickness range: < 1 μm – 1 mm</p> <p>Viscosity range: 10 mPas – 10 Pas</p> <p>Printing speed: < 100 m^2/min</p>	<ul style="list-style-type: none"> • Exact wet layer thicknesses • Printing of structured actuator electrodes of variable shapes and sizes • Potential for layer-on-layer printing • Incorporation of embedded electric contacts 	<ul style="list-style-type: none"> • Inhomogeneous surface structure at back end of wider stencil depressions due to squeegee bending • Handling of printing plate after printing (maintaining horizontal position) • Difficulties to remove dried films

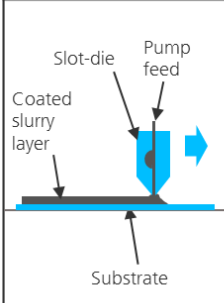
3.4.4 Slot-die coating

Slot-die coating is a technique where the coating material is provided with a feeding pump to the coating head from where it is directly coated onto the substrate. The slurries flow through the head at a determined rate making this process a metered coating process. This means that the wet film thickness is determined by the amount of material placed onto the substrate, which in turn is depending on the pressure provided by the feeding pumps. All

other parameters such as nozzle width, substrate clearance and head pace work to improve the uniformity and stability of the coating.

One major advantage of slot-die coating is that it is scalable and can be used in roll-to-roll processing. However, compared to the other printing techniques, slot-die coating is significantly more complex, with multiple parameters that need to be balanced and optimized to create high-quality thin films. A downside aspect of this technique is that it has high initial setup costs compared to other techniques. Some technical details, expected benefits and potential drawbacks of this method are listed in Table 10.

Table 12 – Details on slot-die coating and its intended use in CNT actuator production

Process Illustration	Print layout	Use cases	Technical parameters	Expected benefits for CNT actuators	Potential drawbacks
 <p>The diagram illustrates the slot-die coating process. A blue 'Pump feed' is shown at the top, with an arrow pointing to a 'Slot-die' nozzle. The nozzle is positioned above a 'Substrate', and a 'Coated slurry layer' is being extruded from the slot-die onto the substrate. An arrow on the right indicates the direction of the substrate movement.</p>	<p>Non-structured</p> <p>No in-situ patterning possible, only continuous wet films of high quality</p>	<p>Industrial:</p> <ul style="list-style-type: none"> • Battery technology • Optical coatings • Thin film electronics • Conductive films with nanofillers 	<p>Thickness range: <math>< 1 \mu\text{m} - 1 \text{mm}</math></p> <p>Viscosity range: 2 mPas – 5 Pas</p> <p>Printing speed: 0.2 m/min – 5.0 m/min</p>	<ul style="list-style-type: none"> • Exact and uniform wet layer thicknesses • Pre-heating of slurries inside slot-die • Potential for layer-on-layer printing • Process upscalability through multiple consecutive coating stages 	<ul style="list-style-type: none"> • Clogging of slot-die nozzle through large MWCNT agglomerates • High pressure in feeding pipes due to high slurry viscosity • Balancing feeding rate, slot-die speed and substrate clearance • Wasting of materials

For this thesis, slot-die coating was performed with the discontinuous coating machine Easycoater EC 63 from Coatema Coating Machinery GmbH (Germany) that was specifically set up and re-designed to meet the requirements of the highly viscous slurries containing volatile organic solvents. Electrode and separator dispersions can be pumped separately into two different slot-die nozzles allowing for automated layer-by-layer printing without changing the slot-die configurations between different layers. Both slot-dies have a nozzle length of 200 mm. The width of the nozzle slot can be adjusted by using spacer blades in the nozzle cavity. When the layers are applied onto the heated printing table with exactly controllable wet layer thickness, hot-air assisted drying can accelerate the evaporation of the solvent. Layer-on-layer printing is possible when the layers are dry enough for the next layer to be printed. Alternatively, layers can be printed individually, extracted from the machine after drying and later heat pressed together for the actuator assembly (see sections 4.3.1 and 4.3.2).

Table 13 – Overview of proposed printing & coating methods

Printing method	General process assessment			Potential assessment for CNT actuators
	Process scalability	Process controllability	Robustness and cost	
Screen printing	<ul style="list-style-type: none"> • Automatable process • Roll-to-roll coating possible, but rarely used 	Moderate control over surface uniformity, thickness homogeneity and texture	High acquisition and maintenance costs	Medium-low
Blade coating	<ul style="list-style-type: none"> • Automatable process • Roll-to-roll coating possible 	<ul style="list-style-type: none"> • Metering blade allows exact control of coating thickness. • No structured coatings possible • Blade contamination 	<ul style="list-style-type: none"> • Highly robust process. • Usable for slurries with high viscosity and solid particles or fibers (e.g. paper industry) • Moderate setup costs 	Medium-high (high for lab-scale fabrication)
Stencil printing	<ul style="list-style-type: none"> • Automatable for batch-to-batch (slow process) • Mainly employed for electronics equipment (PCB soldering) 	<ul style="list-style-type: none"> • Highly accurate shapes and wet layer thickness • Good edge sharpness 	Requires stencil / molds	Medium
Slot die coating	<ul style="list-style-type: none"> • Roll-to-roll coating possible. • Performed in various industrial fabrication processes (battery electrodes, food industry etc.) 	<ul style="list-style-type: none"> • Metered coating process (indirect control of layer thickness) • Usable for non-atmospheric coating processes 	<ul style="list-style-type: none"> • High initial setup and maintenance costs • Usable for hazardous/toxic solvents (explosion-proof/ closed printing chambers) 	Medium-high

3.5 New assembly and integration techniques for CNT actuators

This subchapter explains how the manual and laboratory-scale assembly processes described in section 2.4.4 were modified to make them applicable for industrial scale manufacturing of CNT actuators. Two scalable assembly methods are described that were used to merge printed electrode and electrolyte films. A range of electrically conductive materials is presented that were tested as embedded electric connectors. A simple dip-coating process is proposed to cover the actuators with a thin protective polymer layer.

3.5.1 Assembly methods for printed electrode and electrolyte layers

When the large-scale printed electrode and electrolyte layers are dry, there are two general approaches to obtain small rectangular pieces of tri-layer laminate which constitute operational CNT actuators. It is possible to first fuse the printed layers and subsequently cut out individual actuators of desired size and shape, or the cutting process precedes the fusing process (Figure 29).

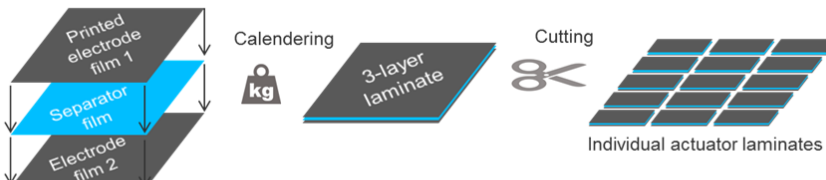
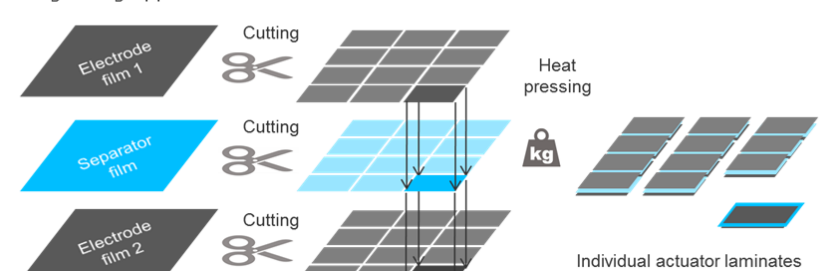
Methods of actuator fabrication from large scale printed films	Expected features
<p>Fusing-cutting approach</p> 	<ul style="list-style-type: none"> ⊕ Fast process ⊖ Electric contacting of individual actuators only possible via external connections (e.g. clamps, glue etc.)
<p>Cutting-fusing approach</p> 	<ul style="list-style-type: none"> ⊕ Integration of individually embedded electric contacts possible! ⊕ Better separation of electrodes because of protruding separator. → Avoiding potential short circuits ⊖ Slower process

Figure 29 – Actuator assembly from printed films.

The latter case produces a large quantity of small pieces of dry film that need to be fused individually via heat-pressing to assemble the desired tri-layer actuators. These actuators are not yet fitted with electric connections.

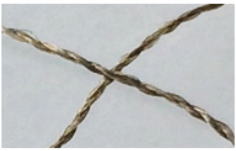


3.5.2 Proposed materials for embedded electric connections

As described in the state-of-the-arts section 2.5.1, soft actuator applications often require embedded electric connections that do not rely on force-locking principles. This is necessary to improve the contact resistance between the main conductor (e.g. a cable) and the polymer electrodes of the actuator. Preferably, such features should have no implications on the actuator performance and should be independent of the type of mechanical attachment required for the individual application.

A number of flexible and conductive materials were pre-selected for practical investigations (Table 14). The most important criteria were small cross-sectional dimensions for minimal electrode interference (the thinner the better) yet low electrical resistance per unit length. Other factors to be considered were the compatibility and connectability to conventional power and control cables and their processibility in view of the overall integration process. The connection materials also had to be resilient against oxidation and maintain their flexibility and electrochemical stability in the presence of aggressive ionic liquids. For example, copper may exhibit a thin passivation film over time and suffer from pitting corrosion on the metal surface when subjected to certain ionic liquids. Silver-plated connectors, however, are not expected to degrade when they are implanted into the CNT/PVDF/IL electrodes.

The solid materials (conductive thread, braid and tape) were embedded into the electrode slurry during mold casting or stencil printing. As an alternative, heat-pressing was tested to integrate the conductors into dry electrode layers. Conductive epoxy glue was used for initial integration experiments only.

Table 14 – Dimension and resistivity values of commercial conductive materials that were proposed for embedded electric contacts into IEAP actuators and sensors (pictures: Raphael Neuhaus, IFF)

Type of connection material	Product used	Thickness / Diameter	Electrical resistivity	Illustration
Silver-plated conductive thread (yarn)	Madeira® HC12	Ø 0.35 mm	< 100 Ω/m	
	Madeira® HC40	Ø 0.18 mm	< 300 Ω/m	
De-soldering copper braid	Solder-Wick® Rosin 50-6-25	0.7 mm	2.1 Ω/m	
Conductive adhesive copper tape	3M® 11816 grounding strap	0.07 mm	0.043 Ω/m	
Conductive epoxy glue	CircuitWorks® CW2400		1 mΩ·cm	

3.5.3 A simple and cost-efficient method for encapsulation of CNT actuator laminates

In contrast to the complex encapsulation methods and materials mentioned in the state-of-the-arts chapter (section 2.4.4), dip-coating of dissolved PVDF(HFP) was chosen as a more frugal approach to this topic. PVDF(HFP) already served as the backbone polymer for both electrode and separator layers, hence a strong cohesion was expected between the encapsulation layer and the surface of the actuators. Other reasons for this material were its high dielectric strength, good resistance to solvents, chemical and biological inertness and low permeability to moisture. With a Young's modulus of 335 MPa, PVDF(HFP) is much softer than parylene (2.5 GPa), so encapsulation was expected to have only minor effects on the displacement amplitude when applied with thinner coating thicknesses. The material was applied to the full wettable actuator surface via dip-coating which is much more time- and cost-efficient compared to the parylene CVD process.

4 Implementation of the proposed methods

This chapter explains how the materials and manufacturing methods proposed in chapter 3 were put into practice. It provides detailed information about the experimental settings and offers qualitative and quantitative data about the scientific results.

The first subchapter describes the implementation of the proposed DoE methods that were used to produce printable slurries for CNT actuator electrodes. It clarifies the effects of stepwise modifications in the material compositions and examines the benefits and drawbacks of the adopted and adapted dispersion techniques.

The second subchapter compares the experimental results obtained during test runs with four different printing techniques. It focusses on semi-automatic discontinuous slot-die coating which was expected to yield the highest automation and industrialization potential. The third subchapter provides insights regarding the pilot implementation of embedded electric contacts for CNT actuator electrodes and evaluates the potential of different connector materials. Moreover, the effect of thin dip-coated encapsulation layers on the actuator performance is investigated.

4.1 DoE – Material compositions and dispersion methods

This subchapter covers the implementation of the DoE methods proposed in section 3.3. The overarching DoE objective was to utilize cheaper and greener raw materials in conjunction with fast and scalable dispersion techniques to obtain printable and functional electrode slurries for CNT actuators. With regards to the experimental procedure introduced in 3.3.2 and in consideration of the dispersion and characterization techniques described in 3.3.3 and 3.3.4, this subchapter describes the modified material compositions, the experimental settings and the relevant observations made in sequential order.

4.1.1 Pretest 1 – Initial investigations of MWCNT slurries and layers

NC7000™ MWCNTs from NanoCyl SA instead of Unidym SWCNTs have been applied to the baseline electrode formulation adopted from (Sugino et al. 2011). The ionic liquid EMI-BF₄ was replaced by BMI-BF₄ and the solvent DMAc was substituted by 4M2P. The materials, their mass fractions and the dispersion methods remained otherwise unchanged and are given in Figure 30.

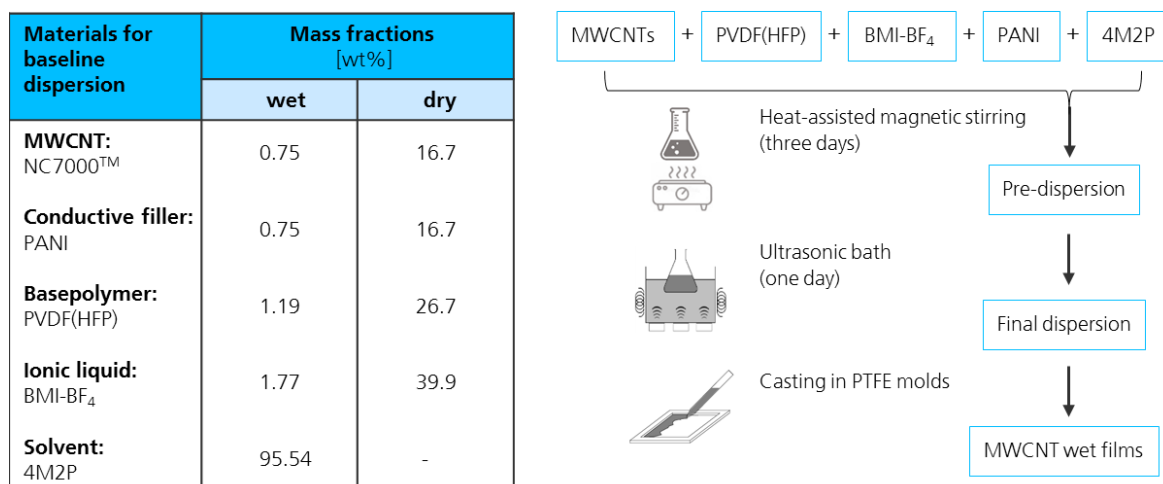


Figure 30 – Baseline material composition and dispersing procedure for making initial MWCNT electrodes for pretest 1

Scanning electron microscopy images that were taken of raw and as-received NC7000™ MWCNT powder show an extremely high degree of agglomeration (Figure 31), with the cross-sectional diameters of agglomerates varying between 10 μm and 150 μm for approximately 90% of the observed particles. It was now compelling to investigate the de-agglomeration behavior of these MWCNTs regarding the much lower binding energy compared to SWCNTs (described in 2.4.2), but also the potential re-agglomeration in standing dispersions.

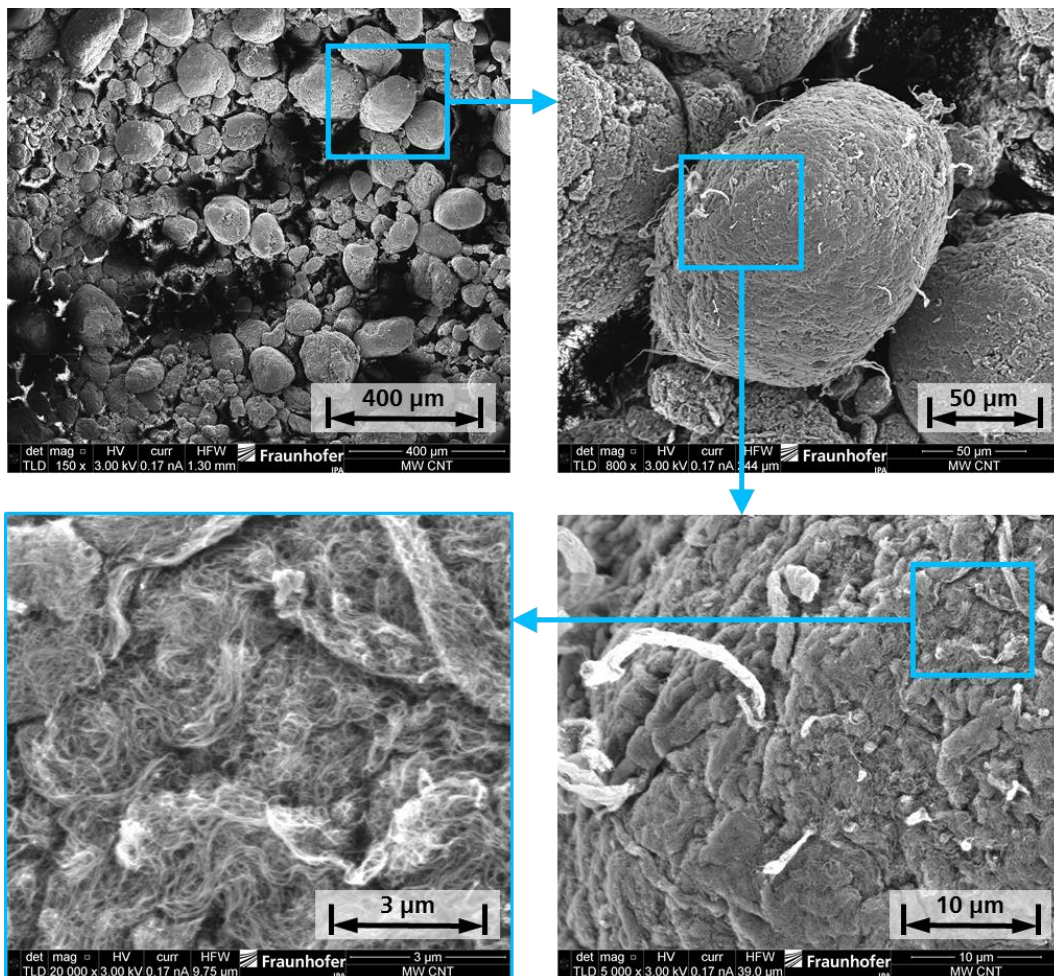


Figure 31 – Scanning electron microscopy images of as-received NC7000 MWCNT powder. Visibility of strongly agglomerated MWCNT bundles (pictures: Julia Jablockin, IFF, 2018).

All materials from Figure 30 were weighed and stirred in a laboratory flask for three days. Throughout the duration of magnetic stirring (80°C heat plate temperature, 300 rpm agitator speed) black particle agglomerates were visible in the dispersion, some of which were adhering to the inner wall of the stirring flask above the surface level. When the stirring

was halted, slow but steady sedimentation of these particles was observed which resulted in phase separation of the mixture (Figure 32).

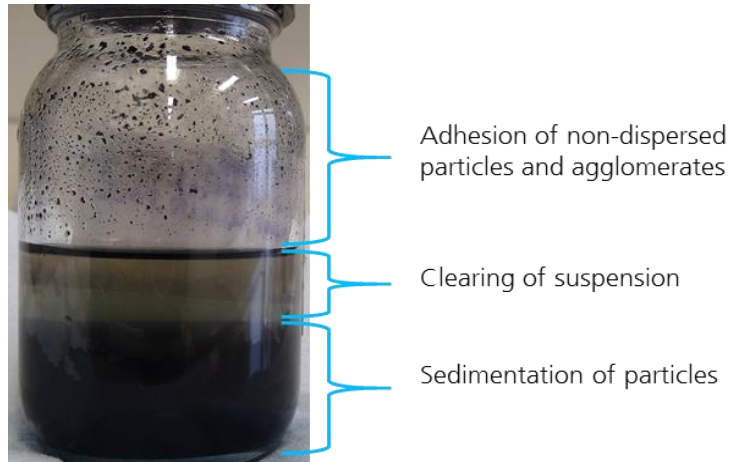


Figure 32 – Agglomeration and sedimentation of non-dispersed particles in the solution during magnetic stirring (picture: Nima Zahiri, IFF/BioMat).

Particles in solution tend to sediment if the ratio between gravitational to Brownian forces becomes greater than one (Lin-Gibson et al. 2004). Assuming a simplified model of spherical particles, this results in the equation

$$\frac{a^4 \Delta \rho g}{k_b T} > 1 \quad (5)$$

with a being the particle size, $\Delta \rho$ the density difference between the solution medium and the particle (0.8 g/cm^3 for 4M2P and 1.4 g/cm^3 for MWCNTs) and $k_b T$ the Brownian attraction factor composed of the Boltzmann constant and the absolute temperature prevalent in the solution. Despite the simplification for spherical particles, the resulting critical particle size of $a > \sim 1 \text{ }\mu\text{m}$ shows that indeed much larger agglomerates are present in the solution. The result furthermore explains why it is generally difficult to obtain stable homogeneous solutions with MWCNTs and MWCNT agglomerates since they commonly have lengths greater than $1 \text{ }\mu\text{m}$. CNT lengths shorter than that would ultimately limit their field of application.

After resuming the stirring process the viscosity of the solution slowly increased and the amount of non-dispersed particles slightly diminished. During subsequent treatment in an

ultrasonic bath for one day, the dispersion transformed into a viscous slurry and no sedimentation could be observed when sonication was interrupted.

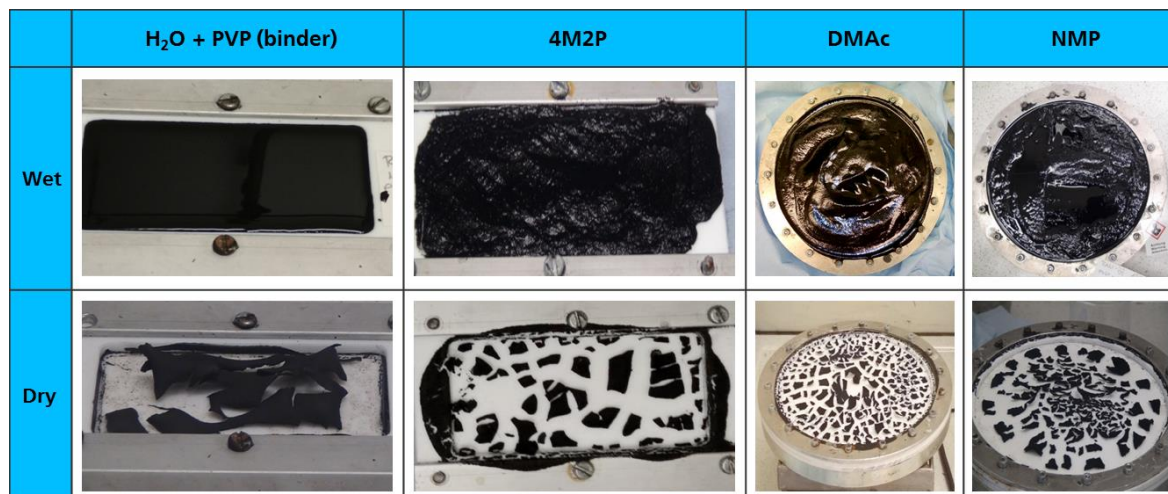
Upon casting the slurry into prepared molds of PTFE, glass or Aluminum with mold diameters of 16 cm, the cast electrode films exhibited cracking during the drying process. This happened regardless of the type of substrate material used and irrespective of whether the layers were dried in air, on a heating plate or in a vacuum oven. After drying, some larger groups of cohering curled-up pieces of film formed inside the molds (Figure 33).



Figure 33 – Disassociation of dried MWCNT electrode layers into small curled-up pieces (pictures: Raphael Neuhaus, IFF)

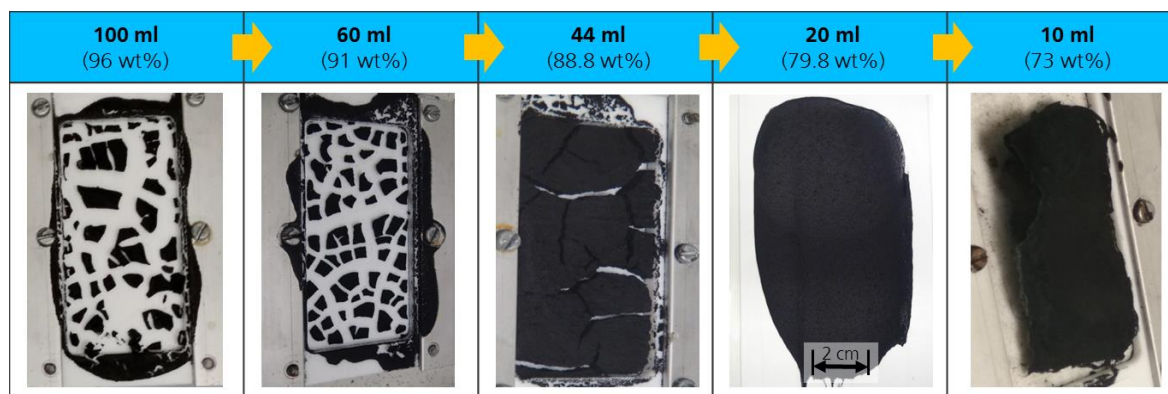
To investigate the possibility of PANI or MWCNTs showing better dispersion behavior in other solvents, a small test series with N-methyl-2-pyrrolidone (NMP), DMAc and water-based solutions was conducted. As seen in Table 15, the choice of different types of solvents had no or little effect on the cracking behavior of air-dried MWCNT dispersions. It was assumed that cracking is the result of the solvents evaporating out of the loosely bonded accumulation of poorly dispersed particle clusters within the cast electrode layers, leaving behind empty cavities in the structure that serve as cracking seeds. Re-agglomeration of formerly wetted particles (MWCNTs and PANI) leads to further volumetric (and thus planar) contraction of the disassociated layer pieces. Concluding from this, a variation – namely a reduction – in proportional solvent quantity should yield less cracking because of fewer volumetric losses during drying.

Table 15 – Influence of different types of solvent on the cracking behavior of non-optimized MWCNT dispersions (pictures: Julia Jablockin, IFF, 2018)



A stepwise reduction of the 4M2P solvent concentration in the baseline formulation indeed resulted in a better cracking behavior of the cast electrode films (Table 16).

Table 16 – Influence of decreasing the amount of 4M2P on the cracking behavior of air-dried MWCNT electrode films. The casting mold dimensions are 100 mm x 50 mm (pictures: Julia Jablockin, IFF, 2018)



When only 10 ml (73 wt%) of 4M2P were utilized for the solution, the resulting dry film was coherent, but exhibited curling and out-of-plane deformations and appeared very stiff. Therefore, the composition with 20 ml of 4M2P (79.8 wt%) was chosen for further material variation experiments even though minor cracks could still be observed.

A potential influence of the presence of PANI on the cracking behavior could be ruled out because all investigations of solvent reduction were repeated without PANI and cracking was still observed.

To further optimize the smoothness and stability of the electrode film, the content of PVDF was doubled to 2.4 wt%. The resulting layers exhibited no cracking, yet optical microscopy images revealed local areas with distributed white spots. These areas were assumed to contain predominantly PVDF material with little CNT or PANI content, hinting towards a regionally poor particle distribution (Figure 34). This assumption is further strengthened by the rugged layer surface visible on the upper side of the dry layer, suggesting large poorly dispersed particle agglomerates.

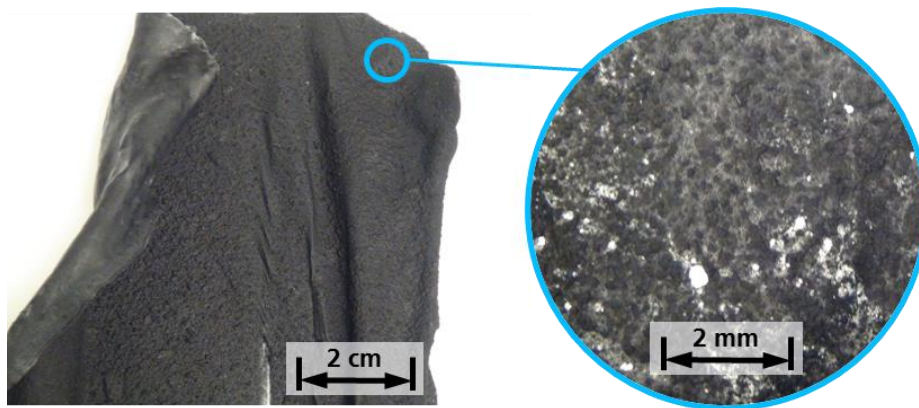
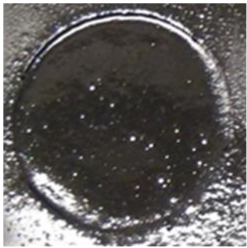
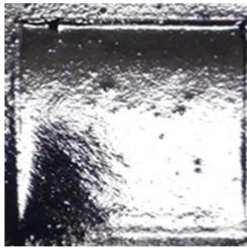
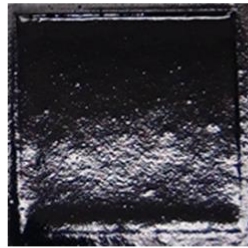
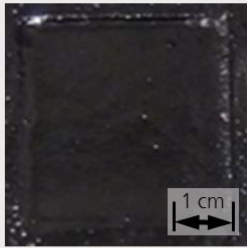
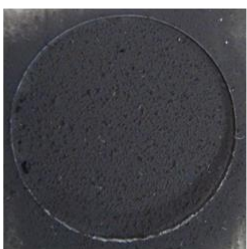


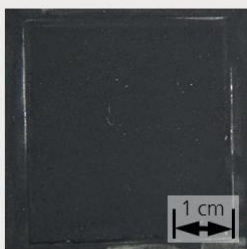
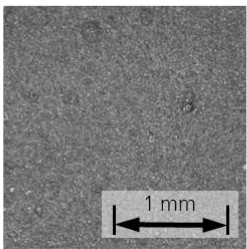
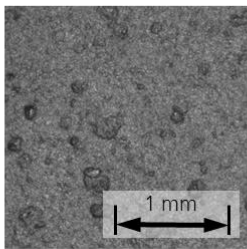
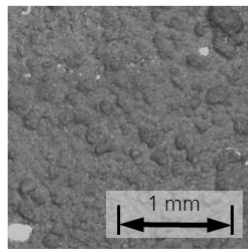
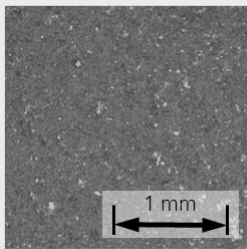


Figure 34 – Optical microscopy of dried layer after doubling the PVDF content. No detectable cracks were found, but local areas rich of PVDF with low particle charge appear as white spots (pictures: Raphael Neuhaus, IFF, 2018)

The last step of pretest 1 examines the effect of lower CNT contents in the electrode layers. The underlying intention is to increase the spacing between individual CNTs or CNT agglomerates within the dispersion (and consequently within the cast layers) to obtain more homogeneous surface structures. Well aware of the fact that fewer CNTs principally means less electrochemically active material, the CNT mass fractions were reduced to 0.5 wt%, 1.0 wt% and 1.5 wt%. As a reference, the exact same material composition and dispersion procedure was repeated using Signis® CG300 SWCNT. Pictures of the wet and dry layers

inside newly made circular and rectangular PTFE casting molds (diameter = width = 3.6 cm) and optical microscopy images of the dry layers are presented in Table 17.

Table 17 – Wet and dry layer quality results for three concentrations of MWCNT and one reference dispersion with SWCNTs (OM* = optical microscopy). (pictures: Julia Jablockin, Raphael Neuhaus, IFF)

	0.5 wt%	1.0 wt%	1.5 wt%	SWCNT (0.75 wt%)
Wet				
Dry				
Dry (OM*)				










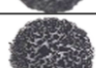




Looking at Figure 34 and Table 17, it was obvious that the size and amount of agglomerated particles in the dry-layers were reduced, but not eliminated due to lower CNT concentrations in the slurries. It was also apparent that CNT mass fractions larger than 1.0 wt% would most likely promote cracking in the dried electrode layers when the baseline dispersing procedure is pursued. Thus, it follows that the baseline dispersing procedure cannot be copied to produce MWCNT actuator electrodes. It needs further adaptation beyond the optimization measures taken in pretest 1. The amount and size of agglomerates need to be reduced – potentially through more intense sonication treatment – and stabilization additives are needed to prevent re-agglomeration and sedimentation.

4.1.2 Pretest 2 – Adaptation of the dispersing techniques and equipment

As stated in 2.4.1, high mass fractions of well-dispersed CNTs are desirable for optimizing actuator performance. For producing a pre-dispersion of NC7000 MWCNTs in 4M2P with an ultrasonic homogenizer, the ideal combination of CNT loading, power settings and time settings (influencing factors) needed to be found and were studied in regard to their individual influence on the lowest possible residual particle sizes and highest possible solution viscosities (target figures). Since only pre-dispersions (without IL, PANI and PVDF) were investigated, the viscosity is not relevant for assessing their printability. However, the viscosity may serve as a degree for the dispersion quality.

A fractional factorial design plan for the experiments was generated in Minitab 18, examining three stages for each of the three factors: CNT mass fractions of 0.6 wt%, 2.3 wt% and 4.0 wt%, sonication periods of 2 min, 8.5 min and 15 min and power settings of 30 W, 80 W and 150 W. The factors and the measured target figures of the experimental sub-set are listed in Table 18.

Table 18 – DoE sonication parameters and results for MWCNT-4M2P pre-dispersions (pictures: Julia Jablockin, IFF, 2018)




Experiment run	Influencing factors				Target figures		Effect on	
	MWCNT mass fraction	Sonication power	Sonication time	Energy input (device measured)	Max. particle size	Viscosity (@100 s ⁻¹ , 25°C)	Wet layer	Dry layer
	[wt%]	[W]	[min]	[kJ]	[µm]	[Pa·s]		
1	4.0	150	2	3.2	> 90	0.22		
2	4.0	80	15	19.2	> 90	0.32		
3	0.6	150	15	56.4	> 80	0.09		
4	2.3	30	2	3.5	> 110	0.16		
5	2.3	80	8.5	21.3	> 70	0.18		
6	4.0	30	15	25.1	> 80	0.28		
7	0.6	30	8.5	15.0	> 80	0.17		

The particle sizes of the seven dispersions obtained were measured manually with a grindometer. The viscosity was measured over a range of strain rates from 0.01 s^{-1} to 10000 s^{-1} .

Independent of the power settings, all ultrasonic homogenization experiments produced dispersions with large residual particle sizes above $70 \mu\text{m}$. The measured viscosities that did not correlate to any of the influencing factors (except for increased viscosities at CNT loads of 4 wt%). Only one combination of power settings and CNT loading (run #7) reproducibly formed smooth non-cracking dry layers with a surface roughness of lower than $20 \mu\text{m}$. All other combinations showed layer cracking, coffee ring effects or inhomogeneous distribution of large agglomerates and were disregarded, irrespective of their larger viscosity values or smaller residual particles, so no further analysis of this fractional factorial design was conducted.

The low CNT mass fraction of 0.6 wt% initially appeared to be in accordance with the findings from pretest 1 and suggested that sonication does not promote higher possible mass fractions of MWCNTs. To verify whether this observation can be transferred to complete electrode slurries, the pre-dispersion from run #7 was completed by sequentially adding PVDF, PANI and IL during magnetic stirring. Thereby, the solution's MWCNT mass fraction decreased from 0.6 wt% to 0.5 wt%. The obtained slurry was treated with a dissolver (see 3.3.3) at two different rotation speeds and three different mixing times. If high shear forces are to be induced into viscous slurries, blade tip speeds between 18 m/s and 25 m/s are recommended, translating into 8600 min^{-1} and 12000 min^{-1} (revolutions per minute). However, during the mixing process at 7000 min^{-1} the suspension's viscosity quickly increased. After just over one minute into the process, the mixer blade did no longer generate the typical vortex and was spinning in air without any interaction with the surrounding stiffened fluid. The mixing speed was reduced to 3500 min^{-1} and a steady vortex could be observed that was stable for more than five minutes. The diameter of the toothed mixer blade was 40 mm and the vessel diameter was 70 mm . The results are shown in Table 19.

Table 19 – DoE blade stirring parameters and results for 0.5 wt% MWCNT full dispersions (pictures: Julia Jablockin, IFF, 2018)

Experiment run	Influencing factors			Target figures		Effect on
	MWCNT mass fraction	Dissolver rotation speed	Dissolver mixing time	Max. particle size	Viscosity (@100 s ⁻¹ , 25°C)	Mixing properties
	[wt%]	[min ⁻¹]	[min]	[μm]	[Pa·s]	
1	0.5	7000	1	> 90	0.42	
2	0.5	7000	10	> 90	1.08	
3	0.5	3500	5	> 80	0.51	

The size of agglomerates was apparently not affected by the blade stirring process, but no further investigations on particle size distribution or concentration were conducted.

Typical viscosity curves for the pre-dispersion after sonication and the full dispersion after dissolver treatment are presented in Figure 35. Even though all dispersions show strong shear-thinning effects, their strain rate depending viscosities are within the appropriate range for all four printing techniques proposed in this thesis.

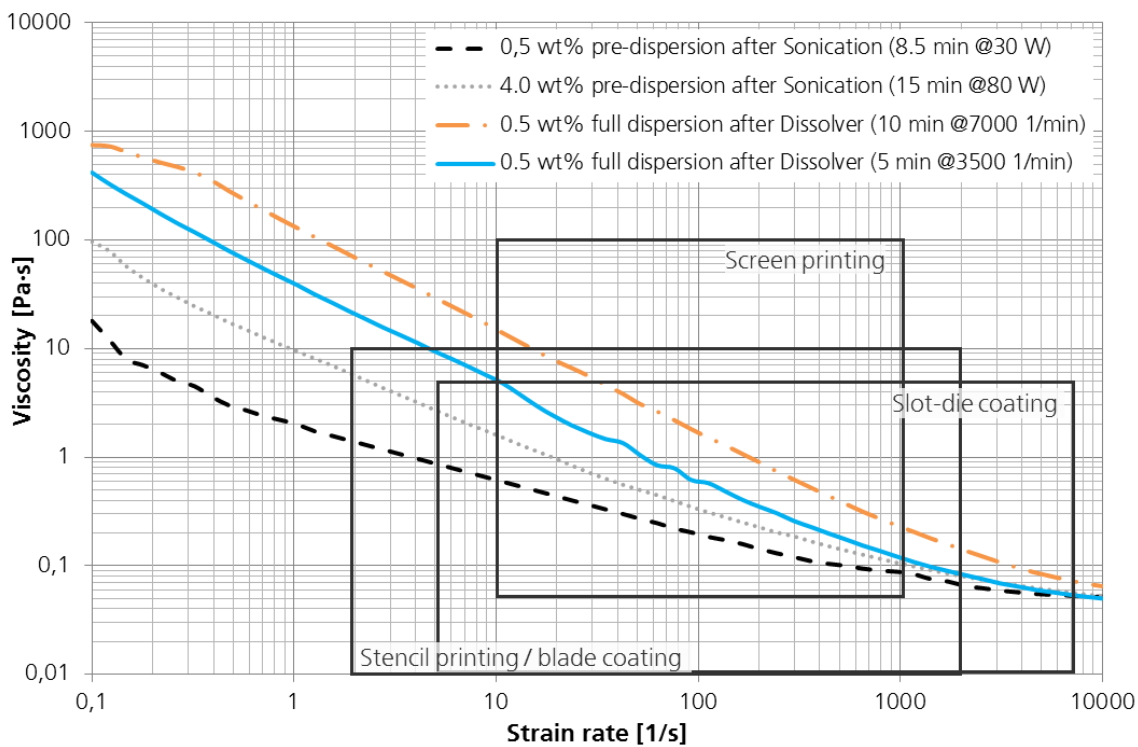


Figure 35 – Dispersion viscosities over strain rates for selected MWCNT actuator electrode slurries

When comparing the full dispersion films that were cast before and after dissolver treatment, no cracking within the air-dried layers could be observed. However, the dissolver treated layers repeatedly showed considerable planar contraction resulting in a clearly visible separation of the layer edges from the mold (Figure 36). Those solutions that were not treated with the dissolver did not show such drying characteristics. A possible explanation for this phenomenon is solvent evaporation during dissolver treatment due to frictional heat generated in the mixture. Another explanation is reagglomeration of well-dissolved PANI particles.

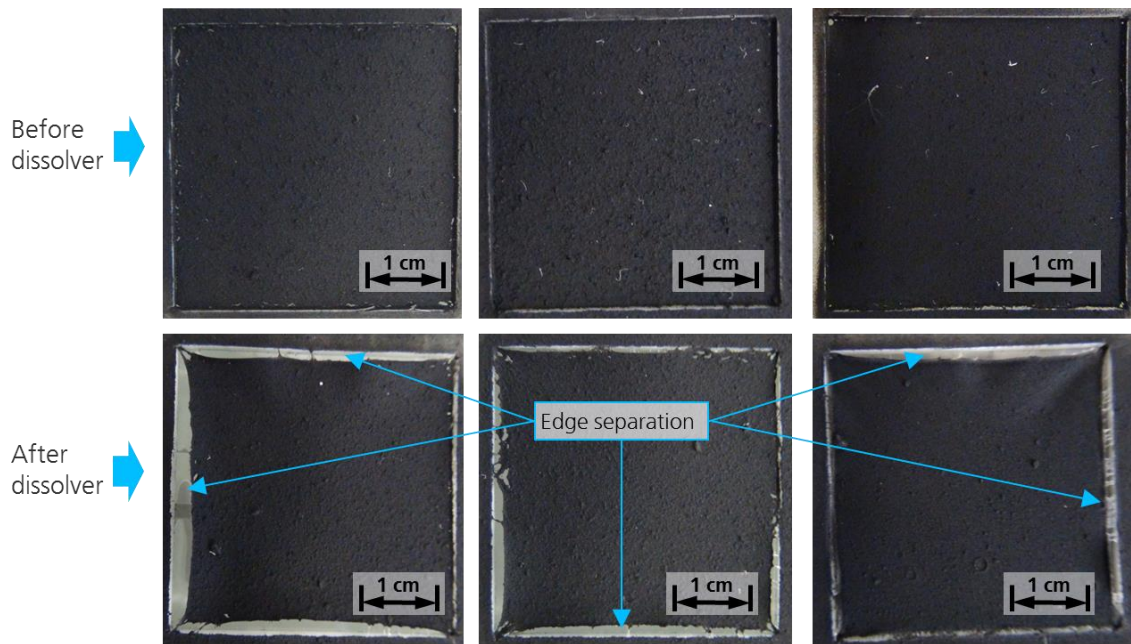


Figure 36 – Edge separation of dried layers of full dispersion after dissolver treatment (pictures: Julia Jablockin, Raphael Neuhaus, IFF, 2018)

In parallel with dissolver trials, a three roll mill was tested with the intention to homogenize the viscous slurries after sonication and to insert strong shear forces for further particle deagglomeration. Three horizontally positioned rolls rotate in opposite directions and with increasing speeds. The solution is poured in between the first roll (feed roll) and the second roll (center roll) and is pressed through a small gap of adjustable width (here $14\ \mu\text{m}$) where it experiences high shear forces and – in theory – larger particles should become crushed (Figure 37a). A thin film of the particle charged solution is then picked up by the faster center roll and transported to the even smaller gap ($11\ \mu\text{m}$) between the center and the third roll (apron roll) that inflicts even higher shear forces. A doctor blade on the apron roll scrapes off the processed material (Figure 37b), which can be transferred back to the initial position for repeated dispersion.

During milling, the large surface area of the solution film is accessible to air. In combination with frictional energy continuously heating the film, fast evaporation of the 4M2P solvent was promoted. This became apparent when tissue-like flakes of semi-dried material exited the last milling stage (Figure 37c). Nevertheless, an attempt was made to obtain a coherent

material layer from these flakes (Figure 37d). The resulting inhomogeneous surface structure of the layers exhibited cracking (Figure 37e), rendering the three-roll milling process impractical for finalizing desired electrode dispersions.

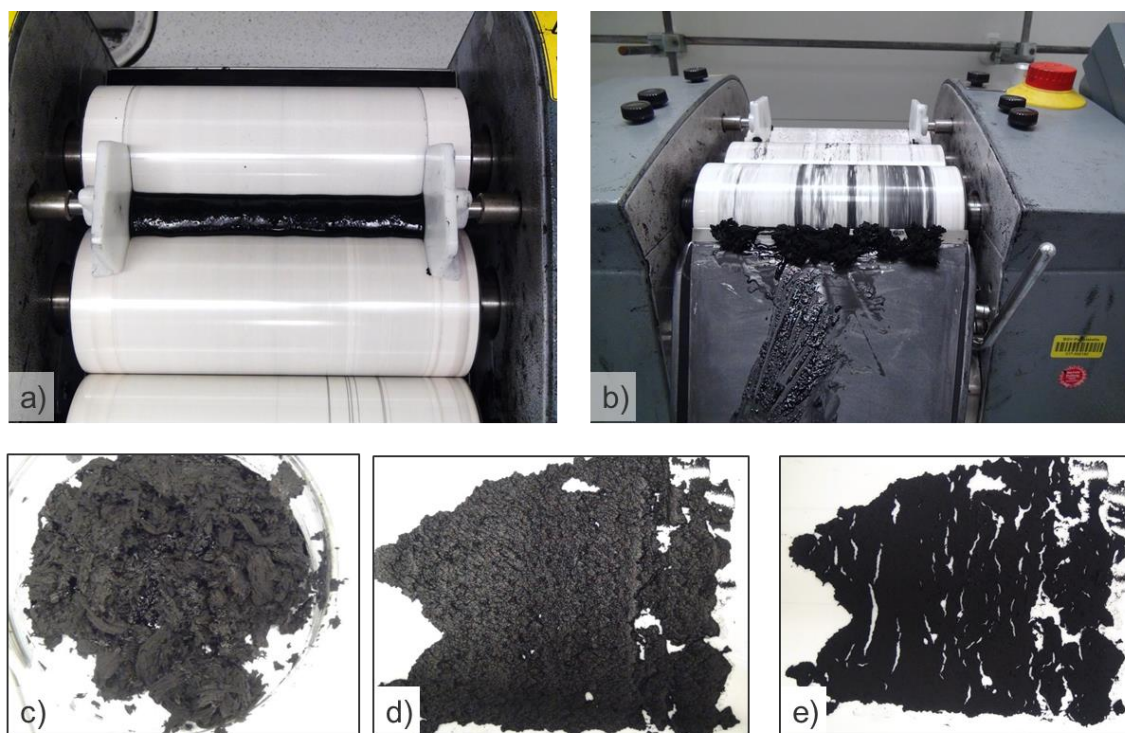


Figure 37 – Experimental three roll milling after the final adaptation of the baseline dispersion, rendering further investigations futile due to inhomogeneous layer formations and cracking. (pictures: Julia Jablockin, IFF, 2019)

Pretest 2 has produced the following results:

- Ultrasonic homogenization treatment of MWCNT-4M2P mixtures may produce homogeneous pre-dispersions that do not show any dry film cracking. Good results were obtained for CNT mass fractions in the range of 0.5 wt% and for power and time settings of 30 W and 8.5 minutes.
- Upon adding PVDF(HFP), PANI and BMI-BF₄ using the mass fractions from pretest 1, further treatment with a dissolver for 5 min at 3500 min⁻¹ will increase the viscosity and may potentially be beneficial for further de-agglomeration of the dispersion.
- Three roll milling is not suitable for high shear force treatment of the dispersion because the solvent evaporates too quickly.

4.1.3 Main experiment

Based on the outcomes of the two pretests, the main experiment investigates

1. the effects of fine-tuning CNT mass fractions,
2. the influence of PANI as a conductive polymer additive and
3. the impact of three different dispersing agents

regarding

- a) the printability of the obtained slurries (viscosity),
- b) the electric properties of the dried electrode layers (conductivity) and
- c) the performance of assembled three-layer actuators (bending strains).

Setting up a fractional factorial design of experiments, the MWCNT mass fractions to be tested were set to 0.5 wt%, 0.75 wt% and 1.0 wt%. The amount of PANI was set to either 0 wt% or 3.4 wt%. The concentrations of the three dispersing agent additives PE/L61, KD1 and KD24 (see 3.2.3) were set to 0 wt%, 0.0065 wt%, 0.0283 wt% and 0.05 wt%. The DoE plan and the number of total test samples are given in Table 20.

Table 20 – Main experiment material compositions and amount of samples used

Material compositions from DoE				# of test samples		
	MWCNT [wt%]	PANI content	Disp. agent [wt%]	viscosity	resistivity & bending	total
3 types of dispersing agents	0.5	Yes	0.05	3	3	18
		No	0.0065	3	3	18
	0.75	Yes	0.0283	3	3	18
		No	0.0283	3	3	18
	1.0	Yes	0.0065	3	3	18
		No	0.05	3	3	18
No dispersing agent used	1.0	Yes	-	3	3	3
		No	-	3	3	3
Sum						<u>114</u>

Three samples for viscosity analysis and three samples for both electrode and actuator measurements were produced for each material combination in order to obtain a meaningful sample size for subsequent statistical interpretation. Every test triplet was fabricated by the same personnel in the same room (20°C air-conditioned chemical laboratory), using the same laboratory equipment and the same batch of basic materials. The viscosity of all dispersions was measured no longer than fifteen minutes after their final dissolver treatment. All cast layers were photographed in their wet state, in at least one intermediate state and in their dried state. All layers were dried for twelve hours in air, resting uncovered under an extraction hood without any change in ambient conditions. No vacuum curing has been done. Possible solvent residues have not been directly measured but could be ruled out by comparing the final weight of all dry layers to the total mass of materials added to the solution during the dispersion process. All dry layer resistivities were measured within 24 hours after drying was completed. All sample actuators were assembled within 48 hours and tested within 72 hours after the drying process was completed.

The measured and calculated effects of different material compositions and additives on the final slurry viscosity are given in Figure 38. Only the viscosity values at a shear rate of 10 s^{-1} are shown. At a shear rate of 100 s^{-1} the viscosities are in the range of one order of magnitude lower, which means that all slurries are within the printable range (compare Figure 35). As expected, the viscosity increases with an increased MWCNT concentration while the presence of PANI has no observable effect. PE/L61 appears to be the only dispersing agent that has influence in combination with higher CNT mass fractions.

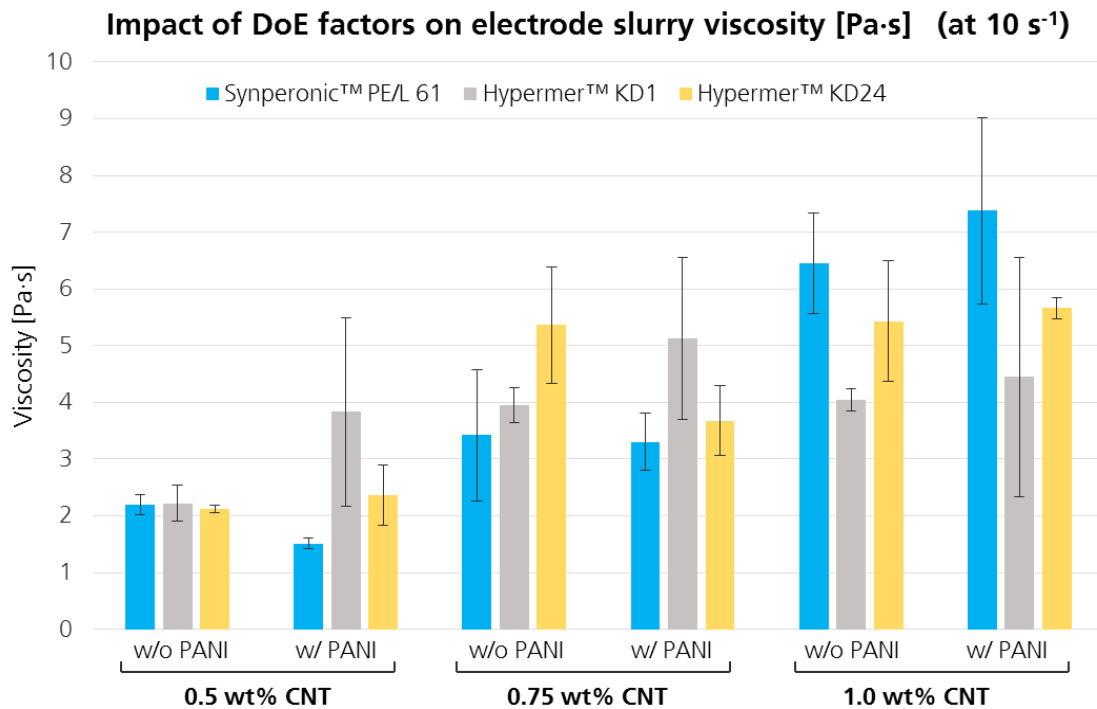


Figure 38 – Effect of CNT mass fractions, the presence of PANI and the type of dispersing agent on the slurry viscosity (mean values of three test samples).

The effect of CNT mass fractions, PANI content and dispersing additives on the electrical conductivity of the dry layers is illustrated in Figure 39. It is not surprising that a higher MWCNT loading promotes a lower resistivity of the electrode layer because the conductive percolation network that is formed by the CNTs inside the dried CNT-IL-polymer layers will be denser. On the other hand, it is remarkable that PANI – when added to the suspensions – appears to have only a minor effect, even though its initial purpose was to increase electrode conductivities to a much larger extent in the first place.

The impact on actuator performance is depicted in Figure 40. The measurements have been conducted with the automated test setup described in 3.3.4.

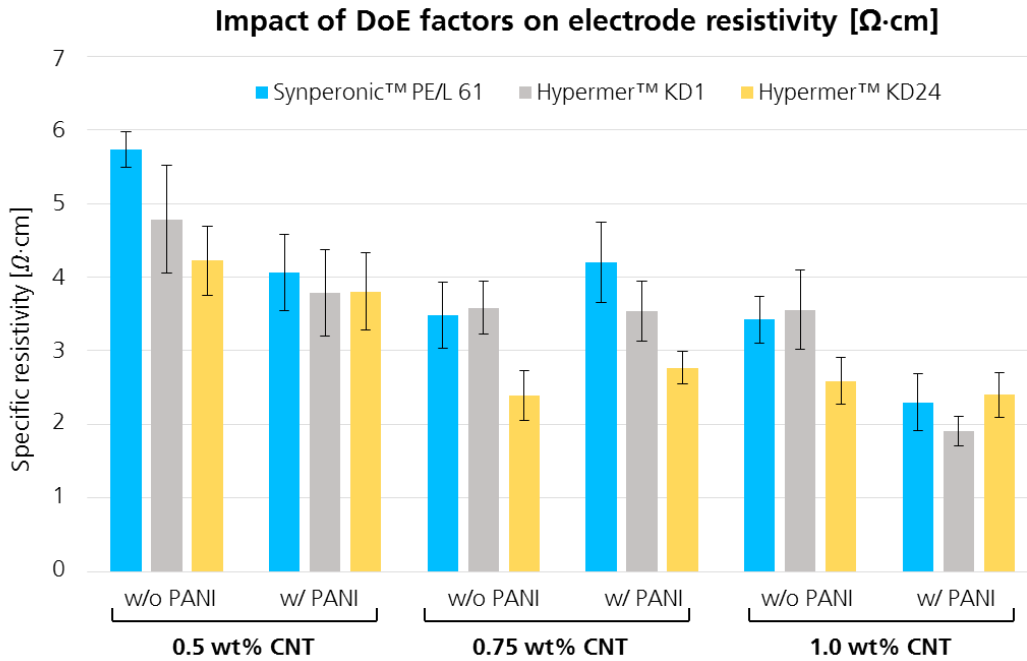


Figure 39 – Effect of CNT mass fractions, the presence of PANI and the type of dispersing agent on the specific resistivity of air-dried electrode films (mean values of three test samples)

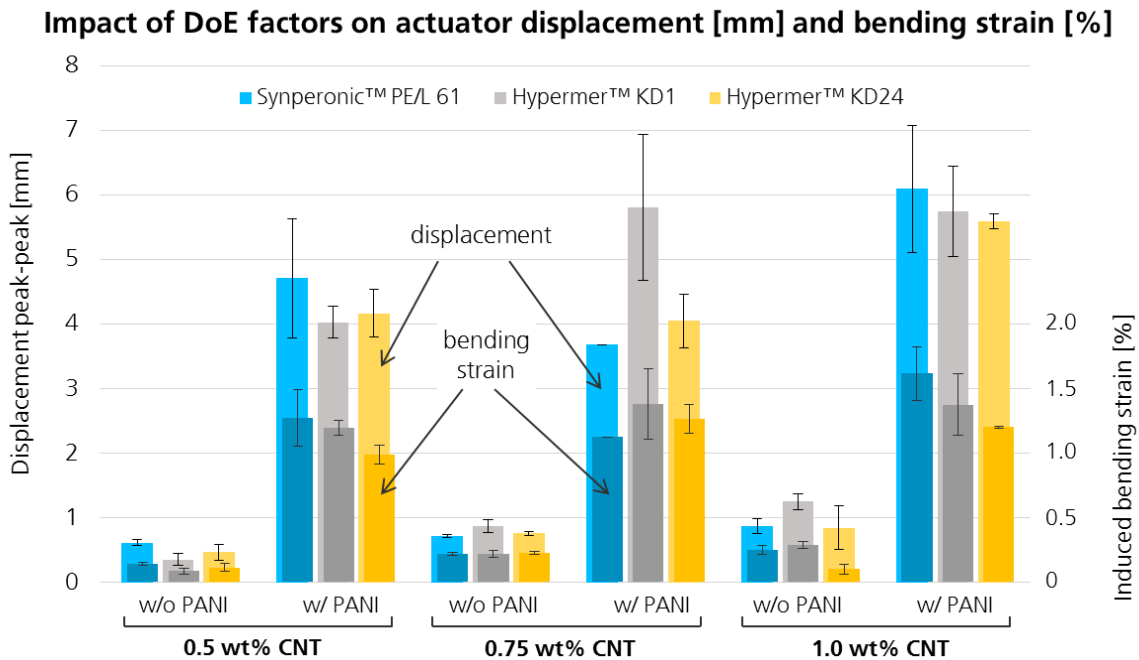


Figure 40 – Effect of CNT mass fractions, the presence of PANI and the type of dispersing agent on the measured tip displacements and induced bending strains of assembled CNT actuators (mean values of three test samples)

The displacement values were obtained at a 3 V square wave excitation applied to the actuators with a frequency of 0.05 Hz. The induced bending strains have been calculated using equation (1) assuming a uniform bending curvature in the fully displaced state. The calculations considered the exact individual thicknesses of the assembled actuators measured with a digital caliper gauge directly after heat pressing (see section 2.4.4). Actuator thicknesses were all within the range of 220 μm and 320 μm . Both the displacement and the induced bending strain values were strongly impacted by the presence of PANI for all investigated CNT mass fractions and all dispersing agents. The Main Effects Plot (MEP) regarding the bending strain of the tested actuators is presented in Figure 41 and confirms the statistical significance of the main effect in terms of PANI being present in the dispersion.

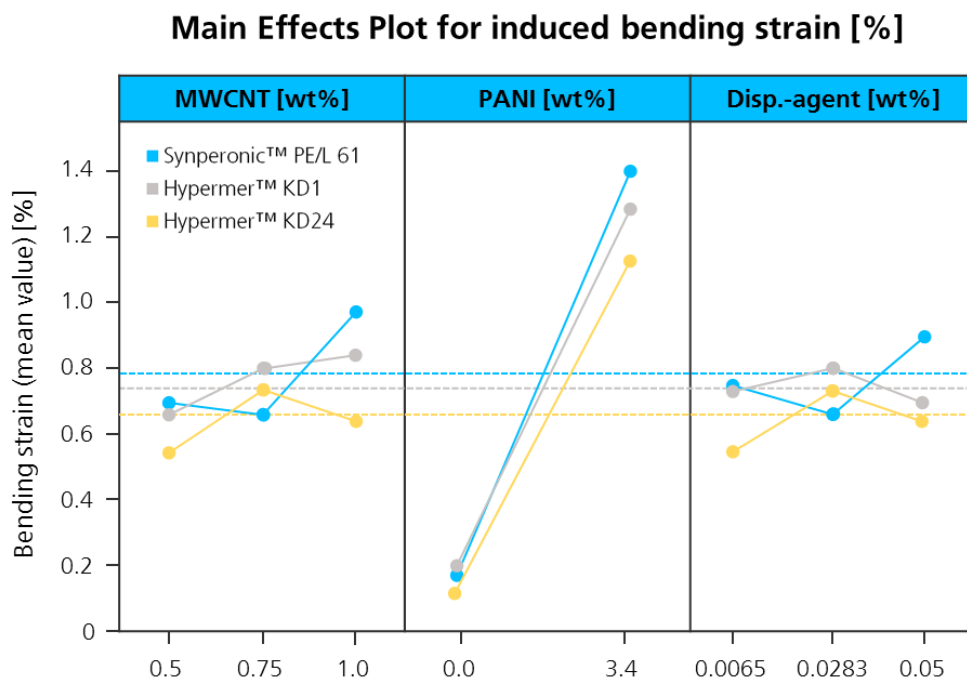


Figure 41 – Main Effects Plot for induced bending strain. The presence of PANI has a significant main effect on actuator performance.

The statistical impacts of the three dispersing agents are not significant regarding the measured and calculated actuator performance. However, microscopic analysis of the dry layers showed that both the size and number of grain-like elevations visible on the electrode surfaces were smaller when PE/L 61 was added to the dispersion (Figure 42).

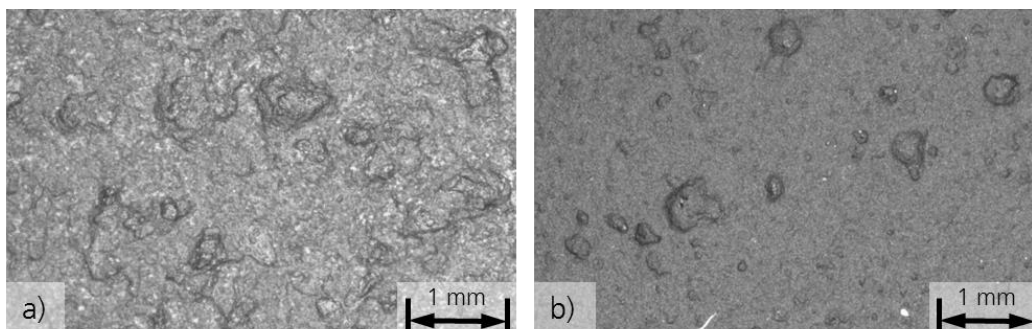


Figure 42 – Microscope images of dried MWCNT electrode layer (a) without and (b) with dispersion agent PE/L 61. (pictures: Julia Jablockin, IFF, 2019)

Digital microscopy measurements of the visible surface grain sizes (encircling diameter) revealed that they were much larger than the maximum particle sizes that were measured with the grindometer in pretest 2. The larger grain dimensions were attributed to smaller agglomerates on the layer surface covered by a thick layer of well-dispersed matrix material. The size distribution and average dimensions of the 25 largest observable surface grains in 1 cm² of dry layer were plotted in Figure 43 for four different electrodes, one fabricated without any dispersing agent and three containing PE/L61, KD1 and KD24, respectively.

The average grain diameters of those electrodes containing dispersing agents were smaller compared to the electrode that was fabricated without these additives. It can therefore be concluded that the dispersing agents seem to reduce re-agglomeration of MWCNTs and PANI particles during stirring and drying. Thus, dispersing agents may arguably have a positive impact on the cycle life of CNT actuators because they might reduce the probability of local hot spots forming in the electrodes during operation that may ultimately lead to failure of the actuator.

Due to the insignificant impact of all dispersing agents on actuator performance and PE/L 61 potentially reducing electrode grain sizes, PE/L 61 was included in the dispersion used for subsequent printing experiments.

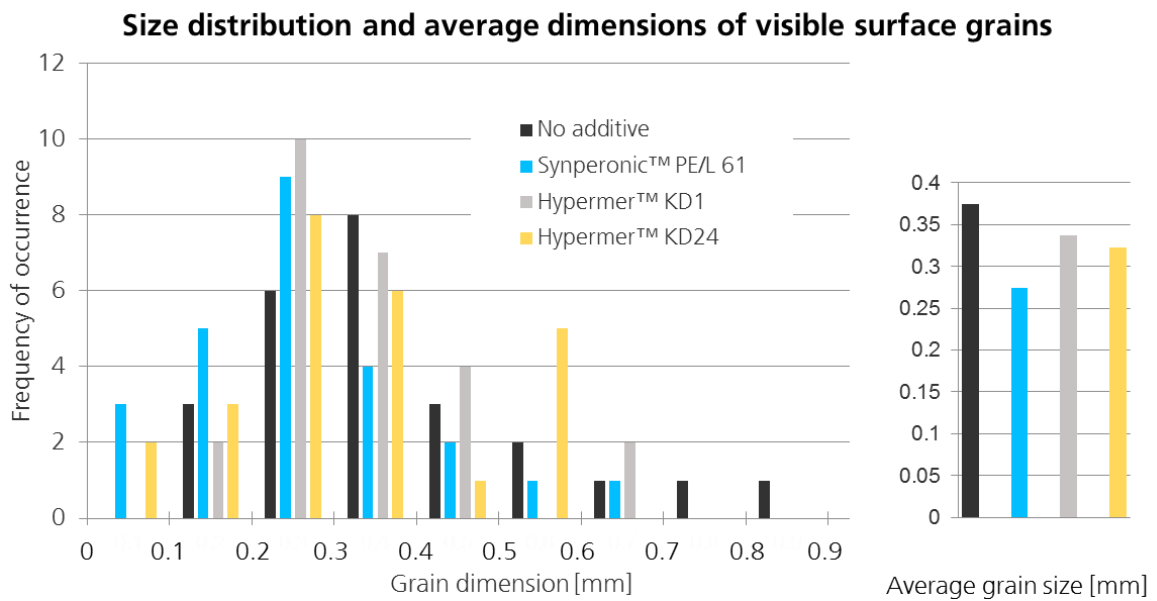


Figure 43 – Size distribution and average dimensions of 25 largest surface grains observable in 1 cm² of dried electrode layer, depending on the type of dispersing agent used.

The phenomenon of edge separation through layer contraction, which was observed for cast electrode layers after dissolver treatment in pretest 2, also occurred in the main experiments. Interestingly, only electrode layers containing PANI contracted during the drying process. From that, it may be concluded that PANI particles tend to reaggregate after being subjected to mechanically induced shear forces.

Table 21 – Compilation of final actuator components , mass fractions and cost breakdown

Component	Function	Mass fraction [wt%]		Cost [€]	
Electrode		Wet state	Dry state	per gram	per electrode^{d)}
PVDF	Backbone polymer	5.4	30.64	0.68	0.01
SWCNT^{a)}	<ul style="list-style-type: none"> • Electrochemically active material • Conductive percolation network 	-	-	1017.-	1.83
MWCNT^{b)}		0.75	4.3	0.25	0.01
PANI	<ul style="list-style-type: none"> • Electrochemically active material • Conductive additive 	3.4	19.2	8.68	0.04
BMI-BF₄	Ionic liquid	8.0	45.7	1.78	0.02
PE/L 61	Dispersing agent	0.03	0.16	0.10	0.01
4M2P	Organic solvent	82.42	-	0.03	0.20
Separator / electrolyte layer				per gram	per separator^{d)}
Nafion®	Separator membrane (commercial)	-	-	-	0.50
PVDF/IL	Separator membrane (self-made)	-	50/50	1.23	0.06
a) CHASM® Signis CG300™ b) Nanocyl® NC7000™ c) 2cm x 1cm, 0.15 mm thickness d) 2cm x 1cm, 0.1 mm thickness					per actuator
				SWCNT	<u>4.29</u>
				MWCNT	<u>0.64</u>

Table 22 – Compilation of dispersion techniques, parameters and manufacturing times for producing dry electrode layers using the baseline dispersion and the dispersion optimized via DoE

Baseline dispersion & drying processes			Optimized dispersion & drying processes		
Technique / steps	Materials	Time	Technique / steps	Materials	Time
Weighing	All	10 min	Weighing	All	10 min
Magnetic stirring (room temperature)	All	1-3 days	Ultrasonic homogenization (30 W – 35 kHz)	MWCNT, 4M2P	8.5 min
	Pre-dispersion			Pre-dispersion	
			Magnetic stirring (80°C heating plate, 300 min ⁻¹)	Add PVDF	50 min
				Add BMI-BF ₄	10 min
				Add PANI	10 min
				Add PE/L 61	10 min
Ultrasonic bath (36 kHz)	All	24 hours	Dissolver (Blade mixing, 3500 min ⁻¹)	All	5 min
	Final dispersion			Final dispersion	
Casting		5 min	Casting (printing)		5min
	Wet electrode layer			Wet electrode layer	
Heat assisted drying (hotplate at 50° C)		12 hours			
Vacuum assisted drying (80° C)		72 hours	Air drying		12h
	Dry electrode layer			Dry electrode layer	
		> 132 hours			< 14 hours

4.2 Printing CNT actuators and components

This section describes the implementation of the individual printing and coating methods proposed in section 3.4 and focuses on the discontinuous slot-die coating machine that was put into operation in the Institute of Industrial Manufacturing and Management (IFF) at the University of Stuttgart. This facility was launched to demonstrate pilot plant scale manufacturing of CNT-based IEAP actuators in particular.

4.2.1 Screen printing of CNT actuator electrodes

To investigate the feasibility of screen-printed CNT actuator electrodes it was necessary to conduct manual printing tests with medium-sized meshes. The procedure is depicted in Figure 44. The electrode dispersion is manually dispensed on the mesh and then printed onto the underlying PTFE or glass substrate with a rubber squeegee. This process may be repeated if the amount of dispersion to cover the printing area is insufficient.

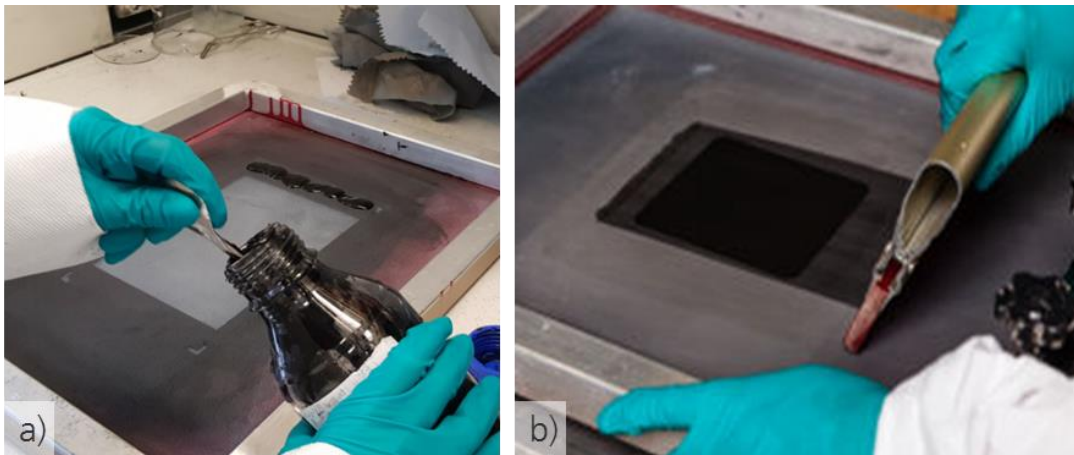


Figure 44 – Manual screen printing of CNT actuator electrodes. a) Dispensing dispersion droplets above the rectangular printing area. b) pressing the dispersion with a squeegee through the mesh (pictures: Veronika Bitzer, IFF 2019)

Two different meshes were employed to produce non-structured layers of rectangular shape. The first mesh had a coarse mesh count of 10-280 (meaning 10 threads per centimeter with a diameter of 280 μm) and a 14° screen angle to produce thick wet layers. The second mesh had a finer mesh count of 39-80 with 0° screen angle. The mesh openings are 710 μm and 172 μm , respectively, so all residual particle agglomerates in the dispersion should be able to penetrate through the mesh.

The screen-printed electrode films showed clearly visible mesh imprints in both wet and dry state. While the coarse mesh produced a closed layer after only one print run, the layers made with the finer mesh exhibited non-coated defective areas even after repeated printing runs (Figure 45). The more runs were conducted, the more clogged areas were observed in the finer mesh's openings. Repeated squeegee strokes then caused slurry agglomerates to penetrate the mesh and settle on the substrate underneath, forming disconnected particle clusters. The dry layers of all print runs demonstrated poor surface homogeneity which was measured by laser spectroscopy (see section 4.2.5).

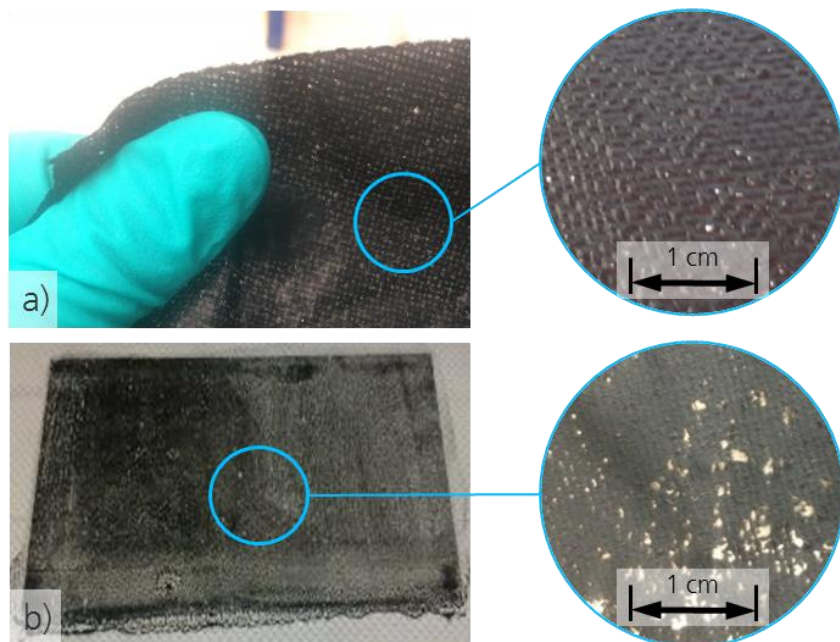


Figure 45 – Screen-printed CNT actuator electrode layers showing visible surface texture. a) dry film produced with a coarse mesh and b) perforated dry film produced with a finer mesh. (pictures: Veronika Bitzer, IFF 2019)

4.2.2 Blade coating

After the electrode dispersion was poured onto the printing table, the semi-automatic blade coater distributed the viscous slurry evenly on the substrate. Polyethylene terephthalate (PET), aluminum, PTFE and glass served as suitable substrates, all of which allowed for straightforward removal of the dry layers after 12 hours of drying in air. Using a knife blade yielded better results compared to spiral blades, which left behind visible grooves that did not recede after the blade reached its ending position. Smooth and homogeneous layers of controllable wet layer thickness were produced as long as the blade speed was kept below 4 m/min. Higher blade speeds caused insufficient adhesion of the slurry to the substrate, the slurry being pushed ahead without wetting the substrate. Printing of thinner layers ($< 500 \mu\text{m}$) repeatedly produced streaks in the wet film due to blade contamination. The results from laser microscopy analysis and actuator performance tests are discussed in section 4.2.5.

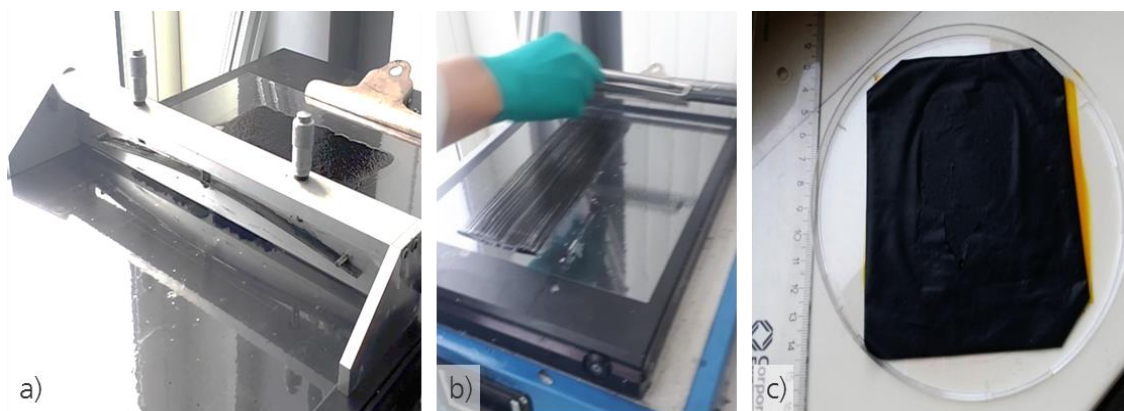


Figure 46 – Blade coating of electrode layers for CNT-based IEAP actuators. a) semi-automatic knife blade coating. b) manual spiral blade process. c) final (cut) electrode layers. (pictures: Raphael Neuhaus, IFF 2018)

4.2.3 Stencil printing

The self-assembled PTFE-based printing plates facilitated the fabrication of differently shaped small electrode films. Circular, triangular and square-shaped films were made (Figure 47). The dried electrode pieces could be easily extracted from their PTFE molds and

were assembled to form measurable actuators. Stencil printing was the preferred method for actuator fabrication during pretest 2 and the main experiment of the DoE. The dry layer surface characteristics and the actuator bending performances are described in section 4.2.5.

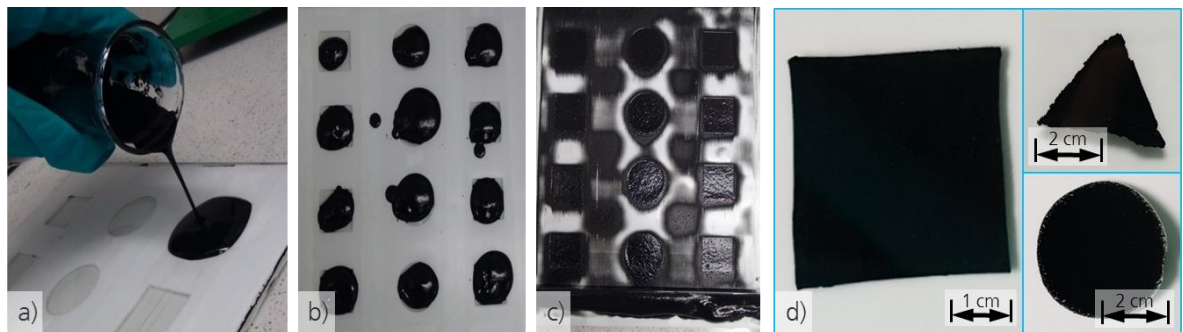


Figure 47 – Stencil-printing of CNT actuator electrodes. a) solution casting into stencil plate molds. b) stencil plate before scraping. c) stencil plate after scraping. d) dry film electrode pieces having various shapes. (pictures: Julia Jablockin, IFF 2018)

4.2.4 Semi-automated discontinuous slot-die coating

For feasibility testing of the slot-die coating technique, the discontinuous coating machine Easycoater EC63 by Coatema Coating Machinery GmbH (Germany) was utilized (Figure 48a). The coating process took place inside a sealed cabin equipped with a vacuum extraction system (Figure 48b). This allowed for quick removal of flammable gases in the cabin and enabled printing runs with solvent-based inks and pastes. Two slot-dies were mounted to two vertically adjustable crossbeams that moved on linear slides across the heatable printing table (Figure 48c).

The mounting rack had modular fittings for different printing devices, thus permitting semi-structured blade or screen printing in the same machine, too. For this thesis, only slot-die coating was performed with the EC63.

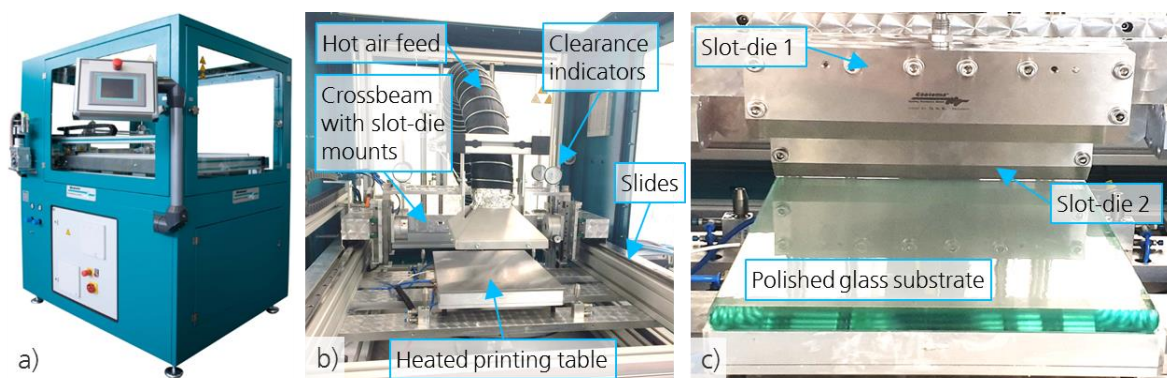


Figure 48 – Discontinuous coating machine Easycoater EC63. a) Exterior view (©Coatema). b) Interior of vacuum-extractable printing cabin (©Coatema). c) Slot-die arrangement and printing table setup (Neuhaus, IFF 2019).

Two high-pressure gear-type feeding pumps (N19-DLC1 from Feinpruef, Germany) were positioned next to the printing cabin, permitting an accurate control of the liquid throughput from a neighboring reservoir (e.g. a capped dispersion flask) to the slot-die nozzle (Figure 49a). They were connected to the slot-dies using hydraulic high-pressure hoses with screw coupling to provide a secure locking system (Figure 49c). The pump chambers and the gearwheels consisted of stainless steel and thus allowed trouble-free handling of dissolved polymer blends or even aggressive media (Figure 49b).

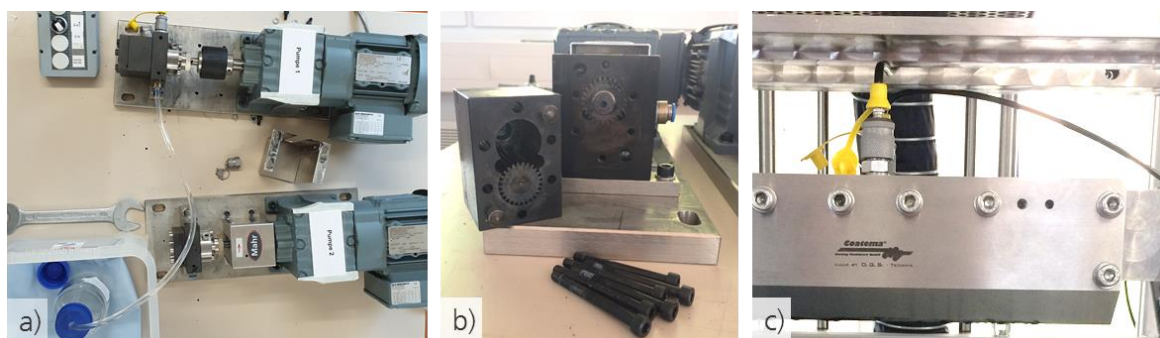


Figure 49 – Illustration of external feeding pump assembly used for supplying the slot-dies inside the printing cabin. a) External supply hose. b) Disassembled pump chamber with exposed gearwheels. c) Attachment of supply hose on the slot-die. (pictures: Veronika Bitzer, IFF 2019)

The pump rate was continuously adjustable from 5% to 100%, which roughly translated into 5 cm³ to 100 cm³ of liquid throughput per minute. The nozzle speed was adjustable

from 0.05 m/min to 5.0 m/min. Trial runs were performed with a non-solvent-based solution of 5 wt% polyvinylpyrrolidone (PVP) dissolved in H₂O to find appropriate settings for the pump rate, the nozzle speed and the substrate clearance. The nozzle's slot width was 100 μ m. When the pumps were switched off at the rear nozzle position, the printing liquid continued to drip out of the slot-die nozzle and flooded the rear part of the substrate (Figure 50a). After the installment of a drip collection basin behind the printing table, the pumps were switched off when the slot-die nozzle position reached the drip collection basin. The issue of delayed dripping will no longer be relevant when continuous slot-die processes are installed.

50% pump rate, 0.2 m/min nozzle speed and 0.8 mm substrate clearance were found as efficient process settings for PVDF-IL-4M2P electrolyte layers. A coherent wet film with a homogeneous thickness of 1.3 mm was reproducibly obtained. When the feeding hoses and the slot-die were cleaned of residual dirt contaminants (Figure 50b), it was finally possible to print unpolluted and homogeneous DIN-A4-sized electrolyte layers (Figure 50c). The average dry film thickness was 115 μ m (\pm 5 μ m), measured at various points on the dried layers.

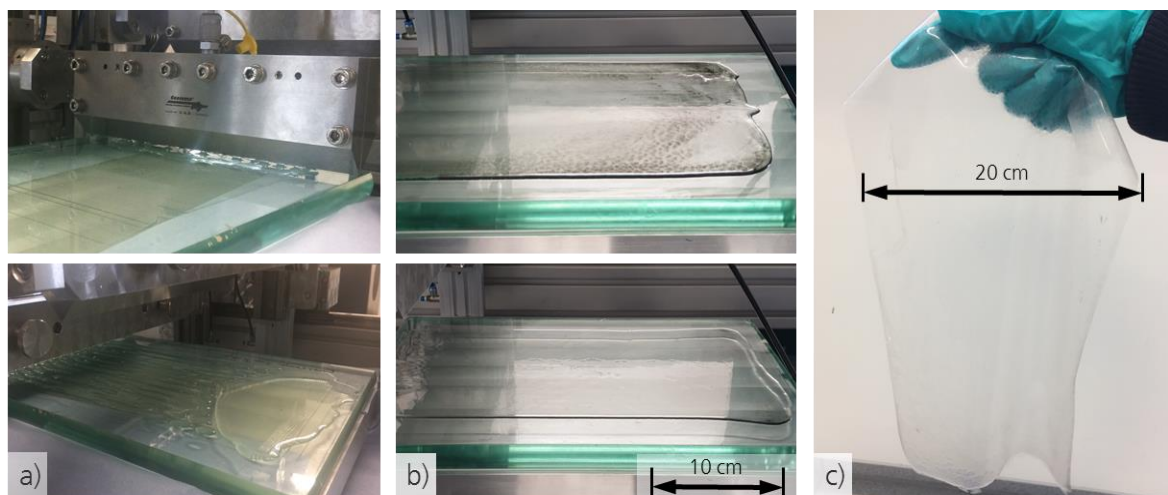


Figure 50 – Slot-die printed large-scale separator layers for CNT actuators. a) Dummy layers for adjustment of printing settings. b) CNT contaminated (top) and non-contaminated separator layer (bottom). c) Large separator layer removed from glass substrate after heat-assisted drying. (pictures: Neuhaus, Bitzer, IFF 2019)

Initial electrode printing tests were performed with the same machine settings, producing heavy streaks in the wet layer due to residual agglomerates in the electrode mixture that

were clogging the slot-die nozzle (Figure 51a). Upon increasing the slot width to 250 μm using spacer blades, the streaks disappeared and coherent wet films were achieved (Figure 51b). The pump rate was increased from 50% to 60% and the substrate clearance was increased to 1.0 mm.

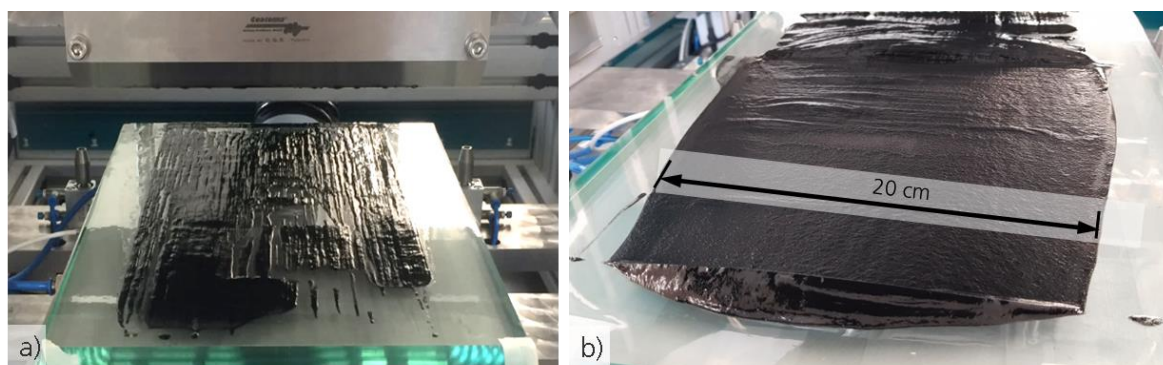


Figure 51 – EC 63 electrode printing tests a) showing heavy streaks in the electrode wet layer due to residual agglomerates clogging the slot-die nozzle, b) producing coherent wet layers after adjustment of nozzle slot width. (Pictures: Raphael Neuhaus, IFF 2019)

A total of eight printing runs were performed to obtain appropriate settings for pilot plant scale electrode fabrication. Every run required at least 500 ml of dispersion because the feeding hoses, the pump chamber and the slot-die reservoir needed to be completely filled with dispersion to enable a uniform flow of liquid out of the slot-die nozzle and onto the glass substrate. Hot air drying by means of a lowerable ventilation funnel was disregarded after the first printing run because the stream of hot air caused ripples in the freshly applied wet layer surface. A homogeneous dry film was achieved after a drying time of 30 min to 60 min when it could be removed from the printing cabin. The results of this printing method have been published by the author (Neuhaus et al. 2019c).

4.2.5 Evaluation of printing methods

Typical results for laser microscopy analysis of dry electrode films printed via screen printing, blade coating, stencil printing and slot-die coating are given in Figure 52.

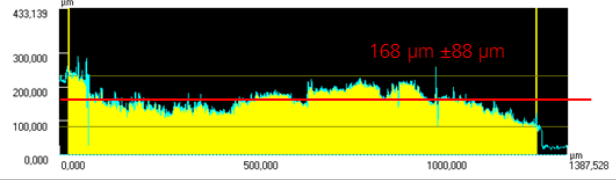
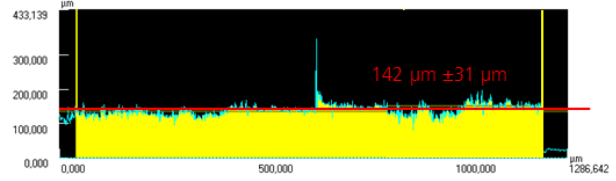
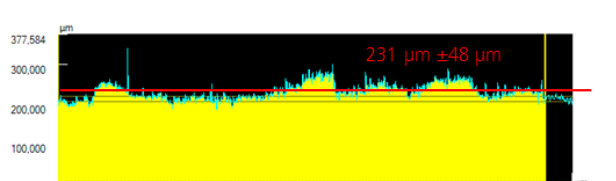
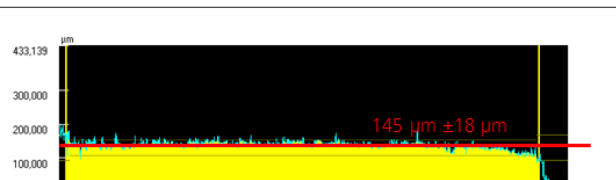
Type	Typical laser microscopy analysis	Average dry layer thickness	Average roughness height R_a
Screen printing		181.7 μm	65.4 μm
Blade coating		157.4 μm	21.5 μm
Stencil printing		217.9 μm	18.3 μm
EC 63 slot-die coating		119.2 μm	12.6 μm

Figure 52 – Laser microscopy analysis of dry film thickness for screen printed, blade coated and slot-die coated CNT actuator electrode layers

The average surface roughness height R_a refers to the arithmetic average of the absolute distances of all profile points from the mean line in one selected cross-section of the layer. This parameter may be extended to all profile points within a given surface area and is automatically calculated by the software using

$$R_a = \frac{1}{L \cdot W} \int_{x=0}^L \int_{y=0}^W |z(x, y)| dy dx \quad (6)$$

where L is the length and W is the width of the investigated surface area on the electrode sample. More than twenty sample electrodes were analyzed for each printing method, each sample being measured at five different locations of 1 mm² surface area. The residual mesh imprints on the screen-printed layers are clearly visible in the surface analysis. The

thicknesses and roughness values were measured on untreated samples (no heat-pressing) directly after the printing runs.

For each of the four printing techniques, a total of six actuators were fabricated using 12 manually cut-out electrode pieces with a size of 2 cm x 0.5 cm. The actuators were assembled using the state-of-the-arts heat-pressing method explained in section 2.4.4. Induced initial bending strains were calculated using equation (1) and are depicted in Figure 53.

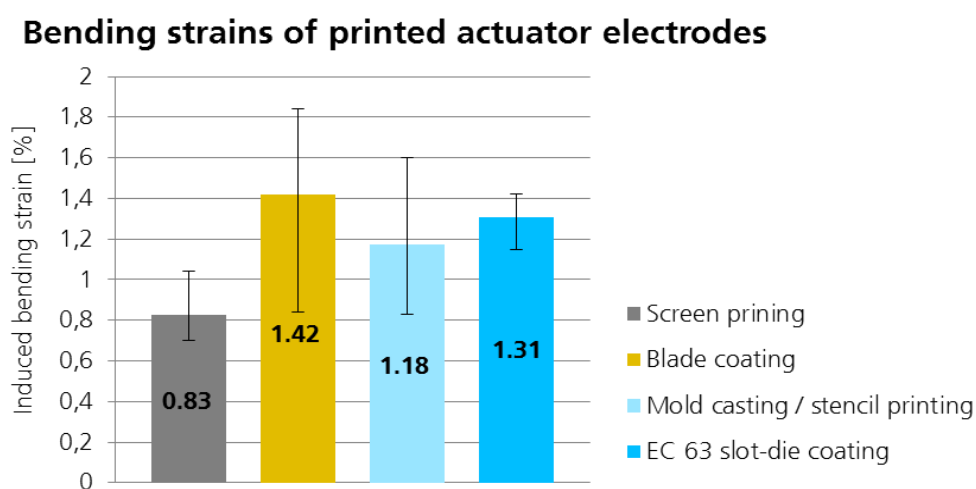


Figure 53 – Induced bending strains of printed electrodes fabricated with different printing techniques. Discontinuous slot-die coating proved to have the lowest spread in performance.

4.2.6 Conclusion

It can be concluded that printing large-scale layers of actuator electrodes and separators is generally feasible. All four printing methods have been demonstrated to produce more or less coherent layers from the optimized CNT slurries of chapter 4.1. All of these layers were successfully processed into functioning CNT actuators.

Nevertheless, the printing methods have different characteristics. While screen-printed electrode films showed clearly visible mesh imprints in both wet and dry state, blade coating repeatedly produced streaks in the wet film due to blade contamination. Both screen and stencil printing are predominantly discontinuous fabrication methods and produce structured films. These methods are not as efficient as industrial roll-to-roll processes like

blade or slot-die coating, but they can produce multi-layer actuators of many different shapes without the need for post-treatment such as cutting.

The most homogeneous thickness distribution of printed electrode layers was achieved with the slot-die coating method. An average surface roughness of 12 μm for a given layer thickness of 120 μm represents a 10% deviation. In view of the dimensional requirements specifications from section 2.1.2 (less than 2% tolerance of component dimensions) this technique thus falls short of the specification. This does not pose a threat to the functionality of the actuator system, so the deviation of the layer thickness is tolerable. Moreover, the lowest spread in induced bending strain was also measured for slot-die-coated electrodes, which represents a significantly better reproducibility of actuator performance than all other printing methods.

Despite the fact that more complex and costly equipment and machinery (slot-dies, pumps) are needed for this method, the slot-die coating method is still superior to blade coating and stencil printing. This is mainly attributed to two distinct features: Firstly, it offers a precise control over the wet layer thickness and its homogeneity. Secondly, it simultaneously minimizes the amount and size of residual agglomerates during the printing process, because it boosts particle distribution in the printing slurry due to high induced shear forces and pressures within the pumps, the feeding hoses and the inner core of the slot-die itself. This special “post-dispersion” in the final stage of production helps to form homogeneous material characteristics within the printed layers.

For these reasons, the author proposes slot-die coating of electrode and separator layers to be the preferred choice in regards to reproducible and cost-efficient layer-by-layer manufacturing of CNT-based IEAP actuators and sensors.

4.3 Actuator assembly from printed layers

This subchapter explains how the printed electrodes and separators from the previous section were converted into operating CNT actuators. It covers different cutting and fusing approaches of mainly slot-die printed layers and investigates the up-scaling potential of this manufacturing stage. It refers to methods and materials for robust and reliable electrical connections and focuses on connectors directly embedded into actuator electrodes. In view of the actuators' potential target application in building envelopes, it covers the effects of dip-coated PVDF encapsulation layers on the actuator performance.

4.3.1 Fusing-cutting approach for large-scale printed actuator layers

As introduced in 3.5.1, there are two ways to obtain small rectangular pieces of tri-layer laminate which constitute operational CNT actuators. It is possible to first fuse the printed electrode and separator layers together and subsequently cut out individual actuators of desired size and shape (fusing-cutting approach), or the printed layers are cut into small pieces, which are subsequently fused together with a heating press (cutting-fusing approach). For the fusing-cutting approach, the uneven edges of two printed electrode layers and one printed separator layer were manually trimmed to form three equally sized rectangular sheets (Figure 54). The sheets were then stacked to achieve a three-layer sandwich with congruent edges.

Subsequently, the resulting sandwich was fed through a heated calender (Figure 55a) with the electrode surfaces protected by aluminum foil (Figure 55b). The aluminum foil is important to avoid direct contact of the electrode layers with the heating stage and the calender rolls. A gap of 0.4 mm between the calender rolls, an initial temperature of 120°C and a feeding speed of 3 m/min were chosen for the pilot trials. The correct temperature range is of utmost importance. If the feeding speed is too slow and the heating block too hot, the polymer composite layers will melt and blisters will cause imperfections in the three-layer compound and ultimately destroy the actuator sheets (Figure 55c).



Figure 54 – Manual preparation of actuator layers for fusing-cutting approach

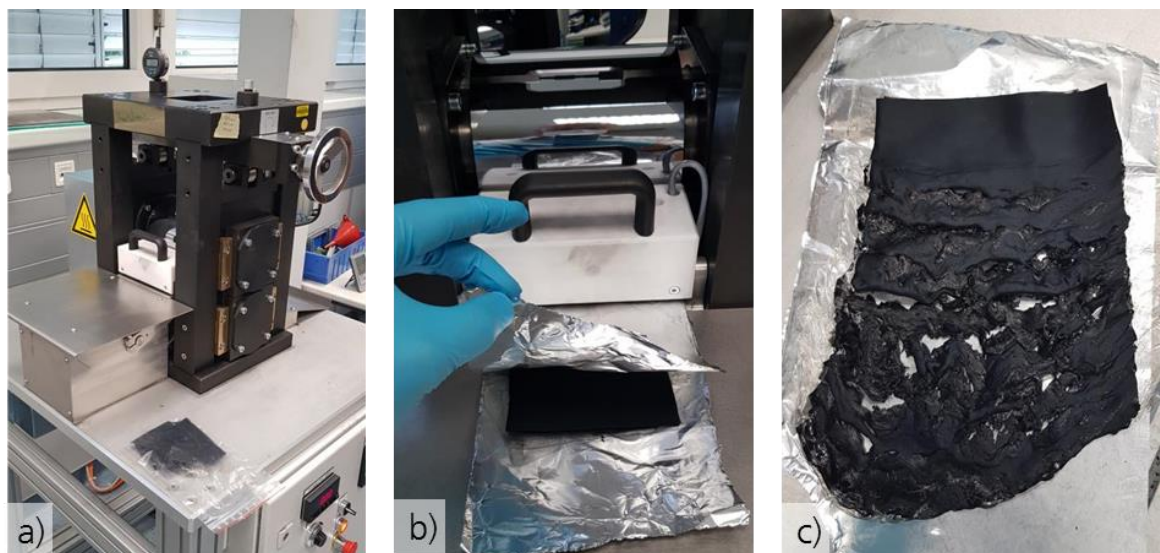


Figure 55 – Calender used to fuse multilayer CNT actuator laminates

At a heating temperature of 80°C no defects occurred and the process was successfully tested (Figure 56a). The three layers could be fused together and did not show any delamination behavior after cooling. The feed roll gap must be adjusted according to the thickness of the three layers before every fusing run. For good results, it should be roughly 20% smaller than the total thickness of the stack of layers. The thickness of the laminate after the calender process is slightly smaller (around 10%) than the sum of the thicknesses of the original sheets.

The subsequent cutting process may be done manually or with the help of a cutting punch to obtain the desired actuator dimensions (Figure 56b). Actuator tests revealed that the fusing-cutting approach may potentially cause short cuts between the upper and lower electrode because the intermediate separator layer does not protrude out of the cutting plane to prohibit local conductive bridges. For this reason, this process can only be applied with very sharp cutting tools, precise cutting moves and intensive caution.

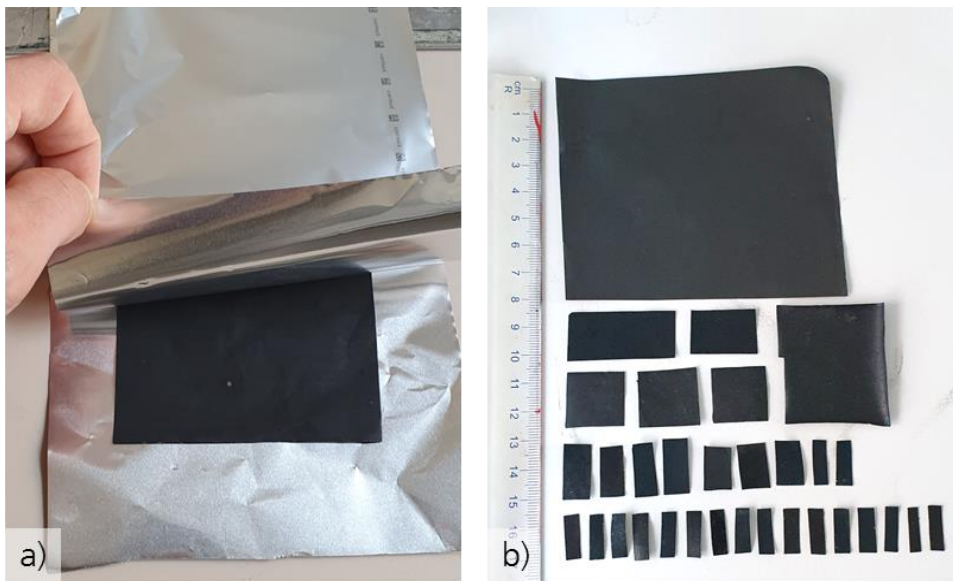


Figure 56 – Successful calendaring and manual cutting of actuator laminates

4.3.2 Cutting-fusing approach

In principle, the cutting-fusing approach represents the same manual manufacturing steps that have been described in section 2.3.4. The printed electrode and separator layers are cut or punched into small rectangular pieces with the separator piece being slightly larger. This ensures that the edges of the separator protrude the laminate sandwich and thus prevent any shortcuts between the upper and the lower electrode pieces. A heat press is used to fuse the three pieces together. This process allows for the integration of electric contacts into the actuator laminate, which is covered in the following section.

4.3.3 Embedded electric contacts

Initially, the solid conductors (conductive yarn, desoldering braid and copper tape) were integrated into wet electrode layers by placing them inside the depressions of the stencil printing plate described in section 3.4.3. When the squeegee was moved over the plate, the conductors became submerged by the electrode dispersion (Neuhaus et al. 2019b). After drying, the connections were evaluated visually and by measuring the contact resistance between the conductor and the electrode materials. Figure 57 shows some examples of embedded contact materials.

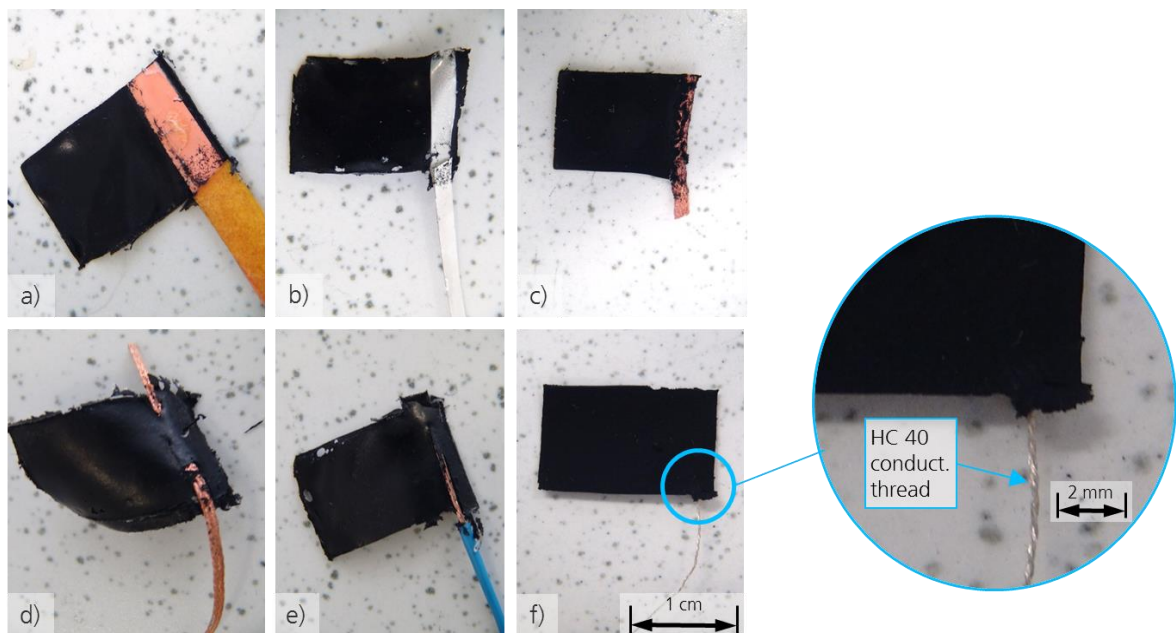


Figure 57 – Illustration of embedded contact materials. a) Roughened copper tape. b) Silver tape. c) Wide copper braid. d) Slim copper braid. e) Copper wire. f) Silver plated conductive yarn. (Pictures: Veronika Bitzer, IFF 2019)

Apart from the conductive yarns, which were the only true limp materials, the supposedly form-locking connections between the polymer electrode and the metal contacts were not mechanically stable. Despite the compliant mechanical characteristics of the slim polymer layers, the metallic stiffness caused the intermediate bonding to loosen quickly. The initial electric contact resistances of all tested connector materials are presented in Figure 58.

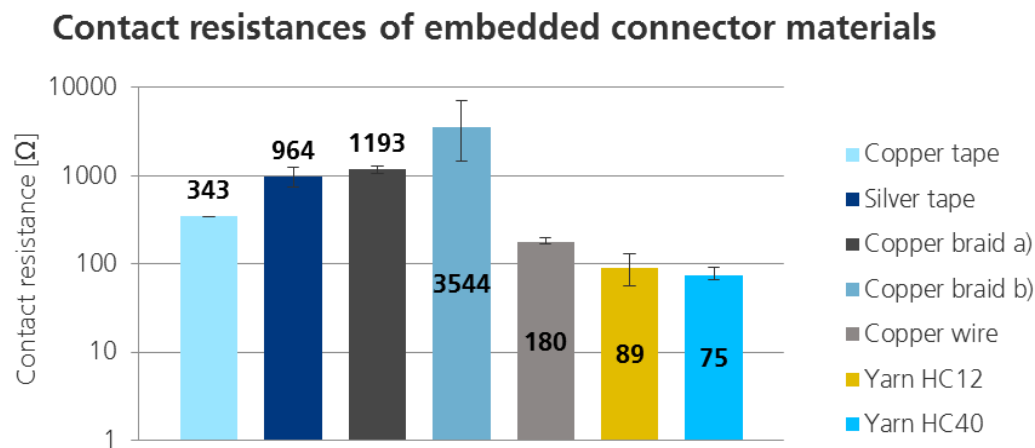


Figure 58 – Measurement results for initial contact resistance of various electric connector materials embedded into wet electrode layers

Having found that silver-plated conductive yarn yielded the lowest initial contact resistance for wet layer integration, the yarn was utilized for the cutting-fusing approach described above. The pre-cut electrode samples were obtained in large quantities from the previously developed automated slot-die printing process.

The end parts of short pieces of conductive yarn HC 12 were sandwiched in between two electrode samples of the preferred shape, which were subsequently fused via heat-pressing. The resulting thick double-layer electrodes now featured firmly embedded electric contacts and had contact resistances of below 10 Ω . The final assembly of the electrode-separator-electrode actuator laminate was again accomplished by heat-pressing and produced a complete tri-layer actuator with two embedded electrode contacts for facilitated system integration (Figure 59).

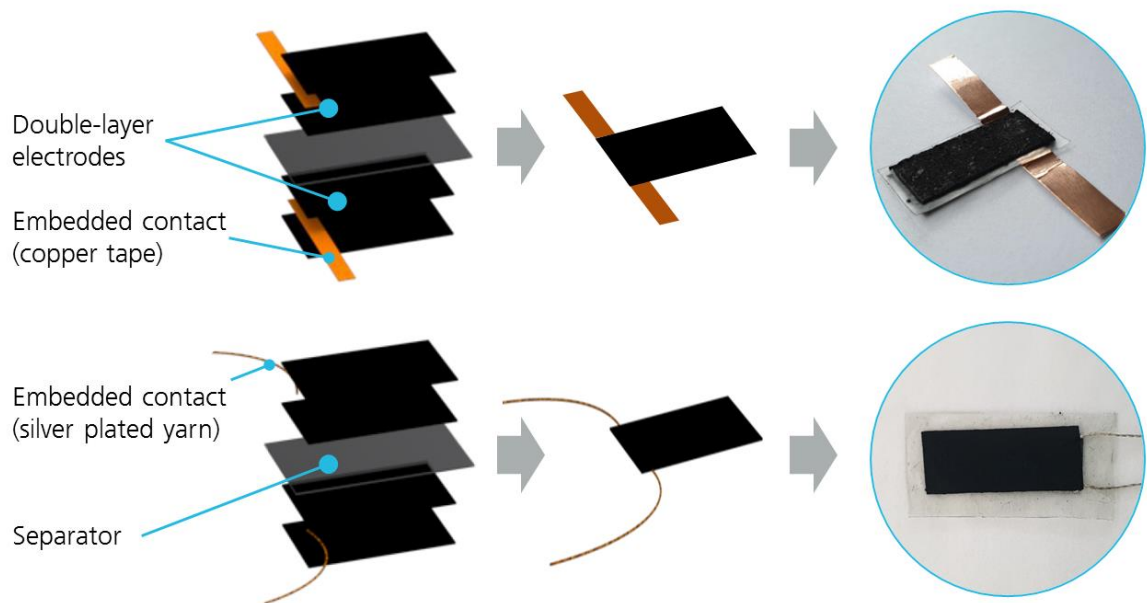


Figure 59 – Embedded electric contacts. Concept and implementation of embedding conductive tapes and yarns into multi-layer electrodes for IEAP actuator assembly. (Illustration & pictures: Nima Zahiri, IFF/BioMat 2019)

Depending on the length of the embedded part of the conductive yarn contacts, the bending deformation of the actuator was affected in different ways. Actuators with contact yarns passing through the entire length of the electrodes quickly developed a remarkably uniform bending curvature over the entire actuator length (Figure 60). On the contrary, actuators with contacts reaching only a few millimeters into the electrodes exhibited a strong bending curvature close to the attachment point only, while the rest of the actuator surface showed almost negligible deformation. The latter constitutes the transmission-line-effect described in section 2.3.4. It was assumed that the longer yarn contacts acted like a charge distributor and simultaneously caused a local increase in electrode stiffness. Diagonally embedded yarn contacts produced short circuits between the upper and lower electrodes at the yarn intersection during heat-pressing.

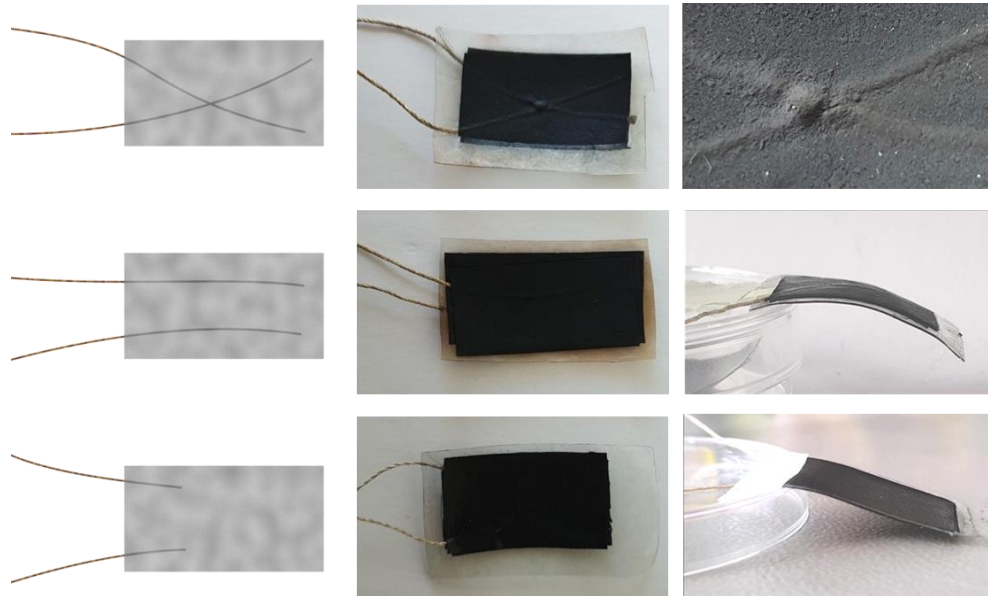


Figure 60 – Influence of embedded contact yarns on CNT actuator bending curvature (Illustration & pictures: Nima Zahiri, IFF/Biomat 2019)

4.3.4 Encapsulation

It has been suggested that while the method of encapsulation has to be suitable for each actuator encapsulant, it has only a minor effect on the final outcome, as compared to the choice of the material (Jaakson et al. 2016). As stated in section 3.5.3, the desired encapsulation material for this project was PVDF, because it bonds easily with the actuator's matrix polymer which is also PVDF. Good adhesion and low performance loss were expected. During manual coating trials (Figure 61a and b) it was found that dip-coating of single actuator elements into a solution of PVDF dissolved in 4M2P (0.5 wt%) resulted in a thick and dripping wet layer of PVDF sticking to the actuator's surface. After drying in air for 24 hours, a very thin (10 – 25 μm) coherent layer of PVDF encapsulation material remained around the submerged part of the actuator (Figure 61c).

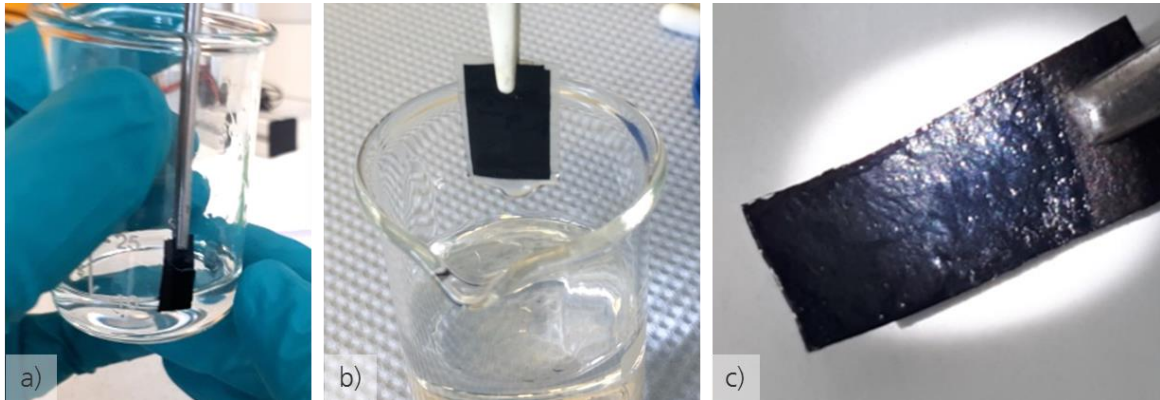


Figure 61 – Actuator encapsulation via dip-coating, a) and b) manual dip-coating trials showing sufficient yet inhomogeneous material coverage on the actuator surface, c) coherent encapsulation layer of on the sample surface after drying in air

Measurements of the electric conductivity of the encapsulation layer indicated a strong dielectric behavior. Submerging the coated part into water did not diminish the actuator's performance for at least 48 hours, thus the additional layer of PVDF prevented the penetration of water into the active layers of the actuator. This implied that it should at least slow down any penetration of water vapor over time, similar to Parylene C (Punning et al. 2014). However, the free-tip bending displacement of coated actuators decreased considerably with each additional encapsulation layer applied (Figure 62). The increased bending resistance resulted from the additional non-active material thickness.

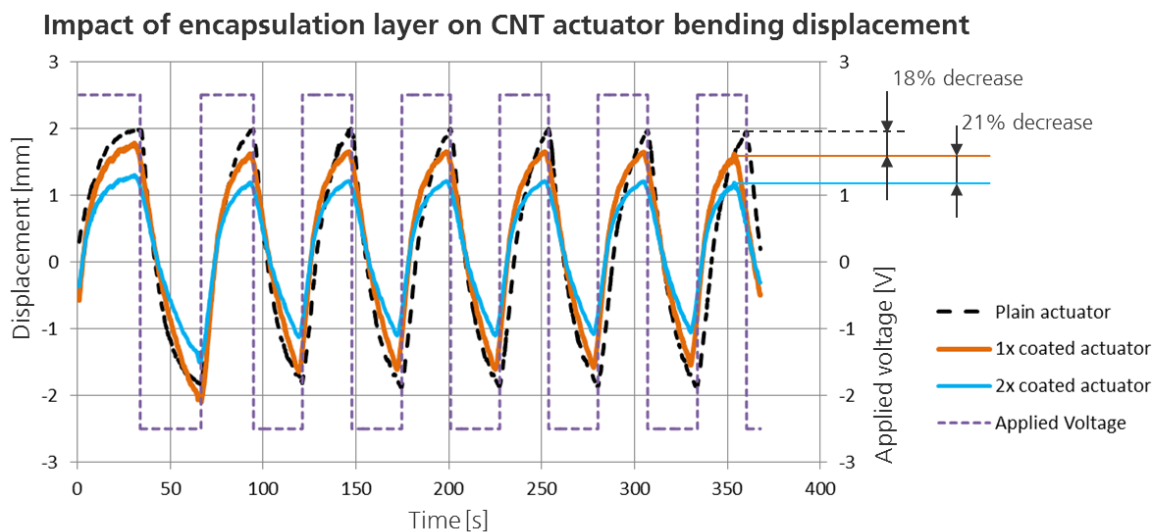


Figure 62 – Impact of dip-coated PVDF encapsulation layers on actuator displacement. Actuator size: 20mm x 8mm x 0.2mm (Diagram: Raphael Neuhaus, IFF 2020)

4.4 Summary and conclusion of Chapter 4

This chapter has described experimental activities to find suitable material compositions, novel dispersion sequences and industrially scalable printing techniques as necessary steps in manufacturing CNT-based actuators and sensors.

The DoE method was used to investigate stepwise modifications in the material compositions and dispersion methods of CNT actuator slurries. The first goal was to obtain coherent dry film layers for MWCNT actuator electrodes. Initial pretests have revealed that conventional dispersing procedures for SWCNT actuators cannot be copied to produce cost-efficient MWCNT actuator electrodes. In this regard, different mass fractions of the active materials were tested to obtain slurry compositions with good drying characteristics. The tests also included experiments with less toxic materials (e.g. 4M2P as a solvent instead of DMAC) and components with better application performance (BMI-BF₄ with a wider operational temperature range). The adaptation of high-power dispersing techniques has triggered investigations on optimized time and power settings. Eventually, suitable process parameters for high shear force treatment of the dispersion were found for both ultrasonic homogenization and blade stirring procedures. On the contrary, three roll milling proved to be an unsuitable method because the solvent evaporated too quickly. In the last DoE stage, the so-called main experiment examined the effects of fine-tuning CNT mass fractions. In a fractional factorial DoE approach, the influence of PANI and the impact of three different dispersing agents on slurry viscosity, residual agglomeration particles and actuator performance was investigated. The result of the total DoE activities was a reliable material composition and a working blueprint for a dispersion procedure for MWCNT-based electrode slurries. The total material cost per unit CNT actuator was reduced by more than 80% through the substitution of SWCNTs with MWCNTs. The total duration of the optimized dispersing sequence for dried electrode films was reduced by 90% to less than 14 hours.

Four different printing technologies have been tested and evaluated to investigate the up-scaling potential for manufacturing CNT-based IEAP actuator electrodes and separators. Despite its complex and costly process infrastructure, slot-die coating has emerged as the method of choice for printing functional layers. It achieved the most homogeneous film

thickness distribution and showed the highest industrialization and up-scaling potential. Furthermore it caused the highest reproducibility of actuator performance compared to the other printing methods which was partly an effect of intense post-dispersion of the electrode slurry inside the printing equipment on its way to the slot-die nozzle. Using the semi-automated discontinuous slot-die coating machine Easycoater EC-63 the author has repeatedly and successfully produced large-scale electrode sheets and multi-layer actuator composites of size DIN-A4 and larger.

In terms of actuator assembly, two distinct approaches of making multiple actuators from large-scale printed electrodes have been described and analyzed. In the cutting-fusing approach, the fragmentation of the large printed electrode films into smaller electrode and separator pieces precedes the process of bonding the pieces together to make individual actuators. The fusing-cutting approach starts with the fusion of large electrode and separator films before the laminates are sliced into the required smaller pieces. The first method has the advantage that electric contacts can be firmly embedded into the small pieces during the heat pressing step, the second method is faster but allows only external means of electric contacts such as clamping or gluing.

A variety of different contact materials have been experimentally tested. Silver-plated conductive yarn proved to be the most flexible material and was easy to integrate into thin-film electrodes. Its small cross-sectional dimensions and low electrical resistance per unit length make it easily compatible with conventional power and control cables. Furthermore, it is resilient against oxidation and relatively stable in the presence of aggressive ionic liquids.

Investigations on thin PVDF coatings made via dip-coating for actuator encapsulation have revealed that the thin layers have a good adhesion to the matrix material and at least slow down the penetration of water or water vapor into the electrochemically active layers of the actuators (and sensors). An expected performance degradation of an actuator (tip to tip displacement) of around 20% per additional layer was observed, depending on the layer thickness.

5 Validation – Experimental Demonstrators

This chapter provides conceptual and experimental results regarding the integration of ionic electroactive polymer actuators and sensors into fabric membranes. The ultimate goal was to examine the practicality of such devices to be employed as motoric control elements in adaptive membrane building skins. Two potential functionalities are investigated: first, a means of ventilation control and humidity regulation by implanting small, actuated apertures into a fabric membrane, and second, an external load monitoring functionality via flexible, energy- and cost-efficient distributed IEAP sensors.

In the first subchapter, a simulation-assisted design method is introduced that was employed to yield viable information about the deformation kinematics of freely movable and constrained IEAP actuators that are firmly attached to thin and flexible fabric structures.

The second subchapter focusses on designing, building and testing two experimental membrane demonstrators with integrated polymer actuators and sensors.

The third subchapter discusses the test results, addresses the challenges encountered and draws conclusions for potential future optimization at the device and system level.

5.1 Simulation of aperture and actuator deformation

The finite element method (FEM) is a widely used engineering tool for solving complex problems in the fields of structural mechanics, heat transfer analysis and computational fluid dynamics. In this thesis, FEM was utilized to simulate the deformation kinematics of individually shaped IEAP actuators and arrays. It was regarded as particularly useful to predict their generated forces and displacements when attached to flexible tensioned membrane structures.

5.1.1 FEM simulation of CNT actuator deformation kinematics

Using ANSYS Workbench, the actuation of a virtually designed tri-layer CNT actuator was initiated by a thermal load assigned to the electric contacts of the actuator. It caused the actuator electrodes to expand and shrink, respectively, due to different thermal expansion coefficients assigned to the two electrodes (Addinall et al. 2014). By matching the thermal conductivity parameters of the electrode material with measured deformation data from real-world rectangular bending actuators, a realistic simulation model could be obtained that was able to predict the motion kinematics of any actuator shape.

A transient thermal FEM simulation was performed that took into consideration the transmission-line effect, which attributes for the slower actuation of actuator regions more distant to the area of electric contact. Figure 63 shows the virtual heat flux density on a virtually clamped CNT actuator. The virtual heat flux density actually indicates the charge density within the actuator electrode, thus the color code exemplifies the gradual decrease in charge density towards the free end of the actuator.

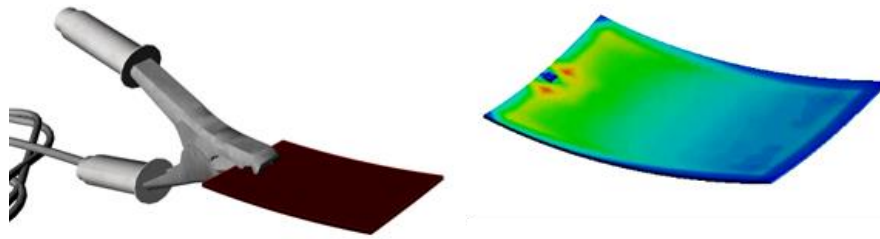


Figure 63 – Simulation of the bimorph bending kinematics of a clamped tri-layer IEAP actuator. (Illustration: Raphael Neuhaus, IFF 2019 / Nima Zahiri, IFF/BioMat 2019)

5.1.2 Evaluation of aperture actuation kinematics

The main simulation target was to find suitable arrangements, sizes and shapes of IEAP actuators that produce the largest ratio of projected opening area per membrane area occupied by the actuator arrangement. There are many possibilities to create controllable apertures in tensioned membrane surfaces using soft bimorph bending actuators. Depending on their shape, their mechanical attachment to the membrane and their power capabilities, different deformation characteristics can be achieved. It was generally assumed that the passage of air should be permitted in the actuated state (open) and blocked in the non-actuated state (closed). The process of opening ought to be performed by applying a voltage of certain polarity to the actuator while the process of closing ought to be accomplished (or assisted) by switching to the opposite polarity.

Apertures can be created by widening slots that were originally closed, lifting flaps that were flush with the surrounding surface or by bending formerly plain strips covering a hole in the membrane surface. Figure 64 shows a variety of potential motion principles that could be accomplished with IEAP bending actuators. The depicted shape-changing surface elements can either consist of thin IEAP actuators themselves or they are a passive flexible material (possibly the same material as the membrane) and their deformation is induced by buckling, bending or twisting motions of IEAPs attached underneath. Some of the geometric patterns could also be used for sensing differences in air pressure produced by wind loads onto the membrane.

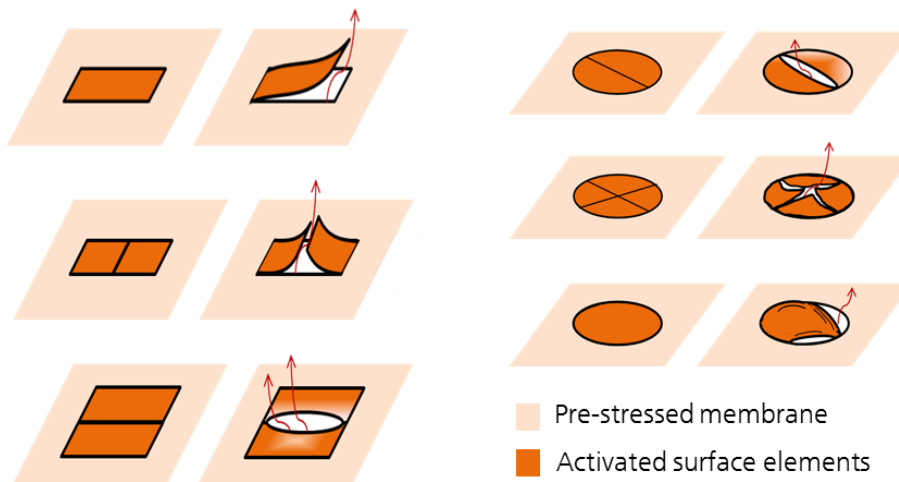
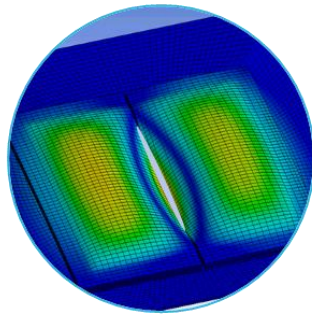


Figure 64 – Motion principles for controllable apertures in pre-stressed membrane structures made of thin and flexible soft actuators (Illustration: Raphael Neuhaus, IFF 2017)

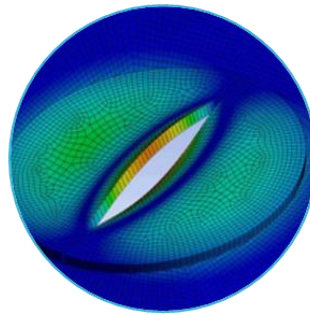
The actual number of adaptive apertures needed per total membrane area depends on the climatic conditions of the target building and other construction settings such as the façade orientation, the volume of the interstitial membrane space and desired thermal insulation properties.

As a result of the analysis, several actuator shapes and deformation kinematics materialized as viable configurations for the proposed application scenarios. The most efficient aperture configuration yielding the largest projected opening area was found to be the forced out-of-plane deflection of passive flaps being bent by soft actuators attached to their lower surface (passive flap cantilever actuator, Figure 65). The aperture configuration with the least out-of-plane motion and yet considerable opening characteristics was found to be a slit expansion generated by two counteracting actuators positioned underneath the edges of the slit. Initial plans to utilize the actuators themselves as opening flaps or slit generators were discarded in view of the much larger actuator sizes required (see also Figure 69), rendering their higher material costs and energy demand inefficient.



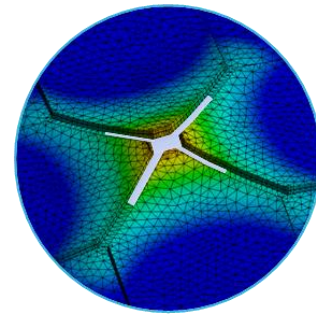
Rectangular
double-
actuator slit

- + Strong forces
- + Little out-of-plane deformation
- Triple-edge membrane attachment → strong deformation constrain
- Small opening area
- No force-supported closing → air gap



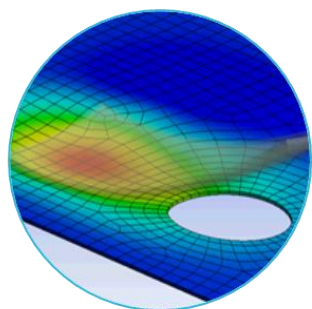
Counteracting
round double-
actuator slit

- + Strong forces
- + Little out-of-plane deformation
- o Medium opening area
- Circular membrane attachment → strong deformation constrain
- No force-supported closing → air gap



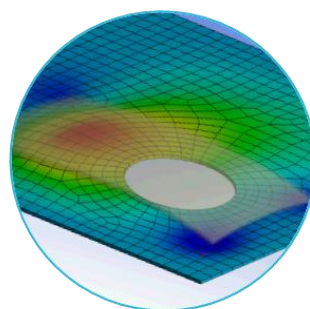
Triangular
multi-actuator
configuration

- + Strong forces
- o Medium opening area
- Complex electric contacts due to multiple actuators
- Asynchronous deformation
- No force-supported closing → air gap



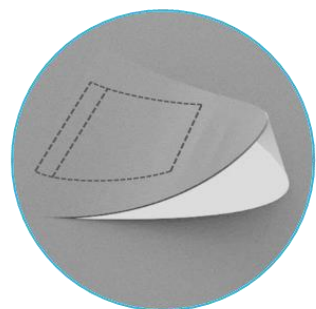
Lifting
cantilever
actuator

- + Single edge membrane attachment
- + large displacement & opening area
- + Force-supported closing
- + Sensor capability
- Large out-of-plane deformation
- Small forces



Buckling
cantilever
actuator

- + Small out-of-plane deformation
- + Single edge membrane attachment
- + Strong membrane counterforces
- Low deformation
- Low sensor capability
- Small forces



Passive flap
cantilever
actuator

- + Large opening area
- + Force-supported closing
- + Sensor capability
- + Simple integration
- Large out-of-plane deformation

Figure 65 – Kinematic simulations of apertures generated by IEAP actuators attached to pre-stressed membranes (Simulation & screenshots: Raphael Neuhaus, IFF 2017)

5.2 Demonstrator design and manufacturing

This subsection describes the materials, techniques and manufacturing procedures that were used to build the physical demonstrators. The principal considerations and first implementations and evaluations of functional models for controllable apertures have been published by the author (Neuhaus et al. 2019a). Most of the design and manufacturing activities described in this section were supported by the Institute for Computational Design and Construction (ICD) of the University of Stuttgart. The author wants to thank Nima Zahiri for his work, whom he supervised in the process of preparing his master thesis (Zahiri 2019).

5.2.1 Demonstrator design

Two demonstrators were designed to investigate the actuation and sensing behavior of IEAPs integrated into a fabric membrane skin. The first demonstrator comprises a double-curved multilayer membrane with controllable apertures in the inner layer. These apertures allow for controlled ventilation of the interstitial space between the two layers and thus prevent the necessity of mechanical air blowers currently employed to avoid condensation. This setup represents a new approach to accomplish switchable breathability in building skins. The reason for the targeted double curvature was to demonstrate the potential of soft IEAP actuators being employed despite complex membrane shapes and in the presence of multilateral tensile forces. A rhomboid-shaped fabric with four equally dished edges was chosen because it permits the creation of a double curvature by pulling apart the two pairs of opposite corners, each with divergent vertical components. In this pre-stressed double-curved state, all apertures in the fabric must remain closed when they are not actuated. One solution is to orientate linear slit cuts in the direction of the main flux of forces within the fabric so that lateral forces are minimized and the edges of each slit are not pulled apart. The stress distribution was analyzed using parameterized geomet-

ric models compiled in Karamba3D and running optimization algorithms regarding the positioning and orientation of the slit cuts. Karamba3D is a parametric structural engineering tool (Preisinger 2019) that can run optimization loops on mechanical problems by changing structural parameters such as material thicknesses, cross-sections, numbers of load-bearing elements and spacing and positioning of these elements within given boundary conditions for internal stresses, strains and structural dimensions. It also proposes auxiliary construction measures if the solution space within a constrained approximation loop is empty. The objective of the optimization for this project was to fill the available fabric area with fifty apertures per square meter that preferably are evenly spaced, translating to twenty properly oriented slit cuts that had to be distributed evenly on the fabric's surface of approximately 0.45 square meters. Additionally, the routing design of the conductive pathways powering the apertures should have minimal length and run either parallel or perpendicular to the local main flux of forces to minimize cable distortion and seam failure when the membrane is stretched into a 3D shape. Another aim of an optimized routing pattern was to have two spatially separated connection areas on the demonstrator membrane, each one collecting all conductive pathways of the same polarity. This arrangement prevents the complex routing patterns that would emerge if each actuator's electric connections had individually separated access points. Furthermore, separated connection areas make it easier to attach electronic control units to power the individual actuators (or to monitor the sensor signals, respectively). Some actuators are connected individually and others are combined into actuator clusters with a single pair of electric connections. A change in routing patterns can easily be implemented due to digital design methods that allow a straightforward transfer to automated fabrication techniques. The conceptual design approach of actuator integration and distribution is depicted in Figure 64 for both demonstrators. The opening of the slit cut will be triggered by one actuator positioned on each side of a slit cut, one bending upwards and one downwards. Due to their flexibility, the actuators will adapt to the local curvature of the membrane fabric without losing their motoric functionality.

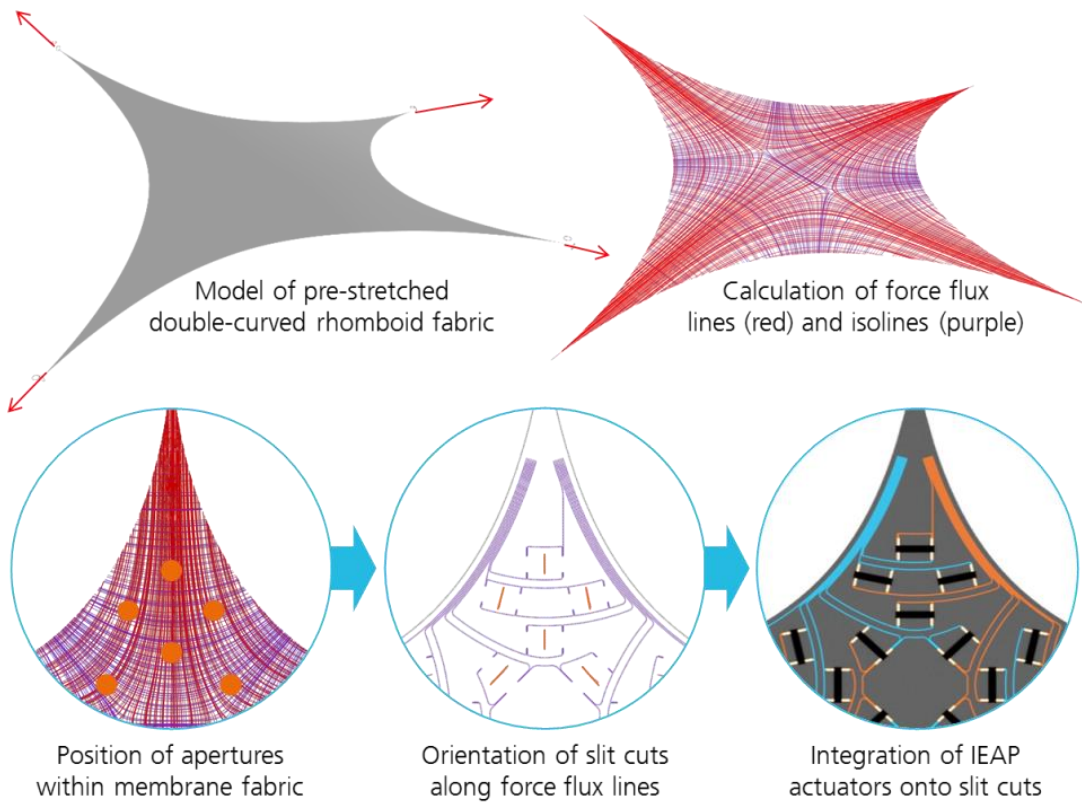


Figure 66 – Simulation assisted demonstrator design . Methodical approach towards optimized positioning and orientation of actuated slit cuts and integration of stretch-resistant conductive pathways. (Illustrations adapted with permission from Zahiri, IFF/BioMat 2019)

The second demonstrator will show both actuator and sensor functionalities in a single planar membrane. Parabola-shaped passive flaps are intended to deflect outwards when the IEAP actuator mounted underneath creates a bending movement. Under wind loads, the flaps should deflect inwards and provide an electrical signal that can be processed by an electronic monitoring and control unit. 17 flap cuts with three different sizes are distributed in a regular pattern on the fabric surface.

The conceptual design approach of actuator integration and distribution is depicted in Figure 67 for both demonstrators.

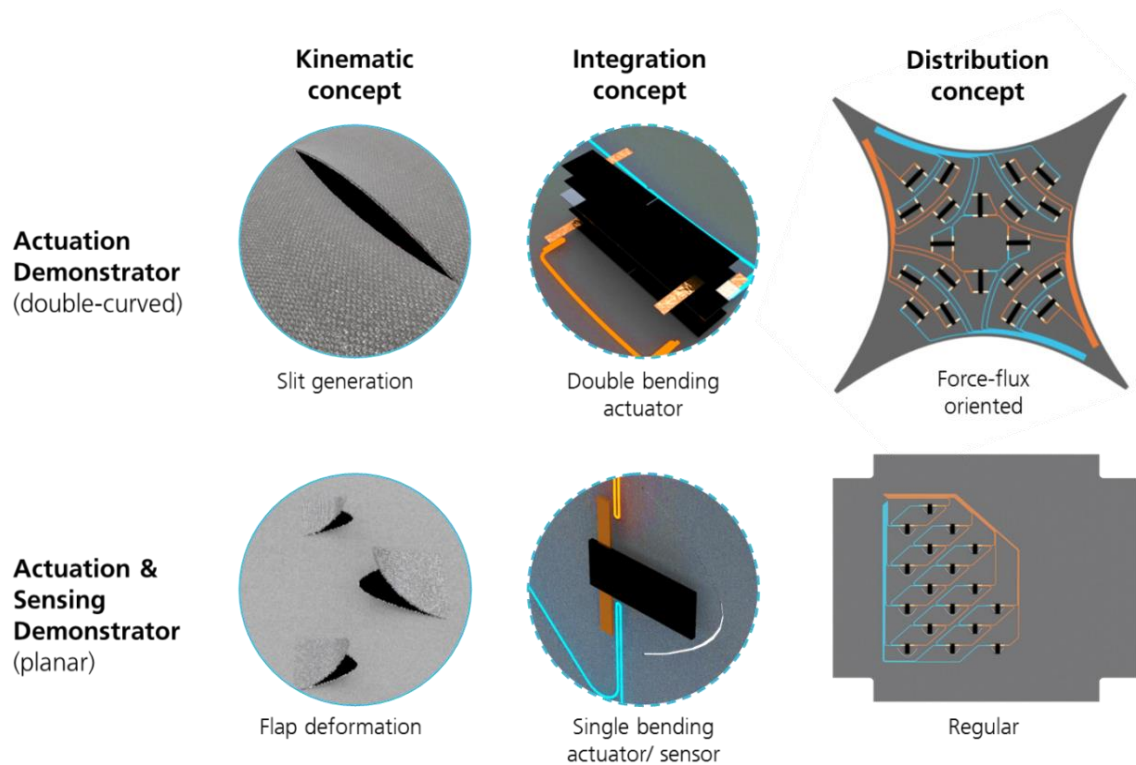


Figure 67 – Concepts for IEAP integration and distribution for an actuation-only demonstrator and an actuation & sensing demonstrator. The orange and blue lines indicate the placement of the electric power distribution (Illustration: Raphael Neuhaus, IFF 2019, adapted with permission from Zahiri, IFF/BioMat 2019).

5.2.2 Preparation of textile membrane fabric

For the demonstrator membrane material, a grey-colored high-strength polymeric fabric made of 47% polyester, 39% polyurethane and 14% polyamide was purchased from Tolko Stoffe GmbH in Germany. The fabric contains two thin layers of a waterproof Gore-Tex membrane (expanded Polytetrafluoroethylene - ePTFE) and is fitted with interwoven rip-stop reinforcement threads in a crosshatch pattern making it highly resistant to tearing and ripping. This fabric was used for both demonstrators.

By employing the same automated methods for the two fabric membranes, they were fitted with electric conductors for power distribution and received their individual patterns of aperture cuts. The conductive pathways were formed by the same conductive threads that were previously tested for the integrated IEAP contacts (Madeira HC 12 silver-plated

conductive thread). Following the pre-designed electric routing pattern, the threads were attached onto the fabric using a fully automated Tailored Fiber Placement (TFP) machine (Tajima 4-head embroidery machine). In this process, the thicker conductor thread is uncoiled from the reel and placed onto the fabric by a cantilever which is attached to the machine's moving stitching head. Simultaneously, a thin auxiliary thread is alternately stitched over the conductor thread locking it firmly into place onto the fabric underneath. This stitching process proved to be a simple and effective method to generate arbitrary yet precise conductive pathways on any fabric surface.

The aperture cuts were made with a fully automated digital 2-axis multi-ply cutting machine (Assyst Bullmer Premiumcut ST). Via software interface, it was possible to automatically assign the cutting patterns that were developed during the design stage to the machine's itinerary and transfer them onto the membrane fabric. Figure 68 illustrates the automated manufacturing steps for the first demonstrator and the resulting membrane fabric equipped with conductive pathways, actuator attachment points and integrated slit cuts.

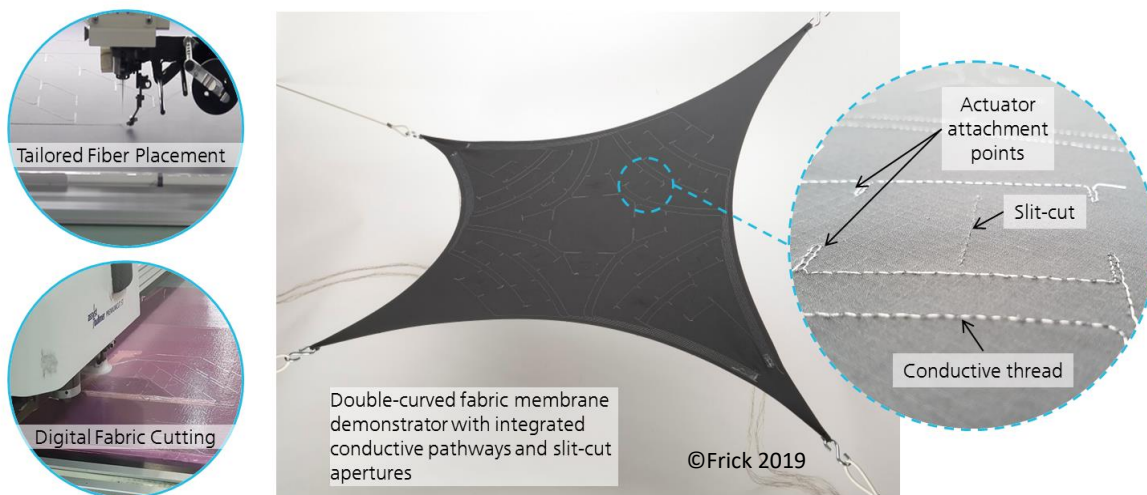


Figure 68 – Automated membrane fabric preparation: Fully automatized manufacturing processes for conductor thread integration (Tailored Fiber Placement) and patterned cutting of pre-designed apertures (Digital Fabric Cutting System). (Round pictures: Nima Zahiri, IFF/BioMat 2019)

5.2.3 Actuator integration

Before turning to the actual demonstrators for IEAP integration, lab-scale tests with individual actuator geometries, aperture designs and electrical connection alternatives were performed (Figure 69). Initially, the focus was on integrating rectangular non-encapsulated CNT actuators with no external electric contacts by using conductive epoxy glue applied to the electrode surfaces. The solvent-based glue, despite its low contact resistance, diffused into the fabric and beyond the intended attachment area during pressure-assisted curing and in many cases caused a short circuit between the two actuator electrodes. Tests with encapsulated and thread-contacted specimens showed no short circuit, but their electrical connection to the conductive pathways is only feasible by manually knotting the threads together. The most simple and robust integration method found was to apply the copper adhesive contact tapes to the provided conductor threads stitched into the fabric. The positive connection between the fabric and the actuator surface was ensured by a thin layer of double-sided adhesive tape. 40 equally shaped CNT actuators for 20 distributed apertures were integrated into the rhomboid-shaped membrane fabric of the first demonstrator. 17 actuators having the same size completed the second demonstrator with its 17 parabola-shaped flaps of three different sizes. The first demonstrator has a diagonal span of 110 mm. The second demonstrator has a width of 600 mm and a length of 800 mm. Both demonstrators – equipped with integrated IEAP actuators – are depicted in Figure 70.



Figure 69 – Illustration examples of IEAP actuator/sensor integration.
(Pictures: Nima Zahiri, IFF/BioMat 2019, edited by Raphael Neuhaus, IFF 2020)

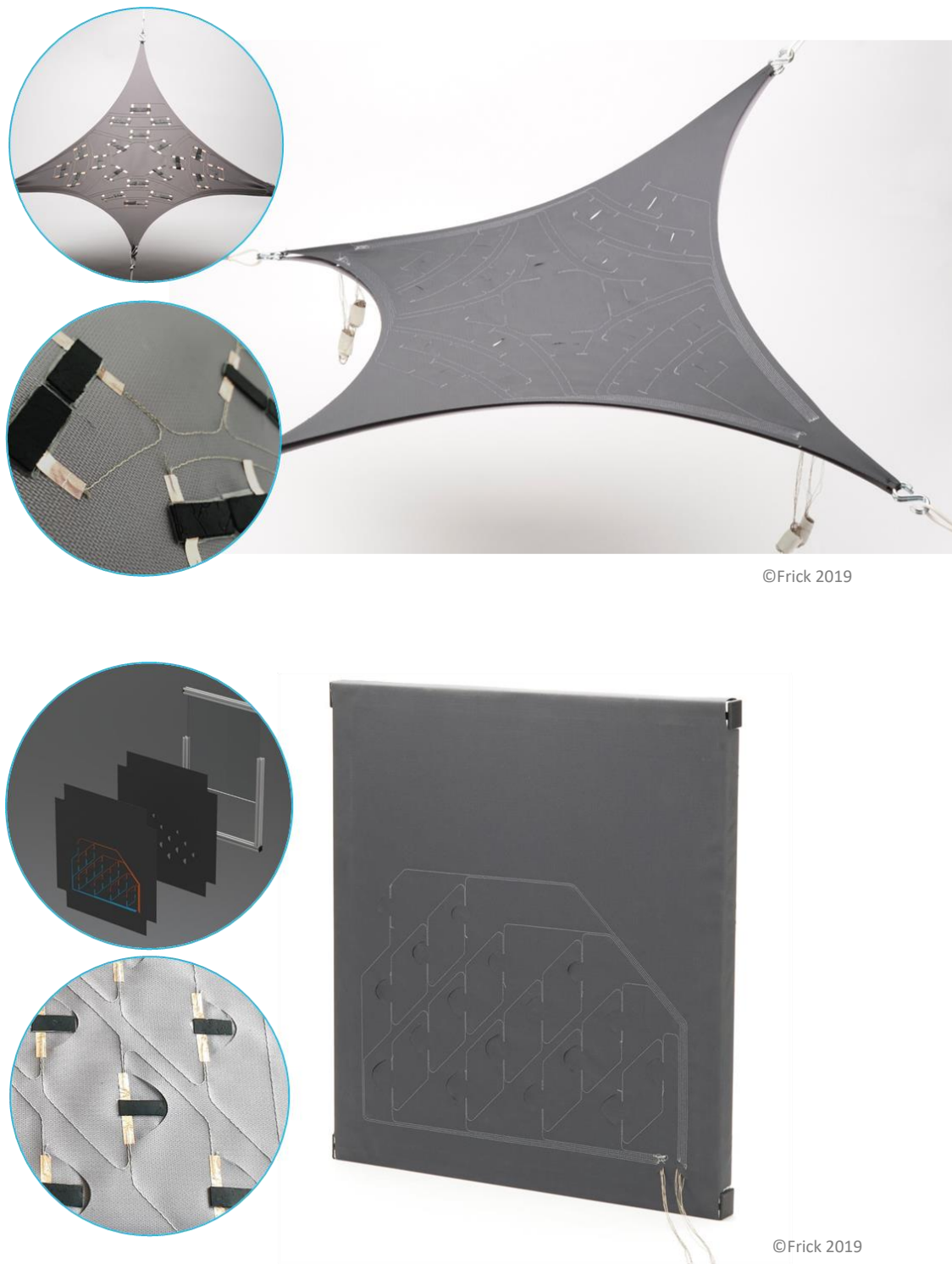


Figure 70 – Final demonstrators: Double-curved 2-layer membrane element with controllable apertures actuated by CNT actuators (top). Planar membrane demonstrator with controllable flaps having both actuator and sensor functionalities through integrated CNT actuators (bottom). (round pictures: Nima Zahiri, IFF/Biomat 2019, edited by Raphael Neuhaus, IFF 2020)

5.3 Experimental test results and evaluation

The displacement and blocking force of all actuators were measured using the LabVIEW-controlled automated test setup before they were integrated into the demonstrators. All actuators produced for both demonstrators had a default length of 2.5 cm, a width of 1 cm and a thickness of 300 - 400 μm . The measured displacement values were converted into induced bending strain values following equation (1). Out of more than 100 actuator samples made, only those that yielded reproducible bending strains between 0.8% and 1.2% and blocking forces between 10.5 mN and 21.5 mN were selected. These results were obtained with an applied square wave voltage of 2.5 V and 0.05 Hz actuation frequency. The blocking forces were measured at 10 mm distance from the clamping (electric contact area). Due to encapsulation, these performance values were considerably lower compared to those of non-encapsulated printed actuators (1.4% and up to 32 mN, respectively). The results have also been published by the author (Neuhaus et al. 2020).

5.3.1 Test setup and procedure

For measuring the actuation performance of the integrated actuators, the pairs of conductor threads leading to the distributed apertures were connected one by one to an adjustable power source. Due to the varying length of the conductor threads and the high contact resistances at the actuator interfaces, it was necessary to adjust the applied voltage levels to much higher values for the actuators to react. For the double-curved demonstrator, the maximum opening distance of the slit-cuts was measured at the actuation peak. For the flap demonstrator, the maximum tip deflection was measured.

On behalf of testing the sensing capabilities of the IEAPs integrated into the second demonstrator, the loose ends of all conductor threads leading to the distributed flaps were connected to the channels of a high-precision galvanostat/potentiostat analysis device (Ivium Octostat 5000) with low current and low voltage measurement capability. With the voltage range set to 10 mV and 500 Hz sampling rate, it is possible to detect and measure very low potential differences as low as 0.01 mV with a sufficient time resolution required to resolve

high-frequency phenomena during sensitivity testing. Two different test scenarios were performed.

In a first scenario, the flap was subject to a smooth and controlled alternating displacement in both inward and outward direction. The displacement and output signal were simultaneously measured. According to Kamamichi et al. 2007 (Kamamichi et al. 2007) a small voltage should be measured as an output signal which is expected to have almost proportional values to the displacement of the IEAP sensor. In a second scenario, a sudden forced displacement of rectangular pattern was applied to the tip of a sensing flap resting in a neutral position (flush with the membrane surface). This pulsed stimulus was repeated irregularly over a 50 second period and varying holding durations. The voltage response signals of both scenarios are depicted in Figure 72 in the results section.

5.3.2 Actuation properties of integrated IEAPs

To counteract the low thread conductivities and high contact resistances in both demonstrators, the square wave voltage levels applied to the individual conductive pathways were slowly increased in a cautious approach of 5 V steps. Every test was conducted twice, first maintaining the testing frequency of 0.05 Hz and second holding the voltage levels at constant polarity until no further reaction could be detected. For the double-curved demonstrator, no displacement response of any IEAP actuator was observed below 10 V. At 15 V some membrane deformation was visible around individual slits, but only at 20 V a true separation of the first slit edges could be identified. The maximum slit opening distance obtained was 3.2 mm at 35 V for one aperture, measured between the highest and the lowest point of the upward and downward bending slit edge, respectively. 11 actuators out of 40 did not perform any bending motion. Out of 20 apertures, only 12 generated true openings, most of which did not exceed a maximum opening distance of 2.0 mm even at higher voltage levels. Figure 71 shows a slit cut aperture generating a gap of 1.8 mm upon polarity switching of ± 20 V.

The same procedure was applied to the second demonstrator with passive flaps. Here again, the first out-of-plane flap deformations were observed at 15 V with no actual separation of the flap from the membrane surface. At the 20 V level six out of 17 flaps produced small openings allowing for air to pass through the membrane while at 30 V all flaps but one visibly bent out of the surface with tip deflections of between 2.1 mm and 3.4 mm. The highest tip deflection of 4.6 mm was measured at 40 V applied to one of the larger flaps located close to the voltage source connector. Some flaps showed a strong bending curvature but did not open because the edges of the parabola-shaped cuts in the fabric did not separate due to friction. Upon switching the polarity all previously deformed IEAPs performed a reverse closing motion until they passed the neutral position flush with the membrane surface. Figure 71 shows the actuation behavior of a medium-sized flap at different voltage levels applied to the conductive pathways, generating a 2.9 mm tip deflection at 30 V.

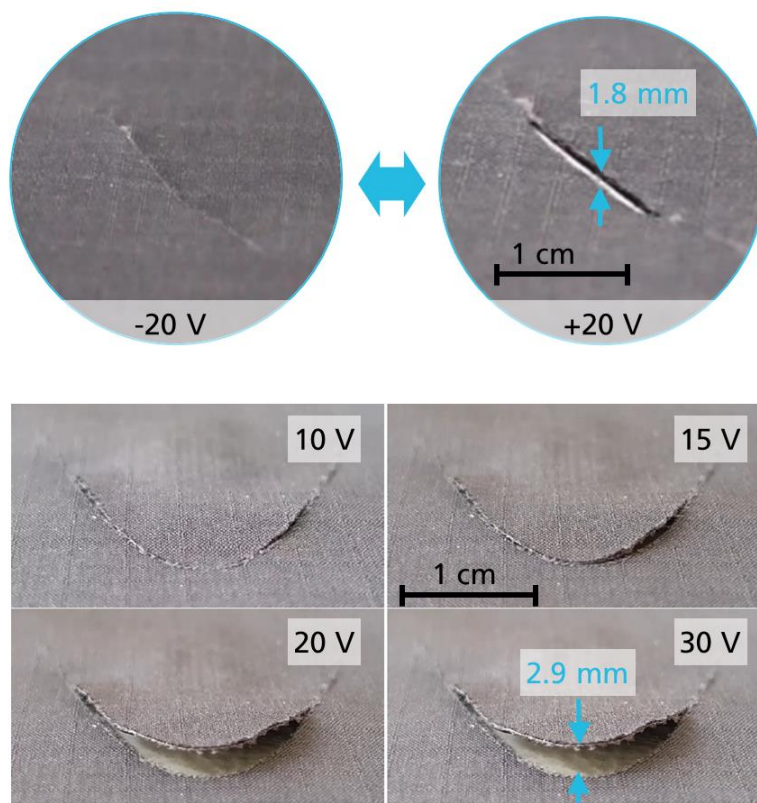


Figure 71 – Examples of successfully controlled membrane apertures in the double-curved slit cut demonstrator (top) and the planar flap cut demonstrator (bottom).

(Pictures: Nima Zahiri, IFF/BioMat 2019, edited with permission by Raphael Neuhaus, IFF 2019)

The general actuation behavior of integrated CNT actuators corresponds with the predicted actuation kinematics obtained via simulations. However, for the slit-cut apertures of the first demonstrator, their overall performance fell short of expectations, and especially the number of dysfunctional actuators came as a surprise.

The causes of failure are manifold and range from electrode contacts detaching during the first operation cycle, electrode delamination and actuator deterioration due to electric hot spots within the electrode structure all the way to the diffusion of heated electrolyte into the contacting threads and short circuits induced by manual handling and integration of actuators. Some of these phenomena such as hot spot generation are well-known from laboratory-scale prototypes and have been reported elsewhere. Other failure phenomena such as diffusion of heated ionic liquid into conductors are specific to this project and – to the best of the author’s knowledge – were encountered for the first time. Regarding actuators that failed during the first operation cycle, the high voltage levels applied to overcome the high contact and line resistances of the conductive pathways proved to be detrimental for some of the actuators. The voltage drop over line and contact resistances is proportional to the electric current flowing through the circuit (and thus through the actuator). Similar to charging a supercapacitor, the initial charging current will quickly decrease as electrochemical double layers form within the actuator electrodes. This decrease in current will cause a smaller voltage drop and consequently much higher given voltage levels at the actuator. Ultimately the voltage level will be much higher than the electrochemical potential window of the ionic liquid permits. Even though the given voltage levels were reduced manually during the actuation period, some actuators were destroyed by overvoltage before any deformation could be observed.

5.3.3 Sensing properties of integrated IEAPs

The scenario with a smooth displacement exerted on the membrane flaps with IEAPs attached underneath triggers a voltage signal that is almost perfectly proportional to the displacement, with only minor latency. The output signal is depicted in Figure 72 and goes

well in line with published findings (Kamamichi et al. 2007). During the short holding intervals and at neutral displacement position the signal appears more rugged than during the active shifting periods. Furthermore, at the neutral position the signal offset increases as it appears to react with a shallower relaxation towards charge equilibrium. This proves that the electrochemical reactions within the IEAP react to the stop of motion in almost real time. The highest measured voltage levels obtained with this test did not exceed 0.1 V for an outward deflection of 4 mm and -0.2 V for an inward deflection of 8 mm. In general, sensors with longer conductive pathways transmitted lower voltage signals compared to sensors closer to the connectors of the measurement device. When they are connected with high-resistance conductive pathways, the increased voltage drop must be taken into consideration for the design and calibration of such membrane sensors.

The forced impact scenario depicted in Figure 72 triggers a sharp voltage rise of up to 1 mV at the beginning of the mechanical impacts, followed by a jagged holding period that ends with another sharp spike when the impact stroke is released. After the spike, the voltage level asymptotically decreases as the flaps slowly relax back to their neutral position. Neither the impact stroke nor different holding periods seem to affect the slope of the relaxation curve. The relaxation curve shows about the same rate of decay for all performed impacts, even if the time intervals between impacts vary and one impact interrupts the relaxation phase of the previous impact. This is a sign of robust sensor functionality without hysteresis of such systems.

The proposed sensing functionalities of IEAPs integrated into membrane skins have been verified. Since the correlations between mechanical input and electric output are known and have now been confirmed, IEAPs might actually pose a viable alternative to other transducers, especially in areas where soft and flexible sensors have an advantage over their rigid and stiff counterparts, for example as health monitoring unit in soft membrane structures. Instead of employing high precision laboratory measurement equipment, it is often desirable to have compact analysis devices that are capable to measure and interpret the small voltage signals generated by deflected IEAPs. Field tests with optimized demonstrators exposed to real wind loads have yet to be conducted. A decline of the sensor functionality over longer operation periods will most likely occur and should be further investigated.

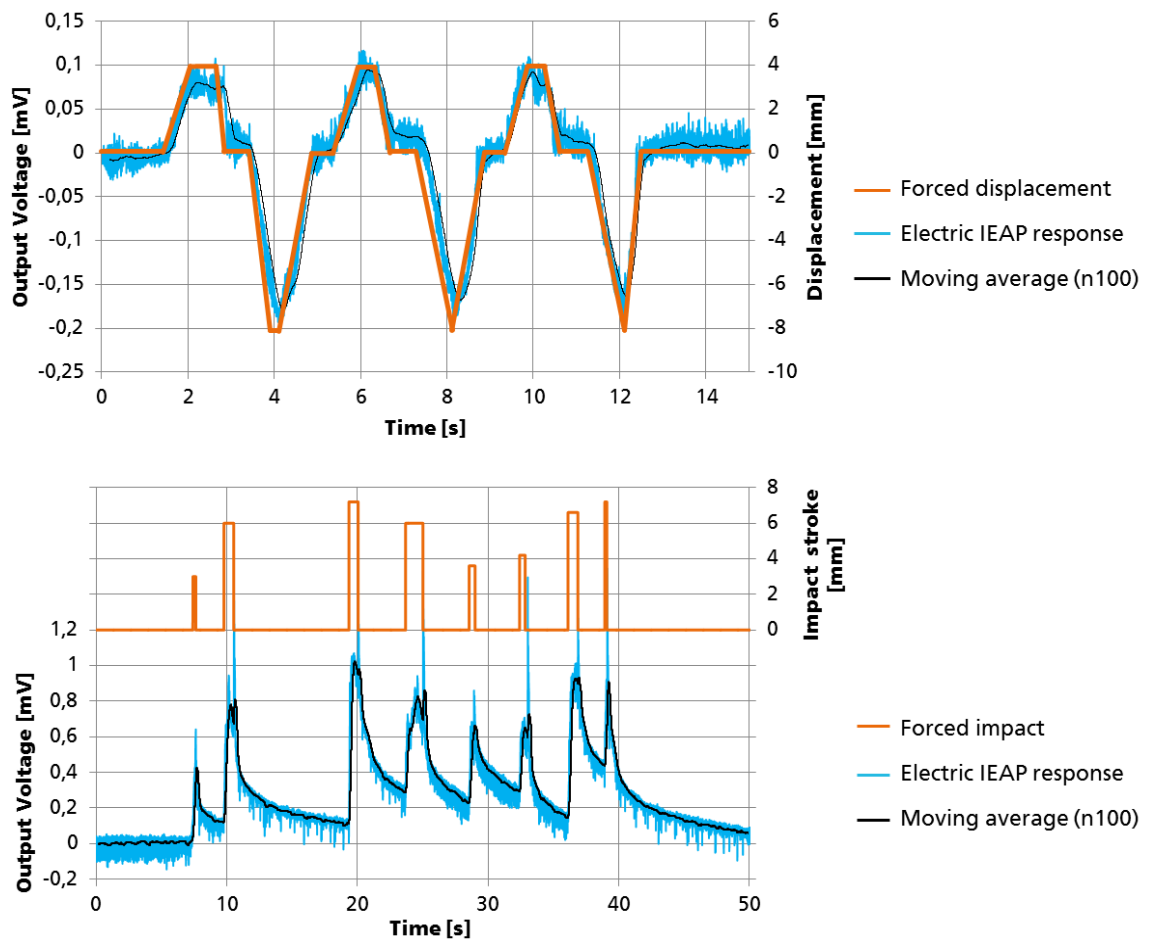


Figure 72 – Results of IEAP sensitivity tests. Voltage response obtained from the smooth forced flap displacement scenario with deflections in both inward and outward directions (top). Voltage response for forced impact and release scenario (bottom).

5.4 Power consumption and Life Cycle Assessment (LCA) of membrane elements with integrated CNT actuators

The environmental impact of an adaptive IEAP-enhanced building skin element has been analyzed by a “cradle to grave” LCA approach, taking into account all energy and materials needed during production, operation and end-of-life treatment. For all three stages, the cumulative energy demand (CED) and the carbon dioxide equivalent (CDE) were calculated and registered using the LCA software tool GaBi-ts 2019 from sphera™. The CDE describes the global warming potential (GWP) of the energy and materials released during the system’s life cycle and thus better reflects the environmental long-term effects of the proposed system. The calculation of CED and CDE was based on the German electricity mix in 2016 and is thus in accordance with reference scenarios recommended by the European Union.

The CED to produce such a system involves the whole inventory of materials and energy necessary for synthesis, dispersion and printing processes required to build the proposed components and structures. The amount of raw materials was calculated for a scenario with fifty actuators built into one square meter of fabric membrane, one actuator consisting of two electrodes and one electrolyte layer (separator), having total dimensions of 2.5 cm x 1.0 cm x 380 μm. For making one electrode, one needs 1.9 mg of NC7000™ MWCNTs, 8.6 mg of polyaniline, 13.7 mg of PVDF(HFP) backbone polymer, 20.8 mg ionic liquid BMI-BF₄, 1.075 g of 4M2P organic solvent, 0.2 g copper adhesive tape, 0.1 g silver-coated conductive thread and negligible amounts of dispersing agents. For making one separator, 18 mg of PVDF(HFP), 18 mg of BMI-BF₄ and 220 mg of 4M2P solvent are needed. Assumptions were made for the silver content of the conductive threads (10%), the exact material thickness of the fabric membrane’s top layer (50 μm) and the energy demand for the catalytic carbon vapor deposition (CCVD) process for synthesizing MWCNTs, which was interpolated from bibliographical references. All catalytic materials needed for the CCVD process such as cobalt, manganese and magnesium, however, were accurately taken into account. Furthermore, it was assumed that the full amount of solvent will evaporate into the air during the drying process after the electrode and separator layers are printed.

The calculation of the CED during system operation was based on the assumption of five actuation events with a determined holding period of 30 min per day, on average. Furthermore, a total of 8000 cycles was considered to be a realistic assessment of the actuator's capabilities, yielding a service life of 4.4 years. The energy needed for opening and closing procedures was calculated by the amount of charge inserted into one actuator. The opening and closing requires 4.78 Joules while the holding period requires 81 Joules, which accumulates to a total of 22.6 kJ per day and 8.26 MJ per year for the fifty actuators integrated into one square meter.

For the calculation of the CED for the end-of-life treatment, it was determined that all materials shall be classified as hazardous waste and be disposed accordingly. Considering the fact that carbon nanotubes are considered as potentially hazardous and that there are indications that some species of ionic liquid – even in rare circumstances – may recombine to neurotoxic substances, this assumption is justified.

The results of the LCA are given in Figure 73. For a realistic assessment of the true energy demand, the calculated CED values for the three stages of production, operation and end-of-life treatment were converted to total primary energy from non-renewable resources (PENRT) values. This was done considering a total energy conversion efficiency of 50% from the caloric energy content of the fuel to the energy output of the power plant. With this in mind, the physical unit of “mega Joules” (CED and PENRT) was converted into the more meaningful unit “kg CO₂ equivalents per square meter per year” (CDE and GWP) in consideration of the functional LCA unit being one square meter of membrane element per one year of operation for a total impact period of 100 years. The PENRT values are 47.94 MJ/m²a for production, 16.5 MJ/m²a for operation and 0.66 MJ/m²a for end-of-life treatment. The GWP values are 2.58 kg CO₂ eq./m²a for production, 1.34 kg CO₂ eq./m²a for operation and 0.21 kg CO₂ eq./m²a for end-of-life treatment.

CML2001 Global Warming Potential (GWP) [kg CO₂ equiv. / m²a]

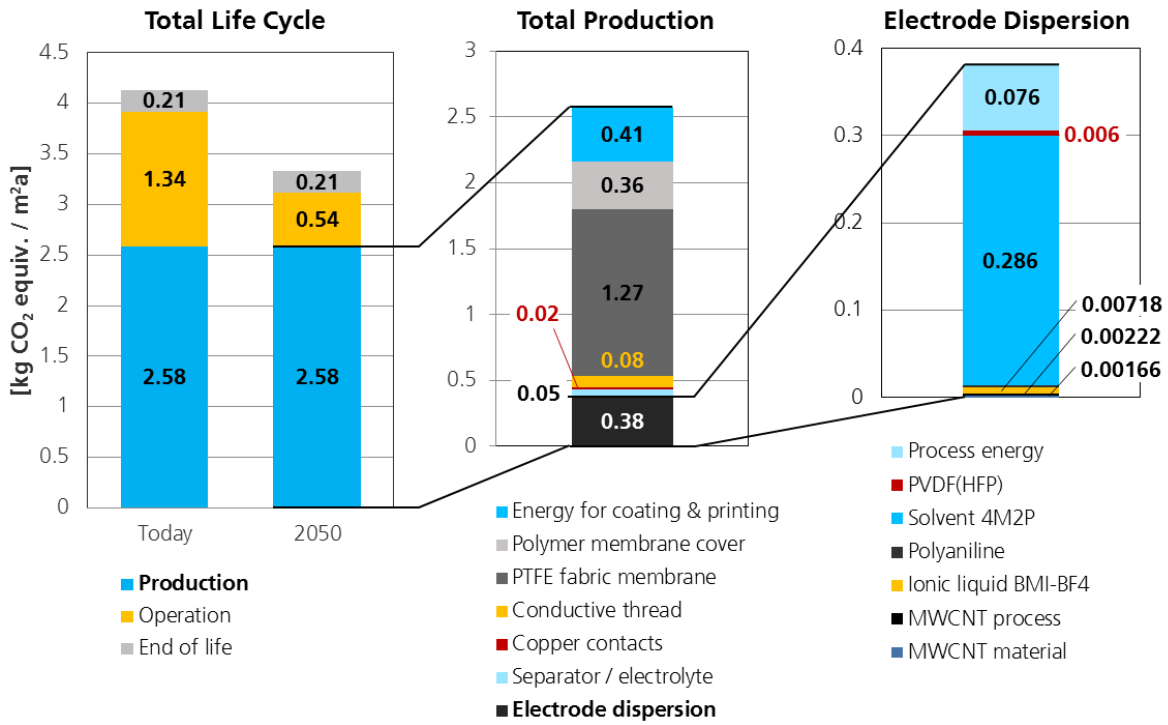


Figure 73 – Results of the Life Cycle Analysis (LCA) regarding the energy and material demand required for production, operation and end-of-life treatment of the assembled system. The diagrams show the global warming potential in kilograms of CO₂ equivalents per square meter IEAP-enhanced building skin per year.

6 Summary and Conclusion

This chapter completes this thesis, which envisioned exploring the potential of one specific type of electroactive polymer to be used as a soft and flexible actuator and sensor for adaptive building skins. The first section briefly summarizes the most important findings and results that were accomplished during the implementation stage described in chapter 4 and the validation stage described in chapter 5. The subsequent conclusion section includes a critical analysis of those results and provides a future outlook.

6.1 Summary of the most important results

In a holistic approach, the complete development chain of a CNT actuator application has been touched in this dissertation: from the selection of raw materials, benchmarking of IEAP technologies, optimization of dispersion and printing techniques, application-specific post-treatment of IEAPs, system integration methods and automated testing procedures. The initial focus of the performed work was to manufacture CNT actuator electrodes faster, cheaper and more reproducible compared to previously employed laboratory processes. An extensive DoE study returned an optimized material composition to produce electrodes with high internal bending strains and good performance reproducibility. Only scalable dispersion techniques such as ultrasonic homogenization and dissolver treatment were tested. The total duration of the dispersion preparation process was reduced from multiple days to less than two hours (see Table 22). This process acceleration, along with the time reduction for casting or printing of the electrode layers and subsequent air drying at room temperature, was achieved with no considerable performance loss. Besides these improvements, the employment of multi-walled carbon nanotubes has resulted in a material cost reduction of about 85% (Table 18) compared to single-walled carbon nanotube actuators. During this study, the reported strong influence of PANI on the actuators' bending displacement was confirmed. However, the investigation of various dispersing agents did not reveal

a strong impact on layer homogeneity or grain size distribution of the residual agglomerates and had no noteworthy effects on the actuator performance. For cast or printed electrode layers, it was observed that residual CNT agglomerates were present in every sample, regardless of the dispersion type or time. While short periods (ca. five minutes) of dissolver treatment has improved the viscosity values and caused slightly fewer agglomerates in the dispersion, three-roll-milling did not work at all because of rapid heat-inflicted solvent evaporation. The elimination of extremely toxic solvents such as DMAC was considered an absolute prerequisite for future market adoption and was successfully implemented.

One of the most important findings of this thesis is that automated printing processes may be suitable for the production of IEAP actuator components. Primarily the automated layer-by-layer slot-die printing process with the discontinuous coating machine EC 63 proved to be not only very time- and cost-efficient, but also very safe and potentially environmentally friendly. All hazardous solvent gases are contained within the explosion-proof printing chamber and can thus be recycled or discharged in a controlled fashion. Large-scale electrode and separator layers were printed quickly and safely, with easily controllable process settings for wet layer thicknesses and pumping speeds. In subsequent calendaring experiments,, it was discovered that the dried layers can be easily fused to form fully functional three-layer actuator laminates. Calendaring thus poses a scalable manufacturing technique that may reduce the manual workload in the future production of IEAP actuator components, without having compromising effects on their performance characteristics.

For facilitated system integration, embedded electric actuator connections were investigated. A double use of the hot press allowed for a firm and robust integration of copper tapes and silver-plated conductive threads into the actuator electrodes, both of which exhibited the lowest contact resistance and good handling characteristics. Both materials form a viable interface to any electrical supply lines in IEAP based actuator and sensor applications.

To provide a strong but flexible protection layer against mechanical forces and to protect the electrochemical processes from ambient humidity, the IEAP actuators and sensors were encapsulated with a thin layer of PVDF which was also used as matrix material for all

actuator layers. A simple and scalable dip-coating process was performed that resulted in a 20% loss of actuation performance regarding both force transmission and bending displacement. It also resulted in an extended cycle life when operated in both water and air.

To exemplify the integration of IEAP actuators and sensors into architectural membrane structures, two functional demonstrators were built and tested. These demonstrators were intended to showcase new functionalities for buildings such as switchable breathability, on-demand ventilation and humidity regulation, and external load detection. CNT-based IEAP actuators were fitted onto pre-stretched membrane fabrics to open and close individually controllable apertures. To some extent, automated fabrication methods were employed to produce the demonstrators. For example, automated cutting and stitching machines were used to make the apertures and the electrical supply lines that power the apertures. The simulation-assisted design approaches for the routing design comprised the evaluation of aperture actuation kinematics and the conceptual strategy for the positioning and distribution of the actuators.

The overall actuation performance fell short of the author's expectations in terms of actuator availability and performance. Due to the experimental character of the demonstrators, the proportion of dysfunctional or malfunctioning actuator samples exceeded 10% at all times. Furthermore, the maximum slit opening distance obtained was only 3.2 mm for the passive actuated flap demonstrator. High driving voltages of up to 30 V were needed to overcome the high contact and line resistances of the electrical supply line network. Even though the failure rate of integrated actuators has been high, the general feasibility, as well as a proof of function of an IEAP-driven building skin with switchable breathability, have been provided.

Looking at the sensor functionality of integrated IEAP, the electric feedback signals confirm a precise and reliable representation of mechanical impact forces. The proposed sensing functionalities of IEAPs integrated into membrane skins have thus been verified.

6.2 Conclusion

6.2.1 General reflection

This first-ever experimental approach of using IEAP technology in a building-related application has shown that a practicable and reliable integration of such complex electrochemical devices remains a challenge, particularly because their performance is still highly sensitive to many non-application-related factors. Material compositions, manufacturing techniques, auxiliary treatments and power controls have to be carefully designed and accurately tailored to yield desired performance characteristics in the first place. The main drawback of IEAPs is their generally weak force generation, which was again demonstrated by this research. Conventional hand-crafted CNT actuators with a length of 20 mm and a width of 10 mm have blocking forces of no more than 30 mN at a bending position 10 mm from the fixation point. The improvements achieved in performance reproducibility and manufacturability in this project, and particularly the additional encapsulation layers came at a cost of even lower bending forces which probably poses the greatest limitation for potential future applications.

When looking at different dispersion processes that have been examined in this thesis, it appears to be very difficult to obtain a truly homogeneous mixture of well-dispersed CNT agglomerates and bundles in a PVDF-4M2P solution. Seemingly, there is no clear trade-off between the duration of any chosen dispersion process and the achieved dispersion quality in terms of residual agglomerates. A much shorter process will never produce a very good dispersion but a sufficiently good one for the desired application scenario. This is the reason why such a tremendous reduction of the overall dispersion time was possible.

Overall, the results obtained for the actuation and sensing capabilities have demonstrated that it is principally possible to use IEAPs for generating controllable apertures in fabric tensile membranes. However, it requires further efforts of optimization to transfer the new discoveries to actual building envelopes.

6.2.2 Measures for future CNT actuator optimization and integration

It is essential to approach potential optimization measures concerning integrated IEAPs in two separate areas: actuator optimization and actuator integration. Regarding the actuator optimization, it is obvious that complex structures such as IEAP will not last forever, due to the decomposition of the polymer matrix and slow evaporation or leakage of electrolytes. As a result, the performance of IEAPs will in most cases decrease over time. The rate of performance drop depends mainly on the number of performed work cycles. This means that IEAPs need to be precisely tailored and optimized to fit their planned application scenario.

In regards to building applications, the hydrophilicity of the ionic liquids may cause performance degradation over time due to humidity inevitably entering the three-layer compound despite any encapsulation efforts. The ionic liquid BMI-BF₄ has been chosen for this project because it provides a wide operational temperature window suitable for building applications. However, other types of ionic liquid have shown greater electrochemical activity and faster ion exchange rates that are more suitable for applications requiring higher actuation displacements and speeds.

Optimization measures such as highly impermeable IEAPs encapsulations, force enhancement through actuator stacking and new electrochemically active nanomaterials and composites are currently explored by the author and other scientists. For operation in building-physical outdoor missions, UV stability is also a topic that still needs to be addressed. Another question that will arise in this context is whether IEAP actuators or sensors will be affected by particle contamination and acidic or basic soiling.

Regarding the actuator integration part, it is self-evident that conductive pathways with much higher electric conductivities are needed to power distributed actuators and sensors. The unpredictable contact resistances and low conductivities of the conductive threads

triggered inaccurate power settings for the connected IEAPs and resulted in unknown system states. It is essential to transfer sensor signals and electric power to the actuators more reliably and over much longer distances. Thin copper cables might be a solution with similar automatable handling characteristics (TFP). Furthermore, these conductors should have electrical insulation just as the copper tapes used for integrated electrode contacts in order to shield them from environmental influences. Concerning the parabola-shaped flaps in the second demonstrator, the friction between the edges needs to be reduced to allow for a smoother and unobstructed opening.

6.2.3 Outlook

The author of this thesis believes that the technical readiness of IEAPs is constantly improving and that more and more research related to macroscopic applications will emerge within the next few years. It is clear that efforts are intensified globally to exploit their unique characteristics and to experiment with them in different areas of technology. IEAP might have particularly high potential in areas where high forces are not required. Actuator arrays could be implemented for morphing indoor surfaces and structures, enabling novel ways of system interaction between users and technical appliances. For years car manufacturers and interior designers have been looking for soft materials that are capable of creating visual or haptic feedback via surface texturing. Once the accuracy and reliability have reached a sufficient state, these transducers may be employed in miniaturized high-precision applications such as optical systems, microscopic sample manipulation and biomedical use cases.

For sensor applications, IEAPs might actually pose a viable alternative to other transducers, especially in areas where soft and flexible sensors have an advantage over their rigid and stiff counterparts, for example as health monitoring units in soft membrane structures. The intrinsic sensor properties of IEAPs may promote intelligent fabrics in the field of textile engineering and wearables and provide integrated monitoring functionalities.

Investigations on building-related usability of IEAPs in general and CNT-based sensors and actuators in particular will be continued by the author. The interdisciplinary collaboration with architects, process engineers and experts in building physics resulted in a very fruitful and enriching scientific environment with much room for new ideas and great infrastructure for the development and testing of hardware. The author believes that he has contributed a small part to the accelerating real-world application and market adoption of IEAP.

7 Bibliography

- Abergel et al. 2017** Abergel, Thibaut; Dean, Brian; Dulac, John, 2017. *Towards a zero-emission, efficient, and resilient buildings and construction sector.* Global Status Report 2017. ISBN 978-92-807-3686-1
- Adamczewski 2008** Adamczewski, Piotr, 2008. *Hochhausfassaden aus Membranen: Untersuchung transparenter Folien als vorgespanntes Membrantragwerk bei Hochhausfassaden.* Berlin, TU, 2008
DOI: 10.14279/depositonce-1833
- Addinall et al. 2014** Addinall, Raphael; Sugino, Takushi; Neuhaus, Raphael; Kosidlo, Urszula; Tonner, Friedemann; Glanz, Carsten; Kolaric, Ivica; Bauernhansl, Thomas; Asaka, Kinji, 2014. Integration of CNT-based actuators for bio-medical applications — Example printed circuit board CNT actuator pipette. In: IEEE/ASME (Ed.). In: *International Conference on Advanced Intelligent Mechatronics*, Besacon, 08.07.2014 - 11.07.2014, pp. 1436–1441
DOI: 10.1109/AIM.2014.6878284
- Aelenei et al. 2016** Aelenei, Daniel; Aelenei, Laura; Vieira, Catarina Pacheco, 2016. Adaptive Façade: Concept, Applications, Research Questions. *Energy Procedia* **91**, pp. 269–275
DOI: 10.1016/j.egypro.2016.06.218
- Akita et al. 2002** Akita, Seiji; Nakayama, Yoshikazu, 2002. Manipulation of Nanomaterial by Carbon Nanotube Nanotweezers in Scanning Probe Microscope. *Japanese Journal of Applied Physics* **41** (Part 1, No. 6B), pp. 4242–4245
DOI: 10.1143/JJAP.41.4242
- Akle et al. 2007** Akle, Barbar; Nawshin, Saila; Leo, Donald, 2007. Reliability of high strain ionomeric polymer transducers fabricated using the direct assembly process. *Smart Materials and Structures* **16** (2), 256–261
DOI: 10.1088/0964-1726/16/2/S09
- Albag et al. 2020** Albag, Ofir; Anishchenko, Maria; Grassi, Giulia; Paoletti, Ingrid, 2020. Adaptive Skins: Towards New Material Systems. In: Daniotti, Bruno; Gianinetto, Marco; Della Torre, Stefano (Eds.): *Digital Transformation of the Design, Construction and Management Processes of the Built Environment*. Cham: Springer International Publishing, pp. 209–219
ISBN 978-3-030-33569-4
DOI: 10.1007/978-3-030-33570-0_19
- Andrew 2018** Andrew, Robbie M., 2018. Global CO₂ emissions from cement production, 1928–2017. *Earth System Science Data* **10** (4), pp. 2213–2239
DOI: 10.5194/essd-10-2213-2018
- Anquetil et al. 2004** Anquetil, Patrick A; Rinderknecht, Derek; Vandesteeg, Nathan A; Madden, John D; Hunter, Ian W., 2004. Large strain actuation in polypyrrole actuators. In: Bar-Cohen, Yoseph (Ed.). In: *Smart Structures and Materials 2004: Electroactive Polymer Actuators and Devices (EAPAD)*, San Diego, CA, Sunday 14 March 2004, p. 380
DOI: 10.1117/12.540141

- Arena et al. 2006** Arena, Paolo; Bonomo, Claudia; Fortuna, Luigi; Frasca, Mattia; Graziani, Salvatore, 2006. Design and control of an IPMC wormlike robot. *IEEE transactions on systems, man, and cybernetics. Part B, Cybernetics* **36** (5), pp. 1044–1052
DOI: 10.1109/TSMCB.2006.873188
- Attia et al. 2018** Attia, Shady; Bilir, Senem; Safy, Taha; Struck, Christian; Loonen, Roel; Goia, Francesco, 2018. Current trends and future challenges in the performance assessment of adaptive façade systems. *Energy and Buildings* **179**, pp. 165–182
DOI: 10.1016/j.enbuild.2018.09.017
- Bar-Cohen 2003** Bar-Cohen, Yoseph (Ed.), 2003. *Smart Structures and Materials 2003: Electroactive Polymer Actuators and Devices (EAPAD)*. San Diego, 2.3.2003–6.3.2003
- Barisci 2004** Barisci, Jose, 2004. Investigation of ionic liquids as electrolytes for carbon nanotube electrodes. *Electrochemistry Communications* **6** (1), pp. 22–27
DOI: 10.1016/j.elecom.2003.09.015
- Barisci et al. 2000** Barisci, Joseph N; Wallace, Gordon G; Baughman, Ray H., 2000. Electrochemical Characterization of Single-Walled Carbon Nanotube Electrodes. *Journal of The Electrochemical Society* **147** (12), p. 4580
DOI: 10.1149/1.1394104
- Baughman et al. 1999** Baughman, Cui; Zakhidov, Iqbal; Barisci, Spinks; Wallace, Mazzoldi; Rossi, D. de; Rinzler; Jaschinski; Roth; Kertesz, 1999. Carbon nanotube actuators. *Science (New York, N.Y.)* **284** (5418), pp. 1340–1344
DOI: 10.1126/science.284.5418.1340
- Bay et al. 2003** Bay, Lasse; West, Keld; Sommer-Larsen, Peter; Skaarup, Steen; Benslimane, Mohammed, 2003. A Conducting Polymer Artificial Muscle with 12 % Linear Strain. *Advanced Materials* **15** (4), pp. 310–313
DOI: 10.1002/adma.200390075
- Bennett et al. 2004** Bennett, Matthew D; Leo, Donald J., 2004. Ionic liquids as stable solvents for ionic polymer transducers. *Sensors and Actuators A: Physical* **115** (1), pp. 79–90
DOI: 10.1016/j.sna.2004.03.043
- Berardi 2010** Berardi, Umberto, 2010. Dielectric electroactive polymer applications in buildings. *Intelligent Buildings International* **2** (3), pp. 167–178
DOI: 10.3763/inbi.2010.0043
- Bhandari et al. 2012** Bhandari, Binayak; Lee, Gil-Yong; Ahn, Sung-Hoon, 2012. A review on IPMC material as actuators and sensors: Fabrications, characteristics and applications. *International Journal of Precision Engineering and Manufacturing* **13** (1), pp. 141–163
DOI: 10.1007/s12541-012-0020-8
- Biso et al. 2009** Biso, Maurizio; Ricci, Davide, 2009. Multi-walled carbon nanotubes plastic actuator. *physica status solidi (b)* **246** (11-12), pp. 2820–2823
DOI: 10.1002/pssb.200982282
- Biso et al. 2010** Biso, Maurizio; Ansaldo, Alberto; Futaba, Don N; Hata, Kenji; Ricci, Davide, 2010. Benchmarking bucky gel actuators: Chemically modified commercial carbon nanotubes versus super-growth carbon nanotubes. *physica status solidi (b)* **247** (11-12), pp. 3055–3058
DOI: 10.1002/pssb.201000214
- Biso et al. 2011** Biso, Maurizio; Ansaldo, Alberto; Futaba, Don N; Hata, Kenji; Ricci, Davide, 2011. Cross-linking super-growth carbon nanotubes to boost the performance of bucky gel actuators. *Carbon* **49** (7), pp. 2253–2257
DOI: 10.1016/j.carbon.2011.01.057
- Biso et al. 2012** Biso, Maurizio; Ansaldo, Alberto; Picardo, Elisa; Ricci, Davide, 2012. Increasing the maximum strain and efficiency of bucky gel actuators by pyrrole oxidative polymerization on carbon nanotubes dispersed in an ionic liquid. *Carbon* **50** (12), pp. 4506–4511
DOI: 10.1016/j.carbon.2012.05.032
- Bronikowski et al. 2001** Bronikowski, Michael J; Willis, Peter A; Colbert, Daniel T; Smith, K. A; Smalley, Richard E., 2001. Gas-phase production of carbon single-walled nanotubes from carbon monoxide via the HiPco process: A parametric study. *Journal of Vacuum Science & Technology A: Vacuum, Surfaces, and Films* **19** (4), pp. 1800–1805
DOI: 10.1116/1.1380721

- Bubak et al. 2014** Bubak, Grzegorz; Ceseracciu, Luca; Ansaldo, Alberto; Futaba, Don N; Hata, Kenji; Ricci, Davide, 2014.
Carbon nanotubes plastic actuator: Towards lightweight, low-voltage haptic devices.
In: *2014 IEEE Haptics Symposium (HAPTICS)*, Houston, TX, USA, 23.02.2014 - 26.02.2014, pp. 499–503
DOI: 10.1109/HAPTICS.2014.6775506
- Bubak et al. 2015** Bubak, Grzegorz; Ansaldo, Alberto; Gendron, David; Brayda, Luca; Ceseracciu, Luca; Ricci, Davide, 2015.
Parylene coated carbon nanotube actuators for tactile stimulation.
In: Bar-Cohen, Yoseph (Ed.).
In: *Electroactive Polymer Actuators and Devices (EAPAD) 2015*, San Diego, California, United States, 8.3.2015, 94300V
DOI: 10.1117/12.2084233
- Carpi et al. 2010** Carpi, F; Rossi, D. de, 2010.
Electroactive polymer artificial muscles: an overview.
In: Brebbia, C. A; Carpi, A. (Eds.). In: *Design and Nature V*, Pisa, Italy, 28.06.2010 - 30.06.2010, pp. 353–364
DOI: 10.2495/DN100311
- Chang et al. 2018** Chang, Longfei; Liu, Yanfa; Yang, Qian; Yu, Linfeng; Liu, Jiaqin; Zhu, Zicai; Lu, Pin; Wu, Yucheng; Hu, Ying, 2018. Ionic Electroactive Polymers Used in Bionic Robots: A Review.
Journal of Bionic Engineering **15** (5), pp. 765–782
DOI: 10.1007/s42235-018-0065-1
- Chen et al. 2010** Chen, Zheng; Shataru, S; Tan, Xiaobo, 2010. Modeling of Biomimetic Robotic Fish Propelled by An Ionic Polymer–Metal Composite Caudal Fin.
IEEE/ASME Transactions on Mechatronics **15** (3), pp. 448–459
DOI: 10.1109/TMECH.2009.2027812
- Cho et al. 2007** Cho, Misuk; Seo, Hyunjo; Nam, Jedo; Choi, Hyoukryeol; Koo, Jachoon; Lee, Youngkwan, 2007.
High ionic conductivity and mechanical strength of solid polymer electrolytes based on NBR/ionic liquid and its application to an electrochemical actuator.
Sensors and Actuators B: Chemical **128** (1), pp. 70–74
DOI: 10.1016/j.snb.2007.05.032
- RAC 2014** Committee for Risk Assessment, 2014.
Opinion proposing harmonised classification and labelling at EU level of N,N-Dimethylacetamide (DMAC): Helsinki
From: <https://www.echa.europa.eu/documents/10162/a435d3fc-a05f-b558-3f51-9aff166f2de0>
- Cremers et al. 2016** Cremers, Jan; Palla, Nansi; Buck, Doris; Beck, Andreas; Biesinger, Andreas; Brodkorb, Swen, 2016.
Analysis of a Translucent Insulated Triple-layer Membrane Roof for a Sport Centre in Germany.
Procedia Engineering **155**, pp. 38–46
DOI: 10.1016/j.proeng.2016.08.005
- Dewidar 2013** Dewidar, Khaled, 2013.
Living Skins: A New Concept of Self Active Building Envelope Regulating Systems.
In: *Sustainable Buildings Dubai: National Conference on Advancing the Green Agenda*. Dubai, [Seiten von–bis fehlt!]
- Dresselhaus et al. 1996** Dresselhaus, Mildred S; Dresselhaus, Gene; Eklund, Peter C., 1996.
Science of Fullerenes and Carbon Nanotubes: Their Properties and Applications.
1. Aufl.: Amsterdam. Elsevier professional.
ISBN 9780080540771
- Dresselhaus et al. 2001** Dresselhaus, Mildred S; Dresselhaus, Gene; Avouris, Phaedon, 2001.
Carbon Nanotubes: Synthesis, Structure, Properties, and Applications: Berlin, Heidelberg. Springer.
Topics in Applied Physics 80.
ISBN 978-3540410867
DOI: 10.1007/3-540-39947-X
- Dresselhaus et al. 2002** Dresselhaus, Mildred S; Dresselhaus, Gene, 2002. Intercalation compounds of graphite.
Advances in Physics **51** (1), pp. 1–186
DOI: 10.1080/00018730110113644
- Eatemadi et al. 2014** Eatemadi, Ali; Daraee, Hadis; Karimkhanloo, Hamzeh; Kouhi, Mohammad; Zarghami, Nosratollah; Akbarzadeh, Abolfazl; Abasi, Mozghan; Hanifehpour, Younes; Joo, Sang Woo, 2014. Carbon nanotubes: properties, synthesis, purification, and medical applications.
Nanoscale research letters **9** (1), p. 393
DOI: 10.1186/1556-276X-9-393

- Ebbesen et al. 1992 Ebbesen, T. W; Ajayan, P. M., 1992. Large-scale synthesis of carbon nanotubes. *Nature* **358** (6383), pp. 220–222
DOI: 10.1038/358220a0
- Fang et al. 2007 Fang, Bo-Kai; Ju, Ming-Shaung; Lin, Chou-Ching K., 2007. A new approach to develop ionic polymer–metal composites (IPMC) actuator: Fabrication and control for active catheter systems. *Sensors and Actuators A: Physical* **137** (2), pp. 321–329
DOI: 10.1016/j.sna.2007.03.024
- Fraysse et al. 2001 Fraysse, J; Minett, A.I; Gu, G; Roth, S; Rinzler, A.G; Baughman, R.H, 2001. Towards the demonstration of actuator properties of a single carbon nanotube. *Current Applied Physics* **1** (4-5), pp. 407–411
DOI: 10.1016/S1567-1739(01)00048-7
- Fukuda et al. 2011 Fukuda, Kenjiro; Sekitani, Tsuyoshi; Zschieschang, Ute; Klauk, Hagen; Kuribara, Kazunori; Yokota, Tomoyuki; Sugino, Takushi; Asaka, Kinji; Ikeda, Masaaki; Kuwabara, Hirokazu; Yamamoto, Tatsuya; Takimiya, Kazuo; Fukushima, Takanori; Aida, Takuzo; Takamiya, Makoto; Sakurai, Takayasu; Someya, Takao, 2011. A 4 V Operation, Flexible Braille Display Using Organic Transistors, Carbon Nanotube Actuators, and Organic Static Random-Access Memory. *Advanced Functional Materials* **21** (21), pp. 4019–4027
DOI: 10.1002/adfm.201101050
- Fukushima et al. 2003 Fukushima, Takanori; Kosaka, Atsuko; Ishimura, Yoji; Yamamoto, Takashi; Takigawa, Toshikazu; Ishii, Noriyuki; Aida, Takuzo, 2003. Molecular ordering of organic molten salts triggered by single-walled carbon nanotubes. *Science* **300** (5628), pp. 2072–2074
DOI: 10.1126/science.1082289
- Fukushima et al. 2005 Fukushima, Takanori; Asaka, Kinji; Kosaka, Atsuko; Aida, Takuzo, 2005. Fully plastic actuator through layer-by-layer casting with ionic-liquid-based bucky gel. *Angewandte Chemie* **44** (16), pp. 2410–2413
DOI: 10.1002/anie.200462318
- Fuller 1997 Fuller, J., 1997. Ionic Liquid-Polymer Gel Electrolytes. *Journal of The Electrochemical Society* **144** (4), L67
DOI: 10.1149/1.1837555
- Gangoli et al. 2019 Gangoli, Varun Shenoy; Godwin, M. Anto; Reddy, Gadhadar; Bradley, Robert Kelley; Barron, Andrew R., 2019. The State of HiPco Single-Walled Carbon Nanotubes in 2019. *Journal of Carbon Research* **5** (4), p. 65
DOI: 10.3390/c5040065
- Goya et al. 2017 Goya, Kenji; Fuchiwaki, Yusuke; Tanaka, Masato; Addinall, Raphael; Ooie, Toshihiko; Sugino, Takushi; Asaka, Kinji, 2017. A micropipette system based on low driving voltage carbon nanotube actuator. *Microsystem Technologies* **23** (7), pp. 2657–2661
DOI: 10.1007/s00542-016-2943-y
- Guan et al. 2008 Guan, Lunhui; Suenaga, Kazu; Iijima, Sumio, 2008. Smallest carbon nanotube assigned with atomic resolution accuracy. *Nano letters* **8** (2), pp. 459–462
DOI: 10.1021/nl072396j
- Gupta et al. 2006 Gupta, Vinay; Miura, Norio, 2006. Polyaniline/single-wall carbon nanotube (PANI/SWCNT) composites for high performance supercapacitors. *Electrochimica Acta* **52** (4), pp. 1721–1726
DOI: 10.1016/j.electacta.2006.01.074
- Haase et al. 2011 Haase, Walter; Klaus, Thorsten; Schmid, Fabian; Sobek, Werner; Sedlbauer, Klaus; Schmidt, Timo; Synold, Martin, 2011. Adaptive textile und folienbasierte Gebäudehüllen. *Bautechnik* **88** (2), pp. 69–75
DOI: 10.1002/bate.201110005
- Habermann et al. 2004 Habermann, Karl J; Koch, Klaus-Michael, 2004. *Membrane structures: Innovative building with film and fabric*: Munich. Prestel Publishing Ltd. ISBN 978-3-7913-3049-5
- Hao et al. 2019 Hao, Muyu; Wang, Yanjie; Zhu, Zicai; He, QingSong; Zhu, Denglin; Luo, Minzhou, 2019. A Compact Review of IPMC as Soft Actuator and Sensor: Current Trends, Challenges, and Potential Solutions From Our Recent Work. *Frontiers in robotics and AI* **6**, p. 129
DOI: 10.3389/frobt.2019.00129

- Hara et al. 2004** Hara, Susumu; Zama, Tetsuji; Takashima, Wataru; Kaneto, Keiichi, 2004. Artificial Muscles Based on Polypyrrole Actuators with Large Strain and Stress Induced Electrically. *Polymer Journal* **36** (2), pp. 151–161
DOI: 10.1295/polymj.36.151
- HARRY 2016** HARRY, SACHIN, 2016. Dynamic Adaptive Building Envelopes – an Innovative and State-of-The-Art Technology. *Creative Space* **3** (2), pp. 167–184
DOI: 10.15415/cs.2016.32011
- Hata et al. 2004** Hata, Kenji; Futaba, Don N; Mizuno, Kohei; Namai, Tatsunori; Yumura, Motoo; Iijima, Sumio, 2004. Water-assisted highly efficient synthesis of impurity-free single-walled carbon nanotubes. *Science* **306** (5700), pp. 1362–1364
DOI: 10.1126/science.1104962
- Higuchi et al. 2010** Higuchi, Toshiro; Suzumori, Koichi; Tadokoro, Satoshi, 2010. *Next-Generation Actuators Leading Breakthroughs*: London. Springer London. ISBN 978-1-84882-990-9
DOI: 10.1007/978-1-84882-991-6
- Huang et al. 2012** Huang, Yan Yan; Terentjev, Eugene M., 2012. Dispersion of Carbon Nanotubes: Mixing, Sonication, Stabilization, and Composite Properties. *Polymers* **4** (1), pp. 275–295
DOI: 10.3390/polym4010275
- Hunter et al. 1992** Hunter, Ian W; Lafontaine, Serge, 1992. A comparison of muscle with artificial actuators. In: *Technical Digest IEEE Solid-State Sensor and Actuator Workshop*, Hilton Head Island, SC, USA, 22-25 June 1992, pp. 178–185
DOI: 10.1109/SOLSEN.1992.228297
- Iijima 1991** Iijima, Sumio, 1991. Helical microtubules of graphitic carbon. *Nature* **354** (6348), pp. 56–58
DOI: 10.1038/354056a0
- Iijima et al. 1993** Iijima, Sumio; Ichihashi, Toshinari, 1993. Single-shell carbon nanotubes of 1-nm diameter. *Nature* **363** (6430), pp. 603–605
DOI: 10.1038/363603a0
- Ikuno et al. 2005** Ikuno, Takashi; Honda, Shin-ichi; Yasuda, Tatsuro; Oura, Kenjiro; Katayama, Mitsuhiro; Lee, Jung Goo; Mori, Hiroto, 2005. Thermally driven nanomechanical deflection of hybrid nanowires. *Applied Physics Letters* **87** (21), p. 213104
DOI: 10.1063/1.2133919
- Isaacs et al. 2010** Isaacs, J. A; Tanwani, A; Healy, M. L; Dahlben, L. J., 2010. Economic assessment of single-walled carbon nanotube processes. *Journal of Nanoparticle Research* **12** (2), pp. 551–562
DOI: 10.1007/s11051-009-9673-3
- Jaakson et al. 2016** Jaakson, P; Aabloo, A; Tamm, T., 2016. Encapsulation of ionic electroactive polymers: reducing the interaction with environment. In: Bar-Cohen, Yoseph; Vidal, Frédéric (Eds.). In: *Electroactive Polymer Actuators and Devices (EAPAD) 2016*, Las Vegas, Nevada, United States, Sunday 20 March 2016, p. 979825
DOI: 10.1117/12.2219053
- Jager et al. 2000** Jager, E. W; Smela, E; Inganäs, O., 2000. Microfabricating conjugated polymer actuators. *Science (New York, N.Y.)* **290** (5496), pp. 1540–1545
DOI: 10.1126/science.290.5496.1540
- Janocha 2004** Janocha, Hartmut, 2004. *Actuators: Basics and Applications*: Berlin, Heidelberg. Springer. ISBN 978-3-662-05587-8
DOI: 10.1007/978-3-662-05587-8
- Janssens 1998** Janssens, Arnold, 1998. *Reliable control of interstitial condensation in lightweight roof systems : calculation and assessment methods*. Heverlee, Belgium, Katholieke Universiteit Leuven, 1998
<http://lib.ugent.be/catalog/rug01:000697239>
- Journet et al. 1997** Journet, Catherine; Maser, Wolfgang K; Bernier, Patrick; Loiseau, A; La Chapelle, Marc Lamy de; Lefrant, Serge; Deniard, Philippe; Lee, Ron; Fischer, John E., 1997. Large-scale production of single-walled carbon nanotubes by the electric-arc technique. *Nature* **388** (6644), pp. 756–758
DOI: 10.1038/41972

- Journet et al. 1998** Journet, Catherine; Bernier, Patrick, 1998. Production of carbon nanotubes. *Applied Physics A: Materials Science & Processing* **67** (1), pp. 1–9
DOI: 10.1007/s003390050731
- Juaristi et al. 2018** Juaristi, Miren; Monge-Barrio, Aurora; Knaack, Ulrich; Gómez-Acebo, Tomás, 2018. Smart and Multifunctional Materials and their possible application in façade systems. *Journal of Facade Design and Engineering* **6** (3), pp. 19–33
DOI: 10.7480/jfde.2018.3.2475
- Kaasik et al. 2017** Kaasik, Friedrich; Must, Indrek; Baranova, Inna; Põldsalu, Inga; Lust, Enn; Johanson, Urmas; Punning, Andres; Aabloo, Alvo, 2017. Scalable fabrication of ionic and capacitive laminate actuators for soft robotics. *Sensors and Actuators B: Chemical* **246**, pp. 154–163
DOI: 10.1016/j.snb.2017.02.065
- Kamamichi et al. 2007a** Kamamichi, Norihiro; Yamakita, Masaki; Kinji; Luo, Zhi-Wei; Mukai, Toshiharu, 2007. Experimental verifications on control and sensing of bucky gel actuator/sensor. In: *2007 IEEE/RSJ International Conference on Intelligent Robots and Systems*, San Diego, CA, USA, 29.10.2007 - 02.11.2007, pp. 1172–1177
DOI: 10.1109/IROS.2007.4399078
- Kamamichi et al. 2007b** Kamamichi, Norihiro; Yamakita, Masaki; Asaka, Kinji; Luo, Zhi-Wei; Mukai, Toshiharu, 2007. Sensor Property of a Novel EAP Device with Ionic-liquid-based Bucky Gel. In: *IEEE Sensors*, Atlanta, GA, USA, 28.10.2007 - 31.10.2007, pp. 221–224
DOI: 10.1109/ICSENS.2007.4388376
- Kamamichi et al. 2010** Kamamichi, Norihiro; Maeba, Toshiharu; Yamakita, Masaki; Mukai, Toshiharu, 2010. Printing Fabrication of a Bucky Gel Actuator/Sensor and Its Application to Three-Dimensional Patterned Devices. *Advanced Robotics* **24** (10), pp. 1471–1487
DOI: 10.1163/016918610X505585
- Kaneto et al. 1995** Kaneto, Keiichi; Saito, Hiroyuki; Min, Young Geun; MacDiarmid, Alan G., 1995. “Artificial muscle”: Electromechanical actuators using polyaniline films. *Synthetic Metals* **71** (1-3), pp. 2211–2212
DOI: 10.1016/0379-6779(94)03226-V
- Karagiozis et al. 2001** Karagiozis, Achilles; Salonvaara, Mikael, 2001. Hygrothermal system-performance of a whole building. *Building and Environment* **36** (6), pp. 779–787
DOI: 10.1016/S0360-1323(00)00063-9
- Ke et al. 2004** Ke, Changhong; Espinosa, Horacio D., 2004. Feedback controlled nanocantilever device. *Applied Physics Letters* **85** (4), pp. 681–683
DOI: 10.1063/1.1767606
- Khan et al. 2017** Khan, Obaid ullah; Lughmani, Waqas Akbar; Wakeel, Aneela; ur Rehman, Sami, 2017. Finite element modeling of blocking force of ionic polymer metal composites (IPMC) in micro gripper. In: *2017 13th International Conference on Emerging Technologies (ICET)*, Islamabad, Pakistan, 27.12.2017 - 28.12.2017, pp. 1–5
DOI: 10.1109/ICET.2017.8281754
- Kim et al. 2003** Kim, Byungkyu; Kim, Byung M; Ryu, Jaewook; Oh, In-Hwan; Lee, Seung-Ki; Cha, Seung-Eun; Pak, Jung-ho, 2003. Analysis of mechanical characteristics of the ionic polymer metal composite (IPMC) actuator using cast ion-exchange film. In: Bar-Cohen, Yoseph (Ed.). In: *Smart Structures and Materials 2003: Electroactive Polymer Actuators and Devices (EAPAD)*, San Diego, 2.3.2003-6.3.2003, p. 486
DOI: 10.1117/12.484296
- Kim et al. 2002** Kim, Kwang; Shahinpoor, Mohsen, 2002. A novel method of manufacturing three-dimensional ionic polymer–metal composites (IPMCs) biomimetic sensors, actuators and artificial muscles. *Polymer* **43** (3), pp. 797–802
DOI: 10.1016/S0032-3861(01)00648-6
- Kiyohara et al. 2011** Kiyohara, Kenji; Sugino, Takushi; Asaka, Kinji, 2011. Molecular mechanism of ionic electroactive polymer actuators. *Smart Materials and Structures* **20** (12), p. 124009
DOI: 10.1088/0964-1726/20/12/124009

- Klein et al. 2015** Klein, Tillmann; Knaack, Ulrich, 2015. Adaptive building envelopes, component development as well as implementation strategies.
Journal of Facade Design and Engineering **3** (2)
DOI: 10.7480/jfde.2015.2.1011
- Kolodziej et al.** Kolodziej, Przemyslaw; Rak, Jozef.
Responsive Building Envelope as a Material System of Autonomous Agents.
In: *Proceedings of the 18th International Conference on Computer-aided Architectural Design Research in Asia (CAADRIA 2013)*, pp. 945-954
- Kolodziej et al. 2013** Kolodziej, Przemyslaw; Zylka, Pawel, 2013.
Experimental research of the adaptive building envelope (ABE).
In: Obrebski, Jan; Tarczewski, Romuald (Eds.).
In: *Proceedings of the International Association for Shell and Spatial Structures (IASS) Symposium*,
Wroclaw, Poland,
23.-27.09.2013
- Kosidlo et al. 2013** Kosidlo, U; Omastová, M; Micusík, M; Ćirić-Marjanović, G; Randriamahazaka, H; Wallmersperger, T; Aabloo, A; Kolaric, I; Bauernhansl, T., 2013. Nanocarbon based ionic actuators—a review.
Smart Materials and Structures **22** (10), p. 104022
DOI: 10.1088/0964-1726/22/10/104022
- Košir 2016** Košir, Mitja, 2016.
Adaptive Building Envelope: An Integral Approach to Indoor Environment Control in Buildings.
In: Ponce, Pedro; Gutierrez, Arturo M; Ibarra, Luis M. (Eds.): *Automation and Control Trends*:
InTech, pp. 121-148
ISBN 978-953-51-2670-6
DOI: 10.5772/64951
- Kotal et al. 2016** Kotal, Moumita; Kim, Jaehwan; Kim, Kwang J; Oh, Il-Kwon, 2016. Sulfur and Nitrogen Co-Doped Graphene Electrodes for High-Performance Ionic Artificial Muscles.
Advanced Materials **28** (8), pp. 1610–1615
DOI: 10.1002/adma.201505243
- Kretzer et al. 2012** Kretzer, Manuel; Rossi, Dino, 2012. ShapeShift.
Leonardo **45** (5), pp. 480–481
DOI: 10.1162/LEON_a_00451
- Kroto et al. 1985** Kroto, H. W; Heath, J. R; O'Brien, S. C; Curl, R. F; Smalley, R. E., 1985. C60: Buckminsterfullerene.
Nature **318** (6042), pp. 162–163
DOI: 10.1038/318162a0
- Krueger 2007** Krueger, Anke, 2007.
Neue Kohlenstoffmaterialien: Eine Einführung: Wiesbaden. B.G. Teubner Verlag / GWV Fachver-
lage GmbH Wiesbaden.
ISBN 978-3519005100
DOI: 10.1007/978-3-8351-9098-6
- Kruusamäe et al. 2014a** Kruusamäe, Karl; Mukai, Ken; Sugino, Takushi; Asaka, Kinji, 2014. Impact of viscoelastic properties on bucky-gel actuator performance.
Journal of Intelligent Material Systems and Structures **25** (18), pp. 2235–2245
DOI: 10.1177/1045389X14538538
- Kruusamäe et al. 2014b** Kruusamäe, Karl; Mukai, Ken; Sugino, Takushi; Asaka, Kinji, 2014. Mechanical behaviour of bending bucky-gel actuators and its representation.
Smart Materials and Structures **23** (2), p. 25031
- Kruusamäe et al. 2015a** Kruusamäe, Karl; Sugino, Takushi; Asaka, Kinji, 2015. Ionic and viscoelastic mechanisms of a bucky-gel actuator.
Journal of Applied Physics **118** (1), p. 14502
DOI: 10.1063/1.4923351
- Kruusamäe et al. 2015b** Kruusamäe, Karl; Punning, Andres; Aabloo, Alvo; Asaka, Kinji, 2015. Self-Sensing Ionic Polymer Actuators: A Review.
Actuators **4** (1), pp. 17–38
DOI: 10.3390/act4010017
- Laurent et al. 2001** Laurent, G; Piat, D., 2001.
Efficiency of swimming microrobots using ionic polymer metal composite actuators.
In: *Proceedings 2001 ICRA. IEEE International Conference on Robotics and Automation (Cat. No.01CH37164)*, Seoul, South Korea,
21-26 May 2001, pp. 3914–3919
DOI: 10.1109/ROBOT.2001.933227

- Leemets et al. 2018** Leemets, Kaur; Mäeorg, Uno; Aabloo, Alvo; Tamm, Tarmo, 2018. Effect of contact material and ambient humidity on the performance of MWCNT/PDMS multimodal deformation sensors. *Sensors and Actuators A: Physical* **283**, pp. 1–8
DOI: 10.1016/j.sna.2018.09.042
- Li et al. 2013** Li, Kaiyuan; Eres, Gyula; Howe, Jane; Chuang, Yen-Jun; Li, Xufan; Gu, Zhanjun; Zhang, Litong; Xie, Sishen; Pan, Zhengwei, 2013. Self-assembly of graphene on carbon nanotube surfaces. *Scientific Reports* **3**, p. 2353
DOI: 10.1038/srep02353
- Lin-Gibson et al. 2004** Lin-Gibson, Shen; Pathak, Jai A; Grulke, E. A; Wang, Haonan; Hobbie, Erik K., 2004. Elastic flow instability in nanotube suspensions. *Physical Review Letters* **92** (4), p. 48302
DOI: 10.1103/PhysRevLett.92.048302
- Liu et al. 2010a** Liu, Sheng; Liu, Wenjuan; Liu, Yang; Lin, Jun-Hong; Zhou, Xin; Janik, Michael J; Colby, Ralph H; Zhang, Qiming, 2010. Influence of imidazolium-based ionic liquids on the performance of ionic polymer conductor network composite actuators. *Polymer International* **59** (3), pp. 321–328
DOI: 10.1002/pi.2771
- Liu et al. 2010b** Liu, Yang; Liu, Sheng; Lin, Junhong; Wang, Dong; Jain, Vaibhav; Montazami, Reza; Heflin, James R; Li, Jing; Madsen, Louis; Zhang, Q. M., 2010. Ion transport and storage of ionic liquids in ionic polymer conductor network composites. *Applied Physics Letters* **96** (22), p. 223503
DOI: 10.1063/1.3432664
- Loonen et al. 2015** Loonen, Roel C.G.M; Favoino, Fabio; Rico-Martinez, Jose Miguel; Brzezicki, Marcin, 2015. Design for façade adaptability: Towards a unified and systematic characterization. In: *10th Conference on Advanced Building Skins*, Bern, 3.11.-4.11.2015, pp. 1284–1294
- Loonen et al. 2013** Loonen, Roel C.G.M; Trčka, Marija; Cóstola, Daniel; Hensen, Joannes L.M., 2013. Climate adaptive building shells: State-of-the-art and future challenges. *Renewable and Sustainable Energy Reviews* **25**, pp. 483–493
DOI: 10.1016/j.rser.2013.04.016
- Lu et al. 2012** Lu, Luhua; Liu, Jinghai; Hu, Ying; Zhang, Yuewei; Randriamahazaka, Hyacinthe; Chen, Wei, 2012. Highly stable air working bimorph actuator based on a graphene nanosheet/carbon nanotube hybrid electrode. *Advanced Materials* **24** (31), pp. 4317–4321
DOI: 10.1002/adma.201201320
- Lumia et al. 2008** Lumia, Ron; Shahinpoor, Mohsen, 2008. IPMC microgripper research and development. *Journal of Physics: Conference Series* **127**, p. 12002
DOI: 10.1088/1742-6596/127/1/012002
- Madden et al. 2007** Madden, John D; Rinderknecht, Derek; Anquetil, Patrick A; Hunter, Ian W., 2007. Creep and cycle life in polypyrrole actuators. *Sensors and Actuators A: Physical* **133** (1), pp. 210–217
DOI: 10.1016/j.sna.2006.03.016
- McDaid et al. 2014** McDaid, Andrew John; Aw, Kean C., 2014. *Ionic polymer metallic composite transducers for biomedical robotics applications*: Barcelona. IFSA Publishing, S.L.
ISBN 9788461676699
- McGinnis 2013** McGinnis, Peter Merton, 2013. *Biomechanics of sport and exercise*. Third edition: Champaign, IL, Windsor, ON, Leeds, United Kingdom. Human Kinetics.
ISBN 978-0-7360-7966-2
- Melling et al. 2019** Melling, Daniel; Martinez, Jose G; Jager, Edwin W. H., 2019. Conjugated Polymer Actuators and Devices: Progress and Opportunities. *Advanced materials* **31** (22), e1808210
DOI: 10.1002/adma.201808210
- Menges et al. 2013** Menges, Achim; Krieg, Oliver David; Reichert, Steffen, 2013. *HygroSkin – Meteorosensitive Pavilion*
From: <https://www.detail.de/artikel/hygroskin-meteorosensitive-pavilion-11029/>
- Meyyappan 2005** Meyyappan, Meyya, 2005. *Carbon nanotubes: Science and applications*: Boca Raton, FL. CRC Press.
ISBN 9780849321115

- Minitab GmbH 2018** Minitab GmbH, 2018.
Minitab : Statistical Software.
Version 18, Computer Software: Munich
- Mossé et al. 2012** Mossé, Aurélie; Gauthier, David; Kofod, Guggi, 2012. Towards Interconnectivity: Appropriation of Responsive Minimum Energy Structures in an Architectural Context.
Studies in Material Thinking **7**
- Mukai et al. 2008** Mukai, Ken; Asaka, Kinji; Kiyohara, Kenji; Sugino, Takushi; Takeuchi, Ichiro; Fukushima, Takanori; Aida, Takuzo, 2008. High performance fully plastic actuator based on ionic-liquid-based bucky gel.
Electrochimica Acta **53** (17), pp. 5555–5562
DOI: 10.1016/j.electacta.2008.02.113
- Mukai et al. 2009** Mukai, Ken; Asaka, Kinji; Sugino, Takushi; Kiyohara, Kenji; Takeuchi, Ichiro; Terasawa, Naohiro; Futaba, Don N; Hata, Kenji; Fukushima, Takanori; Aida, Takuzo, 2009. Highly Conductive Sheets from Millimeter-Long Single-Walled Carbon Nanotubes and Ionic Liquids: Application to Fast-Moving, Low-Voltage Electromechanical Actuators Operable in Air.
Advanced Materials **21** (16), pp. 1582–1585
DOI: 10.1002/adma.200802817
- Must et al. 2015** Must, Indrek; Kaasik, Friedrich; Põldsalu, Inga; Mihkels, Lauri; Johanson, Urmas; Punning, Andres; Aabloo, Alvo, 2015. Ionic and Capacitive Artificial Muscle for Biomimetic Soft Robotics.
Advanced Engineering Materials **17** (1), pp. 84–94
DOI: 10.1002/adem.201400246
- Nakshatharan et al. 2018a** Nakshatharan, S. Sunjai; Punning, Andres; Johanson, Urmas; Aabloo, Alvo, 2018. Effect of porosity and tortuosity of electrodes on carbon polymer soft actuators.
Journal of Applied Physics **123** (1), p. 14502
DOI: 10.1063/1.5007147
- Nakshatharan et al. 2018b** Nakshatharan, Sunjai; Vunder, Veiko; Põldsalu, Inga; Johanson, Urmas; Punning, Andres; Aabloo, Alvo, 2018. Modelling and Control of Ionic Electroactive Polymer Actuators under Varying Humidity Conditions.
Actuators **7** (1), p. 7
DOI: 10.3390/act7010007
- Nessim 2010** Nessim, Gilbert D., 2010. Properties, synthesis, and growth mechanisms of carbon nanotubes with special focus on thermal chemical vapor deposition.
Nanoscale **2** (8), pp. 1306–1323
DOI: 10.1039/b9nr00427k
- Neuhaeuser et al. 2013** Neuhaeuser, Stefan; Weickgenannt, Martin; Witte, Christoph; Haase, Walter; Sawodny, Oliver; Sobek, Werner, 2013. Stuttgart SmartShell - A Full Scale Prototype of an Adaptive Shell Structure.
Journal of the International Association for Shell and Spatial Structures (54), pp. 259–270
- Neuhaus et al. 2019a** Neuhaus, R; Glanz, C; Kolaric, I; Siegert, J; Bauernhansl, T., 2019. Manufacturing, optimization and design of electroactive CNT-actuators for adaptive building envelopes.
In: Zingoni, Alphonse (Ed.): *Advances in Engineering Materials, Structures and Systems: Innovations, Mechanics and Applications*: CRC Press, pp. 983–988
ISBN 9780429426506
DOI: 10.1201/9780429426506-171
- Neuhaus et al. 2019b** Neuhaus, Raphael; Glanz, Carsten; Kolaric, Ivica; Bauernhansl, Thomas, 2019. Electroactive CNT-Polymer-Actuators : State of Science and Technology and their slow Approach into Architectural Applications.
In: Nanoinitiative Bayern GmbH/Cluster Nanotechnology (Ed.).
In: *NanoCarbon Annual Conference*, Würzburg
- Neuhaus et al. 2019c** Neuhaus, Raphael; Bitzer, Veronika; Jablockin, Julia; Glanz, Carsten; Kolaric, Ivica; Siegert, Jörg; Bauernhansl, Thomas, 2019. Ionic CNT actuators and arrays – towards cost-efficient manufacturing through scalable dispersion and printing processes.
In: *2019 IEEE/ASME International Conference on Advanced Intelligent Mechatronics (AIM)*, Hong Kong, China, 08.07.2019 - 12.07.2019, pp. 56–61
DOI: 10.1109/AIM.2019.8868428
- Neuhaus et al. 2020** Neuhaus, Raphael; Zahiri, Nima; Petrs, Jan; Tahouni, Yasaman; Siegert, Jörg; Kolaric, Ivica; Dahy, Hanaa; Bauernhansl, Thomas, 2020. Integrating Ionic Electroactive Polymer Actuators and Sensors into Adaptive Building Skins – Potentials and Limitations.
Frontiers in Built Environment, Design and Control of Adaptive Civil Structures
DOI: 10.3389/fbuil.2020.00095

- Nichols et al. 2002** Nichols, Gary; Byard, Stephen; Bloxham, Mark J; Botterill, Joanne; Dawson, Neil J; Dennis, Andrew; Diart, Valerie; North, Nigel C; Sherwood, John D., 2002. A review of the terms agglomerate and aggregate with a recommendation for nomenclature used in powder and particle characterization. *Journal of pharmaceutical sciences* **91** (10), pp. 2103–2109
DOI: 10.1002/jps.10191
- Nikolaev et al. 1999** Nikolaev, Pavel; Bronikowski, Michael J; Bradley, R.Kelley; Rohmund, Frank; Colbert, Daniel T; Smith, K.A; Smalley, Richard E., 1999. Gas-phase catalytic growth of single-walled carbon nanotubes from carbon monoxide. *Chemical Physics Letters* **313** (1-2), pp. 91–97
DOI: 10.1016/S0009-2614(99)01029-5
- Novoselov et al. 2004** Novoselov, Konstantin S; Geim, Andre K; Morozov, Sergey V; Jiang, Da; Zhang, Yuanbo; Dubonos, Sergey V; Grigorieva, Irina V; Firsov, Anatoly A., 2004. Electric field effect in atomically thin carbon films. *Science* **306** (5696), pp. 666–669
DOI: 10.1126/science.1102896
- Oberlin et al. 1976** Oberlin, Agnès; Endo, Morinobu; Koyama, Tsuneo, 1976. High resolution electron microscope observations of graphitized carbon fibers. *Carbon* **14** (2), pp. 133–135
DOI: 10.1016/0008-6223(76)90124-X
- Oh et al. 2019** Oh, Chungik; Kim, Suran; Kim, Hongjun; Park, Gun; Kim, Jaegyung; Ryu, Jeongjae; Li, Panpan; Lee, Sunghwan; No, Kwangsoo; Hong, Seungbum, 2019. Effects of membrane thickness on the performance of ionic polymer–metal composite actuators. *RSC Advances* **9** (26), pp. 14621–14626
DOI: 10.1039/C9RA01751H
- Okuzaki et al. 1999** Okuzaki, Hidenori; Funasaka, Keiichi, 1999. Electrically Driven Polypyrrole Film Actuator Working in Air. *Journal of Intelligent Material Systems and Structures* **10** (6), pp. 465–469
DOI: 10.1106/6CRB-FK02-FX04-4PCG
- Okuzaki et al. 2014** Okuzaki, Hidenori; Takagi, Satoshi; Hishiki, Fumiya; Tanigawa, Ryo, 2014. Ionic liquid/polyurethane/PEDOT:PSS composites for electro-active polymer actuators. *Sensors and Actuators B: Chemical* **194**, pp. 59–63
DOI: 10.1016/j.snb.2013.12.059
- Osawa 1970** Osawa, Eiji, 1970. Superaromaticity. *Kagaku* **25**, pp. 854–863
- Paech 2016** Paech, Christoph, 2016. Structural Membranes Used in Modern Building Facades. *Procedia Engineering* **155**, pp. 61–70
DOI: 10.1016/j.proeng.2016.08.007
- Palmre et al. 2012** Palmre, Viljar; Torop, Janno; Arulepp, Mati; Sugino, Takushi; Asaka, Kinji; Jänes, Alar; Lust, Enn; Aabloo, Alvo, 2012. Impact of carbon nanotube additives on carbide-derived carbon-based electroactive polymer actuators. *Carbon* **50** (12), pp. 4351–4358
DOI: 10.1016/j.carbon.2012.04.071
- Palmre et al. 2013** Palmre, Viljar; Hubbard, Joel J; Fleming, Maxwell; Pugal, David; Kim, Sungjun; Kim, Kwang J; Leang, Kam K., 2013. An IPMC-enabled bio-inspired bending/twisting fin for underwater applications. *Smart Materials and Structures* **22** (1), p. 14003
DOI: 10.1088/0964-1726/22/1/014003
- Palmre et al. 2014** Palmre, Viljar; Pugal, David; Kim, Kwang J; Leang, Kam K; Asaka, Kinji; Aabloo, Alvo, 2014. Nanothorn electrodes for ionic polymer-metal composite artificial muscles. *Scientific Reports* **4**, p. 6176
DOI: 10.1038/srep06176
- Paredes et al. 2004** Paredes, Juan I; Burghard, Marko, 2004. Dispersions of individual single-walled carbon nanotubes of high length. *Langmuir: the ACS journal of surfaces and colloids* **20** (12), pp. 5149–5152
DOI: 10.1021/la049831z
- Park et al. 2018a** Park, Minjeong; Kim, Joohee; Song, Hanjung; Kim, Seonpil; Jeon, Minhyon, 2018. Effects of Thickness and Multi-Walled Carbon Nanotube Incorporation on the Performance of Nafion Membrane-Based Ionic Polymer–Metal Composite Actuators. *Nanoscience and Nanotechnology Letters* **10** (8), pp. 1121–1125
DOI: 10.1166/nnl.2018.2759

- Park et al. 2018b** Park, Minjeong; Kim, Joohee; Song, Hanjung; Kim, Seonpil; Jeon, Minhyon, 2018. Fast and Stable Ionic Electroactive Polymer Actuators with PEDOT:PSS/Graphene-Ag-Nanowires Nanocomposite Electrodes. *Sensors* **18** (9)
DOI: 10.3390/s18093126
- Pinault et al. 2004** Pinault, M; Mayne-L'Hermite, M; Reynaud, C; Beyssac, O; Rouzaud, J. N; Clinard, C., 2004. Carbon nanotubes produced by aerosol pyrolysis: growth mechanisms and post-annealing effects. *Diamond and Related Materials* **13** (4-8), pp. 1266–1269
DOI: 10.1016/j.diamond.2003.12.015
- Plesse et al. 2005** Plesse, Cédric; Vidal, Frédéric; Randriamahazaka, Hyacinthe; Teyssié, Dominique; Chevrot, Claude, 2005. Synthesis and characterization of conducting interpenetrating polymer networks for new actuators. *Polymer* **46** (18), pp. 7771–7778
DOI: 10.1016/j.polymer.2005.03.103
- Põldsalu et al. 2018** Põldsalu, Inga; Rohtlaid, Kätlin; Nguyen, Tran Minh Giao; Plesse, Cedric; Vidal, Frédéric; Khorram, Mahdi Safaei; Peikolainen, Anna-Liisa; Tamm, Tarmo; Kiefer, Rudolf, 2018. Thin ink-jet printed trilayer actuators composed of PEDOT:PSS on interpenetrating polymer networks. *Sensors and Actuators B: Chemical* **258**, pp. 1072–1079
DOI: 10.1016/j.snb.2017.11.147
- Prasad et al. 2002** Prasad, K.Rajendra; Munichandraiah, N., 2002. Fabrication and evaluation of 450 F electrochemical redox supercapacitors using inexpensive and high-performance, polyaniline coated, stainless-steel electrodes. *Journal of Power Sources* **112** (2), pp. 443–451
DOI: 10.1016/S0378-7753(02)00419-6
- Prasek et al. 2011** Prasek, Jan; Drbohlavova, Jana; Chomoucka, Jana; Hubalek, Jaromir; Jasek, Ondrej; Adam, Vojtech; Kizek, Rene, 2011. Methods for carbon nanotubes synthesis—review. *Journal of Materials Chemistry* **21** (40), p. 15872
DOI: 10.1039/C1JM12254A
- Preisinger 2019** Preisinger, Clemens, 2019. *Karamba3D : parametric engineering*. Version 1.3.2, Computer Software: Vienna. Bollinger und Grohmann ZT GmbH, From: www.karamba3D.com
Viewed: 20.04.2020
- Punning et al. 2014** Punning, Andres; Must, Indrek; Põldsalu, Inga; Vunder, Veiko; Temmer, Rauno; Kruusamäe, Karl; Kaasik, Friedrich; Torop, Janno; Rinne, Pille; Lulla, Tõnis; Johanson, Urmas; Tamm, Tarmo; Aabloo, Alvo, 2014. Lifetime measurements of ionic electroactive polymer actuators. *Journal of Intelligent Material Systems and Structures* **25** (18), pp. 2267–2275
DOI: 10.1177/1045389X14546656
- Radushkevich et al. 1952** Radushkevich, L. V; Lukyanovich, V. M., 1952. The Structure of Carbon Forming in Thermal Decomposition of Carbon Monoxide on an Iron Catalyst. *Russian Journal of Physical Chemistry* **26**, pp. 88–95
- Reichert et al. 2015** Reichert, Steffen; Menges, Achim; Correa, David, 2015. Meteorosensitive architecture: Biometric building skins based on materially embedded and hygroscopically enabled responsiveness. *Computer-Aided Design* **60**, pp. 50–69
DOI: 10.1016/j.cad.2014.02.010
- Rinne et al. 2019** Rinne, Pille; Põldsalu, Inga; Johanson, Urmas; Tamm, Tarmo; Põhako-Esko, Kaija; Punning, Andres; van den Ende, Daan; Aabloo, Alvo, 2019. Encapsulation of ionic electromechanically active polymer actuators. *Smart Materials and Structures* **28** (7), p. 74002
DOI: 10.1088/1361-665X/ab18c0
- Roth et al. 2002** Roth, Siegmara; Baughman, Ray H., 2002. Actuators of individual carbon nanotubes. *Current Applied Physics* **2** (4), pp. 311–314
DOI: 10.1016/S1567-1739(02)00116-5
- Roth et al. 2015** Roth, Siegmara; Carroll, David Loren, 2015. *One-dimensional metals: Conjugated polymers, organic crystals, carbon nanotubes and graphene*. Third completely revised and enlarged edition: Stuttgart. Wiley-VCH.
ISBN 978-3527335572
- Ru et al. 2019** Ru, Jie; Bian, Changsheng; Zhu, Zicai; Wang, Yanjie; Zhang, Junshi; Horiuchi, Tetsuya; Sugino, Takushi; Liu, Xiaofeng; Chen, Hualing; Asaka, Kinji, 2019. Controllable and durable ionic electroactive polymer actuator based on nanoporous carbon nanotube film electrode. *Smart Materials and Structures* **28** (8), p. 85032
DOI: 10.1088/1361-665X/ab2a28

- Saito et al. 1998** Saito, Riichiro; Dresselhaus, Gene; Dresselhaus, Mildred S., 1998. *Physical properties of carbon nanotubes*: London. Imperial College Press. ISBN 978-1860942235
- Shabani et al. 2012** Shabani, Roxana; Cho, Hyoung J., 2012. Nanomaterials in Actuators—A Review. *Reviews in Nanoscience and Nanotechnology* **1** (2), pp. 85–102
DOI: 10.1166/rnn.2012.1006
- Shahinpoor et al. 2001** Shahinpoor, Mohsen; Kim, Kwang J., 2001. Ionic polymer-metal composites: I. Fundamentals. *Smart Materials and Structures* **10** (4), pp. 819–833
DOI: 10.1088/0964-1726/10/4/327
- Shahinpoor et al. 2003** Shahinpoor, Mohsen; Kim, Kwang J.; Leo, Don J., 2003. Ionic polymer-metal composites as multi-functional materials. *Polymer Composites* **24** (1), pp. 24–33
DOI: 10.1002/pc.10002
- Simaite 2015** Simaite, Aiva, 2015. *Development of ionic electroactive actuators with improved interfacial adhesion : towards the fabrication of inkjet printable artificial muscles*. Toulouse, INSA de Toulouse, 2015, <https://tel.archives-ouvertes.fr/tel-01591571>
- Singh et al. 2020** Singh, Sandip K; Savoy, Anthony W., 2020. Ionic liquids synthesis and applications: An overview. *Journal of Molecular Liquids* **297**, p. 112038
DOI: 10.1016/j.molliq.2019.112038
- Smits 1958** Smits, F. M., 1958. Measurement of Sheet Resistivities with the Four-Point Probe. *Bell System Technical Journal* **37** (3), pp. 711–718
DOI: 10.1002/j.1538-7305.1958.tb03883.x
- Sobek 2015** Sobek, Werner, 2015. Das Triple Zero-Gebäude: null Energie, null Emissionen, null Abfall. In: *15. Münchner Wissenschaftstage: Städte der Zukunft*, München, 14.-17.11.2015
- Spinks et al. 2002** Spinks, Geoffrey M; Wallace, Gordon G; Fifield, Leonard S; Dalton, Larry R; Mazzoldi, Alberto; Rossi, Danilo de; Khayrullin, Ilyas I; Baughman, Ray H., 2002. Pneumatic Carbon Nanotube Actuators. *Advanced Materials* **14** (23), pp. 1728–1732
DOI: 10.1002/1521-4095(20021203)14:23<1728:AID-ADMA1728>3.0.CO;2-8
- Spinks et al. 2006** Spinks, Geoffrey M; Mottaghitlab, Vahid; Bahrami-Samani, Mehrdad; Whitten, Philip G; Wallace, Gordon G., 2006. Carbon-Nanotube-Reinforced Polyaniline Fibers for High-Strength Artificial Muscles. *Advanced Materials* **18** (5), pp. 637–640
DOI: 10.1002/adma.200502366
- Sugino et al. 2011** Sugino, Takushi; Kiyohara, Kenji; Takeuchi, Ichiroh; Mukai, Ken; Asaka, Kinji, 2011. Improving the actuating response of carbon nanotube/ionic liquid composites by the addition of conductive nanoparticles. *Carbon* **49** (11), pp. 3560–3570
DOI: 10.1016/j.carbon.2011.04.056
- Sugino et al. 2018** Sugino, Takushi; Shibata, Yoshiyuki; Kiyohara, Kenji; Asaka, Kinji, 2018. Actuation mechanism of dry-type polymer actuators composed by carbon nanotubes and ionic liquids. *Sensors and Actuators B: Chemical* **273**, pp. 955–965
DOI: 10.1016/j.snb.2018.05.006
- Sul et al. 2009** Sul, Onejae; Yang, Eui-Hyeok, 2009. A multi-walled carbon nanotube-aluminum bimorph nanoactuator. *Nanotechnology* **20** (9), p. 95502
DOI: 10.1088/0957-4484/20/9/095502
- Sung 2011** Sung, Doris Kim, 2011. Skin Deep: Making Building Skins Breathe With Smart Thermobimetals. In: Pérez Gómez, Alberto; Cormier, Anne; Pedret, Annie (Eds.): *Where do you stand*. Washington, DC: ACSA Press, pp. 145-152
ISBN 978-0-935502-77-0
- Takeuchi et al. 2009a** Takeuchi, Ichiroh; Asaka, Kinji; Kiyohara, Kenji; Sugino, Takushi; Terasawa, Naohiro; Mukai, Ken; Shiraishi, Soshi, 2009. Electromechanical behavior of a fully plastic actuator based on dispersed nano-carbon/ionic-liquid-gel electrodes. *Carbon* **47** (5), pp. 1373–1380
DOI: 10.1016/j.carbon.2009.01.029

- Takeuchi et al. 2009b** Takeuchi, Ichiroh; Asaka, Kinji; Kiyohara, Kenji; Sugino, Takushi; Terasawa, Naohiro; Mukai, Ken; Fukushima, Takanori; Aida, Takuzo, 2009. Electromechanical behavior of fully plastic actuators based on bucky gel containing various internal ionic liquids. *Electrochimica Acta* **54** (6), pp. 1762–1768
DOI: 10.1016/j.electacta.2008.10.007
- Tamagawa et al. 2019** Tamagawa, Hirohisa; Okada, Kazuki; Mulembo, Titus; Sasaki, Minoru; Naito, Keishi; Nagai, Gakuji; Nitta, Takahiro; Yew, Khai-Chun; Ikeda, Kota, 2019. Simultaneous Enhancement of Bending and Blocking Force of an Ionic Polymer-Metal Composite (IPMC) by the Active Use of Its Material Characteristics Change. *Actuators* **8** (1), p. 29
DOI: 10.3390/act8010029
- Tanaka et al. 2010** Tanaka, Kazuhiro; Sugiura, Motonobu; Yamakita, Masaki; Kamamichi, Norihiro; Mukai, Toshiharu, 2010. Integrated Actuator-Sensor System of Bucky Gel Device. In: *Proceedings of SICE Annual Conference 2010*, pp. 2472–2478
- Tang et al. 2019** Tang, Teng; Yang, Dong-Hui; Wang, Lei; Zhang, Jian-Ren; Yi, Ting-Hua, 2019. Design and application of structural health monitoring system in long-span cable-membrane structure. *Earthquake Engineering and Engineering Vibration* **18** (2), pp. 461–474
DOI: 10.1007/s11803-019-0484-y
- Tauber et al. 2019** Tauber, Matthias; Feldkamp, Daniel; Christian Guse; Ailke Heidemann; Till Zupancic; Tobias Schriebl, 2019. *Building the Housing of the Future*
From: <https://www.bcg.com/publications/2019/building-the-housing-of-the-future.aspx>
- Terasawa et al. 2011** Terasawa, Naohiro; Ono, Norihiro; Hayakawa, Yoshio; Mukai, Ken; Koga, Tomoyuki; Higashi, Nobuyuki; Asaka, Kinji, 2011. Effect of hexafluoropropylene on the performance of poly(vinylidene fluoride) polymer actuators based on single-walled carbon nanotube–ionic liquid gel. *Sensors and Actuators B: Chemical* **160** (1), pp. 161–167
DOI: 10.1016/j.snb.2011.07.027
- Terasawa et al. 2012** Terasawa, Naohiro; Ono, Norihiro; Mukai, Ken; Koga, Tomoyuki; Higashi, Nobuyuki; Asaka, Kinji, 2012. A multi-walled carbon nanotube/polymer actuator that surpasses the performance of a single-walled carbon nanotube/polymer actuator. *Carbon* **50** (1), pp. 311–320
DOI: 10.1016/j.carbon.2011.08.072
- Terasawa et al. 2016** Terasawa, Naohiro; Asaka, Kinji, 2016. Electrochemical and Electromechanical Properties of Activated Multi-walled Carbon Nanotube Polymer Actuator that Surpass the Performance of a Single-walled Carbon Nanotube Polymer Actuator. *Materials Today: Proceedings* **3**, S178-S183
DOI: 10.1016/j.matpr.2016.02.030
- Terasawa 2017** Terasawa, Naohiro, 2017. High-performance ionic and non-ionic fluoropolymer/ionic liquid gel hybrid actuators based on single-walled carbon nanotubes. *RSC Advances* **7** (5), pp. 2443–2449
DOI: 10.1039/C6RA24925F
- Thess et al. 1996** Thess; Lee; Nikolaev; Dai; Petit; Robert; Xu; Kim; Rinzler; Colbert; Scuseria; Tomanek; Fischer; Smalley, 1996. Crystalline Ropes of Metallic Carbon Nanotubes. *Science* **273** (5274), pp. 483–487
DOI: 10.1126/science.273.5274.483
- Thomsen et al. 2004** Thomsen, C; Reich, S; Maultzsch, J., 2004. *Carbon Nanotubes: Basic Concepts and Physical Properties*: Weinheim. Wiley-VCH. ISBN 9783527403868
DOI: 10.1002/9783527618040
- Torop et al. 2011** Torop, Janno; Palmre, Viljar; Arulepp, Mati; Sugino, Takushi; Asaka, Kinji; Aabloo, Alvo, 2011. Flexible supercapacitor-like actuator with carbide-derived carbon electrodes. *Carbon* **49** (9), pp. 3113–3119
DOI: 10.1016/j.carbon.2011.03.034
- Tripathi et al. 2019** Tripathi, A. S; Chattopadhyay, B. P; Das, S., 2019. Cost-effective fabrication of ionic polymer based artificial muscles for catheter-guidewire maneuvering application. *Microsystem Technologies* **25** (3), pp. 1129–1136
DOI: 10.1007/s00542-018-4152-3
- Ulrich et al. 1976** Ulrich, Peter; Hill, Wilhelm, 1976. Wissenschaftstheoretische Grundlagen der Betriebswirtschaftslehre (Teil I und II). *Zeitschrift für Ausbildung und Hochschulkontakt* **5** (7+8), pp. 304–309

- United Nations 2017** United Nations, 2017.
World population prospects: The 2017 revision : key findings and advance tables.
2017 revision: New York. United Nations.
Department of Economic & Social Affairs ESA/P/WP. 248.
ISBN 9211515319
- Vidal et al. 2008** Vidal, Frederic; Plesse, Cedric; Palaprat, Guillaume; Juger, Jonathan; Citerin, Johann; Kheddar, Abderrahmane; Chevrot, Claude; Teyssié, Dominique, 2008. Synthesis and Characterization of IPNs for Electrochemical Actuators.
Advances in Science and Technology **61**, pp. 8–17
DOI: 10.4028/www.scientific.net/AST.61.8
- Vidal et al. 2004** Vidal, Frédéric; Plesse, Cédric; Teyssié, Dominique; Chevrot, Claude, 2004. Long-life air working conducting semi-IPN/ionic liquid based actuator.
Synthetic Metals **142** (1-3), pp. 287–291
DOI: 10.1016/j.synthmet.2003.10.005
- Vunder et al. 2012** Vunder, Veiko; Punning, Andres; Aabloo, Alvo, 2012. Mechanical interpretation of back-relaxation of ionic electroactive polymer actuators.
Smart Materials and Structures **21**, p. 115023
DOI: 10.1088/0964-1726/21/11/115023
- Wang et al. 2017** Wang, Dongxing; Lu, Chao; Zhao, Jingjing; Han, Song; Wu, Minghong; Chen, Wei, 2017. High energy conversion efficiency conducting polymer actuators based on PEDOT:PSS/MWCNTs composite electrode.
RSC Advances **7** (50), pp. 31264–31271
DOI: 10.1039/c7ra05469f
- Wang et al. 2018** Wang, Xinya; Xiao, Changfa; Liu, Hailiang; Huang, Qinglin; Fu, Hao, 2018. Fabrication and properties of PVDF and PVDF-HFP microfiltration membranes.
Journal of Applied Polymer Science **135** (40), p. 46711
DOI: 10.1002/app.46711
- Wu et al. 2014** Wu, G; Li, G. H; Lan, T; Hu, Y; Li, Q. W; Zhang, T; Chen, W., 2014. An interface nanostructured array guided high performance electrochemical actuator.
J. Mater. Chem. A **2** (40), pp. 16836–16841
DOI: 10.1039/c4ta04268a
- Xie et al. 2000** Xie, Sishen; Li, Wenzhi; Pan, Zhengwei; Chang, Baohe; Sun, Lianfeng, 2000. Carbon nanotube arrays.
Materials Science and Engineering: A **286** (1), pp. 11–15
DOI: 10.1016/S0921-5093(00)00657-2
- Yamato et al. 2012** Yamato, Kentaro; Mukai, Ken; Hata, Kenji; Asaka, Kinji, 2012. Fast-moving bimorph actuator based on electrochemically treated millimeter-long carbon nanotube electrodes and ionic liquid gel.
International Journal of Smart and Nano Materials **3** (4), pp. 263–274
DOI: 10.1080/19475411.2011.652992
- Yan et al. 2017a** Yan, Bingxi; Wu, Yu; Guo, Liang, 2017. Recent Advances on Polypyrrole Electroactuators.
Polymers **9** (12), p. 446
DOI: 10.3390/polym9090446
- Yan et al. 2017b** Yan, Yunsong; Santaniello, Tommaso; Bettini, Luca Giacomo; Minnai, Chloé; Bellacicca, Andrea; Porotti, Riccardo; Denti, Ilaria; Faraone, Gabriele; Merlini, Marco; Lenardi, Cristina; Milani, Paolo, 2017. Electroactive Ionic Soft Actuators with Monolithically Integrated Gold Nanocomposite Electrodes.
Advanced Materials **29** (23)
DOI: 10.1002/adma.201606109
- Yeom et al. 2009** Yeom, Sung-Weon; Oh, Il-Kwon, 2009. A biomimetic jellyfish robot based on ionic polymer metal composite actuators.
Smart Materials and Structures **18** (8), p. 85002
DOI: 10.1088/0964-1726/18/8/085002
- Yokomichi et al. 2008** Yokomichi, Haruo; Ichihara, Masaki; Nimori, Shigeki; Kishimoto, Naoki, 2008. Morphology of carbon nanotubes synthesized by thermal CVD under high magnetic field up to 10T.
Vacuum **83** (3), pp. 625–628
DOI: 10.1016/j.vacuum.2008.04.037
- Zahiri 2019** Zahiri, Nima, 2019.
Electroactive Skin: Towards Bio-inspired Soft Responsive Envelopes.
Stuttgart, University of Stuttgart, 2019

- Zhang et al. 2009** Zhang, Hao; Cao, Gaoping; Wang, Weikun; Yuan, Keguo; Xu, Bin; Zhang, Wenfeng; Cheng, Jie; Yang, Yusheng, 2009. Influence of microstructure on the capacitive performance of polyaniline/carbon nanotube array composite electrodes. *Electrochimica Acta* **54** (4), pp. 1153–1159
DOI: 10.1016/j.electacta.2008.09.004
- Zhang et al. 1998** Zhang, Q. M; Bharti, Vivek; Zhao, X., 1998. Giant Electrostriction and Relaxor Ferroelectric Behavior in Electron-irradiated Poly(vinylidene fluoride-trifluoroethylene) Copolymer. *Science* **280** (5372), pp. 2101–2104
DOI: 10.1126/science.280.5372.2101
- Zhang et al. 1999** Zhang, Y; Iijima, S., 1999. Elastic Response of Carbon Nanotube Bundles to Visible Light. *Physical Review Letters* **82** (17), pp. 3472–3475
DOI: 10.1103/PhysRevLett.82.3472
- Zhao et al. 2021** Zhao, Dongxu; Ru, Jie; Wang, Tong; Wang, Yanjie; Chang, Longfei, 2021. Performance Enhancement of Ionic Polymer-Metal Composite Actuators with Polyethylene Oxide. *Polymers* **14** (1)
DOI: 10.3390/polym14010080
- Zhao et al. 2013** Zhao, Yang; Xu, Bing; Zheng, Gaofeng; Zheng, Jianyi; Qiu, Xiaochun; Zhuang, Mingfeng; Sun, Daoheng, 2013. Improving the performance of IPMCs with a gradient in thickness. *Smart Materials and Structures* **22** (11), p. 115035
DOI: 10.1088/0964-1726/22/11/115035
- Zhao et al. 2018** Zhao, Yang; Di Xu; Sheng, Jiazheng; Meng, Qinglong; Wu, Dezhi; Wang, Lingyun; Xiao, Jingjing; Lv, Wenlong; Chen, Qinnan; Sun, Daoheng, 2018. Biomimetic Beetle-Inspired Flapping Air Vehicle Actuated by Ionic Polymer-Metal Composite Actuator. *Applied bionics and biomechanics* **2018**, p. 3091579
DOI: 10.1155/2018/3091579
- Zhou et al. 2003** Zhou, Dezhi; Spinks, Geoffrey M; Wallace, Gordon G; Tiyaipoonchaiya, Churat; MacFarlane, Douglas R; Forsyth, Maria; Sun, Jiazeng, 2003. Solid state actuators based on polypyrrole and polymer-in-ionic liquid electrolytes. *Electrochimica Acta* **48** (14-16), pp. 2355–2359
DOI: 10.1016/S0013-4686(03)00225-1

Appendix

A.1.1 Hygrothermal conflicts in building envelopes

The basic function of a building envelope with structural-physical relevance is to balance the building requirement for daylight and ventilation while taking care of moisture and thermal protection pertinent to the micro-climate of the place where the building is located (HARRY 2016). Maintaining acceptable temperatures in buildings by artificial heating and cooling is responsible for a large proportion of global energy consumption. In conventional buildings the exterior walls are equipped with insulation layers to keep the heat inside in winter and outside during hot summer days. The insulation layers are made from material compounds with low thermal conductivity serving as a heat barrier. They are attached to the inside or outside (or both) of the load-bearing wall structure. The insulation compound is mostly made up of air, which has very low heat conductivity.

The thermal conductivity through the walls is approximately proportional to the temperature difference ΔT between the inside and the outside, the surface area of thermal contact and the inverse of the thickness of the wall material d . Air always contains water in the form of water vapor and has a certain water vapor pressure, which is usually well above the saturation water pressure or dew point. Warm air can hold more water than cold air, meaning that the saturation water pressure is also dependent on air temperature.

When there is an insulation layer in the wall, the temperature drop between the inside and the outside can be significant. Once the vapor pressure sets below the saturation pressure at some area within the wall condensation occurs in that area, often within the insulation material.

Condensation in building construction is an unwanted phenomenon as it may cause dampness, mold health issues, wood rot, corrosion, weakening of mortar and masonry walls, and energy penalties due to increased heat transfer. To alleviate these issues, the indoor air humidity needs to be lowered, or air ventilation in the building needs to be improved. However, most conventional wall materials such as concrete, masonry and bricks are highly porous materials and thus capable of capillary diffusion and water sorption (Figure A1, top). This means that humidity from condensation can be stored inside the walls for some time, before it will be transported back to the external surface of the wall where it will be dried out over time (Figure A1, bottom). A material's capability of transporting water vapor is also called water vapor permeability or *breathability*. The water vapor transmission characteristics of aerated concrete is described in (Karagiozis et al. 2001).

For multi-layer membrane constructions this process is slightly different. Once water vapor is trapped inside the membrane interspace, there is no breathable material capable of capillary diffusion. Once condensation occurs, the water is trapped inside the membrane construction and the insulation layer may be soaked with water, leading to the formation of ice crystals and subsequent failure of the insulating functionality.

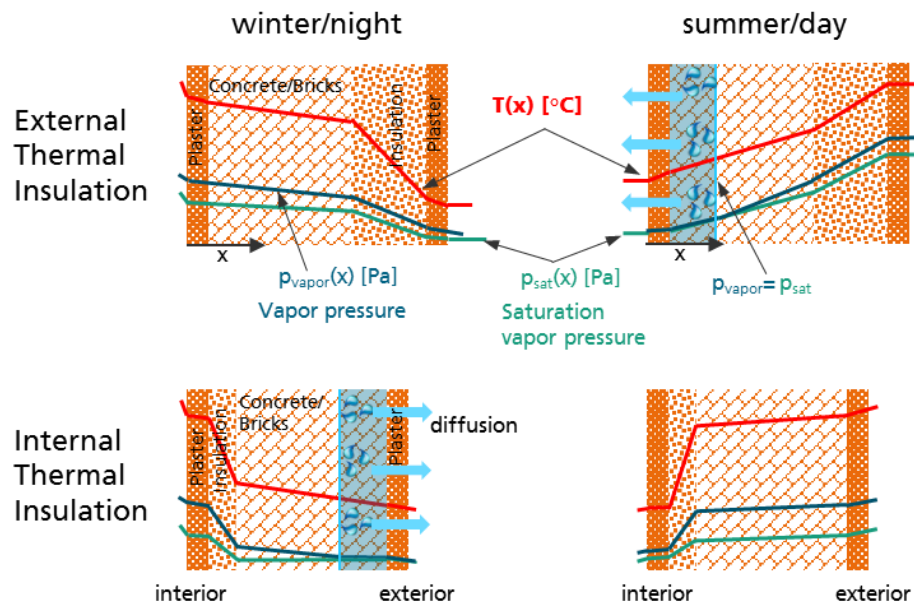


Figure A1 – Depiction of hygrothermal management in conventional building envelopes made of masonry walls and insulation material composites.

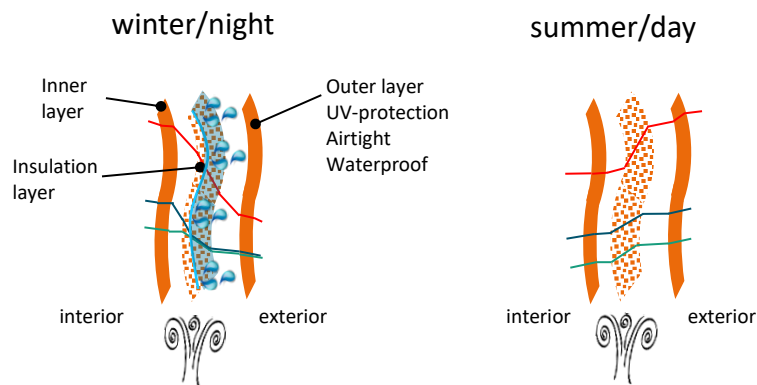


Figure A2 – Depiction of hygrothermal phenomena in multi-layer membrane envelopes. Trapped condensation is dried out with the help of mechanical fan heaters

A.1.2 Author's reasoning for quantitative IEAP requirements

“Material cost < 1 €/cm² of actuator laminate”

The total material cost is one of the most stated obstacles when discussing market adoption and real-world applicability of IEAP actuators and sensors. The threshold of 1 €/cm² of actuator laminate was chosen because some literature statements (e.g. Oh et al 2019) have postulated that the total material price for IPMCs will drop below this margin within the next decade, provided that some mass industrialization will take place in the upcoming years. As CNT-based actuators – especially those made with MWCNTs – are cheaper, this value may serve as a conservative estimate for a reasonable cost requirement.

“Production capacity > 10000 pieces / week / line”

With a fictional packing density of fifty actuators integrated into one square meter of building envelope, an average three-story building with 200 square meters of visible textile cladding would require 10000 actuator pieces. This number reflects that one production line must be capable of producing this number of actuators to permit the construction of at least one adaptive building envelope per week. Furthermore, this number was chosen to eliminate those potential IEAP candidates that require highly complex and costly manufacturing equipment such as vapor deposition chambers and polymerization reactors, which are not suitable for mass fabrication and thus cause higher fabrication cost and longer production cycles. In principle, 2000 working pieces of properly dimensioned, contacted, encapsulated and tested IEAP actuators per day require a continuous roll-to-roll manufacturing process.

“Tolerances of component dimensions < ± 2%”

This is a general construction requirement for prototype IEAP systems that the author deemed suitable for such small dimensions. The width, length and thickness values for

CNT-based actuators have a direct impact on their performance and should thus be within a reasonable yet achievable range.

A.1.3 Benchmarking parameters for IEAPs

The following three tables include manufacturing times for individual fabrication steps and cost estimates for the materials used vor IMPC, PC and CNT-based actuators.

Type	Vidal et al. (2004)		Cho et al. (2007)		Kim et al. (2013)		Jiang et al. (2016)		Wang et al. (2017)		Park et al. (2018)		Poldisalu et al. (2018)	
	Steps	Time	Steps	Time	Steps	Time	Steps	Time	Steps	Time	Steps	Time	Steps	Time
PEO based (semi) IPN / ionic liquid CP actuator	Weighing (30min) and mixing (30min) of chemicals in solution	1h	Preparation of NBR electrolyte film	2h	Mixing of anhydrous THF, MeOH, and PSS-b-PMB copolymer and IL	24h*	Preparation of Graphene Oxide (GO) solution	24h	TPU and EMI-BF4 in DMF @80°C for electrolyte solution	24h	Nafion membrane in LiCl solution for ion exchange	12h	Mixing PVA and water, NBR and solvent (both overnight)	24h
	Casting of PB/PEO film in glass mold and heating at 50°C	3h	Preparation of PEDOT/NBR/BMITFSI composite film	6h	Casting and drying under Argon atmosphere @RT	48h	Drying of GO film at 40°C in Petri dish	48h	Casting & drying @80°C on glass substrate	48h	Vacuum drying @120°C and 0.66 Pa	12h	Spincoating and drying PVA layer @80°C	1h
Preparation of Electrodes	Post-curing @80°C	1h	Washing with methanol	2h	Vacuum drying at 70°C	168h	Exposition to polypropylene monomer vapor - synthesis of pGO-PPy film	72h	Dispersing MWCNT in PEDOT:PSS for electrode (magnetic stirring)	6h	Ion substitution with ionic liquid @150°C	4.5h	Add PEO to NBR, Stirring	0.5h
	Soaking of PB/PEO film in EDOT	1h	Vacuum drying at RT	24h	Pressing for parallel orientation of microdomains	12h	Reduction to G-PPy film using Hydrogen iodide (HI, 54%)	24h	Ultrasonic bath treatment	2h	Heat pressing	1h	Add DCPD to PEO, Stirring	0.5h
Actuator	Immersing in FeCl3 solution	24h	Cutting off edges, layer treatment	2h	Stirring of SWCNT, PvdF-HFP and EMIM-BF ₄ in DMAC	24h	Ethanol washing	3h	Casting & drying @60°C on glass substrate	24h	Preparation of graphene on Cu substrate	24h*	Spincoating NBR/PEO on PVA, curing @50°C	4h
	Methanol washing and cleaning	5h*	Immersing in 50/50 CH ₂ Cl ₂ /BMITFSI solution	24h	Ultrasonic bath treatment	6h	Drying at room temperature	12h	Heat pressing of electrode/electrolyte laminate @170°C	4h	Spin-coating of PMMA on Cu/graphene, Cu etching	4h	Inkjet printing of 10 layers of PEDOT:PSS ink @45°C, 1mbar	1h*
Sum	Vacuum dry in @60°C	24h	Evaporation of residual solvent in air	24h*	Casting and vacuum drying at 80°C	24h	Actuator preparation	2h*	Cooling to RT and actuator preparation (cutting)	4h*	Vacuum drying	24h*	Vacuum drying	12h*
	Immersing in 50/50 CH ₂ Cl ₂ /EMITFSI solution	24h	Hotpressing of actuator laminate and cutting	2h*									Dissolution of PVA layer in water, drying @RT (overnight)	24h
Cost	> 5 €/cm ² *	83h	> 3 €/cm ² *	84h	> 10 €/cm ² *	308h	> 15 €/cm ² *	185h	> 2 €/cm ² *	112h	> 5 €/cm ² *	97.5h	< 3 €/cm ² *	71h
*) Author's assumption														

Type	Fukushima et al. (2005)		Biso and Ricci (2009)		Sugino et al. (2011)		Biso et al. (2012)		Terasawa et al. (2016)		Neuhaus et al. (2019c)		Ru et al. (2019)		
	Steps	Time	Steps	Time	Steps	Time	Steps	Time	Steps	Time	Steps	Time	Steps	Time	
Preparation of Electrolyte	SWCNT Bucky Gel actuator through layer-by-layer casting		Pure MWCNT Bucky Gel actuator		PANI-enhanced SWCNT Bucky Gel actuator		Bucky Gel SWCNT/Polypyrrole hybrid actuator		MWCNT based Bucky Gel actuator		Fast MWCNT Bucky Gel actuator without vacuum drying		Commercial SWCNT electrode sheet Nafion		
	Magnetic stirring of PVDF, IL in 4M2P	2h	Dissolving (3h) of 50/50 PVDF and BMIM-BF ₄ in THF and mixing (3h) for electrolyte preparation	6h	Magnetic stirring of PVDF, IL in 4M2P	2h	Mixing of PVDF and BMIM-BF ₄ for electrolyte preparation	2h	Mixing of PVDF and BMIM-BF ₄ in DMAc for electrolyte preparation	2h*	Magnetic stirring of PVDF, IL in 4M2P	1h	Mixing of 50wt% Nafion and EMIM-BF ₄ in DMAc for electrolyte preparation	4h	
			Casting and drying	24h	Casting and drying (overnight)	(24h)	Casting and drying (overnight)	24h	Casting and drying	24h	Casting (only a portion of the mixture) and drying	(12h)	Casting and vacuum drying @80°C	12h	
			Pressing and cutting	1h			Pressing and cutting	1h					Annealing @120°C and cutting before hot-pressing	2h	
	Preparation of Electrodes	Grinding of SWCNT suspension in IL and transfer to dissolved PDVF solution	1h	Grinding MWCNTs in IL (EMI-TFSI) and mixing in PVDF in THF	1h	Magnetic stirring of SWCNT, Pani, PVDF, IL in 4M2P	24 - 72h	Grinding SWCNTs in IL (EMI-TFSI) and mixing of Pyrrole	6h*	Ultrasonication of PVDF, EMI-BF ₄ , MWCNT in DMAc	5h	Adding MWCNTs, Pani and continue magnetic stirring	1h		
		3x casting of SWCNT mixture and electrolyte mixture into Al-mold	1h	Sonication	1h	Ultrasonic bath (36kHz)	24h	Polymerization in nitrogen atmosphere	20h	Casting and drying	12h	Ultrasonication @35kHz, 8.5min	0.2h		n.a.
		Repeated cooling	2h*	Mold casting and drying	24h*	Casting and heat-plate assisted drying	12h	Filtration of hybrid powder, washing and drying (overnight)	24h	Vacuum drying @80°C	24h	Dissolver treatment @3500 rpm	0.2h		
		drying (overnight)	24h			Vacuum assisted drying @80°C	72h	Grinding hybrid powder with IL (BMIM-BF ₄), adding PVDF & DMAc	12h			Casting and heat-assisted air drying	12h		
		Vacuum assisted drying	48h*	Hot-pressing of bucky gel and electrolyte layers and cutting of actuator stripes	2h	Cutting, heat pressing	1h	Sonication	0.5h	Cutting, heat pressing	1	Cutting electrodes and separators and hot-pressing actuators	1h	Sandwiching electrolyte layer between two commercial SWCNT sheets	1h*
								Mold casting & drying	24h*					hot-pressing under vacuum conditions	12h*
Actuator Preparation							Hot-pressing of bucky gel and electrolyte layers and cutting of actuator stripes	2h					Hot-pressing under atmospheric conditions @180°C	0.5h	
Sum				59h		183h		115-5h		68h		16h		31.5h	
Cost	< 4 €/cm ² *		0.85 €/cm ²		> 2 €/cm ²		4.80 €/cm ²		0.55 €/cm ² *		< 0.40 €/cm ²		0.50 €/cm ² *		
*) Author's assumption															

A.1.4 Buckypaper fabrication and electrochemical analysis

The preparation of Buckypaper involved vacuum filtration of aqueous SWCNT dispersion on a membrane filter, washing with water and methanol for removal of amorphous carbon and catalyst residues, air drying and subsequent removal from the filter. Cyclic voltammetric (CV) measurements between ± 0.8 V at different scan rates in 1.0 M NaCl, 7.0 M H₂SO₄, and 5.0 M KOH suggested that minor redox reactions occur at the carbon/electrolyte interface. It was assumed that oxygen-containing residues and functional groups are present in the Buckypaper despite the mentioned washing procedure after fabrication. Furthermore, the absence of strong scan rate effects on the capacitance in conjunction with the lack of influence of the electrolyte nature on the voltammetry and capacitance of each Buckypaper sample indicated that all ions, regardless of size and charge, were able to penetrate the pores of the material. Nonetheless large deviations in specific capacitance values between individual electrode samples (14 F/g up to 40 F/g) hinted towards different specific surface areas of the electrodes that are accessible to the electrolyte ions, which in turn is a strong indication of inconsistent CNT bundle densities due to fabrication inaccuracies. Some CV curves showed that not only non-faradaic charge balance, but also faradaic pseudo-capacitive phenomena are present for some electrolyte species. This strengthened the initial assumption of a strong similarity between the operation principles of Buckypaper actuators and supercapacitor electrodes.

It has been observed that higher charge densities within the CNT structures of Buckypaper electrodes yield higher actuation strains. Thus it is evident that the ability to store charge determines the performance capabilities of such actuator applications. As already stated in the previous paragraph, more charges can be inserted into the Buckypaper electrodes when they are immersed in an electrolyte solution with counter-ions balancing the electronic charges within an electrochemical double layer at the carbon/electrolyte interface. The ability to charge the carbon structure is thus dependent on the

inert electrochemical potential window of the electrolyte, given the inert nature of carbon. A variety of organic and inorganic electrolytes have been tested for a general investigation of the electrochemical behavior of Buckypaper in the presence of different ion species (Barisci et al. 2000). The ultimate goal was to predict and optimize their actuation performance.

In 2002, a giant actuator response of ~3% in planar direction and of >300% in thickness direction has been reported by Spinks et al. 2002 (Spinks et al. 2002) for unannealed SWCNT sheets immersed in an aqueous NaCl solution with very high concentration (5M). The effect emerged after a few iterations of square-wave cycling at high potentials (+1.5V) and was attributed to the electrochemical generation and re-oxidization of hydrogen gas within pneumatic chambers trapped inside the Buckypaper nanotube mesh, increasing the Buckypaper thickness to over threefold. The energy conversion efficiency of such actuators was not believed to be competitive to the expected achievements with non-faradaic systems or with electrostrictive actuators based on elastomers. Furthermore, only a few hundred cycles could be achieved with such actuator strokes.

To further increase actuation responses of Buckypaper actuators, ionic liquids (IL) have been tested as electrolytes (Barisci 2004). They are basically salts that are liquid at room temperature. Latest findings regarding ILs in CNT-based actuators and their application potential for architectural uses have been gathered and illustrated in chapter 3.2.1. Their wide electrochemical potential windows (up to 5.3V for P-TFSA) combined with their environmental stability and non-volatile nature were expected to enhance actuator strokes by allowing much higher potential differences compared to aqueous or organic electrolytes. Using cyclic voltammetry and impedance spectroscopy, a positive correlation between electrolyte conductivity and electrode capacitance was found for all investigated species of IL. Despite the higher potentials applied to the Buckypaper, measurements yielded some loss of capacitance and charging rate compared to conventional electrolytes. Even though no actuation responses were reported, the use of IL

electrolytes in conjunction with CNT electrodes has proved possible and advantageous. Additionally, the first CNT-based electrode operable in air was successfully tested with a Buckypaper deposited on a porous PVDV membrane and soaked in IL.

A.1.5 Web of Science Search Terms

For collecting information about the number of published scientific articles per year referring to EAPs and its sub-species, the following search terms were used:

TOPIC	ADVANCED SEARCH TERM
Electroactive Polymers (EAP = general term)	TS=((electroactive OR electro-active) AND polymer*)
Dielectric Elastomer Actuators (DEA)	TS=(((electronic OR dielectric) (elastomer OR polymer* OR EAP) actuat*) NOT ionic)
Ionic Polymer-Metal Composite Actuators (IPMC)	TS=(("ion* polymer metal composite*" OR IPMC*) actuat* NOT dielectric)
Conjugated Polymer Actuators	TS=(("conductive polymer*" OR "conjugated polymer*") actuat* NOT dielectric)
CNT / Bucky-Gel Actuators	TS=(("bucky gel*" OR bucky-gel* OR "bucky paper" OR ("Carbon nanotube*" OR CNT* OR SWCNT* OR MWCNT*) AND ionic)) AND actuat*)

The "TS" stands for a "Topic Search", taking into consideration the publication's title, abstract, author keywords and keywords plus (Web of Science, 2020).

